This electronic thesis or dissertation has been downloaded from the King's Research Portal at https://kclpure.kcl.ac.uk/portal/

KING'S College LONDON

Unified theory of double twinning in magnesium confirmed by experiment

Ruffino, Martina

Awarding institution:
King's College London

The copyright of this thesis rests with the author and no quotation from it or information derived from it may be published without proper acknowledgement.

END USER LICENCE AGREEMENT

Unless another licence is stated on the immediately following page this work is licensed

under a Creative Commons Attribution-NonCommercial-NoDerivatives 4.0 International

licence. https://creativecommons.org/licenses/by-nc-nd/4.0/

You are free to copy, distribute and transmit the work

Under the following conditions:

- Attribution: You must attribute the work in the manner specified by the author (but not in any way that suggests that they endorse you or your use of the work).
- Non Commercial: You may not use this work for commercial purposes.
- No Derivative Works - You may not alter, transform, or build upon this work.

Any of these conditions can be waived if you receive permission from the author. Your fair dealings and other rights are in no way affected by the above.

Take down policy

If you believe that this document breaches copyright please contact librarypure@kcl.ac.uk providing details, and we will remove access to the work immediately and investigate your claim.

Download date: 08. Oct. 2023

Unified theory of double twinning in magnesium confirmed by experiment

Martina Ruffino

Supervisors: Prof. Tony Paxton, Dr. George Booth

Department of Physics

King's College London

This dissertation is submitted for the degree of Doctor of Philosophy.

August 2023

Publications

The following publications are mentioned in this thesis:

- Martina Ruffino, Guy C. G. Skinner, Eleftherios I. Andritsos, Anthony T. Paxton. Ising-like models for stacking faults in a free electron metal. *Proceedings of the Royal Society A: Mathematical, Physical and Engineering Sciences.* 476(2242), 2020.

- Martina Ruffino, John Nutter, Xun Zeng, Dikai Guan, W. Mark Rainforth, Anthony T. Paxton. Triple and double twin interfaces—the role of disconnections and facets. *Scientific Reports.* 13(1), 2023.

Acknowledgements

This thesis has been three and a half years in the making, and while it bears my name, I did not walk alone in this journey. My first acknowledgement goes to my supervisor, Tony Paxton, who not only believed in me from the start, but guided and supported me throughout my PhD, including, and perhaps most importantly, during the difficult months of isolation brought on by the pandemic. I would also like to acknowledge my second supervisor, George Booth, who was of great help with technical matters. Particular thanks go to Bob Pond, whose topological models are the foundation of this thesis and whose stimulating discussion has been invaluable.

I would specially like to thank Luxfer MEL Technologies for sponsoring this PhD, and particularly Matt Murphy, head of Magnesium R&D. I thoroughly enjoyed the time I spent at the site in Swinton, and I thank Alex Charlesworth and everyone at Magnesium R&D for their warm welcome and for taking the time to introduce me to something new.

When I was not commuting to Manchester, I was in Sheffield, and heartfelt thanks go to Mark Rainforth for hosting me with his group at the Department of Materials Science and Engineering. If someone had told me, when I started this PhD, that I would work on experiment and enjoy it, I would not have believed them. But it happened, and I owe that to Dikai Guan and Xun Zeng, who first introduced me to electron microscopy, and most of all to John Nutter, who showed me that you can have a good time hanging out in a basement if there is a big enough microscope in it (and a pub close by for when technical issues inevitably arise).

I have quite a few people to thank at King's, including former and current members of Tony's group, whose help and support were truly appreciated. Lefteri Andritsos, who cheerfully introduced me to most diverse pastimes: DFT codes and Dungeons & Dragons. Tigany Zarrouk, whose solidarity and encouragement I constantly felt despite the fact that I only got to sit next to him for three months. Guy Skinner, who readily shared his expertise with me. Sasha Lozovoi, for his incredible kindness towards me and his sunny attitude, and for sharing with me his passion

for the writings of the Strugatsky brothers. Ivo Katsarov, who often offers a *memento mori* (though his wisdom is certainly not limited to that). Dimitar Pashov, who knows everything about computers and is always ready to help out. Luke Simpson, who did not take it badly when he found out that for years I had been confused by his accent. Rob Jones, whose recommendation of Terry Pratchett's books turned out to be a gold mine. Paul Le Long, for making me feel welcome in the department since my undergraduate days (though he once shot me with his Nerf gun) and for the D&D sessions; thank you also to Simone Kippins and the rest of the admin at the Physics department, whose help deserves a shoutout.

A big acknowledgement goes to my family. Mamma, Papà, Ele and Nonna have supported me my whole life, and though in the last few years they have done this from afar, I have felt their affection just as strongly. Deeply felt thanks go to my friends, who always cheer me on. Marta Baldracchi, with whom I have moved many times and always managed to make a home even of less than ideal places. Christian Righetti, who has been my best friend for as long as I can remember and without whom I can't imagine my life. Sonia Ben Cheikh, who is probably the person with whom I have laughed the most. Anna Chiara Muci, with whom I bonded over missing home and who has been a great friend ever since. Dom Robson, who listens to my rants and turns them into anecdotes, while introducing me to the best pubs in the country. Eddie Lambden, for helping to keep me sane while I was writing this thesis and for always being fun. Edoardo Righelli, the big brother I never had, who first made me watch The Lord of the Rings and had no idea that he was about to open Pandora's box and unleash my obsession. Chiara Autelli, whose sarcasm always inspires my own. Fede Albertini, whose videocalls cheered me up during the lockdowns. And Amardeep Chawla, who unfailingly believes in me. Last but not least, a thank you goes to little Carotino: he may not be the smartest ball of fur around, but he is irresistibly cute when he wants to be.

Abstract

Magnesium alloys find application in a variety of industries, such as the aerospace, automotive and medical industries, due to magnesium's high strength-to-weight ratio. A number of magnesium alloys contain rare earth elements, which randomise the otherwise strong basal texture of the materials, thus improving their ductility and formability. Recently, rare-earth texture has been obtained in rare-earth-free alloys containing calcium, and the importance of double twins in inducing the nucleation of recrystallised grains with randomised orientations has been shown. Double twinning itself is not a well-understood phenomenon, and the experimental work carried out on magnesium alloys has highlighted the need for further theoretical research on the topic. With the term double twin we indicate a twin that retwins internally for a second time, and in magnesium the most common double twinning sequence is $(10\bar{1}1) - (10\bar{1}2)$. In this thesis we focus on the structure of double twin to matrix interfaces, whose orientation within the parent grain has not been measured unambiguously so far. The foundations of this work are bicrystallography and the topological theory of interfacial defects, which exploit crystal symmetry to predict the admissible defects in an interface. They are applied in chapter 2 to classical twinning, which in magnesium occurs on the $(10\bar{1}2)$, $(10\bar{1}1)$ and $(10\bar{1}\bar{3})$ planes; twinning disconnections accomplishing the twinning shears are derived. In chapter 3 the phenomenological theories of double twinning as a simple shear occurring on an invariant plane in a one-step process are reviewed. These are then contrasted with the topological model, according to which double twinning entails a two-step process where a primary twin is first formed by the nucleation and motion of primary twinning disconnections and internal retwinning is then mediated by secondary twinning disconnections. In particular, it is shown that the predictions for the double twin habit planes of the phenomenological theory may be reproduced in the topological model by requiring that the final double twin to matrix interface be rendered free of misfit. The phenomenological and topological approaches are thus unified, and their differences and similarities

are pointed out. In chapter 4, the case of faceted twin interfaces is considered. Facets have been shown to exist in experimental observations of single twin interfaces, and they have been modelled theoretically as accumulations of twinning disconnections; here the topological model is used to predict the emergence of commensurate facets in double twin to matrix interfaces as a result of the combination of primary and secondary twinning disconnections. High-resolution transmission electron microscopy is then used to seek validation of theoretical predictions: a hot rolled rare-earth magnesium alloy is investigated, and $(\bar{1}012) - (\bar{1}011)$ double twins are observed. The commensurate facets envisaged in the topological model are reported to exist in the double twin to matrix interfaces, and are found to cause the interfaces to deviate from the orientation of the primary twinning plane; this is proposed to be the reason for the lack of agreement between measurements of the macroscopic orientation of double twin interfaces in the literature. Moreover, $(\bar{1}012) - (\bar{1}011) - (\bar{1}012)$ triple twins are found in the specimen, and the interface between a triple twin and the matrix is observed for the first time. This interface is found to be fully incommensurate, as predicted by analysis carried out using the topological model.

Table of contents

List of figures **10**

List of tables **13**

List of abbreviations **14**

1 Introduction **16**

1.1 Rare-earth texture and double twinning 16

1.2 The hexagonal basis and Miller-Bravais indices 21

1.3 Early theories of classical twinning 29

1.3.1 Classical twins in magnesium 37

1.4 Atomistic simulations: the adaptive Generalized Pseudopotential Theory (aGPT) 39

1.5 Structure of this thesis 42

2 Bicrystallography and the topological theory of interfacial defects **44**

2.1 Theory 44

2.1.1 Bicrystallography 45

2.1.2 The topological theory of line defects 57

2.2 Application to classical twins in magnesium 64

2.2.1 The $(10\bar{1}2)$ twin as a bicrystal 64

2.2.2 The $(10\bar{1}1)$ compression twin and its reciprocal $(10\bar{1}\bar{3})$ mode 70

2.2.3 Twinning disconnections at the $(10\bar{1}2)$, $(10\bar{1}1)$ and $(10\bar{1}\bar{3})$ twin boundaries 74

3 Double twinning **86**

3.1 Double twin misorientation relations 87

3.2 Crocker's theory of double twinning 94
3.2.1 $(10\bar{1}1)-(10\bar{1}2)$ double twinning and equivalent modes 100
3.2.2 $(10\bar{1}2)-(10\bar{1}1)$ double twinning and equivalent mechanisms 103
3.3 Bevis & Crocker's theory of non-classical twinning 105
3.3.1 Application to the hexagonal lattice and double twinning 114
3.4 Topological treatments of double twinning 121
3.4.1 Disconnections impinging on a flat interface 121
3.4.2 Mechanistic model of interfaces containing disconnections 126
3.5 Comparison between the topological and phenomenological models 134

4 Faceting at twin interfaces **138**
4.1 Topological models of facets 138
4.1.1 Facets in $(10\bar{1}2)$, $(10\bar{1}1)$ and $(10\bar{1}\bar{3})$ twin interfaces 139
4.1.2 Faceting in double twin boundaries 147
4.1.3 Triple twinning and facets in triple twin interfaces 155
4.2 TEM observations of twin interfaces 157
4.2.1 Experimental methods 158
4.2.2 Materials and preliminary results 165
4.2.3 Experimental results 168
4.2.4 Discussion of experimental results 177

5 Further work and conclusions **182**

References **189**

List of figures

1.1 Rare-Earth texture formation in Mg-0.8Zn-0.2Ca alloy 19
1.2 Hexagonal unit cell and basis vectors 26
1.3 Shape changes resulting from invariant-plane strains 30
1.4 Twinning elements 31
1.5 Possible choices for the hexagonal bases 37
1.6 Projection of the hcp structure onto the $(1\bar{2}10)$ plane illustrating atomic shuffles for $(10\bar{1}2)$ and $(10\bar{1}1)$ twinning 39

2.1 Dissymmetrization scheme 57
2.2 Volterra-like procedure for the creation of defects in bicrystals 58
2.3 Dichromatic patterns of the $(10\bar{1}2)$ twin 66
2.4 Dichromatic complexes of the $(10\bar{1}2)$ twin 67
2.5 $(10\bar{1}2)$ twin 68
2.6 Relaxation of $(10\bar{1}2)$ twin. 69
2.7 Dichromatic pattern of the $(10\bar{1}1)$ twin 71
2.8 Dichromatic complexes of the $(10\bar{1}1)$ twin 72
2.9 $(10\bar{1}1)$ twin 73
2.10 Relaxation of $(10\bar{1}1)$ twin. 74
2.11 Dichromatic pattern of the $(10\bar{1}\bar{3})$ twin 75
2.12 Dichromatic complexes of the $(10\bar{1}\bar{3})$ twin 76
2.13 $(10\bar{1}\bar{3})$ twin 77
2.14 Relaxation of $(10\bar{1}\bar{3})$ twin. 78
2.15 Twinning disconnection of the $(10\bar{1}2)$ twin 79

2.16 Atomic shuffles associated with the twinning disconnection of the $(10\bar{1}2)$ twin . 80
2.17 Twinning disconnection of the $(10\bar{1}1)$ twin 81
2.18 Atomic shuffles associated with the twinning disconnection of the $(10\bar{1}1)$ twin . 83
2.19 Twinning disconnection of the $(10\bar{1}\bar{3})$ twin 84
2.20 Atomic shuffles associated with the twinning disconnection of the $(10\bar{1}\bar{3})$ twin . 84

3.1 Shape changes following the deformation of a sphere into an ellipsoid 97
3.2 Secondary twinning disconnections impinging on a flat primary twin boundary in compression-tension double twinning 122
3.3 Secondary twinning disconnections impinging on a flat primary twin boundary in tension-compression double twinning 125
3.4 Application of the Frank-Bilby equation to twin interfaces 129
3.5 Misfit compensation across compression-tension double twin interfaces 134
3.6 Misfit compensation across tension-compression double twin interfaces 135

4.1 Facets in $(10\bar{1}2)$ twin interfaces 140
4.2 Disclination dipole description of an interfacial facet in a $(10\bar{1}2)$ twin 141
4.3 Formation of facets in $(10\bar{1}2)$ twin interfaces via interaction of matrix dislocations with the twin boundary 143
4.4 Facets in $(10\bar{1}1)$ and $(10\bar{1}\bar{3})$ twin interfaces 146
4.5 Facets in $(10\bar{1}1) - (10\bar{1}2)$ double twin to matrix interfaces 149
4.6 Facets in $(10\bar{1}\bar{3}) - (10\bar{1}2)$ double twin to matrix interfaces 150
4.7 Facets in $(10\bar{1}2) - (10\bar{1}1)$ double twin to matrix interfaces 153
4.8 Facets in $(10\bar{1}2) - (10\bar{1}\bar{3})$ double twin to matrix interfaces 154
4.9 Reciprocal and real space projections along the $[1\bar{2}10]$ direction of the hexagonal lattice 163
4.10 SEM images of the microstructure of a Mg alloy 165
4.11 EBSD maps of the microstructure of a Mg alloy 166
4.12 Photograph of the JEOL dual tilt beryllium holder used in TEM observations . 167
4.13 TEM bright field images and SAD patterns of a compression twin in a Mg alloy 168
4.14 HRTEM image of a compression twin tip in a Mg alloy 169

4.15 TEM bright field images of a long twin-like object and a cluster of twins in a Mg alloy 170
4.16 Low resolution bright field image, SAD pattern and HRTEM images of a tension-compression double twin to matrix interface in a Mg alloy 173
4.17 Low resolution bright field image, SAD patterns and HRTEM images of a tension-compression-tension triple twin to matrix interface in a Mg alloy 174
4.18 Low resolution bright field image, SAD patterns and HRTEM images of a compression-tension double twin to matrix interface in a Mg alloy 175
4.19 TEM bright field images of a long twin-like object and a cluster of twins in a Mg alloy, colour coded by twin kind 176

List of tables

2.1 Parameters of the twinning disconnections associated with the $(10\bar{1}2)$, $(10\bar{1}1)$ and $(10\bar{1}\bar{3})$ twinning modes. 85

3.1 Minimum axis/angle pairs describing the misorientation relations of double twin variants for $(10\bar{1}1)-(10\bar{1}2)$ and $(10\bar{1}\bar{3})-(10\bar{1}2)$ double twins, $\gamma = 1.624$ . . . 92

3.2 Minimum axis/angle pairs describing the misorientation relations of double twin variants for $(10\bar{1}1)-(10\bar{1}2)$ and $(10\bar{1}\bar{3})-(10\bar{1}2)$ double twins, $\gamma = \sqrt{\frac{21}{8}} = 1.620$ 93

3.3 Features of the equivalent simple twinning mode describing compression-tension double twinning in magnesium, $\gamma = 1.624$, according to Crocker's theory. . . . 102

3.4 Features of the equivalent simple twinning mode describing tension-compression double twinning in magnesium, $\gamma = 1.624$, according to Crocker's theory . . . 104

3.5 Angles rotated through by the primary twin interface due to the impingement of a secondary twinning disconnection, for compression-tension and tension-compression double twin mechanisms. 126

3.6 Angles defining misfit-free interfaces with added rotational distortion as described by the topological model, for compression-tension and tension-compression double twin mechanisms. 136

4.1 Labels and axis/angle pairs of some magnesium triple twinning modes, $\gamma = 1.624$. 156

List of abbreviations

3Py Third Pyramidal (plane)

AHS Austin-Heine-Sham

B Basal (plane)

BC Band Contrast

C-T Compression-Tension (double twinning)

CRSS Critically Resolved Shear Stress

CSL Coincident Site Lattice

DFT Density Functional Theory

DT Double Twin

DTIN Deformation Twin Induced Nucleation

EAM Embedded Atom Model

EBSD Electron Back-Scatter Diffraction

FFT Fast Fourier Transform

FIRE Fast Inertial Relaxation Engine

GPT Generalized Pseudopotential Theory

aGPT adaptive Generalized Pseudopotential Theory

hcp hexagonal close packed

HRTEM High-Resolution Transmission Electron Microscope

IPS Invariant-Plane Strain

LDA Local Density Approximation

ND Normal Direction

P Prismatic (plane)

PSN Particle Stimulated Nucleation

Py First Pyramidal (plane)

RD Rolling Direction

RE Rare Earth

SAD Selected-Area Diffraction

SEM Scanning Electron Microscope

STEM-EDS Scanning Transmission Electron Microscopy Energy Dispersive X-ray Spectroscopy

T-C Tension-Compression (double twinning)

T-C-T Tension-Compression-Tension (triple twinning)

TD Transverse Direction

TEM Transmission Electron Microscope

Chapter 1

Introduction

"*If adventures will not befall a young lady in her own village, she must seek them abroad.*"

Northanger Abbey, JANE AUSTEN

1.1 Rare-earth texture and double twinning

Ever since it was first isolated by Davy in 1808, magnesium and its use in technological applications have been the subject of persistent research. Indeed, magnesium presents a number of advantageous properties, among which is first and foremost its low density compared to that of aluminium; in combination with the typical mechanical properties, this produces in magnesium an optimal strength-to-weight ratio [1]. Nevertheless, magnesium is not used in pure form, and all commercial uses of the material require the addition of alloying elements. However, even commercial magnesium alloys are not exempt from flaws; in particular, when undergoing thermomechanical processing, they generally exhibit a strong basal texture, due to the hexagonal crystal structure [2–7], which is usually enhanced after annealing [8, 9]. This means that when hot rolled sheets of material recrystallise, large grains are formed with the orientation of their [0001] axis (called the *c*-axis) being nearly perpendicular to the sheet; this mechanism yields poor formability and ductility in conventional magnesium alloys, and for this reason research in recent years has been focused on weakening the strong basal texture [10]. The solution to this problem has come from the addition of rare earth (RE) elements to magnesium alloys, which

have been shown to improve formability by producing recrystallised grains with randomised orientations that weaken the texture of the alloy [2, 11–14], creating the so-called "RE texture", a process that takes place either during the thermomechanical processing or during annealing [15]. The large atomic radius of RE elements compared to that of magnesium leads to segregation of RE solute atoms to grain boundaries, thus creating obstacles to dislocation motion: this behaviour has been reported to play an important role in RE texture formation [16–19].

However, more recently the limitations of RE alloys have become apparent. The extraction and processing of REs represent an environmental concern, and the manufacturing of each RE magnesium alloy requires distinct processes, hereby increasing production costs. Moreover, although RE elements are not actually rare, increasing demand and rising economical tensions have resulted in an increase in the price of REs. For these reasons, industry-driven research has been endeavouring to find alternatives to RE elements, to be added in so-called "RE-free" magnesium alloys to maintain the RE texture whilst eliminating the drawbacks of RE extraction, purchasing and processing.

For this purpose, a systematic study of the formation of RE texture in magnesium alloys is necessary, both from experimental and theoretical points of view. In this sense, recent experimental studies have been concentrating on the observation of the recrystallisation process, mainly through the use of electron back-scatter diffraction (EBSD) methods. The main goals of these experiments are to identify the mechanisms that give rise to RE texture within the alloy and to track the evolution of the texture throughout the recrystallisation process. In the past few years, various candidates have been proposed as the main contributors to RE texture, and researchers have been struggling to find an agreement, though many concur that more than one process is likely to be at work. One major candidate was thought to be particle stimulated nucleation (PSN), and it was shown that particles could provide nucleation sites for the growth of grains with randomised orientations [20, 21]; however, diluted alloys containing practically no second-phase particles were shown to exhibit the same weakened texture [22]. Another proposed site for the nucleation of randomised grains is shear bands [23], i.e. narrow areas of intense deformation caused by shear [24]; but shear bands have been shown to be also present in alloys that do not contain REs, and that exhibit a strong recrystallised basal texture [25]. A third proposed mechanism for the formation of RE texture is deformation twin induced nucleation (DTIN)

[3, 26], and recent studies have shown that the role of DTIN had been previously underestimated. In particular, by observing the recrystallisation process during static annealing of a commercial RE magnesium alloy, it was found that the principal sites for nucleation were double twins, and that the recrystallised grains originating from intersections between double twins as well as between double twins and grain boundaries quickly grew into the deformed grains with randomised orientations [15, 27].

The identification of the main nucleation sites is key to the design of RE-free alloys. A likely substitute for RE elements in magnesium alloys has been proposed to be calcium, due to its large atomic radius, a characteristic it shares with RE elements. Indeed, in recent experimental observations carried out by Dikai Guan and coworkers at the University of Sheffield it was found that the addition of a small amount of calcium to magnesium alloys weakens the basal texture of the material [28, 29]. Moreover, it was shown that the preferred nucleation sites for grain growth are double twins, suggesting that calcium acts in a similar way to RE elements in the production of RE texture, and indeed segregates similarly to REs along grain boundaries. The recrystallisation process of such a Mg-Zn-Ca alloy is depicted in figure 1.1 [29]. It is then evident that twinning, and double twinning in particular, plays an important part in the development of RE texture in recrystallised magnesium alloys, thus meriting further consideration. It should be emphasised that the twins that are of interest in regards to the formation of rare-earth texture are deformation twins and not annealing twins, as they are introduced during deformation and not during recrystallisation. This can be seen from figure 1.1a, which shows an electron micrograph of the material after cold rolling and prior to annealing, and where the twins and double twins formed during cold rolling are highlighted by red and blue boundaries respectively. Hence, deformation twinning is the object of this study.

Twinning has a major role in the deformation of magnesium, as it operates concertedly with basal slip, making up for the lack of at least five independent basal slip systems [30]. Only two independent slip systems exist for basal slip, i.e. deformation via the motion of slip dislocations on the basal plane, such that basal slip on its own fails to meet the von Mises criterion [31] for uniform deformation of polycrystalline materials that does not cause failure at grain boundaries [32], which requires five independent slip systems. Thus, though basal slip is the most common

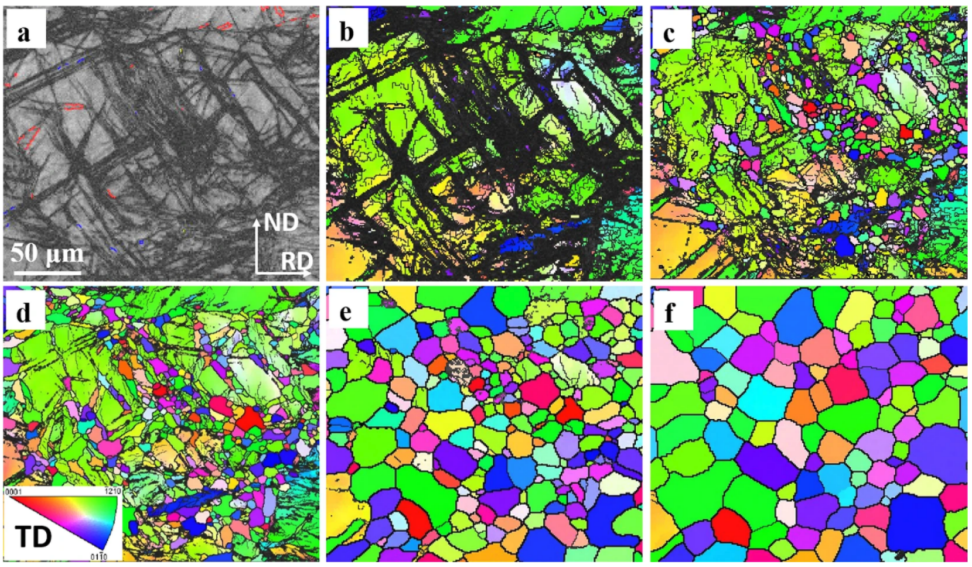

Fig. 1.1 (a) cold-rolled Mg-0.8Zn-0.2Ca sample: band contrast (BC) map superimposed by twin boundaries. (b) cold-rolled sample EBSD inverse pole figure image and at annealing intervals of (c) 520 s, (d) 880 s, (e) 2110 s, and (f) 6910 s. Reproduced from [29] under CC BY 4.0 license (https://creativecommons.org/licenses/by/4.0/).

deformation mode at room temperature, it is usually associated with prismatic slip or twinning to accommodate deformation.

In magnesium, the most commonly occurring twinning mode is $(10\bar{1}2)$ twinning, also called tension twinning as it is associated with extension of the c-axis [33, 34]. Secondly, $(10\bar{1}1)$ twinning as well as its reciprocal mode, $(10\bar{1}\bar{3})$ twinning, have been observed, and they are often labelled as compression twinning as they are reported in relation to compression of the c-axis [35–38]. However, twinning on planes other than these was reported as early as the 1950s [39, 40], and it was then established that these modes can be attributed to internal or secondary twinning of the material inside the primary twin [41]: these are the double twins object of the present study. In magnesium the most commonly reported double twinning sequence is $(10\bar{1}1) - (10\bar{1}2)$ [42–47], where the notation indicates that secondary twinning occurs on the $(10\bar{1}2)$ plane of the primary twin; this was the double twinning mode referred to in studies of RE texture in magnesium alloys introduced above. But so-called extension double twins, i.e. $(10\bar{1}2) - (10\bar{1}2)$ double twins have also been observed and studied [48, 49].

In order to assess the feasibility of a given deformation mode, the critical resolved shear stress (CRSS) is often considered. The CRSS is given by the value of the shear stress resolved in the direction of slip or twinning necessary to initiate dislocation motion and thus plastic deformation

[50]. The resolved shear stress is related to the applied stress by Schmid's law, where the proportionality constant is called the Schmid factor [51]; deformation modes with high Schmid factors require lower applied stress to reach the CRSS than those with low Schmid factors, and can thus be deemed to be the active ones. For example, assessment of the Schmid factor has been used to explain variant selection of tension twins in magnesium [52]. Considering now the case of $(10\bar{1}1)-(10\bar{1}2)$ double twinning, due to hexagonal symmetry secondary twinning may occur on any of six equivalent $\{10\bar{1}2\}$ planes for each $\{10\bar{1}1\}$ plane, such that 36 double twin variants exist for any given twinning sequence; only four are geometrically distinct, and we will examine them further in chapter 3. However it is noted here that the four double twin variants are not observed to occur with equal probability: investigation of the Schmid factors for a given applied stress for each variant may be used to ascertain the likelihood of activation of the double twin variants. However, Barnett et al. [45] and Martin et al. [46] have found that variant selection for $(10\bar{1}1)-(10\bar{1}2)$ double twinning does not always follow Schmid's law: while type 4 double twin variants are favoured by high Schmid factors, the type 1 variants, though commonly observed, are associated with lower Schmid factors. It has thus been concluded that criteria other than the CRSS should be considered as well, namely the ease of growth of a given variant, associated with the angle between the twinning planes of the component mechanisms, and the associated accommodation strains.

Double twin nucleation is also not well understood, and it has been suggested that variant selection can be explained by first understanding the underlying mechanism of secondary twin formation. For $(10\bar{1}1)-(10\bar{1}2)$ type 1 and 2 double twinning, a nucleation pathway was first proposed by Mendelson [53], who envisaged the interaction of $\langle \mathrm{c} \rangle$ or $\langle \mathrm{c}+\mathrm{a} \rangle$ slip dislocations (where the notation indicates that the Burgers vector of the dislocation has length e.g. c, and a is the lattice constant while c is the length of the $[0001]$ axis) with the primary twin interface, resulting in the creation of secondary twinning dislocations. The activation of the $\langle \mathrm{c}+\mathrm{a} \rangle$ slip system is unfavourable, and more recently an alternative mechanism was proposed by Beyerlein et al. [54]. They suggested that type 1 and 2 double twin variants may nucleate as a consequence of a series of dislocation reactions involving mixed basal dislocations and the primary twin interface, while type 3 and 4 variants would require $\langle \mathrm{c}+\mathrm{a} \rangle$ slip dislocations. These are the only

theoretical treatments of double twin nucleation proposed so far for magnesium, indicating that more research is needed on this front.

Finally, a long-standing question regarding double twinning is the determination of the orientation of the double twin to matrix interface. In this respect, a theory based on the assumption that a double twinning transformation corresponds to a simple shear was first proposed by Crocker [41]. This theory focused on prediction of the invariant planes associated with the double twin shear, and posed not only the question of the orientation of the final double twin interface, but also that of double twin nucleation: Crocker suggested that a double twin should grow on an invariant plane of the transformation, i.e. that double twin formation should occur in one step. Conversely, the nucleation theories proposed above assume that a fully formed primary twin retwins internally, thus requiring two steps for the formation of the double twin. Experimental observations suggest that the two-step process likely applies to double twins in magnesium, as primary twins that have only partially retwinned are often reported. However, unambiguous measurement of the orientation of the double twin to matrix interface has not yet been achieved, even for the most commonly occurring $(10\bar{1}1)-(10\bar{1}2)$ variant. Thus, investigation of the interface between double twin and matrix is the objective of the present thesis, with reviews of approaches envisaging both one- and two-step processes.

In the rest of this chapter, we first introduce some crystallographic notions for magnesium, with a particular focus on coordinate systems that may appropriately describe hexagonal symmetry. We then discuss the subject of classical twinning as expounded by early theories, which were responsible for the introduction of the notation of twinning still in use to this day. We continue to a presentation of the computational methods used for atomistic simulations in chapter 2, and we finish with an overview of the structure of this thesis.

1.2 The hexagonal basis and Miller-Bravais indices

Magnesium is a metal with hexagonal close-packed (hcp) crystal structure. Its lattice constant is $a = 0.3208$ nm, while the length of the c-axis is $c = 0.5209$ nm, resulting in axial ratio $\gamma = 1.624$ [34], close to the ideal axial ratio of 1.633. In order to exploit the hexagonal symmetry of the crystal, when dealing with hcp structures a four-dimensional system of basis vectors which

makes this symmetry apparent is often used; in this section we will give a brief description of this system of basis vectors, as well as of the corresponding Miller-Bravais indices, i.e. the hexagonal version of the widely used Miller indices. Finally, we will show how the (non-orthogonal) Miller-Bravais coordinate system can be generalised to an orthogonal four-dimensional system, yielding a useful tool in crystallographic computations.

A lattice is an infinite set of points defined by integer linear combinations of a set of linearly independent lattice vectors [55], namely $\mathbf{a}_1$, $\mathbf{a}_2$ and $\mathbf{a}_3$, such that any point of the lattice is described by a vector $\mathbf{r}_{[u_1u_2u_3]}$:

$$\mathbf{r}_{[u_1u_2u_3]} = u_1\mathbf{a}_1 + u_2\mathbf{a}_2 + u_3\mathbf{a}_3, \qquad u_1, u_2, u_3 \in \mathbb{Z}.$$

Or, more compactly

$$\mathbf{r} = u_i\mathbf{a}_i \quad i = 1,2,3, \tag{1.1}$$

where the repeated index i is summed over according to the Einstein summation convention. In this way, we have defined the vector $\mathbf{r}$ in the basis $\mathbf{a}_i$, whose three non-coplanar lattice vectors outline the unit cell of the crystal. The volume of the unit cell is found as the scalar triple product of the lattice vectors, i.e.

$$V = (\mathbf{a}_1 \times \mathbf{a}_2) \cdot \mathbf{a}_3, \tag{1.2}$$

and when V is minimum the vectors are primitive vectors, and define a primitive unit cell of the Bravais lattice [56].

The basis $\mathbf{a}_i$ is, in general, non-orthogonal; hence, the magnitude of a vector expressed in this basis is found as follows:

$$|\mathbf{r}| = \sqrt{r_i\mathbf{a}_i r_j\mathbf{a}_j} = \sqrt{r_i r_j \mathbf{a}_i \cdot \mathbf{a}_j} = \sqrt{r_i r_j G_{ij}}, \tag{1.3}$$

where

$$G_{ij} = \mathbf{a}_i \cdot \mathbf{a}_j = a_i a_j \cos\theta_{ij}, \tag{1.4}$$

with θ_{ij} the angle between vectors $\mathbf{a}_i$ and $\mathbf{a}_j$. G_{ij} is defined as the direct metric tensor of the basis; if one were to take the Cartesian unit vectors as a basis, the direct metric tensor would simply be the identity matrix, i.e. $G_{ij} = \delta_{ij}$. As in crystallography it is often advantageous to

work in other reference frames, the direct metric tensor is a useful concept, because it allows for a description of the metric properties of any kind of N-dimensional space in any coordinate system [57].

Let us now discuss how directions and planes are specified within crystallographic conventions. If the set of integers u_i defines the position of a lattice point at some distance from the origin, then one may define all the lattice points lying in a straight line passing through the origin via the equation

$$\mathbf{r} = Cu_i\mathbf{a}_i = U_i\mathbf{a}_i, \tag{1.5}$$

Where C takes all integer values between $-\infty$ and $+\infty$. And going further, one can represent all the lattice points lying in a parallel line going through a lattice point at position $\mathbf{r}_k$ with the equation

$$\mathbf{r} = \mathbf{r}_k + U_i\mathbf{a}_i, \tag{1.6}$$

such that, for any given set of u_i, all the lattice points are specified. The lattice is then described as sets of points lying on parallel straight lines; conventionally, the u_i are called the direction indices of the line, indicated as $[u_1u_2u_3]$, while a family of directions required to be equivalent by symmetry is represented as $\langle u_1u_2u_3\rangle$ [56].

One may also look at the lattice points as arranged on planes. Considering the plane on which the two lattice vectors $\mathbf{a}_1$ and $\mathbf{a}_2$ lie, one can represent the normal to this plane as the vector

$$\mathbf{a}_3^* = \frac{\mathbf{a}_1 \times \mathbf{a}_2}{v_a}, \tag{1.7}$$

where v_a is a constant. As the area of the face of the unit cell defined by $\mathbf{a}_1$ and $\mathbf{a}_2$ is given by $|\mathbf{a}_1 \times \mathbf{a}_2|$, the spacing between adjacent planes in the $\mathbf{a}_3^*$ direction is

$$\frac{V}{|\mathbf{a}_1 \times \mathbf{a}_2|} = \frac{(\mathbf{a}_1 \times \mathbf{a}_2)\cdot \mathbf{a}_3}{|\mathbf{a}_1 \times \mathbf{a}_2|}. \tag{1.8}$$

Taking $v_a = V$, one finds that the length of the vector $\mathbf{a}_3^*$ is equal to the interplanar spacing, and that $\mathbf{a}_3 \cdot \mathbf{a}_3^* = 1$. Following the same procedures for the other two planes defined by the lattice

vectors, one finds the so-called reciprocal lattice vectors, which obey the relationship

$$\mathbf{a}_i \cdot \mathbf{a}_j^* = \delta_{ij}. \tag{1.9}$$

The reciprocal lattice vectors may be taken to define a new basis, such that the position of a lattice point can be specified as

$$\mathbf{r} = u_i^* \mathbf{a}_i^*. \tag{1.10}$$

The orientation of a plane can be described by the distances at which it intercepts the axes $\mathbf{a}_i$, e.g. the distances $1/h_1^*, 1/h_2^*, 1/h_3^*$ from the origin. On this plane lie the vectors $(\mathbf{a}_1/h_1^* - \mathbf{a}_2/h_2^*)$ and $(\mathbf{a}_2/h_2^* - \mathbf{a}_3/h_3^*)$, whose vector product, which we call $B\mathbf{h}$, is parallel to the normal to the plane:

$$B\mathbf{h} = \frac{V}{h_1^* h_2^* h_3^*}(h_1^* \mathbf{a}_1^* + h_2^* \mathbf{a}_2^* + h_3^* \mathbf{a}_3^*).$$

If we take $B = \frac{V}{h_1^* h_2^* h_3^*}$, we can specify the plane via the normal vector

$$\mathbf{h} = h_i^* \mathbf{a}_i^*, \tag{1.11}$$

such that now the lengths h_i^* are the components of the vector $\mathbf{h}$ in the reciprocal basis. Moreover, the h_i^* can be used to represent the orientation of all the parallel planes intersecting the axes at lengths C_2/h_i, such that each plane is described by the equation

$$h_1^* u_1 + h_2^* u_2 + h_3^* u_3 - C_2 = 0, \tag{1.12}$$

where each u_i is now a continuous variable. C_2 takes integer values between $-\infty$ and $+\infty$, meaning that equation 1.12 represents an infinite set of equally spaced parallel planes, and thus encompasses all the lattice points. By construction, the vector $\mathbf{h}$ is perpendicular to the set of planes, and the distance between planes is thus found by projecting the vector $\mathbf{a}_1/h_1^*$ onto the direction $\mathbf{h}$, i.e.

$$d_h = \frac{\mathbf{h} \cdot \mathbf{a}_1/h_1^*}{|\mathbf{h}|} = \frac{1}{|\mathbf{h}|}. \tag{1.13}$$

Conventionally, in crystallography the orientation of a plane is described simply via the notation $(h_1^* h_2^* h_3^*)$, where the h_i^* are called the Miller indices of the plane, and a family of equivalent planes

is denoted by $\{h_1^* h_2^* h_3^*\}$. This notation has a distinct advantage: upon seeing the Miller indices for a plane, one may immediately tell which is the direction normal to the plane in reciprocal space, i.e. $[h_1^* h_2^* h_3^*]$. Now however one may wish to know which direction this corresponds to in real space, i.e. what are the indices $[h_1 h_2 h_3]$; this is where the metric finds one of its uses.

The metric tensor for the reciprocal basis is called the indirect metric tensor, and it is defined as

$$G_{ij}^* = \mathbf{a}_i^* \cdot \mathbf{a}_j^*. \tag{1.14}$$

But using equation 1.9, it is easy to show that

$$\mathbf{G}^* = \mathbf{G}^{-1}, \tag{1.15}$$

i.e. that the indirect metric tensor is the inverse of the direct metric tensor. Now, a vector exists independently of the reference frame it is expressed in; hence, a vector $\mathbf{p}$ expressed in the basis $\mathbf{a}_i$ must be equivalent to $\mathbf{p}$ expressed in the reciprocal basis $\mathbf{a}_i^*$:

$$\begin{aligned} \mathbf{p} &= p_i \mathbf{a}_i = p_i^* \mathbf{a}_i^* \\ p_i \mathbf{a}_i \cdot \mathbf{a}_j^* &= p_i^* \mathbf{a}_i^* \cdot \mathbf{a}_j^* \\ p_i \delta_{ij} &= p_i^* G_{ij}^* \\ p_j &= p_i^* (G^{-1})_{ij}, \end{aligned} \tag{1.16}$$

where in the second line we have multiplied both sides by $\cdot \mathbf{a}_j^*$. Thus the direct metric tensor provides a bridge between quantities expressed in reciprocal space and real space: the direction we were looking for in real space may simply be found as

$$[h_1 h_2 h_3] = [h_1^* h_2^* h_3^*] \mathbf{G}^{-1}. \tag{1.17}$$

We are now equipped with the necessary knowledge to describe hexagonal systems. A possible choice of axes in this case is depicted on the left hand side of figure 1.2, with the unit cell described by two vectors of length a, $\mathbf{a}_1$ and $\mathbf{a}_2$, forming a 120° angle, and a vector $\mathbf{c}$ of

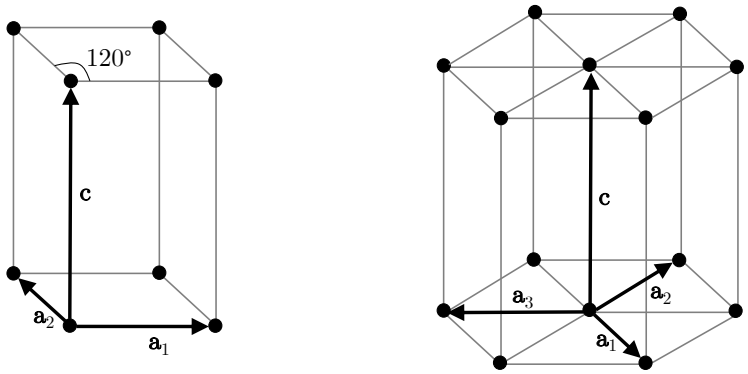

Fig. 1.2 Schematic illustration of the hexagonal unit cell and basis vectors. The left hand side shows the three standard hexagonal basis vectors, $\mathbf{a}_1$, $\mathbf{a}_2$ and $\mathbf{c}$, whereas the right hand side shows the basis vectors used in the Miller-Bravais system, where a vector $\mathbf{a}_3$ co-planar to $\mathbf{a}_1$ and $\mathbf{a}_2$ is added in order to make the symmetry of hexagonal structures apparent.

length c perpendicular to $\mathbf{a}_1$ and $\mathbf{a}_2$, such that the quantity $\gamma = c/a$ is the axial ratio. For this system of axes, the direct metric tensor (here termed ${}^{\text{hex}}\mathbf{G}$) can be represented by the matrix

$$ {}^{\text{hex}}\mathbf{G} = \begin{pmatrix} 1 & -\frac{1}{2} & 0 \\ -\frac{1}{2} & 1 & 0 \\ 0 & 0 & \gamma^2 \end{pmatrix} a^2. \tag{1.18} $$

As outlined above, when we are given the Miller indices of a plane for a hexagonal system, all we have to do to find the direction perpendicular to the plane in real space is use equation 1.17. Therefore, for a plane (hkl) (from now on we shall use these letters and omit the asterisks when dealing with planes) the corresponding normal direction in real space is given by

$$ [g_1 g_2 g_3] = [hkl]({}^{\text{hex}}\mathbf{G})^{-1} = \frac{2}{3} a^2 [2h + k \; h + 2k \; l/\Lambda^2], \tag{1.19} $$

where we have defined a new quantity $\Lambda = \gamma\sqrt{2/3}$ which will be useful presently.

However, the choice of axes described above does not make the symmetry of the hexagonal crystal immediately apparent. For this reason, a system of four axes is often used: a third axis $\mathbf{a}_3$ co-planar to $\mathbf{a}_1$ and $\mathbf{a}_2$ is added, such that $\mathbf{a}_3 = -(\mathbf{a}_1 + \mathbf{a}_2)$, as shown on the right hand side of

figure 1.2. A vector in this basis is then represented by

$$\mathbf{u} = u_i \mathbf{a}_i \qquad (i = 1, ..., 4), \tag{1.20}$$

with $\mathbf{a}_4 \equiv \mathbf{c}$ and a requirement that

$$u_1 + u_2 + u_3 = 0. \tag{1.21}$$

Defining as before a lattice plane using its reciprocal intercepts $(hkil)$ (called the Miller-Bravais indices) with the axes $\mathbf{a}_i$, we find that they obey a similar relation to 1.21:

$$h + k + i = 0. \tag{1.22}$$

The advantage of this four-dimensional system of indices with conditions 1.21 and 1.22 for hexagonal crystals is that crystallographically equivalent directions and planes are expressed as cyclic permutations of the indices, such that the symmetries are readily visible [56].

However we encounter some complications when trying to represent normals to planes as directions in reciprocal space. If we write down the direct metric tensor for the Miller-Bravais basis, we find

$$\underset{\text{MB}}{\overset{\text{hex}}{}}\mathbf{G} = \begin{pmatrix} 1 & -\frac{1}{2} & -\frac{1}{2} & 0 \\ -\frac{1}{2} & 1 & -\frac{1}{2} & 0 \\ -\frac{1}{2} & -\frac{1}{2} & 1 & 0 \\ 0 & 0 & 0 & \gamma^2 \end{pmatrix} a^2. \tag{1.23}$$

This is a singular matrix, i.e. its determinant is zero, due to the fact that the basis vectors are not linearly independent. As a consequence, the metric cannot be inverted, and therefore it will not be possible to define the reciprocal basis vectors such that equation 1.9 holds. Instead, we design a set of reciprocal lattice vectors that obeys the relation 1.22, starting from the reciprocal of the three-dimensional hexagonal basis, i.e. $\mathbf{a}_1^*$, $\mathbf{a}_2^*$ and $\mathbf{c}^*$. We will denote the Miller-Bravais reciprocal basis using the superscript $^+$, i.e. $\mathbf{a}_1^+$, $\mathbf{a}_2^+$, $\mathbf{a}_3^+$ and $\mathbf{c}^+$. Noting that

$V = \mathbf{a}_1 \cdot (\mathbf{a}_2 \times \mathbf{c}) = \sqrt{3}a^2c/2$, we find that the 3D hexagonal reciprocal basis is

$$\mathbf{a}_1^* = \frac{\mathbf{a}_2 \times \mathbf{c}}{V} = \frac{2}{3a^2}(2\mathbf{a}_1 + \mathbf{a}_2), \tag{1.24}$$

$$\mathbf{a}_2^* = \frac{\mathbf{c} \times \mathbf{a}_1}{V} = \frac{2}{3a^2}(\mathbf{a}_1 + 2\mathbf{a}_2), \tag{1.25}$$

$$\mathbf{c}^* = \frac{\mathbf{a_1} \times \mathbf{a}_2}{V} = \frac{\mathbf{c}}{\gamma^2 a^2}. \tag{1.26}$$

We then want the transformation

$$h\mathbf{a}_1^* + k\mathbf{a}_2^* + l\mathbf{c}^* \rightarrow h\mathbf{a}_1^+ + k\mathbf{a}_2^+ + i\mathbf{a}_3^+ + l\mathbf{c}^+ \tag{1.27}$$

to preserve equation 1.22; hence we must define the new Miller-Bravais reciprocal basis in the following way [58]:

$$\mathbf{a}_i^+ = \frac{2}{3a^2}\mathbf{a}_i \qquad (i = 1, ..., 3), \tag{1.28}$$

$$\mathbf{c}^+ = \frac{\mathbf{c}}{\gamma^2 a^2}. \tag{1.29}$$

In this way, the vector $h\mathbf{a}_1^+ + k\mathbf{a}_2^+ + i\mathbf{a}_3^+ + l\mathbf{c}^+$ is automatically perpendicular to the plane $(hkil)$; moreover we can readily find the reciprocal direction $[hkil]$ in real space by using the fact that a vector must be equivalent when expressed in either basis:

$$\begin{aligned} g_1\mathbf{a}_1 + g_2\mathbf{a}_2 + g_3\mathbf{a}_3 + g_4\mathbf{c} &= h\mathbf{a}_1^+ + k\mathbf{a}_2^+ + i\mathbf{a}_3^+ + l\mathbf{c}^+ \\ g_1\mathbf{a}_1 + g_2\mathbf{a}_2 + g_3\mathbf{a}_3 + g_4\mathbf{c} &= \frac{2}{3a^2}h\mathbf{a}_1 + \frac{2}{3a^2}k\mathbf{a}_2 + \frac{2}{3a^2}i\mathbf{a}_3 + \frac{1}{\gamma^2 a^2}l\mathbf{c} \\ \implies [g_1 g_2 g_3 g_4] &= \frac{2}{3a^2}[hkil/\Lambda^2], \end{aligned} \tag{1.30}$$

where $\Lambda = \gamma\sqrt{2/3}$.

We notice that for a particular value of the axial ratio, i.e. $\gamma = \sqrt{3/2}$, $\Lambda = 1$. In this case, the direction in real space normal to a plane $(hkil)$ is $[hkil]$ (here we discard the constant factor of $\frac{2}{3a^2}$ as we are only interested in the direction), such that the four-dimensional system of axes is cubic, in the sense that the metric tensor is given by the identity. Then we may consider crystals with any other axial ratio as derived from the case $\gamma = \sqrt{3/2}$ by means of an affine

transformation, specifically a stretching of the lattice along the c axis by a factor of Λ [59]. Hence, a crystallographic direction denoted by $[g_1 g_2 g_3 g_4]$ in the Miller-Bravais system is expressed in the 4D Cartesian system as $[g_1\ g_2\ g_3\ \Lambda g_4]_4$, where the subscript of the square brackets denotes a Cartesian 4-vector. It follows readily from equation 1.30 that the Cartesian 4-vector normal to a plane with Miller-Bravais indices $(hkil)$ is $[hkil/\Lambda]_4$ [60].

Though the conversion between the Miller-Bravais system and the 4D Cartesian system is simple, it is very advantageous to be able to perform crystallographic calculations in the Cartesian 4-vector notation, because the coordinate system is orthogonal, and there is no need to use the metric tensor. In particular, it is now straightforward to calculate dot products between vectors expressed in the Miller-Bravais system: this is done by calculating the dot product of the corresponding 4-vectors as

$$[g_1\ g_2\ g_3\ \Lambda g_4]_4 \cdot [m_1\ m_2\ m_3\ \Lambda m_4]_4 = g_1 m_1 + g_2 m_2 + g_3 m_3 + \Lambda^2 g_4 m_4, \tag{1.31}$$

in units of $(\frac{3}{2})a^2$ [61]. We shall use this property to find unit normals of planes, as well as the magnitude of the Burgers vectors of the dislocations that we will consider. Pond and co-workers [62] have also designed a method to obtain transformation matrices in the 4-vector system, and they have tabulated these matrices for all the symmetry operations of the $P6/mmm$ space group. These will be particularly useful in chapter 3, when determining the minimum axis/angle pairs describing double twin misorientation relations.

1.3 Early theories of classical twinning

In order to understand double twinning, it is necessary to first become acquainted with twinning. In this section we present early theories of classical deformation twinning, which are based on the notion of simple shear on an invariant plane and on the individuation of so-called "classical" orientation relations between the primitive unit cell of the parent and that of the twin.

In order to illustrate the concept of a simple shear, we hereby remind ourselves of the definition of invariant-plane strain (IPS), i.e. a homogeneous transformation in which a plane is left undistorted and unrotated [63]. This can be illustrated with the aid of figure 1.3, where the coordinate system is such that the invariant plane is the x-y plane, and the z-axis is parallel to its

normal. In figure 1.3a the shape change is a uniaxial strain, where the strain is applied in the direction of the normal to the invariant plane, such that a volume change is involved. In figure 1.3b, there is no such volume change, for the initial shape is strained in a direction which lies in the invariant plane: this is a simple shear. A general invariant-plane strain, depicted in figure 1.3c, includes both a dilatation and a shear, such that the simple shear is a special case of the IPS.

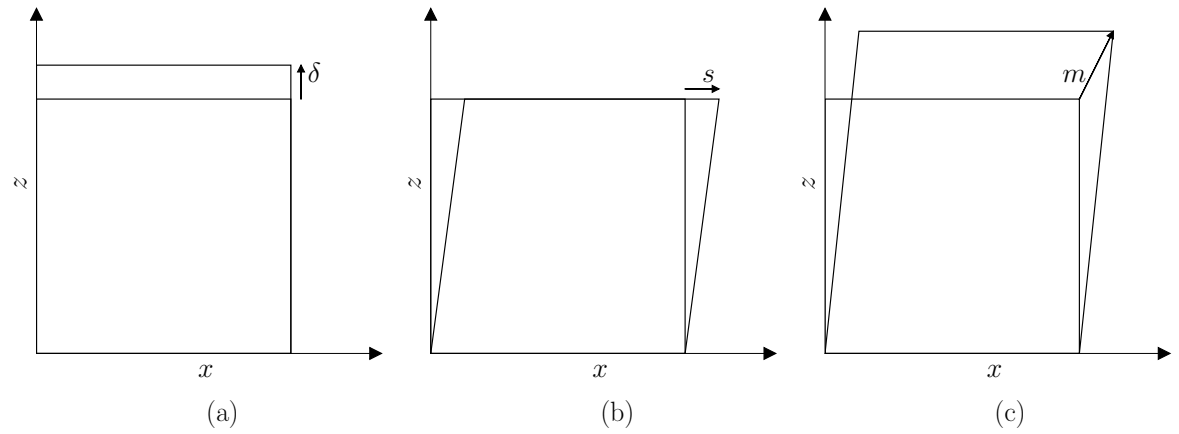

Fig. 1.3 Shape changes resulting from invariant-plane strains; the invariant plane is the $x-y$ plane, where the axis y points away from the reader. (a): a uniaxial dilatation where the strain with magnitude δ is applied perpendicular to the invariant plane; (b): a simple shear where the strain with magnitude s is applied parallel to the invariant plane; (c): a general invariant plane strain, where the magnitude of the strain is m, and both a dilatation and a simple shear are applied.

Deformation twinning is defined as a change in shape caused by stress being applied to the crystal, and a twin is formed by the displacement of atoms in the parent lattice in a transformation equivalent to a simple shear **S**. The twinning elements are depicted in figure 1.4, and defined as follows: K_1 is the invariant plane on which the shear occurs, and $\boldsymbol{\eta}_1$ is the shear direction; K_2 is the second undistorted (conjugate) plane, the plane of shear P is the one containing the normals to K_1 and K_2, as well as $\boldsymbol{\eta}_1$, and the conjugate shear direction $\boldsymbol{\eta}_2$ is the intersection between K_2 and P [64]. When K_1 and $\boldsymbol{\eta}_2$ (or K_2 and $\boldsymbol{\eta}_1$) are specified, a *twinning mode* is defined. A conjugate or reciprocal twinning mode may be obtained by interchanging K_1 and K_2, and $\boldsymbol{\eta}_1$ and $\boldsymbol{\eta}_2$. Moreover, twins can be classified as type I, when K_1 and $\boldsymbol{\eta}_2$ are respectively a rational plane and a rational direction of the parent lattice, type II, when K_2 and $\boldsymbol{\eta}_1$ are rational, or compound,

when all twinning elements are rational. This classification[1] emerges from classical treatments of twinning [65–69], where it is assumed that as the shear transformation leaves the original lattice intact except for orientation, a unit cell of the parent lattice must be sheared into an equivalent unit cell in the twinned lattice. In order to define a unit cell, we may take three non-coplanar vectors lying in K_1 and K_2, such that the corresponding unit cell in the twin is then a reflection of the original unit cell in K_1 for type I twins and a rotation of 180° about $\boldsymbol{\eta}_1$ for type II twins.

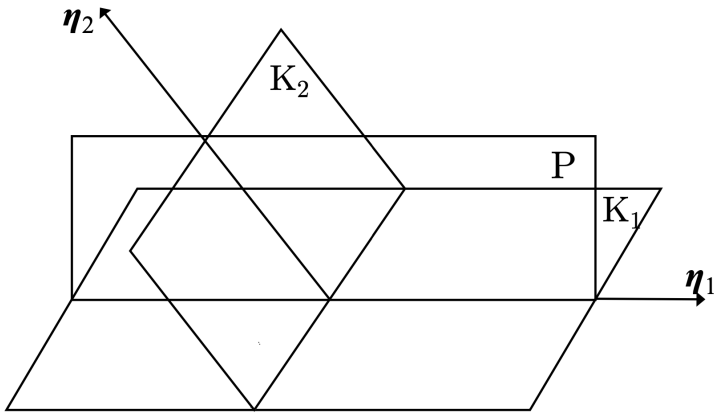

Fig. 1.4 Schematic illustration of twinning elements. K_1 is the twinning plane, $\boldsymbol{\eta}_1$ is the shear direction, K_2 is the second undistorted plane, $\boldsymbol{\eta}_2$ is the conjugate shear direction and P is the plane of shear.

This classification is reflected in the proper and improper rotations used to describe the orientation relations between the parent lattice and the twin. In classical theories of twinning, these rotations must leave the K_1 plane invariant, such that the following relations between the parent and the twin lattices are obtained [64]:

1. reflection in K_1 (type I twin);
2. rotation of 180° about $\boldsymbol{\eta}_1$ (type II twin);
3. reflection in the plane normal to $\boldsymbol{\eta}_1$;
4. rotation of 180° about the normal to K_1.

[1]The notation of type I and II used here for classical twins is easily confused with that used for double twin variants, which are called types 1-4. Despite this, we have retained the use of this notation for double twin variants for the sake of continuity with the experimental literature.

A rotation of θ about the unit vector $\hat{\mathbf{n}}$ can be represented via the following formula for the matrix $\mathbf{R}$ in Cartesian coordinates:

$$R_{ij} = \cos\theta\,\delta_{ij} + \hat{n}_i\hat{n}_j(1-\cos\theta) - \varepsilon_{ijk}\hat{n}_k\sin\theta, \tag{1.32}$$

where ε_{ijk} is the Levi-Civita tensor and the repeated index k is summed over (this convention will be followed throughout this section). If $\theta = 180^\circ$, this reduces to $R_{ij} = -\delta_{ij} + 2\hat{n}_i\hat{n}_j$. A reflection in a plane with unit normal $\hat{\mathbf{n}}$ can be represent by the matrix $\mathbf{M}$, with $M_{ij} = \delta_{ij} - 2\hat{n}_i\hat{n}_j$; it is seen that $R_{ij} = -M_{ij}$ when $\theta = 180^\circ$, as expected. Therefore, operations 1 and 4, as well as operations 2 and 3 produce the same orientations when applied to the parent lattice. However, in the case of crystals with more than one atom in the basis, the rotation and the reflection in each pair are equivalent only if the structure has a centre of symmetry. Moreover, it can be seen that orientations 1 and 2 are related by a reflection in P, the plane of shear; thus, if the plane of shear is a mirror plane of the crystal, these two orientations are equivalent, and so are orientations 3 and 4 [64]. This is the case for compound twins, and if the crystal is also centrosymmetric, all four orientation relations are equivalent.

The earliest attempts at systematic theories of twinning were based on the notion of minimum shear, i.e. the idea that the most likely twinning modes are those that produce the smallest possible magnitude of shear. In particular, Jaswon and Dove [70–72] devised a method to calculate the smallest possible twinning shear in accord with the assumption that for structures with one atom in the unit cell, all atoms are sheared directly to twin positions. In the case where there are two atoms in the unit cell, the shears are accompanied by atomic shuffles to restore the original lattice in a new orientation; in order to describe these shuffles, Jaswon and Dove associated a rigidly-moving unit of two atoms to each lattice point, which was placed at the mid-point between the two atoms, which is also the centre of symmetry. They then found the simplest modes to be obtained by applying the condition that all or one half of the lattice points be sheared straight into position. Kiho [73, 74] also postulated that the magnitude of the shear should be taken into account when selecting operative twinning modes. In his treatment of a parent to twin interface, he made the assumption that each atom should move to the nearest available twin position and that the shuffle vectors should sum up to zero, and he thus recovered the mechanisms described by Jaswon and Dove.

The division of the total atomic displacements into a sum of shears and shuffles introduced by Jaswon and Dove was also taken up by Bilby and Crocker [75] in their more comprehensive theory. We briefly review it here, following the notation of Christian and Mahajan [64].

A simple shear $\mathbf{S}$ of magnitude s on a plane with unit normal $\mathbf{m} = m_i^* \mathbf{a}_i^*$ in the direction $\mathbf{l} = l_i \mathbf{a}_i$, where $\mathbf{a}_i$ and $\mathbf{a}_i^*$ are the direct and reciprocal bases respectively, is given by

$$\mathbf{S} = \mathbf{I} + s\mathbf{l}\mathbf{m}^{\mathrm{T}}. \tag{1.33}$$

Applying $\mathbf{S}$ to a lattice vector $\mathbf{x}$, we obtain

$$\mathbf{y} = \mathbf{S}\mathbf{x}. \tag{1.34}$$

If the original lattice vector is to be reproduced in the twin in a new orientation, then $\mathbf{y}$ must satisfy

$$\mathbf{y} = \mathbf{L}\mathbf{z}, \tag{1.35}$$

where $\mathbf{L}$ is a rotation. On the other hand, $\mathbf{z}$ must be related to $\mathbf{x}$, the original lattice vector:

$$\mathbf{z} = \mathbf{C}\mathbf{x}. \tag{1.36}$$

The matrix $\mathbf{C}$ is called the correspondence matrix, and we will discuss it in more detail in chapter 3. Bilby and Crocker showed that if $\mathbf{x}$ is a lattice vector of the parent lattice, then, for orientations 1 and 2, the vector $\mathbf{x}+\mathbf{z}$ lies in the K_1 plane, and specifically it is parallel to $\boldsymbol{\eta}_1$ for orientation 2; for orientations 3 and 4, the vector $\mathbf{x}-\mathbf{z}$ lies in K_1, and is parallel to $\boldsymbol{\eta}_1$ for orientation 3. In addition, $\mathbf{x}-\mathbf{z}$ lies in K_2 for orientations 1 and 2, being parallel to $\boldsymbol{\eta}_2$ for orientation 1, and the same is true for orientations 3 and 4 with respect to $\mathbf{x}+\mathbf{z}$, which is parallel to $\boldsymbol{\eta}_2$ for orientation 4. The consequence of these proofs is that if the classical orientation relations are to hold, K_1 and $\boldsymbol{\eta}_2$ are necessarily rational for orientations 1 and 4, which describe type I twinning, and K_2 and $\boldsymbol{\eta}_1$ must be rational for orientations 2 and 3, which in turn describe type II twinning; it was thus Bilby and Crocker in their seminal treatment who proved the claim we made at the beginning of this section.

From equation 1.33, we see that **S** may be determined by knowledge of K_1 and $\boldsymbol{\eta}_1$; however, we have previously said that a twinning mode is defined when either K_1 and $\boldsymbol{\eta}_2$ or K_2 and $\boldsymbol{\eta}_1$ are given. Bilby and Crocker showed that $\boldsymbol{\eta}_1$ can be obtained from K_1 and $\boldsymbol{\eta}_2$ as follows:

$$s\mathbf{l} = 2\Big(\mathbf{m} - \frac{\mathbf{g}}{\mathbf{g}\cdot\mathbf{m}}\Big), \tag{1.37}$$

where **g** is a unit vector in the direction of $\boldsymbol{\eta}_2$. Squaring this equation, we obtain an expression for the magnitude of the shear:

$$s^2 = 4\Big(\frac{1}{(\mathbf{g}\cdot\mathbf{m})^2} - 1\Big). \tag{1.38}$$

We are now going to present Bilby and Crocker's treatment of atomic shuffles. Consider a primitive lattice vector $\mathbf{j} = j_i\mathbf{a}_i$ in the $\boldsymbol{\eta}_2$ direction; its projection along the unit normal to the K_1 plane is given by

$$\mathbf{j}\cdot\mathbf{m} = qd_{K_1}, \tag{1.39}$$

where q is a integer and d_{K_1} is the distance between lattice K_1 planes. Then an equivalent position of the interface is found by moving upward by a distance qd_{K_1}, and the atom displacements are the same in every group of q planes.

Now take any lattice point $\mathbf{c} = c_i\mathbf{a}_i$ that lies in the K_1 plane closest to the origin, such that $\mathbf{c}\cdot\mathbf{m} = d_{K_1}$. Secondly, all sites belonging to the parent lattice within the q planes in one group are given by $pc_i\mathbf{a}_i$, where p is an integer smaller than or equal to q. After the shear **S**, these parent sites are displaced to

$$pc_i\mathbf{a}_i + spd_{K_1}\mathbf{l} = pc_i\mathbf{a}_i - \frac{2p}{q}j_i\mathbf{a}_i + 2pd_{K_1}\mathbf{m}, \tag{1.40}$$

where we have used equation 1.37.

If we then express the twin sites relative to their own coordinate system, i.e. in basis $\mathbf{b}_i$, we see that the parent site **j** becomes the twin site $\mathbf{u} = u_i\mathbf{b}_i$, and

$$-\mathbf{u}\cdot\mathbf{m} = qd_{K_1}. \tag{1.41}$$

Similarly to the case of the parent, all other twin sites relative to this site are represented by $rc_i\mathbf{b}_i$, where $r \leq q$ for the sites within the q planes under consideration. If $p+r=q$, then the twin site with a value of r lies in the same K_1 plane as the parent site with value p. It follows that all the twin lattice sites within the q planes are given by $(u_i+rc_i)\mathbf{b}_i$. We now seek to understand how the twin lattice sites are related to the parent lattice sites by the shuffles. For type I twinning, we may assume that all sites in a particular K_1 plane shuffle in the same way; we can then describe these shuffles as the difference between the positions of the lattice sites and those of the parent sites, i.e.

$$\Delta^{\mathrm{I}} = (u_i+c_i)\mathbf{b}_i - pc_i\mathbf{a}_i - \frac{2p}{q}j_i\mathbf{a}_i + 2pd_{\mathrm{K}_1}\mathbf{m}. \tag{1.42}$$

The lattice vectors $\mathbf{a}_i$ and $\mathbf{b}_i$ are related by the orientation relations we defined earlier; thus, for orientation 1, i.e. a reflection in K_1, we have that

$$\mathbf{b}_i = \mathbf{a}_i - 2(\mathbf{a}_i\cdot\mathbf{m})\mathbf{m}, \tag{1.43}$$

such that we can write

$$c_i\mathbf{b}_i = c_i\mathbf{a}_i - 2d_{\mathrm{K}_1}\mathbf{m}, \tag{1.44}$$

$$u_i\mathbf{b}_i = u_i\mathbf{a}_i + 2qd_{\mathrm{K}_1}\mathbf{m}. \tag{1.45}$$

Therefore, the shuffles referred to basis $\mathbf{a}_i$ are given by

$$\Delta^{\mathrm{I}} = \left[(r-p)c_i + \frac{2p}{q}j_i + u_i\right]\mathbf{a}_i + 2d_{\mathrm{K}_1}(q-r-p)\mathbf{m}. \tag{1.46}$$

It is assumed that the shuffles will be so as to minimise $|\Delta^{\mathrm{I}}|$; if q is 1 or 2, the parameters can also be chosen so as to ensure that $\Delta^{\mathrm{I}}=0$ for all sites. For $q=1$, this is evident, since $p=1$, $r=0$ and $u_i=-j_i=-c_i$ The same choice of r and u_i ensures that for any value of q, the sites on the plane with $p=q$ do not have to shuffle and are shear directly into position, as required. Now let us examine the case $q=2$, and the sites on the plane with $p=1$. If $r=1$ and $j_i=-u_i$, the shuffles for sites on this plane are zero. In general, if q is even, lattice sites on plane $p=q/2$ and $p=q$ do not have to shuffle to arrive to twin positions, provided that $r=p$ and $u_i=-j_i$ are chosen.

Shuffle vectors may be similarly derived for type II twinning, though we shan't dwell on the full analysis here. A parameter $\bar{q}$ is defined to equal the number of K_2 lattice planes crossed by a primitive lattice vector parallel to $\boldsymbol{\eta_1}$; then no lattice shuffles are necessary for $\bar{q} = 1, 2$, and by assuming that for type II twinning all sites in a given K_2 plane shuffle in the same manner, equations for Δ^{II} are obtained.

Thus, the second criterion for the feasibility of twinning modes in early theories of twinning is the presence of shuffles which should be as simple as possible, along with the notion that modes with small shear magnitude are more likely to occur. It is not entirely clear why the latter criterion yields such accurate predictions for the occurrence of twinning modes, since the volume of twins necessary to produce a given plastic strain varies with $1/s$. However the stress field of a lenticular twin embedded in the matrix with a fixed aspect ratio (i.e. the ratio of length to thickness of the twin) varies with s^2, so that in principle it is more feasible to produce a given strain via a large number of twins with small shear magnitude than via a small number of twins with large twinning shear [64].

Both concepts of minimum shear and simple shuffles were retained when the theory of classical twinning was extended by Bevis and Crocker [76, 77] to include so-called non-classical twins, i.e. twinning modes where the parent and twin lattices are related by a simple shear, but the orientation relations 1 to 4 are not necessarily obeyed. We will explore this theory in greater detail in chapter 3, when dealing with phenomenological theories of double twinning.

Of course, the shuffles derived above only apply to lattice sites. If there is more than one atom in the unit cell, atomic shuffles will be required to restore the original structure during twinning. If there are two atoms in the unit cell, the origin of the cell may be picked as the centre of symmetry, such that the two atoms can be represented by $x_i + \xi_i$ and $x_i - \xi_i$, where ξ_i is the position of one of the atoms relative to the cell origin. Then the required shuffles for the atoms (termed structure shuffles by Christian [69]) can be inferred from those of the lattice sites. However, instead of reproducing this derivation here, we will examine the shuffles for the specific case of twinning occurring in magnesium; this is done in the following section.

1.3.1 Classical twins in magnesium

In the case of magnesium, there are two atoms in the unit cell. Typically, one is placed at a lattice point such as the origin, while the other is placed at e.g. $\frac{1}{2}[10\bar{1}1]$. However, in this configuration, the existence of a centre of symmetry is not apparent. In contrast, if basis atoms are placed at e.g. $\frac{1}{12}[40\bar{4}9]$ and $\frac{1}{12}[04\bar{4}3]$, lattice points are centres of symmetry [78]; the two different bases are compared in figure 1.5. If the latter configuration is chosen, it is evident that applying operations 1 and 4 to the hcp structure yields the same twin, and the same is valid for operations 2 and 3.

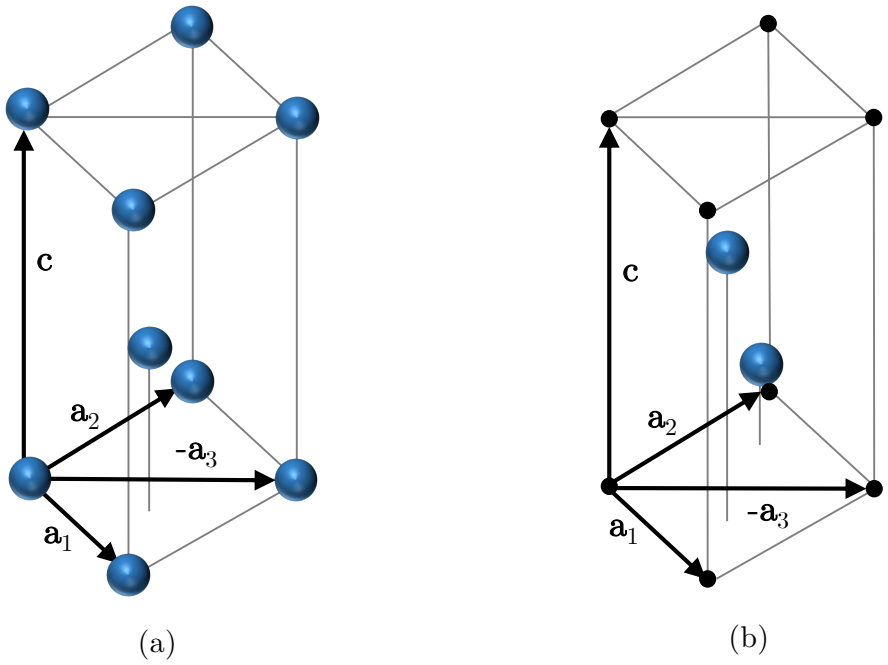

Fig. 1.5 Hexagonal unit cells decorated with two choices of atomic bases; atoms are given in blue, lattice points in black. In (a) one of the atoms in the unit cell is placed at a lattice point, in (b) atoms are placed such that the lattice points are centres of symmetry.

The most common twinning mode in magnesium is $\{10\bar{1}2\}$ twinning, which actually occurs in all hcp metals. This mode is characterised by the following twinning elements, given in the form $K_1K_2\boldsymbol{\eta}_1\boldsymbol{\eta}_2$,P;$s$:

$$\{10\bar{1}2\} \quad \{10\bar{1}\bar{2}\} \quad \langle 10\bar{1}\bar{1}\rangle \quad \langle 10\bar{1}1\rangle \quad \{1\bar{2}10\}\,; \quad \frac{\Lambda^2-2}{\sqrt{2}\Lambda}\,. \tag{1.47}$$

The shear magnitude for this twinning mode is the lowest of all modes with $q \leq 4$, for all axial ratios corresponding to real materials, such that it is not surprising that it is widely reported. For

magnesium, $c/a = 1.624$, the magnitude of the shear is $s = -0.129$. It should be noted that for $\gamma < \sqrt{3}$, this twinning mode is produced by extension along the c-axis, whereas for $\gamma > \sqrt{3}$ it is produced by compression: thus, the $\{10\bar{1}2\}$ twin is a "tension" twin for materials with $\gamma < \sqrt{3}$, such as magnesium, and a "compression" twin for materials such as cadmium and zinc, which have $\gamma > \sqrt{3}$ [79].

A projection of the hcp structure for magnesium onto the $(1\bar{2}10)$ plane is depicted in figure 1.6a; here the lattice points are shown as centres of symmetry, given by open symbols. The first piece of information that we gather from this figure is that twinning on $(10\bar{1}2)$ is a $q = 4$ mode, such that an equivalent interface may be recovered by moving upward by a distance corresponding to 4 $(10\bar{1}2)$ planes. Moreover, since the $(1\bar{2}10)$ plane is a mirror plane of the hexagonal lattice, orientations 1 and 2 are equivalent, and this is a compound twin; combined with the fact that the primitive unit cell is centrosymmetric, any of the orientations 1 to 4 may be used to describe the relationship between parent and twin lattice vectors for this twinning mode. From figure 1.6a we can also see how atoms are to be paired up in the so-called "motif units", i.e. the atom pairs associated with lattice points that shuffle rigidly in Jaswon and Dove's theory, as well as in Bilby and Crocker's; blue lines have been drawn in the figure connecting these pairs, as envisaged by Crocker [80]. The associated atomic shuffles are all then either parallel to $\boldsymbol{\eta}_1$ or perpendicular to K_1. The $\{10\bar{1}2\}$ twinning mode is thus characterised by a combination of low shear and a particularly simple shuffle mechanism, which are strong indicators as to its feasibility.

The other two observed classical twinning modes in magnesium are $\{10\bar{1}1\}$ twinning and its reciprocal mode, $\{10\bar{1}\bar{3}\}$ twinning; these are both "compression" modes. The twinning elements $\mathrm{K}_1\mathrm{K}_2\boldsymbol{\eta}_1\boldsymbol{\eta}_2,\mathrm{P};s$ are given by

$$\{10\bar{1}1\} \quad \{10\bar{1}\bar{3}\} \quad \langle 10\bar{1}\bar{2}\rangle \quad \langle 30\bar{3}2\rangle \quad \{1\bar{2}10\}; \quad \frac{\sqrt{2}(2\Lambda^2-3)}{4\Lambda}\,. \tag{1.48}$$

For the axial ratio of magnesium, the shear magnitude for this mode is given by $s = 0.138$, which is appreciably low. However, this is a $q = 8$ mode, as we can see from figure 1.6b, such that more lattice points are required to shuffle compared to $\{10\bar{1}2\}$ twinning: more precisely, only a quarter of lattice points is sheared directly into position. The corresponding atomic shuffles however remain relatively simple due to the fact that the "motif unit" is contained in the plane

of shear, as was the case for the tension twin. Indeed, the plane of shear for this mode is also $\{1\bar{2}10\}$, such that this mode is compound similarly to the $\{10\bar{1}2\}$ mode. Nevertheless, it is less common than tension twinning, as mentioned in the introduction.

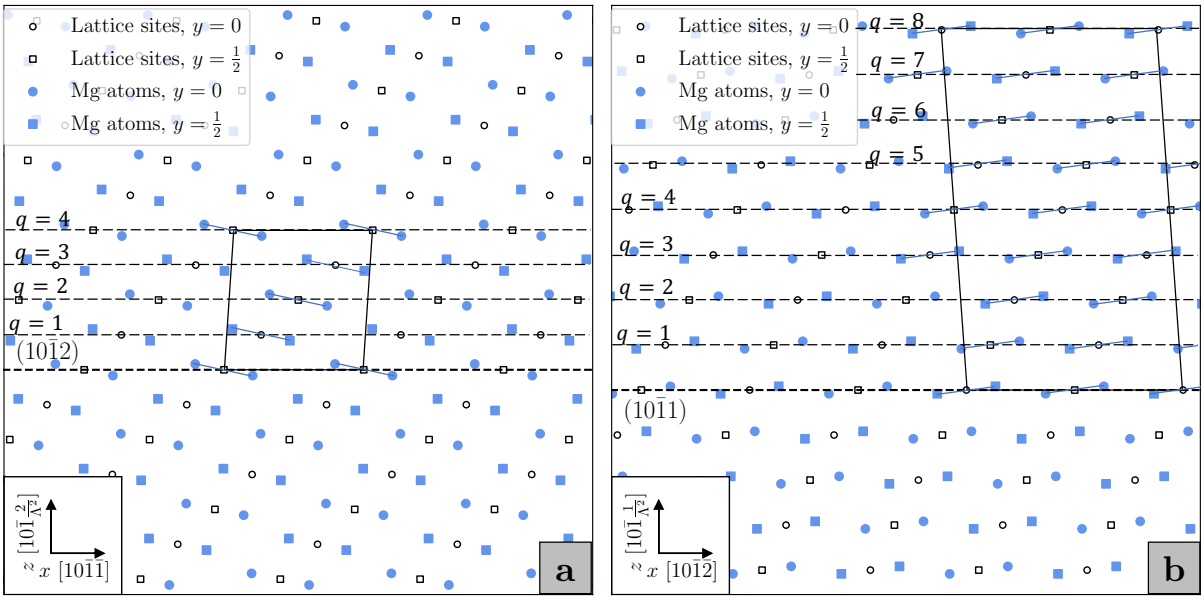

Fig. 1.6 Projection of the hcp structure onto the $(1\bar{2}10)$ plane illustrating atomic shuffles for $(10\bar{1}2)$ (a) and $(10\bar{1}1)$ (b) twinning. Open circles and squares represent lattice points, blue circles and squares indicate basis atoms. Pairs of atoms related to a lattice point are linked by blue lines, and shuffle rigidly in Jaswon and Dove's theory of atomic shuffles.

1.4 Atomistic simulations: the adaptive Generalized Pseudopotential Theory (aGPT)

The results reported in the previous section were based on the geometry of magnesium crystals, and so are the topological theories proposed by Pond that are introduced in the following chapter and are the main subject of this thesis. Pond's theories are based on the conservation of crystal symmetry, and though they allow us to exhaustively predict the admissible interfacial structures, they cannot be used to determine which of these structures have lower energies and are thus likely to occur in reality. The reason for this is that symmetry cannot account for interactions between atoms; hence the need for atomistic simulations, in which the interatomic forces are switched on, and the total energy of a structure may be calculated.

For the purpose of this thesis, atomistic simulations are used to ascertain the lowest energy configurations of relaxed twin interfaces, as is detailed in chapter 2. The chosen method for these calculations is density functional theory (DFT). In particular, we make use of the pair potential formulation of its total energy within the generalized pseudopotential theory (GPT), taking advantage of the fact that magnesium is a simple metal, for which the expansion truncated at the two-body term has been proved to be well converged [81–84]. Hence the total energy is written as

$$E_{\mathrm{tot}}(\{\mathbf{R}\},\Omega) = NE_{\mathrm{vol}}(\Omega) + \frac{1}{2}{\sum_{ij}}' v_2(R_{ij},\Omega), \tag{1.49}$$

where Ω is the average atomic volume and R_{ij} are the bond lengths between atoms i and j. The pair potential v_2 is long ranged and oscillating, as one would expect from a free electron metal, which has a sharp discontinuity in the electron occupation number across the Fermi surface; the oscillations are consistent with those of the Lindard screening function in the asymptotic limit [85]. Exchange and correlation are taken into account within the screening of the perturbed free electron gas, such that the GPT goes beyond the local density approximation by using a local field correction. In the implementation of the GPT employed here for magnesium, we use an energy dependent non local pseudopotential in Austin-Heine-Sham (AHS) form [86] within a small core, screened self-consistently to first order by means of the dielectric function of Ichimaru and Utsumi [87] based on the correlation energy of Vosko et al. [88]. The GPT in this form yields accurate results when compared to experiment and standard DFT calculations [89, 84, 90, 91], and it predicts for magnesium a lattice constant $a = 0.324$ nm and axial ratio $\gamma = 1.620$.

Since Ω in equation 1.49 is the average atomic volume, the dependence of E_{vol} and v_2 on Ω is global, and not local. As a consequence, introducing some empty space, such as a vacancy, has no effect on E_{vol}, because the change in the form of the interaction is the same for all atoms, independently of their distance from the vacancy. Therefore the formation energy of vacancies, as well as defects that entail the presence of some free volume and surfaces, is generally underestimated in the GPT. This problem is solved in the adaptive generalized pseudopotential theory (aGPT), which introduces local volume corrections in the formulation of the total energy [90, 92].

In the aGPT, the GPT total energy 1.49 is first expressed in terms of the average electron density $\bar{n}$:

$$E_{\text{tot}}(\mathbf{R},\bar{n}) = NE_{\text{vol}}(\bar{n}) + \frac{1}{2}{\sum_{ij}}' v_2(R_{ij},\bar{n}). \tag{1.50}$$

The pseudoatoms are then allowed to adjust according to the local electron density environment, such that equation 1.50 is rewritten to take this into account [93]:

$$E_{\text{tot}}(\mathbf{R},n_{\text{val}}) = \sum_i \left[E_{\text{vol}}(\bar{n}_i) + \frac{1}{2}\sum_{j\neq i} v_2(R_{ij},\bar{n}_{ij}) \right], \tag{1.51}$$

where $\bar{n}_i$ is the average local electron density of site i and $\bar{n}_{ij} = (\bar{n}_i + \bar{n}_j)/2$. In this way, the interaction between sites i and j depends also on the relative positions of all other atoms in the local neighbourhood; in a perfect crystal, where all ion positions are equivalent, equation 1.51 reduces to equation 1.50.

In order to derive the local electron density $\bar{n}_i$ we start with the GPT valence electron density n_{val}:

$$n_{\text{val}}(\mathbf{r}) = n_{\text{unif}} + \delta n_{\text{scr}}(\mathbf{r}) + \delta n_{\text{oh}}(\mathbf{r}), \tag{1.52}$$

where $n_{\text{unif}} = Z/\Omega$, δn_{scr} is a perturbation of the electron density due to screening and δn_{oh} is the orthogonalisation-hole density. But n_{val} can also be written as the sum of self-consistently screened pseudoatom densities n_{pa}:

$$n_{\text{val}}(\mathbf{r}) = \sum_i n_{\text{pa}}(\mathbf{r}-\mathbf{R}_i). \tag{1.53}$$

In order to connect the valence electron density to the aGPT total energy in equation 1.51, the GPT valence electron density is spatially averaged about the site i; in a bulk crystal with equivalent ion sites, this is equal to the uniform valence electron density n_{unif}. Then, using equations 1.52 and 1.53 and solving for n_{unif}, we find

$$\bar{n}_i \equiv n_{\text{unif}} = \sum_j \bar{n}_{\text{pa}}(R_{ij},\Omega) - \delta\bar{n}^i_{\text{oh}} - \delta\bar{n}^i_{\text{scr}}. \tag{1.54}$$

The approximation is then made that equation 1.54 can be applied generally. Moreover, $\bar{n}_i$ is split into two contributions: an on-site contribution $\bar{n}^i_a = \bar{n}_{\text{pa}}(R_{ii},\Omega) - \delta\bar{n}^i_{\text{oh}} - \delta\bar{n}^i_{\text{scr}}$ and an

off-site contribution $\bar{n}_b^i = \sum_{j \neq i} \bar{n}_{\mathrm{pa}}(R_{ij}, \Omega)$. $\bar{n}_a^i$ is then assumed to be constant, such that $\bar{n}_a^i \equiv \bar{n}_a$ and the on-site component can be calculated from a reference structure (usually the equivalent primitive unit cell) and equation 1.54. The off-site contribution $\bar{n}_b^i$ is then the only site-dependent component, calculated directly from $\bar{n}_{\mathrm{pa}}$ by looping over neighbours.

The local electron density is used to calculate the local atomic volume Ω_i via the definition for the uniform electron density, i.e. $\bar{n}_i = Z/\Omega_i$; this ensures that there are all the instruments needed to compute E_{vol} and pair potential v_2 by interpolating them to their respective atomic volumes. Finally, the contributions from E_{vol} and v_2 are added to calculate the total energy [92].

Hence, though the GPT and aGPT are completely equivalent in bulk, the aGPT is more suitable for calculations involving free surfaces and volumes. We thus employ it in our calculations, as detailed in the following chapter.

1.5 Structure of this thesis

The aim of this thesis is to shed light on the morphology of double twin to matrix interfaces using a combination of theoretical and experimental methods. The main theoretical tool we employ is the topological theory of interfacial defects proposed by Pond [94]; this is based on the study of crystal symmetry and its conservation in bicrystals, which are composites of two semi-infinite crystals. The topological model enables us to predict the admissible defects at an interface; thus a classical twin can be modelled as a bicrystal, and the admissible dislocations for a twin interface may be derived. Hence in chapter 2 we present bicrystallography and the topological theory of interfacial defects, subsequently applying them to all classical twins observed in magnesium with two aims: the first is to find the minimum energy interfacial structure for each twin; the second it to derive the characteristic twinning disconnections, that is special kinds of defects presenting both dislocation and step character that accomplish a given twinning transformation.

In chapter 3, double twinning is introduced. Though $(10\bar{1}1)-(10\bar{1}2)$ double twinning is reportedly the most common double twinning mode in magnesium, we include the cases of $(10\bar{1}\bar{3})-(10\bar{1}2)$, $(10\bar{1}2)-(10\bar{1}1)$ and $(10\bar{1}2)-(10\bar{1}\bar{3})$ twinning. Firstly we introduce the four double twin variants associated with each double twinning sequence, distinguishing them through their misorientation relations with the parent grain. We then present Crocker's theory of

double twinning on an invariant habit plane, as well as ensuing theories of non-classical twinning proposed by Bevis and Crocker [76, 77]. We show that these theories lead to the same result for double twinning in magnesium. Subsequently, topological models of double twinning are introduced, with two cases analysed: secondary twinning disconnections impinging on a flat or stepped primary twin interface. The latter case is shown to reproduce the double twin habit planes predicted by Crocker's theory; the two methods are compared and contrasted, particularly in their leading to descriptions of double twinning as one- and two-step processes.

Chapter 4 comprises of two parts. In the first half of the chapter, a third case is analysed using the topological model: that of secondary twinning disconnections arriving at a faceted primary twin interface. It is shown that commensurate facets in the primary twin boundary may be transformed into commensurate facets of the double twin to matrix interface via the action of secondary twinning disconnections. $(10\bar{1}2)-(10\bar{1}1)-(10\bar{1}2)$ triple twinning is also introduced, and it is found that no commensurate facets may be created in the triple twin to matrix interface. In the second half of the chapter, we focus on experimental observations. An overview of the experimental methods is given, with particular attention bestowed on transmission electron microscopy (TEM). We then present TEM observations of twin interfaces in a hot rolled rare-earth magnesium alloy; in particular, $(\bar{1}012)-(\bar{1}011)$ double twins are imaged, and their interfaces with the matrix are analysed via high-resolution TEM, leading to the discovery of commensurate interfacial facets of the kind predicted by the topological model. Moreover, $(\bar{1}012)-(\bar{1}011)-(\bar{1}012)$ triple twins are found in the specimen, and the interface between triple twins and the matrix is observed for the first time in a magnesium alloy.

Finally, in chapter 5 we summarise the conclusions gathered throughout the thesis, and propose further research on the subject of double twinning.

Chapter 2

Bicrystallography and the topological theory of interfacial defects

"*If you trust in yourself... and believe in your dreams... and follow your star... you'll still get beaten by people who spent their time working hard and learning things and weren't so lazy.*"

The Wee Free Men, TERRY PRATCHETT

This chapter is dedicated to the theory that has been the foundation of most of the theoretical work of this thesis, i.e. Bob Pond's topological theory of interfacial defects. This theory originates in the study of the symmetry of bicrystals, that is composites of two semi-infinite crystalline objects. It will be immediately clear how twins can be described as bicrystals, and thus how the study of their symmetry can lead to the prediction of admissible defects in their interfaces. These defects are the building blocks of all the topological models presented in subsequent chapters, and are here derived for all classical twins observed in magnesium.

2.1 Theory

In the present section, we illustrate the theory of bicrystallography. In particular, we explain how a bicrystal is obtained starting from an infinite perfect crystal, such that to each step in the creation of the bicrystal corresponds the derivation of the symmetry group of the structure. In

order to make sure we possess all the mathematical tools necessary to illustrate the procedure, we first give an introduction to some useful concepts of group theory, and we briefly describe symmetry operations.

We then proceed to describe how the loss of symmetry resulting from the creation of a bicrystal leads to the formation of interfacial defects, and we classify these defects based on the type of symmetry that characterises them. It will be evident that though this is a deeply mathematical theory, it is also firmly rooted in physical intuition, making it an accurate yet natural tool for the study of crystals.

2.1.1 Bicrystallography

We shall start with a brief primer on symmetry. A *symmetry transformation* is the process of making a figure coincide with itself through reflection or any other operation. The geometric elements (i.e. points, lines and planes) used to carry out symmetry transformations are referred to as *symmetry elements*. More formally, a symmetry element is defined as the geometric locus of points which remain stationary during all the transformations of a cyclic group G generated by powers of an arbitrary operation g, where g^n corresponds to the repetition of g n times, and the order n of the operation g, which is also the number of distinct elements of the group G, is determined by the defining equation $g^n = I$ (more on groups will follow shortly). A symmetrical object possesses at least one symmetry element; but since it can be shown that every isometric transformation (i.e. transformations which do not result in a deformation) is equivalent to an appropriate number of reflections carried out one after the other, a symmetrical figure is defined as one that can be made to coincide with itself through successive reflections in planes [95].

We now proceed to describe the symmetry elements of three-dimensional figures as well as the corresponding symbols used to indicate them, following the notation used in the International Tables for Crystallography [96].

- *Symmetry plane m*: imaging mirror plane. A reflection in such a plane brings the image in coincidence with itself. The defining equation for this operation is $m^2 = 1$.

- *Symmetry axis* $n^{\pm}$: a line such that when the figure rotates around it, it is brought into coincidence with itself n times; n is called the order of the axis, and the axis is termed

n-fold. The + or − superscript indicates the sense of the rotation when viewed along the rotation axis in the direction of decreasing values of the parameter describing the axis; + denotes a counter-clockwise rotation, and − a clockwise rotation (when the superscript is not specified, a + is assumed). The defining equation for this operation is $n^n = 1$. It can be noted that the 1-fold symmetry axis coincides with the identity.

- *Mirror-rotation symmetry axis* $\tilde{n}^{\pm}$: a rotation around this axis followed by a reflection in a perpendicular plane m brings the object in coincidence with itself, i.e. $\tilde{n} = nm = mn$. The $\pm$ superscript has the same significance as for the symmetry axis $n^{\pm}$. The defining equation is $\tilde{n}^n = 1$.

- *Inversion rotation axis* $\bar{n}^{\pm}$: a rotation around this axis followed by an inversion through a centre of symmetry brings the figure in coincidence with itself, i.e. $\bar{n} = n\bar{1} = \bar{1}n$. The superscript indicates the sense of rotation as in $n^{\pm}$. The defining equation is $\bar{n}^n = 1$. It should be noted that symmetry transformations of this type have the same effect as the mirror-rotations described above: e.g. $\tilde{2} = \bar{1}$.

- *Axis of finite translations* t: a displacement by a vector $\mathbf{t}$ along this axis brings the figure into coincidence with itself. The defining equation is $t^n = n\mathbf{t}$.

- *Screw axis* $n_j^{\pm}$, $j = 1,2,...,n-1$: a rotation of a rational angle of rotation around this axis followed by a finite translation $\mathbf{t} = \frac{\boldsymbol{\tau}_n}{j}$ along this axis brings the figure into coincidence with itself. The superscript denotes the sense of rotation as above. The defining equation is $n_j^n = \boldsymbol{\tau}$. If the angle of rotation σ is irrational, the screw axis is denoted by σ_t.

- *Glide-reflection plane* g: a reflection in a plane m followed by a translation by a vector $\mathbf{g}/2$ that lies in m brings the figure into coincidence with itself. The defining equation is $g = \mathbf{g}$. When the translation is carried out along an axial direction, i.e. [100], [010] and [001], the symbols a, b and c respectively are used, to indicate an "axial" glide-reflection plane.

The set of symmetry transformations that change the positions of parts of a figure while bringing it into coincidence with itself can be described mathematically as a group. Hence, the group of symmetry transformations of a figure (which may be finite or infinite) is made up of transformations that leave the figure invariant, i.e. that conserve its structure. The space

symmetry group of a figure is called *symmorphic* if it does not contain screw rotation and glide-reflection operations, and *non-symmorphic* if it does.

In order for a set of arbitrary transformations $g_1, g_2, ...$ to be described as an *abstract group* $G = \{g_1, g_2, ...\}$, four conditions have to be met: *i)* an operation of "multiplication" can be defined for the set such that by multiplying any pair of elements belonging to the set, another element of the set is obtained, i.e. if $g_i, g_j \in G$, then $g_i g_j = g_k \in G$; *ii)* the multiplication is associative, i.e. $(g_i g_j)g_k = g_i(g_j g_k)$; *iii)* the set contains an identity element e such that $g_i e = e g_i = g_i$; *iv)* for every g_i there exists an inverse element g_i^{-1} such that $g_i g_i^{-1} = g_i^{-1} g_i = e$. The number of elements of the group is defined as the order of the group. A subset $H = \{h_1, h_2, ...\}$ of the group G which has the properties of a group is called a *subgroup*, $H \subset G$. For any subgroup H of G, left and right *cosets* are defined as follows:

$$g_i H = \{g_i h_1, g_i h_2, ...\}, \tag{2.1}$$

$$H g_i = \{h_1 g_i, h_2 g_i, ...\}, \tag{2.2}$$

where $g_i \notin H$. It can be shown that two cosets are either identical, or have no elements in common [95]; hence, the group G can be decomposed with respect to a subgroup H by listing all the elements of G based on the distinct cosets they belong to in the following way:

$$G = H \cup g_1 H \cup g_2 H ... \cup g_j H. \tag{2.3}$$

The *index of the subgroup* is the number of cosets j in the decomposition of the group with respect to the subgroup being considered; Lagrange's theorem states that the order of a subgroup of a finite group G is a divisor of the order of G, and as a consequence the index of the subgroup will also be a divisor of the order of G [97]. If the left and right cosets for a subgroup H of G are the same, i.e. $H g_i = g_i H$, then H is termed an *invariant subgroup*, or normal divisor, of G, denoted by $H \lhd G$.

An important concept in group theory is that of the *homomorphic mapping* of the elements of a group $G = \{g_1, g_2, ...\}$ onto the elements of the smaller (in order or power) group $F = \{f_1, f_2, ...\}$.

This is a unidirectional mapping defined as $G \to F$:

$$\text{if } \; g_i \to f_i \; \text{ and } \; g_j \to f_j, \; \text{ then } \; g_i g_j \to f_i f_j. \tag{2.4}$$

The establishment of a homomorphism between G and F is particularly useful because it allows us to reduce the study of the multiplication laws of G to the smaller group F. Conversely, one may at times find it convenient to establish an equivalence between two groups, say G and K; this is achieved by setting up a one-to-one correspondence between the elements of the two groups, hence establishing an *isomorphic mapping* between the two groups, $G \leftrightarrow K$:

$$\text{if } \; g_i \leftrightarrow k_i \; \text{ and } \; g_j \leftrightarrow k_j, \; \text{ then } \; g_i g_j \leftrightarrow k_i k_j. \tag{2.5}$$

We now introduce a notation for the symmetry operations contained in a symmetry group. Again, we choose the notation adopted in the International Tables for Crystallography [96], which was used in many works by Pond on the theory of topological defects [98]. According to this notation, the jth space group operation of a crystal is denoted by a matrix pair $(\mathbf{W}_j, \mathbf{w}_j)$. $\mathbf{W}_j$ is a (3×3) matrix, called the rotation part, and $\mathbf{w}_j$ is a vector representing the translation part; $\mathbf{w}_j$ may be split into two contributions, $\mathbf{w}_j = \mathbf{t}_i + \boldsymbol{\alpha}_j$, where $\mathbf{t}_i$ is a translation vector of the lattice, and determines the location of the symmetry element, while $\boldsymbol{\alpha}_j$ is the screw or glide part of the symmetry operation. As we are going to treat bicrystals, we denote the red crystal with λ and the black crystal with μ, such that a space group operation of the red crystal is given by $(\mathbf{W}(\lambda)_j, \mathbf{w}(\lambda)_j)$. Hence, a space group operation of the red crystal acts on a vector $\mathbf{r}$ as follows:

$$(\mathbf{W}(\lambda)_j, \mathbf{w}(\lambda)_j)\mathbf{r} = \mathbf{W}(\lambda)_j \mathbf{r} + \mathbf{w}(\lambda)_j. \tag{2.6}$$

The product of two such operations, e.g. the kth and the jth operations of a crystal, is found by applying equation 2.6 twice, such that:

$$(\mathbf{W}(\lambda)_k, \mathbf{w}(\lambda)_k)(\mathbf{W}(\lambda)_j, \mathbf{w}(\lambda)_j) = (\mathbf{W}(\lambda)_k \mathbf{W}(\lambda)_j, \mathbf{W}(\lambda)_k \mathbf{w}(\lambda)_j + \mathbf{w}(\lambda)_k). \tag{2.7}$$

In general, this product does not commute. From this multiplication rule we can see that the inverse operation must be $(\mathbf{W}(\lambda)_j^{-1}, -\mathbf{W}(\lambda)_j^{-1}\mathbf{w}(\lambda)_j)$, in order to have

$$(\mathbf{W}(\lambda)_j^{-1}, -\mathbf{W}(\lambda)_j^{-1}\mathbf{w}(\lambda)_j)(\mathbf{W}(\lambda)_j, \mathbf{w}(\lambda)_j) = (\mathbf{I}, \mathbf{0}), \tag{2.8}$$

where $\mathbf{I}$ is the identity. In this notation, pure translation operations will be denoted by e.g. $(\mathbf{I}, \mathbf{w}(\lambda)_j)$, and point group operations will be indicated as e.g. $(\mathbf{W}(\lambda)_j, \mathbf{0})$.

Having introduced the basic concepts of group theory as well as the notation we will use, we can proceed to see how group theory is applied to crystallography in a field pioneered by Pond, i.e. that of bicrystallography. A *bicrystal* is a composite object made up of two crystals, conventionally referred to using different colours for each crystal, which we have chosen to be black and red; the border between the black and red crystals is the interface of the bicrystal. One can distinguish between two types of interface: *heterophase* if the black and red crystals do not have the same crystal structure and *homophase* if they do [97]. The latter type of interface is also known as a grain boundary. Twin boundaries are of this type, and hence twins can be modelled with the aid of bicrystallography.

In order to treat the symmetry of a bicrystal, we will avail ourselves of the general principle of the superposition of symmetry groups [99]. In the case of heterophase bicrystals, the composite formed is heterogeneous, and hence its symmetry group is the intersection of the symmetry groups of its constituents. This means that the symmetry of the bicrystal is lower than the symmetry of the black and red crystals; hence the making of a heterophase bicrystal involves a *dissymmetrization*. However, in the case of homophase bicrystals, new operations may arise relating the black and red crystals, as they have the same crystal structure; these operations are referred to as antisymmetry operations or *antioperations*, and we will denote the corresponding symmetry elements in the same way as the ordinary elements listed above with the addition of a prime as a superscript, e.g. m'. Thus, in this case the group obtained via the dissymmetrization may be extended by a symmetrizing group. Whenever a composite is dissymmetrized, crystallographic *variants* arise; these can be identified at each step of the dissymmetrization process. Pond has devised a method for deriving the symmetry group of an interface in four stages; each stage involves dissymmetrization in some measure, and hence the identification of a class of variants, resulting in four classes. The treatment presented here follows Sutton and Balluffi [97].

The starting point of Pond's method is the symmetry of the black and red lattices, considered separately; the lattice will be decorated with basis atoms at a later stage. In this method, the lattice is regarded as the object of maximal symmetry, and hence its space group is denoted as holosymmetric. The space groups of the black and red lattices are indicated respectively by $\Phi^*(\mu)$ and $\Phi^*(\lambda)$, where the asterisk implies that the groups are holosymmetric; Φ is the Russian letter "F", used for the Fedorov space groups of ordinary symmetry operations (i.e. those that do not include antioperations). There are 230 Fedorov groups, obtained as follows: the 32 point groups are combined with the 14 translation groups (i.e. the translation groups of the 14 Bravais lattices) to form 73 symmorphic groups; a further 157 nonsymmorphic space groups are produced from the symmorphic space groups by replacing the generating point group elements with the corresponding glide-reflection planes and screw axes [95].

The next step in Pond's procedure is to rotate one of the two lattices, while the other is kept fixed, and to then allow the two lattices to interpenetrate, forming the *dichromatic pattern*. Focusing on the case of homophase interfaces, the dichromatic pattern may now contain both symmetry and antisymmetry operations, and its group will be an antisymmetry or colour group, also known as Shubnikov group, Ш, pronounced "Sha". There is a total of 1651 Shubnikov groups, which formally include the 230 colourless Fedorov groups, as well as the neutral groups (i.e. those obtained by adding the antiidentity $1'$ to the generators of the Fedorov groups) and the black and red groups[2] [95]. The Shubnikov groups are also known as magnetic space groups, because colour can be likened to a physical property with two values, and specifically to the sign of the magnetic moment of a particle.

If we now adjust the relative translation of the two lattices to obtain maximal colour symmetry, we find that the holosymmetric symmetry group of the dichromatic pattern is $Ш^*(p)$, also known as the *embracing group* [99]. In this first stage of dissymmetrization, variants arise from the absence of some of the ordinary symmetry operations of $\Phi^*(\mu)$ and $\Phi^*(\lambda)$ from $Ш^*(p)$: these operations relate equivalent dichromatic patterns, called *orientational* or *translational variants* depending on whether they arise from the suppression of point group or translational symmetry operations [97].

[2]The number of colours need not be restricted to two. The generalisation of the Shubnikov groups to a number p of colours is given by the Belov groups, Б [100].

In order to derive the symmetry group of the dichromatic pattern, we need to know the relationship between the coordinate systems of the black and red lattices. Using the notation we described above, we can denote a general transformation between the lattice vectors of the black lattice and those of the red lattice by $(\mathbf{P}', \mathbf{p})$; $\mathbf{p}$ is the translation of the black lattice required to bring at least one of its sites in coincidence with a red site, and $\mathbf{P}' = \mathbf{DR}$, where $\mathbf{D}$ is a pure deformation and $\mathbf{R}$ is a pure rotation, and the prime symbol is used as the transformation relates black and red sites. Hence, the black and red lattice vectors are related as $\mathbf{a}(\mu)_i = P'_{ji}\mathbf{a}(\lambda)_j + \mathbf{p}$, and points $\mathbf{r}(\mu)$ and $\mathbf{r}(\lambda)$ of the black and red coordinate systems respectively follow $\mathbf{r}(\lambda) = \mathbf{P}'\mathbf{r}(\mu) + \mathbf{p}$.

Now, we can split the problem of finding the symmetry of the dichromatic pattern into two steps: finding the ordinary operations and the antisymmetry operations. The group of ordinary operations $\Phi(p)$ can be found as the intersection between $\Phi^*(\lambda)$ and $\Phi^*(\mu)$ when they are both expressed in the coordinate system of the red lattice:

$$\Phi(p) = \Phi^*(\lambda) \cap (\mathbf{P}', \mathbf{p})\Phi^*(\mu)(\mathbf{P}', \mathbf{p})^{-1}. \tag{2.9}$$

There are two types of operations in this group: translation and point group operations. Let us consider translations first. The translation operations of the ordinary translation group $T(p)$ of the dichromatic pattern must satisfy equation 2.9:

$$T(p) = (\mathbf{I}, \mathbf{t}(\lambda)_j) \cap (\mathbf{P}', \mathbf{p})(\mathbf{I}, \mathbf{t}(\mu)_i)(\mathbf{P}', \mathbf{p})^{-1}. \tag{2.10}$$

Hence

$$\begin{aligned} (\mathbf{I}, \mathbf{t}(\lambda)_j) &= (\mathbf{P}', \mathbf{p})(\mathbf{I}, \mathbf{t}(\mu)_i)(\mathbf{P}', \mathbf{p})^{-1} \\ (\mathbf{I}, \mathbf{t}(\lambda)_j) &= (\mathbf{I}, \mathbf{P}'\mathbf{t}(\mu)_i) \\ \mathbf{t}(\lambda)_j &= \mathbf{P}'\mathbf{t}(\mu)_i, \end{aligned} \tag{2.11}$$

where $\mathbf{t}(\lambda)_j$ and $\mathbf{t}(\mu)_i$ are the translation vectors of the red and black lattices expressed in their own coordinate frames. The elements of $T(p)$ constitute a coincidence cite lattice (CSL), i.e. the lattice of grey points, which are a superposition of black and red points [101]. Grimmer [102]

has shown that the existence of a 3D CSL in a dichromatic pattern is constrained to systems where $\mathbf{P}'$ has only rational entries. If $\mathbf{P}'$ is a pure rotation $\mathbf{R}$, then for a CSL to exist all the elements of $\mathbf{R}$ have to be rational; moreover, Fortes [103] has shown that in non-cubic materials the square of the axial ratio also has to be rational for a CSL to exist, with the exception of rotations about the c-axis of a hexagonal or tetragonal structure.

Focusing now on ordinary point group operations of the dichromatic pattern, we see that they must also satisfy equation 2.9; hence

$$(\mathbf{W}(\lambda)_j,\mathbf{0}) = (\mathbf{P}',\mathbf{p})(\mathbf{W}(\mu)_i,\mathbf{0})(\mathbf{P}',\mathbf{p})^{-1}, \tag{2.12}$$

and two conditions are obtained:

$$\mathbf{W}(\lambda)_j = \mathbf{P}'\mathbf{W}(\mu)_i{\mathbf{P}'}^{-1}, \tag{2.13}$$

$$\mathbf{P}'\mathbf{W}(\mu)_i{\mathbf{P}'}^{-1}\mathbf{p} = \mathbf{p}. \tag{2.14}$$

Equation 2.13 indicates that in order for point group operations of the black and red crystals to belong to the dichromatic pattern, they have to be brought into orientational alignment. Equation 2.14 means that only point group operations that leave $\mathbf{p}$ invariant are conserved in the dichromatic pattern.

Having found the conditions satisfied by the symmetry operations belonging to $\Phi(p)$, we turn to antisymmetry operations of the dichromatic pattern. Since these can only exist in homophase boundaries, i.e. where the two lattices are identical except for orientation, the antisymmetry operations will have to be point group operations. In particular, antioperations will be given by specifications of $(\mathbf{P}',\mathbf{p})$ that have the form of symmetry operations. The most general specification of $(\mathbf{P}',\mathbf{p})$ that involves no translation is $(\mathbf{P}',\mathbf{p})(\mathbf{W}(\lambda)_l,\mathbf{0})$, and it relates the red lattice to the black one; but if antisymmetry is present, then there must be simultaneously a vector transformation relating the black lattice to the red one, i.e. $(\mathbf{P}',\mathbf{p})^{-1}(\mathbf{W}(\mu)_k,\mathbf{0})$. Expressing everything in the coordinate system of the red lattice, we obtain

$$(\mathbf{P}',\mathbf{p})(\mathbf{W}(\lambda)_l,\mathbf{0}) = (\mathbf{W}(\mu)_k,\mathbf{0})(\mathbf{P}',\mathbf{p})^{-1}, \tag{2.15}$$

such that two conditions are found:

$$\mathbf{P}'\mathbf{W}(\lambda)_l = \mathbf{W}(\mu)_k\mathbf{P}'^{-1}, \tag{2.16}$$

$$\mathbf{W}(\mu)_k\mathbf{P}'^{-1}\mathbf{p} = -\mathbf{p}. \tag{2.17}$$

Equation 2.17 needs a closer look. We have defined $\mathbf{p}$ as the translation required to bring at least one point of the red lattice into coincidence with a black point, and this still applies after the action of $\mathbf{W}(\mu)_k\mathbf{P}'^{-1}$. However the equation does not take into account that the antisymmetry operation exchanges black sites with red, in which case the sign of $\mathbf{p}$ changes; this makes $\mathbf{p}$ a new kind of vector, in whose definition colour is included, and this should be accounted for in equation 2.17. Therefore we define the antisymmetry operation $\mathbf{A}'_n$ such that it includes a change of colour as follows:

$$\mathbf{A}'_n = 1'\mathbf{A}_n, \qquad \mathbf{A}_n = \mathbf{W}(\mu)_k\mathbf{P}^{-1} = \mathbf{P}\mathbf{W}(\lambda)_l, \tag{2.18}$$

where $1'$ is the colour reversing operation. Equation 2.17 becomes

$$\mathbf{A}'_n\mathbf{p} = \mathbf{p}. \tag{2.19}$$

The product of two antioperations has to be an ordinary operation of the dichromatic pattern, because the action of two $1'$ operations one after the other leaves colour unchanged. Hence

$$\mathbf{P}'\mathbf{W}(\lambda)_l\mathbf{P}'\mathbf{W}(\lambda)_s = \mathbf{W}(p)_m,$$

where $\mathbf{W}(p)_m$ is an ordinary point group operation of the dichromatic pattern. Remembering that equivalent specifications of $\mathbf{P}'$ are equally valid, we redefine $\mathbf{P}'$ to be the antisymmetry operation $\mathbf{P}'\mathbf{W}(\lambda)_s$, and we find

$$\begin{aligned}\mathbf{P}'\mathbf{W}(\lambda)_s^{-1}\mathbf{W}(\lambda)_l\mathbf{P}' &= \mathbf{P}'\mathbf{W}(\lambda)_q\mathbf{P}' = \mathbf{W}(p)_m,\\ \mathbf{P}'\mathbf{W}(\lambda)_q &= \mathbf{W}(p)_m\mathbf{P}'^{-1}.\end{aligned} \tag{2.20}$$

According to equation 2.20, all antisymmetry operations can be generated by multiplying just one of them by the group of ordinary point group operations of the dichromatic pattern.

Now that we have found the admissible antisymmetry operations, we have all the operations of the dichromatic pattern: its holosymmetric space group $\text{Ш}^*(p)$ is given by

$$\text{Ш}^*(p) = \Phi^*(p) \cup \mathbf{P}'W^*(p), \tag{2.21}$$

where $W^*(p)$ is the holosymmetric point group of ordinary operations of the pattern, such that the antisymmetry operations are given by the coset $\mathbf{P}'W^*(p)$, and $\Phi^*(p)$ is the holosymmetric version of $\Phi(p)$, obtained by taking $\mathbf{p} = 0$. The determination of $\text{Ш}^*(p)$ allows us to find the orientational variants mentioned above. In particular, we may enumerate them by decomposing $\Phi^*(\lambda)$ and $\Phi^*(\mu)$ with respect to $\Phi^*(p)$, which is a subgroup of both. Hence, as a consequence of Lagrange's theorem, the number of orientational variants is equal to the order of $\Phi^*(\lambda)$ plus the order of $\Phi^*(\mu)$ divided by the order of $\Phi^*(p)$.

In the second stage of dissymmetrization, the basis atoms are placed at lattice sites by carrying out on a chosen point all the symmetry operations of the crystal's space group; the black and red crystals have space groups $\Phi(\mu)$ and $\Phi(\lambda)$, which may be nonholosymmetric (i.e. they might not have the same symmetry as the lattice) and/or non-symmorphic, and are isomorphic to subgroups of $\Phi^*(\mu)$ and $\Phi^*(\lambda)$. The interpenetrating black and red crystals then form the dichromatic complex, whose holosymmetric coloured space group is denoted by $\text{Ш}^*(c)$. If the black and red crystals are holosymmetric and symmorphic, then $\Phi(\mu) = \Phi^*(\mu)$, $\Phi(\lambda) = \Phi^*(\lambda)$, and $\text{Ш}^*(c) = \text{Ш}^*(p)$; but more generally, $\text{Ш}^*(c)$ is a subgroup of $\text{Ш}^*(p)$, and hence the suppressed symmetry elements of $\text{Ш}^*(p)$ relate *complex variants* of $\text{Ш}^*(c)$.

To find the space group of the dichromatic complex $\text{Ш}(c)$ we proceed as done before for $\text{Ш}(p)$. First we find the group of ordinary operations of the dichromatic complex $\Phi(c)$:

$$\Phi(c) = \Phi(\lambda) \cap (\mathbf{P}', \mathbf{p})^{-1}\Phi(\mu)(\mathbf{P}', \mathbf{p}). \tag{2.22}$$

The translation vectors of the dichromatic complex are the same as those of the pattern; hence equation 2.11 is valid for the complex too. However in the case of point group operations, the supplementary displacement required for non-symmorphic operations gives rise to a third

condition for the existence of such an operation in the complex, in addition to equations 2.13 and 2.14. This is because the form of equation 2.12 has to be modified for non-symmorphic operations to include the extra displacements $\boldsymbol{\alpha}$:

$$(\mathbf{W}(\lambda)_j, \boldsymbol{\alpha}(\lambda)_j) = (\mathbf{P}', \mathbf{p})(\mathbf{W}(\mu)_i, \boldsymbol{\alpha}(\mu)_i)(\mathbf{P}', \mathbf{p})^{-1}, \tag{2.23}$$

such that the new condition, in addition to 2.13 and 2.14 is

$$\boldsymbol{\alpha}(\mu)_i = \mathbf{P}'^{-1}\boldsymbol{\alpha}(\lambda)_j. \tag{2.24}$$

The same reasoning applies to antisymmetry operations of the dichromatic complex. In this case, generalising equation 2.15 to include the supplementary displacement gives rise, in addition to equations 2.16 and 2.17, to the condition

$$\boldsymbol{\alpha}(\mu)_k = \mathbf{P}'\boldsymbol{\alpha}(\lambda)_l, \tag{2.25}$$

where both $\boldsymbol{\alpha}(\mu)_k$ and $\boldsymbol{\alpha}(\lambda)_l$ are expressed in the coordinate system of the red lattice.

Having found the conditions satisfied by the operations in $\text{Ш}(c)$, we may find the holosymmetric dichromatic complex with space group symmetry $\text{Ш}^*(c)$, and by decomposing $\text{Ш}^*(p)$ with respect to it we can enumerate the complex variants mentioned above.

The bicrystal is then created in the third stage of dissymmetrization: an interface plane is chosen, and all black atoms are discarded on one side, and red atoms on the other. Conventionally, the atoms are discarded such that the normal to the interface points in the direction of the red crystal. The symmetry of the bicrystal thus produced depends generally on the relative translation of the two complexes as well as on the location chosen for the interface; the holosymmetric space group of the (unrelaxed) bicrystal is $\text{Ш}^*(b)$, and is a subgroup of $\text{Ш}^*(c)$. The variants arising from the suppression of some symmetry operations of $\text{Ш}^*(c)$ in $\text{Ш}^*(b)$ are called *morphological variants*.

The ordinary operation of the dichromatic complex $(\mathbf{W}(c)_j, \boldsymbol{\alpha}(c)_j)$ survives in the bicrystal if it satisfies the following conditions [97]:

$$\mathbf{W}(c)_j \hat{\mathbf{n}} = \hat{\mathbf{n}}, \tag{2.26}$$

$$(\boldsymbol{\alpha}(c)_j + \mathbf{t}_k) \cdot \hat{\mathbf{n}} = 0, \tag{2.27}$$

where $\hat{\mathbf{n}}$ is the boundary normal and $\mathbf{t}_k$ is any lattice translation vector of the black or red lattice. When considering antioperations, we have to take into account the definition of colour intrinsic to the boundary normal, as we did for the translation $\mathbf{p}$. The conditions for an antisymmetry operation of the dichromatic complex to survive in the bicrystal are

$$\mathbf{W}'(c)_i \hat{\mathbf{n}} = \hat{\mathbf{n}}, \tag{2.28}$$

$$(\boldsymbol{\alpha}(c)_i + \mathbf{t}_k) \cdot \hat{\mathbf{n}} = 0. \tag{2.29}$$

In equation 2.28 the boundary normal changes sign twice, i.e. when $\mathbf{W}(c)_i$ transforms the black crystal into the red (and vice versa) and when $1'$ reverses colour. However, the presence of certain antisymmetry operations in $\text{III}(b)$ depends on the location of the interface; this means that different bicrystals related by symmetry may be created by moving the interface plane, and they can be obtained by decomposing the holosymmetric group $\text{III}^*(b)$ with respect to the group of ordinary operations $\Phi(b)$. $\text{III}^*(b)$ is also used to enumerate the morphological variants, by decomposing $\text{III}^*(c)$ with respect to it.

The last stage of the dissymmetrization process involves relaxing the bicrystal by allowing the atoms to move according to interatomic forces. The resulting structure will have space group symmetry $\text{III}(b)$, quite possibly lower than the holosymmetric symmetry group $\text{III}^*(b)$, and any symmetry operations of $\text{III}^*(b)$ that are not present in $\text{III}(b)$ will relate *relaxational variants*. It should be noted that these are the only variants whose existence cannot be postulated using symmetry arguments, as they depend on the interactions between atoms. The four stages of dissymmetrization and the related variants may be summarised with the diagram in figure 2.1, as proposed by Pond [99].

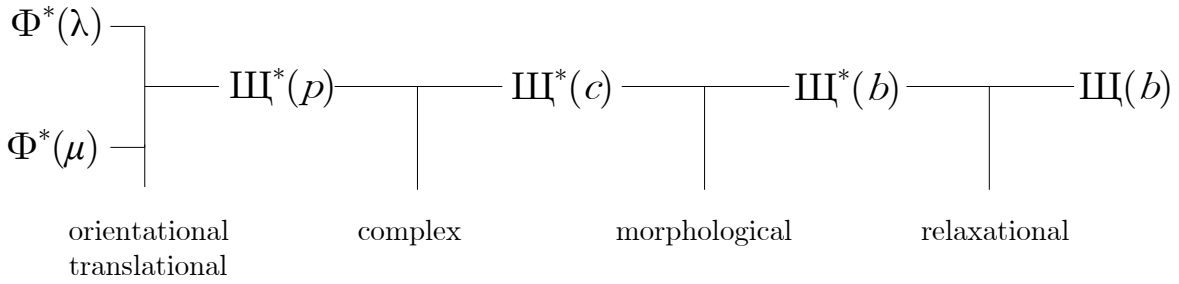

Fig. 2.1 Diagram showing the steps of the dissymmetrization scheme proposed by Pond [99] and the relative variants.

2.1.2 The topological theory of line defects

The application of bicrystallography we are most interested in is the prediction of the line defects that can arise at an interface. In particular, the variants arising from the different steps of dissymmetrization and their interrelation provide us with information on line defects that separate regions of the interface that are related by symmetry [94, 98, 104, 105]. We will see how the character of the admissible line defects of an interface is determined by the extent to which the symmetry operations of the black and red crystals coincide; after Pond [98], whom we follow in the classification of defects, we refer to this concept as bicrystal connexion. The higher the degree of disconnexion of a bicrystal, the more variants arise from dissymmetrization, and the more defect types can reside in the interface. Our spelling of the words connexion and disconnexion will be motivated below; we make this choice to highlight the distinction between the concept of disconnexion just introduced and disconnections, i.e. a type of crystal defect discussed in what follows. In this section we divide line defects into three categories: dislocations, characterised by translation operations; disclinations, characterised by rotation operations; dispirations, characterised by screw rotation operations.

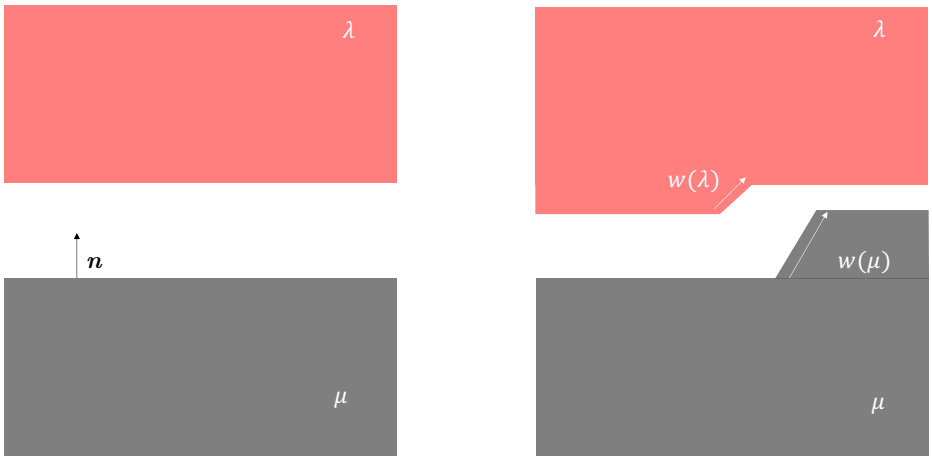

Fig. 2.2 Schematic illustration of the creation of a bicrystal by joining crystals with prepared surfaces. The left hand side shows the creation of a defect-free bicrystal, whereas the right hand side shows the creation of a bicrystal containing a step separating crystallographically equivalent regions of the boundary. This method of graphically creating a bicrystal is known as a Volterra-like procedure, after Volterra [106], who in 1907 devised a procedure to create dislocations in solids.

Let us first see how a defect may be created in a bicrystal; this is illustrated in figure 2.2 for a step. We start out with black and red semi-infinite crystals, whose orientations are related by the transformation $(\mathbf{P}', \mathbf{p})$. The black and red crystals are then brought together to form the bicrystal. But since both the black and red semi-infinite crystals exhibit symmetry, it is possible to expose in both crystals new surfaces which are crystallographically equivalent to the initial one, such that when the new surfaces are brought together a new interface, crystallographically equivalent to the previous one, is formed. The new and the initial interfaces coexisting in the bicrystal are now separated by a line defect, which is characterised by the operation required to bring the black and red surfaces into coincidence. Moreover, the characterising operation is necessarily the combination of a black and a red operation, because of the way the new surfaces were constructed. Hence, if we denote with $(\mathbf{Q}_{i,j}, \mathbf{q}_{i,j})$ the combination of operations $(\mathbf{W}(\lambda)_j, \mathbf{w}(\lambda)_j)$ and $(\mathbf{W}(\mu)_i, \mathbf{w}(\mu)_i)$, we find it has to obey the following equation:

$$(\mathbf{Q}_{i,j}, \mathbf{q}_{i,j}) = (\mathbf{W}(\lambda)_j, \mathbf{w}(\lambda)_j)(\mathbf{P}', \mathbf{p})(\mathbf{W}(\mu)_i, \mathbf{w}(\mu)_i)^{-1}(\mathbf{P}', \mathbf{p})^{-1}, \tag{2.30}$$

where $(\mathbf{P}', \mathbf{p})$ is the operation relating the black and red crystals, as before. If the compound operation $(\mathbf{Q}_{i,j}, \mathbf{q}_{i,j})$ is a translation, the defect is a dislocation, whereas a rotation and a screw rotation will yield a disclination and a dispiration respectively.

The extent of the variety of defects that can potentially arise in an interface is readily illustrated by taking as an example the case of a symmetry operation common to the black and red crystals, but which may or may not be coincident in the two crystals, depending on the transformation relating the crystals. In the former case, the operation is also a symmetry operation of the dichromatic complex, as we have mentioned in the previous section, i.e. $(\mathbf{W}(\lambda)_j, \mathbf{w}(\lambda)_j) = (\mathbf{P}', \mathbf{p})(\mathbf{W}(\mu)_i, \mathbf{w}(\mu)_i)(\mathbf{P}', \mathbf{p})^{-1} = (\mathbf{W}(c)_k, \mathbf{w}(c)_k)$, and if we substitute into equation 2.30, we find that $(\mathbf{Q}_{i,j}, \mathbf{q}_{i,j}) = (\mathbf{I}, \mathbf{0})$, i.e. that coincident symmetry operations of the black and red crystals lead to an interfacial discontinuity that has no defect character. But if the black and red symmetry operations are not coincident, then a defect with character 2.30 will arise at the interface. In this sense, the presence of interfacial defects is a consequence of bicrystal disconnexion. Therefore, the defects can be classified according to the mode of disconnexion that causes them to arise, and dislocations, disclinations and dispirations can be divided further into subclasses, as we will see in the following sections.

Discontinuities with no defect character can still be associated with morphological features, i.e. steps and junctions between crystallographically equivalent facets. In an interface with normal $\hat{\mathbf{n}}$, when there is a coincident symmetry operation $(\mathbf{W}(c)_j, \mathbf{w}(c)_j)$ in the dichromatic complex, equivalent facets can be present with normals parallel to $\mathbf{W}(c)_j\hat{\mathbf{n}}$. In the process of making a defect that we described above, this case corresponds to that of bringing together two complementary surfaces. When $\mathbf{W}(c)_j\hat{\mathbf{n}} = \hat{\mathbf{n}}$, the discontinuity is a step, and when $(\mathbf{W}(c)_j, \mathbf{w}(c)_j) = (\mathbf{I}, \mathbf{t}(c)_j)$, i.e. when the coincident operation is a translation, the height of the step is given by $\hat{\mathbf{n}} \cdot \mathbf{t}(c)_j$; on the other hand, if $(\mathbf{W}(c)_j, \mathbf{w}(c)_j)$ is not a translation and $\mathbf{w}(c)_j \neq \mathbf{0}$, the discontinuity is a demistep with height $\hat{\mathbf{n}} \cdot \mathbf{w}(c)_j$. Similar discontinuities can exist when there are antisymmetry operations in the dichromatic complex, except for steps, since there can be no antitranslation vectors.

Interfacial dislocations

Interfacial dislocations can be divided into three subclasses. The Burgers vectors of the dislocations are found via equation 2.30, and their morphological features can be identified. Hirth [107] argues that defects that present both dislocation and step character are neither pure dislocations nor pure steps, and he proposes for this type of defect the name disconnection. As we noted above, this is not related to the concept of disconnexion, which refers to the degree of dissymmetrization of the bicrystal. In what follows, we will adopt Hirth's terminology, and give the name disconnection to a defect with dislocation and step content.

- **Class 1 : broken translation symmetry.** This type of dislocation arises when a translation of the red lattice $(\mathbf{I}, \mathbf{t}(\lambda)_j)$ and that of the black lattice $(\mathbf{I}, \mathbf{t}(\mu)_i)$ are not coincident. The cause may be that the translation vectors have different magnitudes, or different orientations. The Burgers vector $\mathbf{b}_{i,j}$ for such a dislocation is found using equation 2.30 by substituting $(\mathbf{Q}_{i,j}, \mathbf{q}_{i,j}) = (\mathbf{I}, \mathbf{b}_{i,j})$:

$$(\mathbf{I}, \mathbf{b}_{i,j}) = (\mathbf{I}, \mathbf{t}(\lambda)_j)(\mathbf{P}', \mathbf{p})(\mathbf{I}, \mathbf{t}(\mu)_i)(\mathbf{P}', \mathbf{p})^{-1}, \tag{2.31}$$

  Such that

$$\mathbf{b}_{i,j} = \mathbf{t}(\lambda)_j - \mathbf{P}'\mathbf{t}(\mu)_i, \tag{2.32}$$

  i.e. the Burgers vector is the difference between the two translation vectors expressed in the same coordinate frame (that of the red lattice). Moreover, the vectors $\mathbf{b}_{i,j}$ connect black and red sites in the dichromatic pattern, meaning that they can be found readily while constructing the bicrystal. A step may be associated with the dislocation core, in which case it is a disconnection, and the calculation of its height $h_{i,j}$ requires that the normal to the boundary, $\hat{\mathbf{n}}$, is specified; the height of a surface step characterised by a translation vector $\mathbf{t}$ is simply $h = \hat{\mathbf{n}} \cdot \mathbf{t}$. However, the black and red surfaces on the right of figure 2.2 are characterised by different translation vectors. Initially Pond [98] proposed an approximate expression for the step height of an interfacial disconnection as the average of the heights of the two imaginary free surface steps characterised by $\mathbf{t}(\lambda)_j$ and $\mathbf{P}'\mathbf{t}(\mu)_i$ respectively, i.e.

$$h_{i,j} = \frac{1}{2}\hat{\mathbf{n}} \cdot (\mathbf{t}(\lambda)_j + \mathbf{P}'\mathbf{t}(\mu)_i). \tag{2.33}$$

However, Hirth and Pond [108] later gave a different definition, based on the quantity of material transferred between crystals as a result of the motion of the disconnection. This is the so-called *overlap step*, i.e. the amount of overlapping material of the black and red crystals perpendicular to the interface, measured after bringing the two halves of the bicrystal in figure 2.2 into contact but before either crystal is deformed to match the surfaces together. This definition requires that the two free surface steps have the same sign; then the overlap step is given by the smaller of the two. These defects were studied extensively, and in particular we mention the work of Bollmann [109], who named them DSC dislocations, in the case of a CSL being present in the dichromatic complex.

- **Class 2: frustrated symmetry.** Dislocations of this type arise if at least one of the two crystals is non-symmorphic, and the crystals present mirror-glide planes or screw-rotation axes in orientational alignment, but with different glide displacements $\boldsymbol{\alpha}(\mu)_i$ and $\boldsymbol{\alpha}(\lambda)_j$, corresponding to the case of symmetry operations being present in the dichromatic pattern and being broken in the dichromatic complex. Taking the black and red operations to be respectively $(\mathbf{W}(\mu)_i, \boldsymbol{\alpha}(\mu)_i)$ and $(\mathbf{W}(\lambda)_j, \boldsymbol{\alpha}(\lambda)_j)$ (i.e. setting $\mathbf{t}(\mu)_i = \mathbf{t}(\lambda)_j = \mathbf{0}$), we use equation 2.30 to find the Burgers vector of the dislocation, as was done for class 1 dislocations:

$$\mathbf{b}_{i,j} = \boldsymbol{\alpha}(\lambda)_j - \mathbf{P}'\boldsymbol{\alpha}(\mu)_i + (\mathbf{W}(\lambda)_j - \mathbf{I})\mathbf{p}. \tag{2.34}$$

  We notice that a special case is that of the symmetry elements being translationally aligned, i.e. $\mathbf{p} = \mathbf{0}$; for such a dislocation the Burgers vector is $\mathbf{b}_{i,j} = \boldsymbol{\alpha}(\lambda)_j - \mathbf{P}'\boldsymbol{\alpha}(\mu)_i$. This is also the case if $\mathbf{W}(\lambda)_j\mathbf{p} = \mathbf{p}$, i.e. if the rotation part of the symmetry operation is not misaligned by $\mathbf{p}$. In all other cases, the term $(\mathbf{W}(\lambda)_j - \mathbf{I})\mathbf{p}$ arises, such that the defect separates regions related by $\mathbf{W}(\lambda)_j$.

  The morphology of the defects can be found by specifying the normal to the boundary $\hat{\mathbf{n}}$. If the symmetry operation $\mathbf{W}(\lambda)_j$ leaves the normal invariant, i.e. $\mathbf{W}(\lambda)_j\hat{\mathbf{n}} = \hat{\mathbf{n}}$, then the defect is a disconnection associated with a step of height

$$h_{i,j} = \frac{1}{2}\hat{\mathbf{n}} \cdot (\boldsymbol{\alpha}(\lambda)_j + \mathbf{P}'\boldsymbol{\alpha}(\mu)_i). \tag{2.35}$$

This is the only case in which class 2 disconnections can arise on *planar* interfaces. If the normal is not left invariant by $\mathbf{W}(\lambda)_j$, a stepped facet junction arises: the defect and the step lie along the junction between facets whose normals are $\hat{\mathbf{n}}$ and $\mathbf{W}(\lambda)_j\hat{\mathbf{n}}$.

- **Class 3.** Dislocations in this class are produced by the breaking of coincident symmetry (class 3a) or antisymmetry (class 3b) operations caused by the displacement $\mathbf{p}$. As is shown by equation 2.11, the coincidence of translation vectors does not depend on $\mathbf{p}$; hence we need only concern ourselves with symmetry and antisymmetry point group operations.

  - **Class 3a: broken coincident symmetry.** One of the conditions for coincident symmetry to be conserved in the dichromatic complex is that equation 2.13 is satisfied. Substituting it in equation 2.30 with $(\mathbf{Q}_{i,j}, \mathbf{q}_{i,j}) = (\mathbf{I}, \mathbf{b}_{i,j})$, we find that the Burgers vector of the dislocation is given by

$$\mathbf{b}_{i,j} = (\mathbf{W}(c)_k - \mathbf{I})\mathbf{p}, \tag{2.36}$$

    where $\mathbf{W}(c)_k = \mathbf{W}(\lambda)_j$ (the symmetry operation of the dichromatic complex is given, in general, by $(\mathbf{W}(c)_k, \boldsymbol{\alpha}(c)_k) = (\mathbf{W}(\lambda)_j, \boldsymbol{\alpha}(\lambda)_j)$). Hence $\mathbf{b}_{i,j}$ is nonzero only if coincident symmetry is broken by $\mathbf{p}$, i.e. if $\mathbf{W}(c)_k\mathbf{p} \neq \mathbf{p}$. Hence, dislocations in this class separate structures related by the broken symmetry operation. Similarly to class 2 dislocations, the morphological feature associated with the dislocation core will be a stepped facet junction when $\mathbf{W}(c)\hat{\mathbf{n}} \neq \hat{\mathbf{n}}$, with a step of height $h_{i,j} = \hat{\mathbf{n}} \cdot \boldsymbol{\alpha}(c)$ collinear with the facet junction. In planar interface, this type of defect can only exist if $\mathbf{W}(c)\hat{\mathbf{n}} = \hat{\mathbf{n}}$, and the step height is given by

$$h_{i,j} = \frac{1}{2}\hat{\mathbf{n}} \cdot (\boldsymbol{\alpha}(c)_k + \mathbf{P}'\boldsymbol{\alpha}(c)_k) = \hat{\mathbf{n}} \cdot \boldsymbol{\alpha}(c)_k. \tag{2.37}$$

  - **Class 3b: broken antisymmetry.** Dislocations in this class arise following symmetry breaking analogously to dislocations in class 3a, with the difference that the symmetry operation being broken is an antioperation $(\mathbf{W}', \boldsymbol{\alpha})$. However, since antisymmetry operations do not belong to the space groups of either the red or the black crystal, we cannot simply use equation 2.30. Instead, we see that the operation $(\mathbf{Q}_{i,j}, \mathbf{q}_{i,j})$ is

obtained via a compound operation: initially the black crystal is transformed into the red one by $(\mathbf{P}',\mathbf{p})(\mathbf{W}'(\mu)_i,\boldsymbol{\alpha}(\mu)_i)^{-1}(\mathbf{P}',\mathbf{p})^{-1}$, and then $(\mathbf{W}'(\lambda)_j,\boldsymbol{\alpha}(\lambda)_j)$ transforms the red surface back into the black one, such that

$$(\mathbf{Q}_{i,j},\mathbf{q}_{i,j}) = (\mathbf{W}'(\lambda)_j,\boldsymbol{\alpha}(\lambda)_j)(\mathbf{P}',\mathbf{p})(\mathbf{W}'(\mu)_i,\boldsymbol{\alpha}(\mu)_i)^{-1}(\mathbf{P}',\mathbf{p})^{-1}, \tag{2.38}$$

which has the same form as 2.30. Therefore, similarly to dislocations in class 3a, the Burgers vector of the dislocation is given by

$$\mathbf{b}_{i,j} = (\mathbf{W}'(\lambda)_j - \mathbf{I})\mathbf{p}, \tag{2.39}$$

and is nonzero only if the displacement $\mathbf{p}$ breaks the antisymmetry. Again, the dislocation will separate regions related by the broken antisymmetry operation.

Interfacial disclinations and dispirations

Interfacial disclinations arise when point symmetry operations $(\mathbf{W}(\lambda)_j,\mathbf{w}(\lambda)_j)$ and $(\mathbf{W}(\mu)_i,\mathbf{w}(\mu)_i)$ (both proper or both improper) are not coincident because they are either intrinsically different, orientationally misaligned or a mix of both. Then following equation 2.30 and substituting $(\mathbf{Q}_{i,j},\mathbf{q}_{i,j}) = (\mathbf{Q}_{i,j},\mathbf{0})$, we find that the operation characterising the disclination will be a proper rotation, with

$$\mathbf{Q}_{i,j} = \mathbf{W}(\lambda)_j\mathbf{P}'\mathbf{W}(\mu)_i^{-1}\mathbf{P}'^{-1}. \tag{2.40}$$

Interfacial dispirations are divided into two subclasses.

- **Class 1: non-symmorphic case.** When one or both of the operations $(\mathbf{W}(\lambda)_j,\mathbf{w}(\lambda)_j)$ and $(\mathbf{W}(\mu)_i,\mathbf{w}(\mu)_i)$ in equation 2.30 is nonsymmorphic, then a dispiration characterised by the operation $(\mathbf{Q}_{i,j},\mathbf{q}_{i,j})$ can arise. Then, setting $\mathbf{w}(\lambda)_j = \boldsymbol{\alpha}(\lambda)_j$ and $\mathbf{w}(\mu)_i = \boldsymbol{\alpha}(\mu)_i$, we find

$$\mathbf{Q}_{i,j} = \mathbf{W}(\lambda)_j\mathbf{P}'\mathbf{W}(\mu)_i^{-1}\mathbf{P}^{-1}, \tag{2.41}$$

$$\mathbf{q}_{i,j} = \boldsymbol{\alpha}(\lambda)_j - \mathbf{Q}_{i,j}\mathbf{P}'\boldsymbol{\alpha}(\mu)_i + (\mathbf{W}(\lambda)_j - \mathbf{Q}_{i,j})\mathbf{p}. \tag{2.42}$$

- **Class2: symmorphic case.** If the symmetry operations that give rise to the dispiration are both symmorphic (i.e. $\boldsymbol{\alpha}(\lambda)_j = \boldsymbol{\alpha}(\mu)_i = \mathbf{0}$), but $\mathbf{p} \neq \mathbf{0}$, then we find that $\mathbf{Q}_{i,j}$ has the same form as 2.41, whilst $\mathbf{q}_{i,j}$ is given by

$$\mathbf{q}_{i,j} = (\mathbf{W}(\lambda)_j - \mathbf{Q}_{i,j})\mathbf{p}. \tag{2.43}$$

  This means that although the symmetry operations are symmorphic, $(\mathbf{Q}_{i,j}, \mathbf{q}_{i,j})$ is not, such that defects in this class can be thought of as disclinations that become dispirations because of $\mathbf{p}$.

2.2 Application to classical twins in magnesium

Having presented the theory, we now turn to its application to the classical twins observed in magnesium, namely the $(10\bar{1}2)$ or tension twin, the $(10\bar{1}1)$ or compression twin and its reciprocal mode, the $(10\bar{1}\bar{3})$ twin. For each of these twins we construct a bicrystal, starting from a dichromatic pattern, and derive the space symmetry groups of each object produced in the dissymmetrization scheme; we begin with the $(10\bar{1}2)$ twin, for which we describe the procedure in detail, to then apply the method more rapidly to the $(10\bar{1}1)$ and $(10\bar{1}\bar{3})$ twins. Finally, we use the topological theory of interfacial defects to identify the twinning dislocations associated with each of the twinning shears.

2.2.1 The $(10\bar{1}2)$ twin as a bicrystal

For the $(10\bar{1}2)$ twin in consideration, K_1 is taken to be $(10\bar{1}2)$, $K_2 = (10\bar{1}\bar{2})$, $\boldsymbol{\eta}_1 = [10\bar{1}\bar{1}]$, $\boldsymbol{\eta}_2 = [10\bar{1}1]$; the plane of shear is $P = (1\bar{2}10)$, as shown in chapter 1. It was also mentioned that this is a compound twin, so that we may choose to describe the parent/twin relation as a rotation of 180° about $\boldsymbol{\eta}_1$. It is then clear that the $(10\bar{1}2)$ twin can be seen as a bicrystal with a homophase boundary, such that the black (μ) and red (λ) crystals are related by a rotation about a symmetry axis; hence it can be modelled using the tools of bicrystallography: the symmetry of the interface can be derived, and the existence of crystallographic variants as well as of interfacial line defects can be predicted via symmetry considerations.

We proceed to create a $(10\bar{1}2)$ twin as follows:

1. We create a large supercell of black lattice points and we duplicate it, colouring the second set of sites red. For the purpose of comparison, we do this initially for two values of the axial ratio, i.e. $\gamma = \sqrt{\frac{21}{8}} = 1.620$ (i.e. the optimised axial ratio for magnesium in the GPT), and the experimentally measured axial ratio, $\gamma = 1.624$.

2. We define the transformation that will relate the red and black lattices as a rotation by $\theta = 180^\circ$ about the $\boldsymbol{\eta}_1 = [10\bar{1}\,\bar{1}]$ direction, such that $(\mathbf{P}', \mathbf{p}) = (\mathbf{R}, \mathbf{0})$, where the rotation matrix $\mathbf{R}$ is given by equation 1.32:

$$R_{ij} = -\delta_{ij} + 2(\hat{\eta}_1)_i(\hat{\eta}_1)_j, \tag{2.44}$$

   We then rotate the red sites about $\boldsymbol{\eta}_1$ and label the overlapping sites of the black and red lattices grey. Thus we have obtained the dichromatic patterns shown in figure 2.3, where (a) shows the pattern for $\gamma = \sqrt{\frac{21}{8}}$ and (b) for $\gamma = 1.624$. The patterns are projected along the $[1\bar{2}10]$ direction.

3. Having illustrated the comparison between the CSLs arising from different axial ratios (discussed below), we focus on the case where $\gamma = 1.624$ for the next steps of the procedure. We decorate the lattice sites with the atomic basis of the hcp crystal; we do this for the black and red lattices respectively, such that they are replaced by black and red basis atoms. Here we need to be careful with our choice of basis, as mentioned in the previous section. The *holosymmetric* space symmetry group of dichromatic pattern (i.e. that of maximal symmetry) will be derived using the most symmetric configuration, i.e. the one where lattice points are centres of symmetry, and the basis atoms are placed at $\frac{1}{12}[40\bar{4}9]$ and $\frac{1}{12}[04\bar{4}3]$ [78], figure 2.4a. In addition we construct the dichromatic complex for the less symmetric configuration of the basis, with one atom placed at a lattice point and the other at $\frac{1}{2}[10\bar{1}1]$, for the sake of comparison (figure 2.4b).

4. We define the boundary plane $\mathrm{K}_1 = (10\bar{1}2)$ through the negative of its unit normal $\frac{\Lambda}{2^{1/2}(2+\Lambda^2)^{1/2}}\ [\bar{1}01\bar{2}/\Lambda^2]$ (the reader is reminded of equation 1.30, where $\Lambda^2 = \frac{2}{3}\gamma^2$, for the relation between Miller-Bravais indices and normal directions, as well as of the method

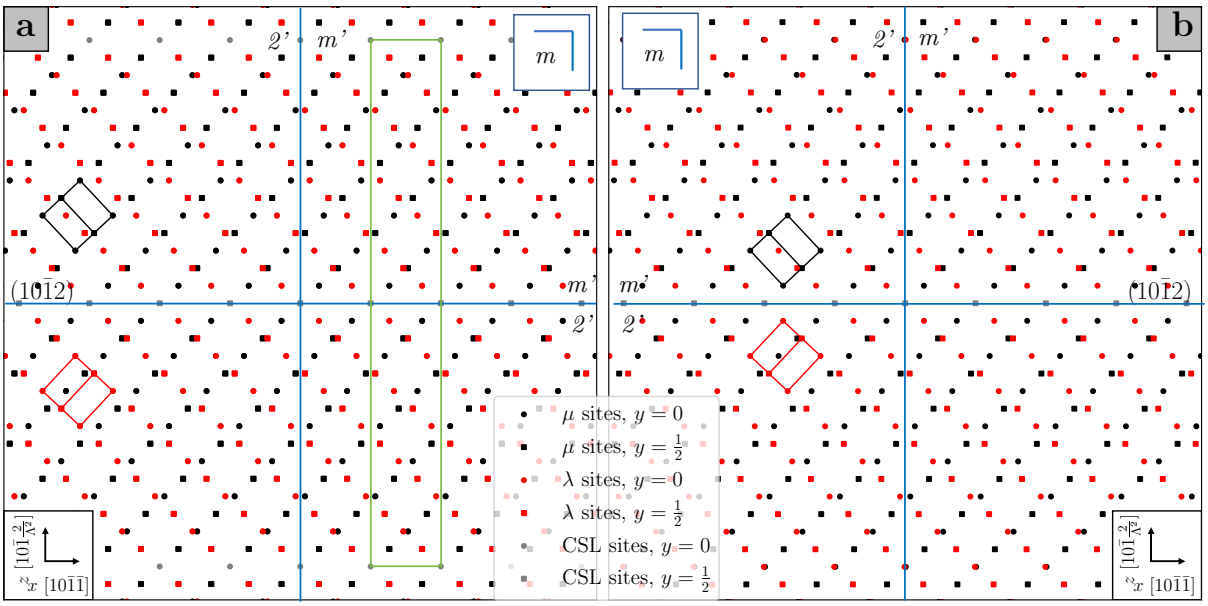

Fig. 2.3 Dichromatic patterns of the $(10\bar{1}2)$ twin, created by interpenetrating the black and red lattices, for $\gamma = \sqrt{\frac{21}{8}}$ (a) and $\gamma = 1.624$ (b). The boundary plane is $(10\bar{1}2)$, and the projection direction is $[1\bar{2}10]$. Grey sites mark overlapping red and black sites, i.e. sites of the CSL; circles and squares are used to indicate different layers. The unit cells of the μ and λ lattices are outlined respectively by black and red lines, and a unit CSL is outlined in green. The symmetry elements of the pattern are drawn in blue, with the exception of the two-fold $[1\bar{2}10]$ axis, which points out of the page.

devised to calculate dot products with the aid of 4-vectors), such that the normal points in the direction of the red crystal, as per convention. We discard all red atoms on one side of the boundary and all black atoms on the other, for both dichromatic complexes obtained in the previous step. The results are two bicrystals i.e. two twins, depicted in figure 2.5.

5. We perform the final step of our analysis only on the structure in figure 2.5a, setting however $\gamma = \sqrt{\frac{21}{8}}$, such that when periodic boundary conditions are applied in the z-direction, identical twin boundaries may be obtained where the crystal is joined with its periodic image. We relax this twin by switching on interactions between atoms. We do this using the aGPT, with a cutoff on neighbours at $R_c = 28.8$ bohr, and the pair potential v_2 is interpolated smoothly to zero between $R_0 = 27.0$ bohr and R_c. The forces are relaxed in the aGPT using the Fast Inertial Relaxation Engine (FIRE) algorithm [110]. As removal and addition of material at the interface are allowed [99], we relax two different structures: the first one is the twin in figure 2.5a, and the second one is the same twin subject to the

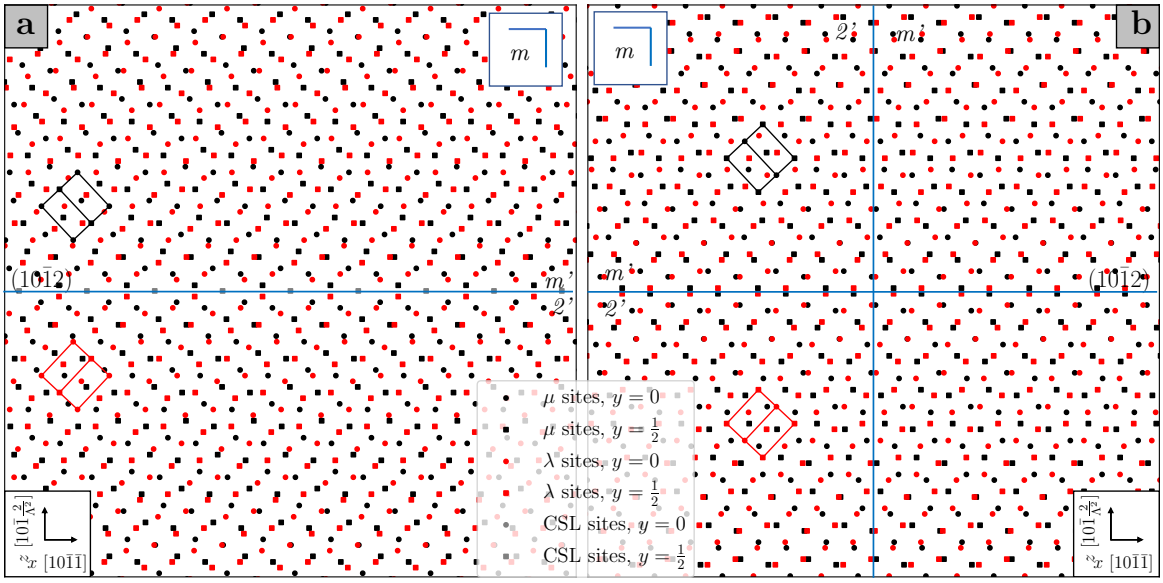

Fig. 2.4 Dichromatic complexes of the $(10\bar{1}2)$ twin with $\gamma = 1.624$, created by interpenetrating the black and red crystals. (a): complex obtained using the less symmetric configuration of the basis atoms; (b) the holosymmetric complex. The boundary plane is $(10\bar{1}2)$, and the projection direction is $[1\bar{2}10]$. Grey sites mark overlapping red and black atoms, i.e. atoms of the CSL; circles and squares are used to indicate different layers of atoms. The unit cells of the μ and λ crystals are outlined respectively by black and red lines. The symmetry elements are drawn in blue, with the exception of the two-fold $[1\bar{2}10]$ axis in (b), which points out of the page.

removal of the layer of atoms directly above the interface. In the first case, the pairs of atoms that lie close above and below the interface move apart during the relaxation; in the second case, the only layer of atoms left closest to the interface migrates to the boundary and is aligned with the grey atoms that were previously in the boundary, while atoms in the bulk are left mostly undisturbed. We find that the latter relaxed structure has the lower energy per atom, as reported by Serra and Bacon [111]; the twin is shown before and after relaxation in figure 2.6.

Focusing first on the dichromatic patterns in figure 2.3, we notice that grey sites outline CSLs for both values of the axial ratio; however, only for $\gamma = \sqrt{\frac{21}{8}}$ this CSL is three dimensional. This is to be expected, given that the square of this axial ratio is rational and so are the elements of $\mathbf{R}$ in equation 2.44; this also ensures that the dichromatic pattern is periodic in all directions, included that normal to the boundary plane. In contrast, for $\gamma = 1.624$, the dichromatic pattern is not periodic in the z-direction.

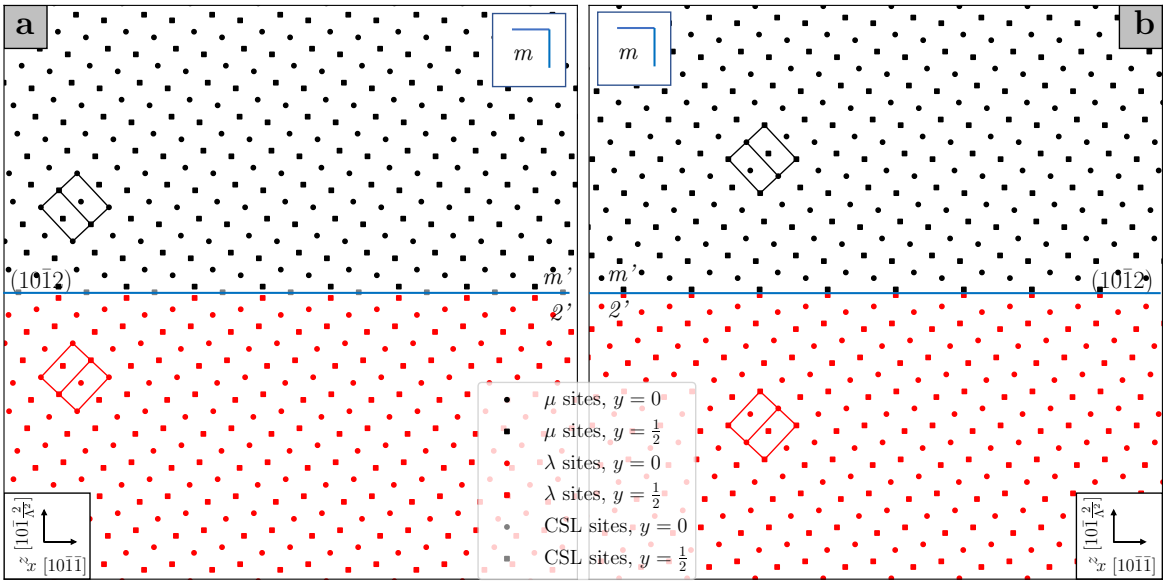

Fig. 2.5 The $(10\bar{1}2)$ twins, created by discarding all black atoms on one side of the boundary and all red atoms on the other side, for each of the dichromatic complexes in figure 2.4. The boundary plane is $(10\bar{1}2)$, and the projection direction is $[1\bar{2}10]$. Circles and squares are used to indicate different layers of atoms. The unit cells of the μ and λ crystals are outlined by black and red lines in the bulk on either side of the boundary. The symmetry elements are drawn in blue.

The black and red lattices have space symmetry groups $\Phi^*(\mu) = \Phi^*(\lambda) = P6/mmm$. The only ordinary operations that survive in the dichromatic patterns are the reflection in the $(1\bar{2}10)$ mirror and the two-fold rotation about the $[1\bar{2}10]$ axis, such that $\Phi^*(p) = P2m1$ for $\gamma = \sqrt{\frac{21}{8}}$ and $\Phi^*(p) = p2m1$ for $\gamma = 1.624$, where the lower case letter p denotes that only two-dimensional translational symmetry is present. This can be checked either by examining the patterns in figure 2.3 or by using equation 2.13. For the latter method, we find the use of the four-vector system particularly instructive: we re-express the transformation matrix $\mathbf{R}$ in the four-vector frame following the procedure devised by Pond [62], and then we check which of the point symmetry operations of $\Phi^*(\lambda)$ and $\Phi^*(\mu)$ (tabulated in their 4D space form in the same article) obey equation 2.13. Conversely, antisymmetry operations arise as reflections about the $(10\bar{1}2)$ and $(\bar{1}010)$ planes relating red and black sites, as well as two two-fold rotations about the $[10\bar{1}\bar{1}]$ and $[10\bar{1}2/\Lambda^2]$ axes. Hence, the space symmetry group of the pattern in figure 2.3a is $\text{Ш}^*(p) = P2mm'$, and that of the pattern in figure 2.3b is $\text{Ш}^*(p) = p2mm'$. The order of the groups $\Phi^*(\lambda)$ and $\Phi^*(\mu)$ is 24, while the order of the $\Phi^*(p)$ group is 4; hence, as a consequence of Lagrange's theorem, there are $(24+24)/(4\cdot 2) = 6$ orientational variants, related by the lost

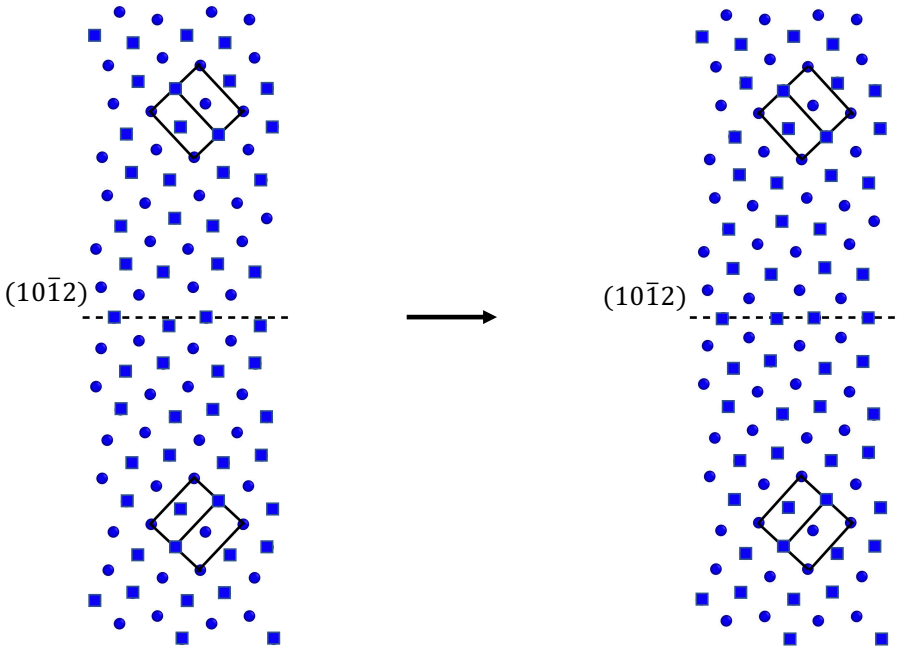

Fig. 2.6 Relaxation of $(10\bar{1}2)$ twin. The left hand side shows the unrelaxed twin, where the layer of atoms directly above the boundary (dashed black line in figure) was removed. The right hand side shows the relaxed twin, where the one layer of atoms left closer to the boundary migrated into the boundary itself. In both figures, the unit cells of the μ and λ crystals are outlined by solid black lines in the bulk on either side of the boundary, and circles and square are used to indicate different layers of atoms.

symmetry operations. In addition, there is an infinite number of translational variants arising from the broken translation operations; these are more in the case of the pattern with $\gamma = 1.624$. Having compared patterns with different axial ratios, we now turn to analysis of the dichromatic complex for $\gamma = 1.624$.

Regarding the symmetry of the dichromatic complex, we can now fully grasp the importance of choosing the right configuration when deriving the holosymmetric space symmetry group of an object. Although both complexes are created from the same black and red crystals, with space symmetry groups $\Phi(\lambda) = \Phi(\mu) = P6_3/mmc$, it is evident that the complex in figure 2.4a has lower symmetry than the one in 2.4b. As mentioned above, this is because the configuration on the left does not fully exploit the symmetry of the system; the result is a lower order ordinary point group, i.e. $\Phi(c) = p1m1$, which via union with the group of antioperations forms the space symmetry group $\text{III}(c) = p2'mm'$. In contrast, the dichromatic complex in figure 2.4b is just as symmetric as the dichromatic pattern in figure 2.3b; no symmetry is lost, and the holosymmetric

space symmetry group of the complex is the same as that of the pattern, i.e. $\text{III}^*(c) = p2mm'$. As a consequence, no so-called complex variants arise from this step of dissymmetrization.

However, symmetry operations are broken by choosing the boundary plane and discarding red and black atoms on each side respectively, hereby creating the bicrystal. It can be noted from figure 2.5 that the loss of symmetry in this step has the same result for both configurations, such that the two bicrystals have the same space symmetry group. The only conserved operations are reflection about the $(1\bar{2}10)$ mirror and the $(10\bar{1}2)$ antimirror, as well as rotation about the $2'$ axis, which leave the interface normal invariant. Hence the holosymmetric space symmetry group of the $(10\bar{1}2)$ twin is $\text{III}^*(b) = p2'mm'$. Since, from the point of view of symmetry, the two bicrystals in figure 2.5 are equivalent, we can continue our discussion using either. We pick the bicrystal obtained from the less symmetric configuration, i.e. that on the left of figure 2.5, for technical reasons and because it is the most common in the literature.

Relaxation further reduces the symmetry of the twin. In particular, the choice of removing a layer of black atoms (i.e. a layer directly above the boundary) or of red atoms (i.e. directly below the boundary) determines the breaking of the $2'$ and m' symmetries, because once the relaxation is complete, the atoms in the boundary are no longer all grey, but some of them are red (or black, depending on which layer is removed). The symmetry breaking gives rise to two relaxational variants, related by $2'$ and m', one with red atoms in the boundary and the other with black atoms, which are completely equivalent to one another, as noted by Pond and coworkers [104]. Thus the space symmetry group of the relaxed twin is $\text{III}(b) = p1m1$.

2.2.2 The $(10\bar{1}1)$ compression twin and its reciprocal $(10\bar{1}\bar{3})$ mode

There are two more classical twinning modes that are observed in magnesium; these are the $(10\bar{1}1)$ compression twin and its reciprocal mode, i.e. the $(10\bar{1}\bar{3})$ twin. Both these modes can be described using the bicrystallographic method introduced in this chapter, much in the same way as the $(10\bar{1}2)$ twin, since both are compound modes and their orientation relations can be specified as rotations of 180° about the shear direction. In this section, we shall not describe the dissymmetrization procedure for these twins with the same amount of detail provided for the $(10\bar{1}2)$ twin; instead, key results will be presented.

The twinning elements of the $(10\bar{1}1)$ twin were given in chapter 1: $K_1 = (10\bar{1}1)$, $K_2 = (10\bar{1}\bar{3})$, $\boldsymbol{\eta}_1 = [10\bar{1}\bar{2}]$, $\boldsymbol{\eta}_2 = [30\bar{3}2]$ [69]. In order to construct this twin, we follow the procedure outlined above for the tension twin. Firstly, we obtain the dichromatic patterns for $\gamma = \sqrt{\frac{21}{8}}$ and $\gamma = 1.624$, shown in figure 2.7a and b respectively, seeking to establish the comparison illustrated in the previous section. It can be noted that these patterns are characterised by the same space symmetry groups as the corresponding patterns of the tension twin, figure 2.3; hence, $\text{III}^*(p) = P2mm'$ for $\gamma = \sqrt{\frac{21}{8}}$, and $\text{III}^*(p) = p2mm'$ for $\gamma = 1.624$.

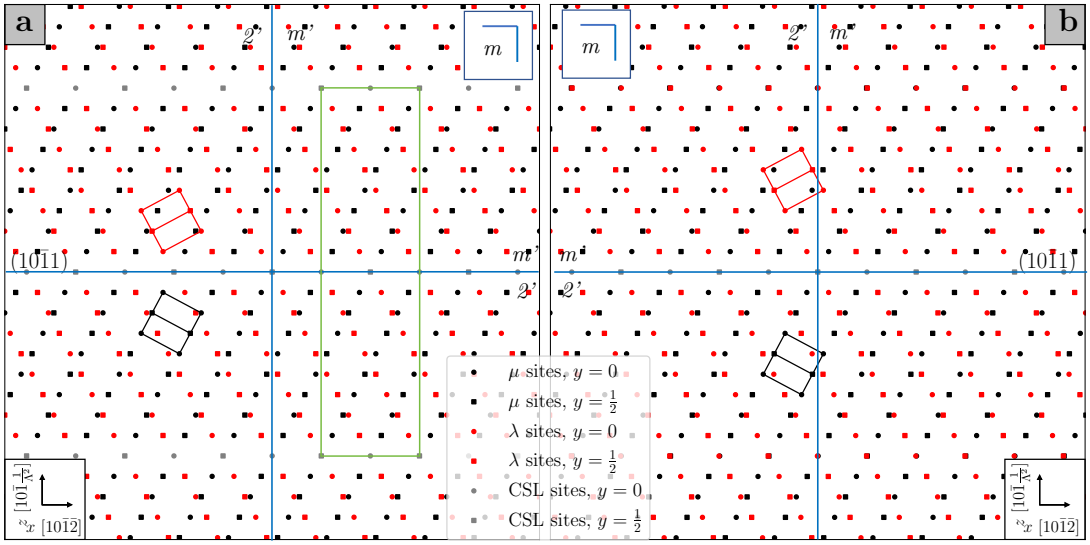

Fig. 2.7 Dichromatic pattern of the $(10\bar{1}1)$ twin, created by interpenetrating the red and black lattices, for $\gamma = \sqrt{\frac{21}{8}}$ (a) and $\gamma = 1.624$ (b). The boundary plane is $(10\bar{1}1)$, and the projection direction is $[1\bar{2}10]$. Grey sites mark overlapping red and black sites, i.e. sites of the CSL; circles and squares are used to indicate different layers. The unit cells of the λ and μ lattices are outlined respectively by red and black lines, and a unit CSL is outlined in green. The symmetry elements are drawn in blue, with the exception of the two-fold $[1\bar{2}10]$ axis, which points out of the page.

We then create the dichromatic complex by adding basis atoms, for the case $\gamma = 1.624$. As in the previous section, we obtain the complex of maximal symmetry by placing the basis atoms so that lattice points are centres of symmetry, i.e. at $\frac{1}{12}[40\bar{4}9]$ and $\frac{1}{12}[04\bar{4}3]$; the result is shown in figure 2.8b, and it can be seen that the symmetry of this complex is identical to that of the pattern, and $\text{III}^*(c) = p2mm'$. For comparison, we also draw the dichromatic complex corresponding to the less symmetric configuration of the basis, i.e. with atomic positions $[0000]$ and $\frac{1}{6}[02\bar{2}3]$, figure 2.8a. The space symmmetry group of this complex is $\text{III}(c) = p2'mm'$.

The twin is then obtained by discarding black or red atoms on either side of the $(10\bar{1}1)$ boundary

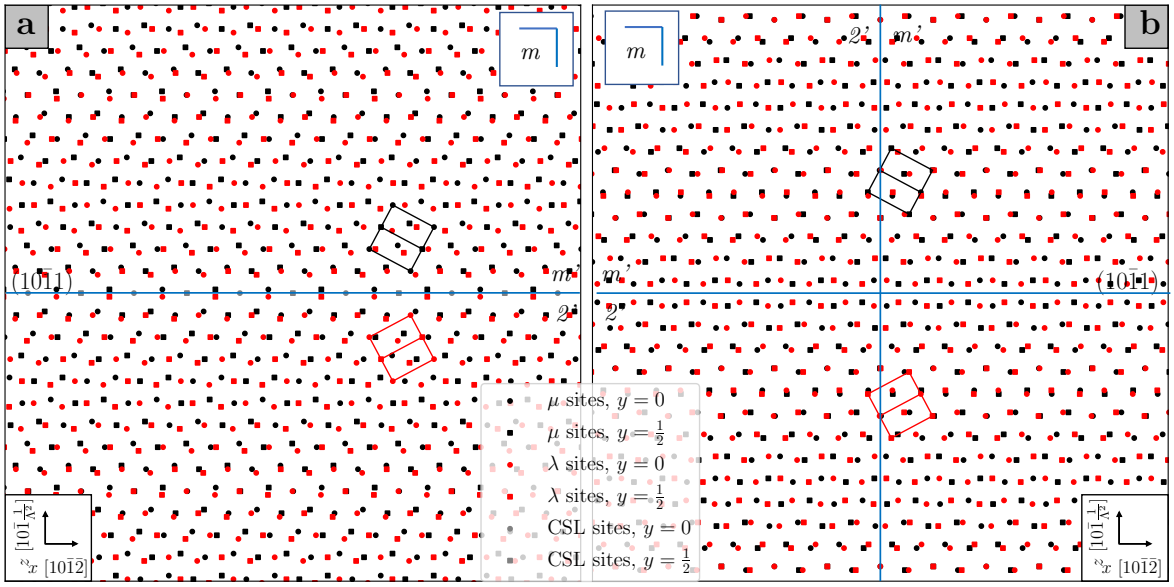

Fig. 2.8 Dichromatic complexes of the $(10\bar{1}1)$ twin, created by interpenetrating the red and black crystals, for $\gamma = 1.624$. (a): the complex obtained using the less symmetric configuration of the basis atoms; (b): the holosymmetric complex. The boundary plane is $(10\bar{1}1)$, and the projection direction is $[1\bar{2}10]$. Grey sites mark overlapping red and black atoms, i.e. atoms of the CSL; circles and squares are used to indicate different layers of atoms. The unit cells of the μ and λ crystals are outlined respectively by black and red lines. The symmetry elements are drawn in blue, with the exception of the two-fold $[1\bar{2}10]$ axis in (b), which points out of the page.

plane. We do this for both dichromatic patterns, and thus create the twins in figure 2.9; these present the same symmetry elements, such that $\text{Ш}^*(b) = p2'mm'$. We then continue our analysis using the twin obtained from the less symmetric atomic positions, i.e. the twin in figure 2.9a. Finally, we relax the $(10\bar{1}1)$ twin using the aGPT, with the same lattice parameters and relaxation algorithm employed for the tension twin in the previous section. Again, we remove a layer of atoms directly above the interface from the black crystal; the starting configuration can be seen on the left of figure 2.10. After relaxation, the black atoms directly below the interface move to position themselves in the boundary plane, as already observed for the case of the $(10\bar{1}2)$ twin. The space symmetry group of the relaxed bicrystal is $\text{Ш}(b) = p1m1$.

We now turn to the $(10\bar{1}\bar{3})$ twin. This is the reciprocal mode of the $(10\bar{1}1)$ twin, meaning that they are characterised by the same amount of shear and the same set of twinning elements, except that the K_1 and K_2 planes are swapped, as well as the $\boldsymbol{\eta}_1$ and $\boldsymbol{\eta}_2$ directions. Hence, the twinning elements of the $(10\bar{1}\bar{3})$ twin are as follows: $K_1 = (10\bar{1}\bar{3})$, $K_2 = (10\bar{1}1)$, $\boldsymbol{\eta}_1 = [30\bar{3}2]$,

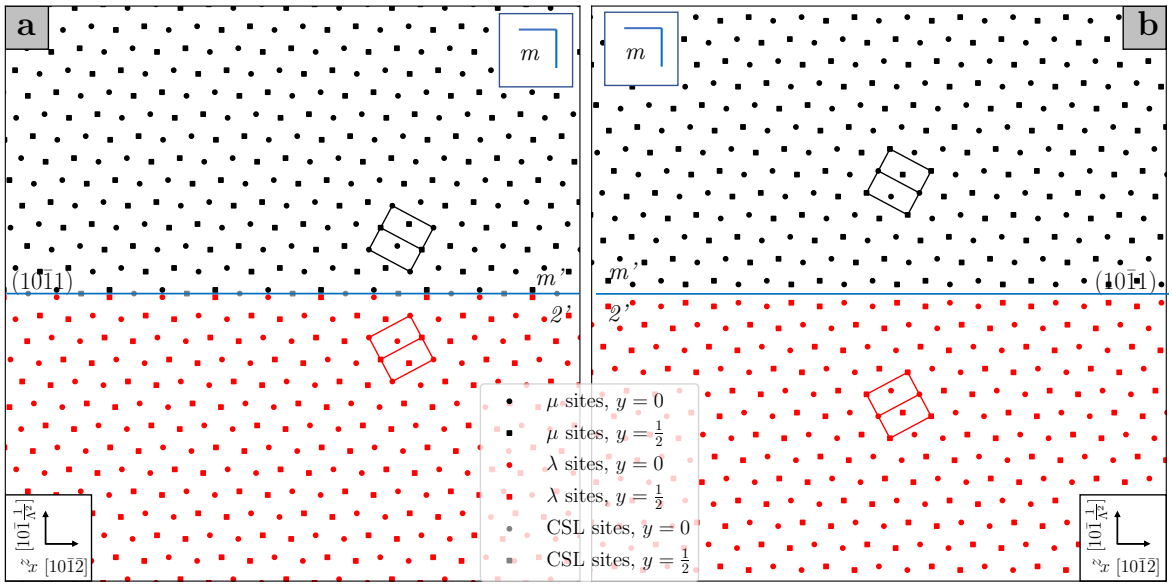

Fig. 2.9 The $(10\bar{1}1)$ twins, created by discarding all red atoms on one side of the boundary and all black atoms on the other side, for both dichromatic complexes in figure 2.8. The boundary plane is $(10\bar{1}1)$, and the projection direction is $[1\bar{2}10]$. Circles and squares are used to indicate different layers of atoms. The unit cells of the μ and λ crystals are outlined by black and red lines respectively; the symmetry elements are drawn in blue.

$\boldsymbol{\eta}_2 = [10\bar{1}\bar{2}]$ [69]. The bicrystallographic analysis of this twin does not differ from that of the $(10\bar{1}\bar{3})$ twin. Indeed, the space symmetry groups of each object are the same as those of the corresponding structures of the $(10\bar{1}\bar{3})$ twin case. The dichromatic pattern is displayed in figure 2.11 for $\gamma = \sqrt{\frac{21}{8}}$ (a) and $\gamma = 1.624$ (b); $\text{III}^*(p) = P2mm'$ for the first case, and $\text{III}^*(p) = p2mm'$ for the second case. The dichromatic complexes for the two atomic configurations examined for previous twins with $\gamma = 1.624$ are shown on the in figure 2.12; $\text{III}^*(c) = p2mm'$ (atomic basis of maximal symmetry, figure 2.12b), $\text{III}(c) = p2'mm'$ (less symmetric atomic basis, figure 2.12a). The $(10\bar{1}\bar{3})$ twins obtained from either atomic basis can be seen in figure 2.13; $\text{III}^*(b) = p2'mm'$, for both bicrystals. Lastly, the relaxation step of the twin obtained from the less symmetric atomic basis is illustrated in figure 2.14; $\text{III}(b) = p1m1$.

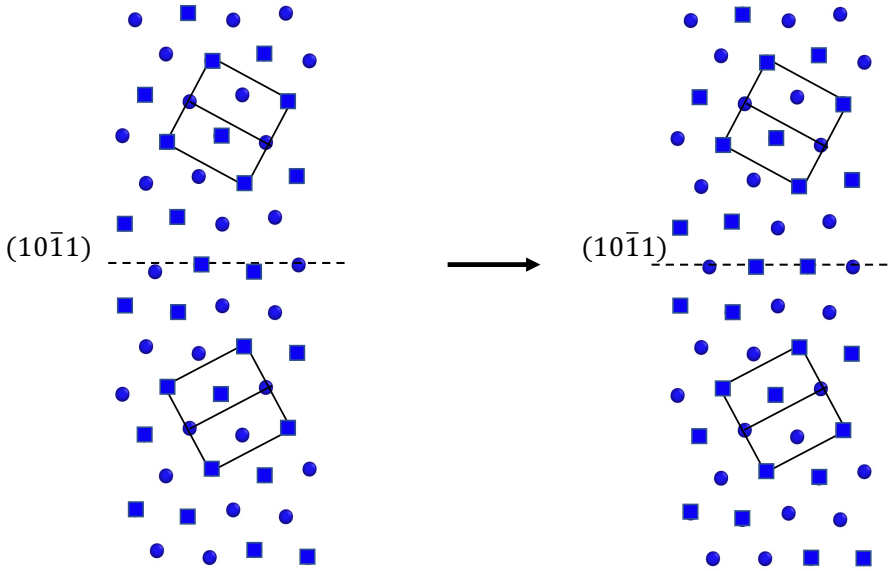

Fig. 2.10 Relaxation of $(10\bar{1}1)$ twin. The left hand side shows the unrelaxed twin, where the layer of atoms directly above the boundary (dashed black line in figure) was removed. The right hand side shows the relaxed twin, where the one layer of atoms left closer to the boundary migrated into the boundary itself. In both figures, the unit cells of the μ and λ crystals are outlined by solid black lines in the bulk on either side of the boundary, and circles and square are used to indicate different layers of atoms.

2.2.3 Twinning disconnections at the $(10\bar{1}2)$, $(10\bar{1}1)$ and $(10\bar{1}\bar{3})$ twin boundaries

Now that we have built our twins as bicrystals and derived their symmetry, we can predict which isolated interfacial defects can arise at their boundaries. In particular, we focus on dislocations; disclinations and dispirations are much less likely to appear in interfaces with a large angle of rotation, as the elastic strain field energy of a disclination scales quadratically with the angle of rotation as well as the size of the supercell [97]. Since the twins in consideration are dissymmetrized in exactly the same way, i.e. the objects created at each step of dissymmetrization present the same symmetry for each bicrystal, the types of allowed interfacial dislocations will be the same for the three twins. In particular, the twin boundaries in consideration can contain class 1 dislocations. Class 2 dislocations are not allowed, because the black and red crystals do not have any aligned mirror-glide planes or screw rotation axes; indeed, no ordinary point group operation is present in the dichromatic patterns that is broken in the holosymmetric dichromatic

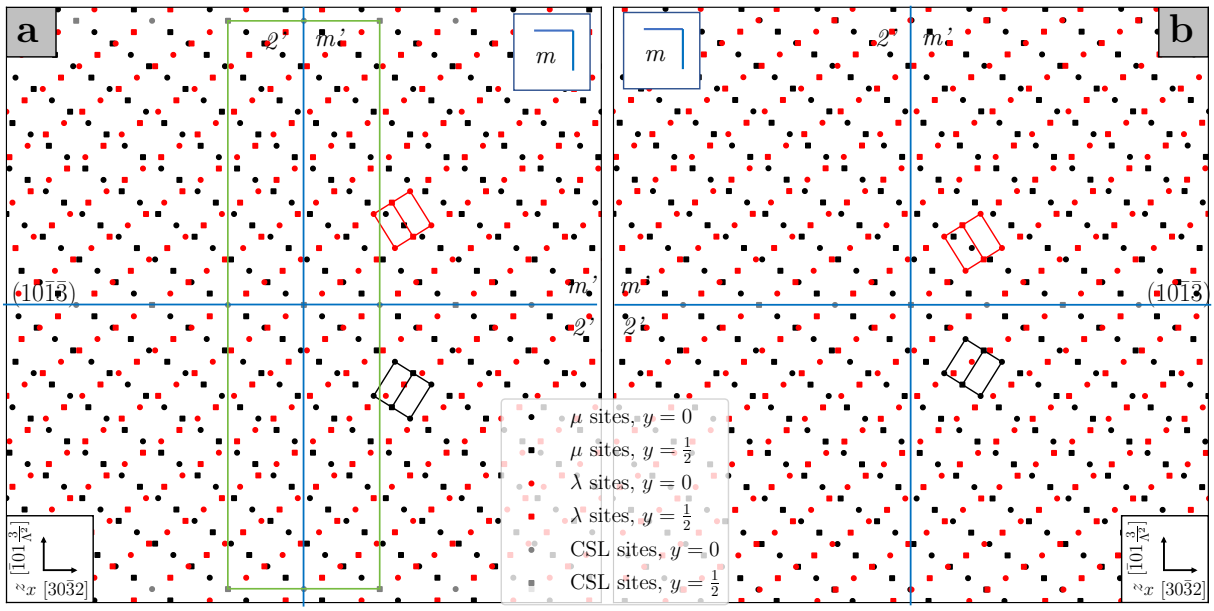

Fig. 2.11 Dichromatic patterns of the $(10\bar{1}\bar{3})$ twin, created by interpenetrating the red and black lattices, for $\gamma = \sqrt{\frac{21}{8}}$ (a) and $\gamma = 1.624$ (b). The boundary plane is $(10\bar{1}\bar{3})$, and the projection direction is $[1\bar{2}10]$. Grey sites mark overlapping red and black sites, i.e. sites of the CSL; circles and squares are used to indicate different layers. The unit cells of the μ and λ lattices are outlined respectively by black and red lines, and a unit CSL is outlined in green. The symmetry elements are drawn in blue, with the exception of the two-fold $[1\bar{2}10]$ axis, which points out of the page.

complexes. Class 3a and 3b dislocations may in principle be present, but no step is associated with them in this case, because $\hat{\mathbf{n}} \cdot \boldsymbol{\alpha}(c)_k = 0$, and the same is true for antioperations.

As previously discussed, class 1 dislocations arise as a consequence of broken translational symmetry, and they separate crystallographically equivalent regions of a bicrystal. Their Burgers vectors are given by equation 2.32, and graphically they can be viewed as vectors connecting red and black sites in the dichromatic pattern. We are particularly interested in twinning disconnections, i.e. steps in the interface [112, 113], whose Burgers vectors are parallel to the $\boldsymbol{\eta}_1$ direction; the motion of twinning disconnections is responsible for the formation of twins in dislocation models of twinning [114]. Among the infinite set of vectors joining black and red sites that one can draw in the dichromatic pattern, those that are more likely to be physically significant are those that yield disconnections with a combination of relatively small $|\mathbf{b}|$ and step height [98]: this is because the elastic strain energy of a disconnection grows with the square of the magnitude of the Burgers vector [114], such that the shorter the Burgers vector, the lower the energy associated with the disconnection. Finally, a set of twinning elements is associated with a

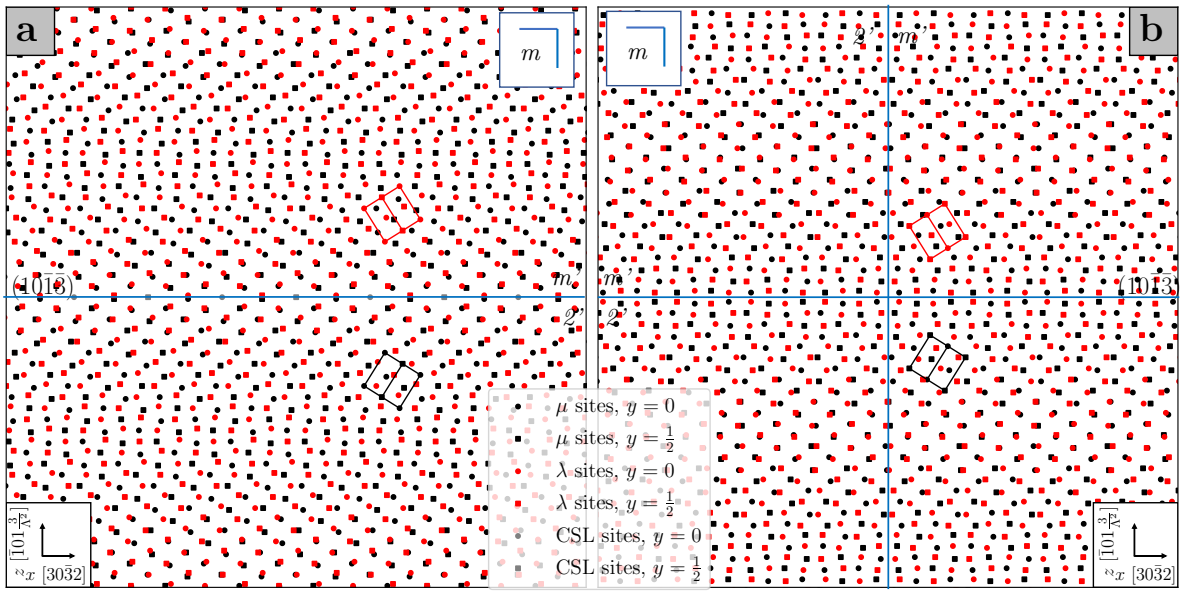

Fig. 2.12 Dichromatic complexes of the $(10\bar{1}\bar{3})$ twin, created by interpenetrating the red and black crystals, for $\gamma = 1.624$. (a): the complex obtained using the less symmetric configuration of the basis atoms; (b): the holosymmetric complex. The boundary plane is $(10\bar{1}\bar{3})$, and the projection direction is $[1\bar{2}10]$. Grey sites mark overlapping red and black atoms, i.e. atoms of the CSL; circles and squares are used to indicate different layers of atoms. The unit cells of the μ and λ crystals are outlined respectively by black and red lines. The symmetry elements are drawn in blue, with the exception of the two-fold $[1\bar{2}10]$ axis in (b), which points out of the page.

certain amount of shear, as per the early theories of twinning; hence, the motion of a twinning disconnection accomplishes the growth of a twin characterised by the shear corresponding to said disconnection [115]. The shear is calculated from the Burgers vector of the disconnection as follows:

$$s = \frac{|\mathbf{b}|}{h}, \tag{2.45}$$

where h is the height of the step associated with the twinning disconnection. It should be noted that in the case of twinning disconnections, the average step height and overlap step height presented in the previous section are equal. This is because the heights of the free surface steps for the black and red crystals are the same, which is easily seen: for a twinning disconnection, $\hat{\mathbf{n}} \cdot \mathbf{b} = 0$; using equation 2.32,

$$\begin{aligned} \hat{\mathbf{n}} \cdot \mathbf{t}(\lambda) - \hat{\mathbf{n}} \cdot \mathbf{P}'\mathbf{t}(\mu) &= 0 \\ h(\lambda) = h(\mu), \end{aligned} \tag{2.46}$$

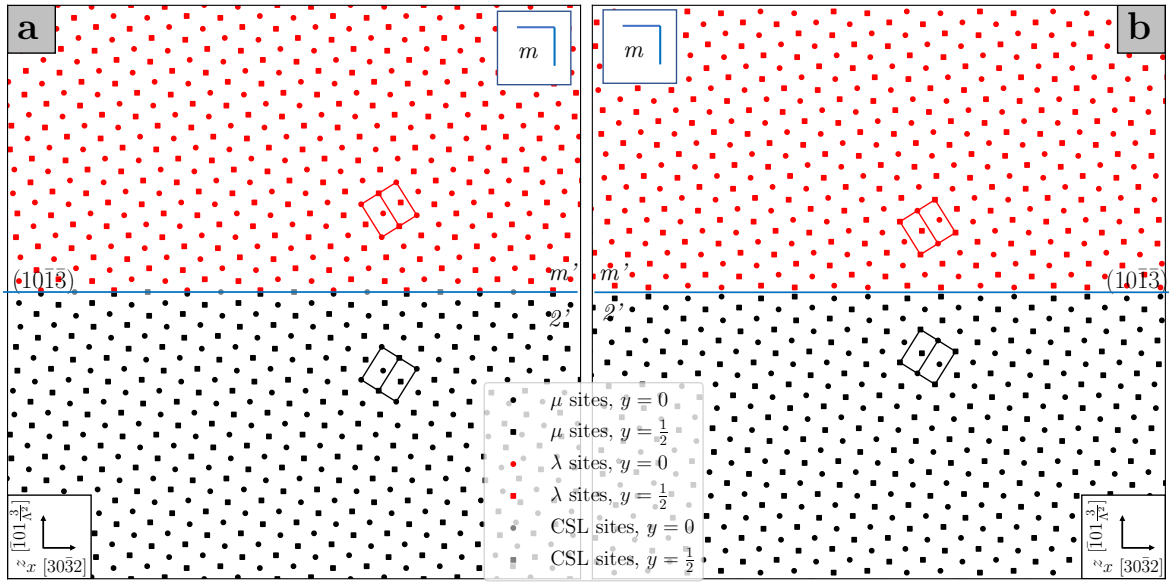

Fig. 2.13 The $(10\bar{1}\bar{3})$ twins, created by discarding all red atoms on one side of the boundary and all black atoms on the other side, for both dichromatic complexes in figure 2.12. The boundary plane is $(10\bar{1}\bar{3})$, and the projection direction is $[1\bar{2}10]$. Circles and squares are used to indicate different layers of atoms. The unit cells of the μ and λ crystals are outlined respectively by black and red lines; symmetry elements are drawn in blue.

where $h(\lambda) = \hat{\mathbf{n}} \cdot \mathbf{t}(\lambda)$ and $h(\mu) = \hat{\mathbf{n}} \cdot \mathbf{P}'\mathbf{t}(\mu)$ are respectively the free surface step heights associated with the red and black translation vectors. Therefore, it is only necessary to calculate one of the surface step heights, e.g. $h(\lambda) = h$.

Finally, it should be noted that twinning disconnections may be used to model the growth of lenticular twins within the matrix: the creation of loops of such disconnections leads to the expansion of the twin by enlargement of the diameter of the loops [64].

In the dichromatic pattern of the $(10\bar{1}2)$ twin the smallest vector parallel to $\boldsymbol{\eta}_1$ that can be drawn is e.g. the one joining a red and a black circle two layers above the interface [116], as shown in figure 2.15. This is the Burgers vector characterising a twinning disconnection arising from the fact that the red and black translation vectors $\mathbf{t}(\lambda) = [10\bar{1}0]$ and $\mathbf{t}(\mu) = [000\bar{1}]$ are not coincident when expressed in the same coordinate frame. Hence, using equation 2.32, the Burgers vector is given by $\mathbf{b} = \frac{2-\Lambda^2}{2+\Lambda^2}[10\bar{1}\bar{1}]$, as can readily be found by using the same 4-vector formulation of the rotation matrix $\mathbf{R} = \mathbf{P}'$ employed in the derivation of the symmetry of the dichromatic pattern and complex. For $\gamma = 1.624$, $\mathbf{b} \approx \frac{1}{15}[10\bar{1}\bar{1}]$. The height of the step associated with this disconnection can be calculated in units of $a\sqrt{3/2}$ as $h = -2d_{(10\bar{1}2)} = -\frac{\sqrt{2}\Lambda}{\sqrt{2+\Lambda^2}}$. This

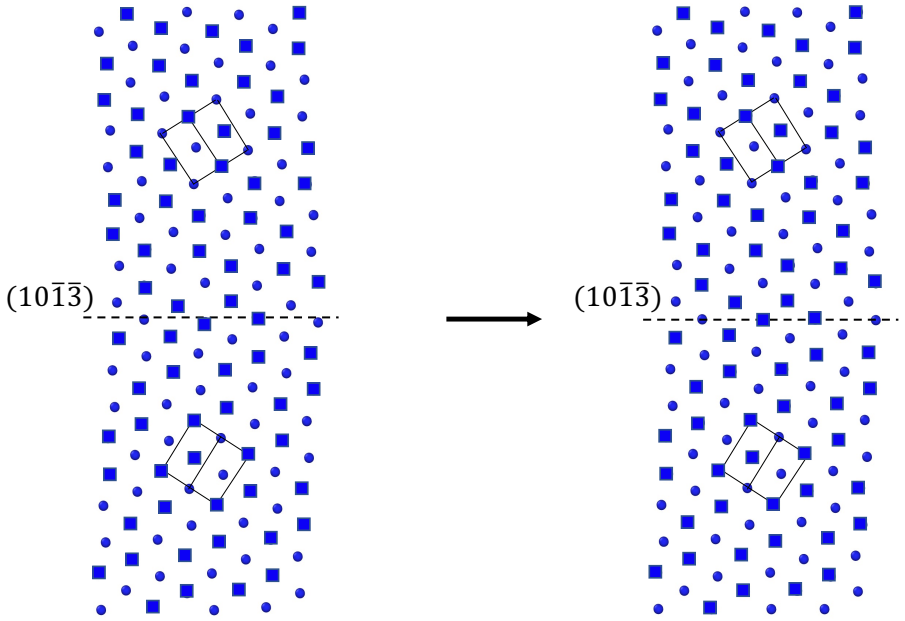

Fig. 2.14 Relaxation of $(10\bar{1}\bar{3})$ twin. The left hand side shows the unrelaxed twin, where the layer of atoms directly above the boundary (dashed black line in figure) was removed. The right hand side shows the relaxed twin, where the one layer of atoms left closer to the boundary migrated into the boundary itself. In both figures, the unit cells of the μ and λ crystals are outlined by solid black lines in the bulk on either side of the boundary, and circles and square are used to indicate different layers of atoms.

is equivalent to twice the interplanar spacing between K_1 planes; this is the smallest possible step height, because a disconnection with half this step height would separate crystallographically inequivalent regions of the interface [78]. In turn, the height of the step can be used to calculate the magnitude of the shear of the twinning disconnection as $s = |\mathbf{b}|/h = \frac{\Lambda^2-2}{\sqrt{2}\Lambda}$, which corresponds to the observed shear for the $(10\bar{1}2)$ twin [69]. Additionally, it can be seen from the dichromatic pattern in figure 2.15 that for any other admissible disconnections whose Burgers vector is parallel to the shear direction, the Burgers vector is also an integer multiple of that of the 2-layer disconnection; computer simulations of hcp metals have shown that such disconnections decompose into 2-layer disconnections that move apart [78], or 2-layer disconnections and residual immobile defects [117].

Though loops of twinning disconnections may be created spontaneously in a twin boundary under high shear stress [118], other sources for the nucleation of 2-layer $(10\bar{1}2)$ twinning disconnections were thoroughly investigated in computer simulations: matrix dislocations

interacting with a $(10\bar{1}2)$ twin boundary were found to provide a source for loops of twinning disconnections with the same Burgers vector and opposite line sense, which subsequently moved apart, leading to growth of the twin. This was observed for impinging basal dislocations with Burgers vector inclined to the interface plane [116, 119, 120]. More recently, thanks to the development of a boundary condition technique that allows the twin interface to move via the glide of twinning disconnections [121, 122], the interaction between moving 2-layer twinning disconnections and matrix dislocations was also studied, leading to similar conclusion as those of earlier work: the matrix dislocations cause loops of twinning disconnections to nucleate in the twin interface, and where these interact with a twinning disconnection with opposite Burgers vector, one of the disconnections in the loop annihilates it [123].

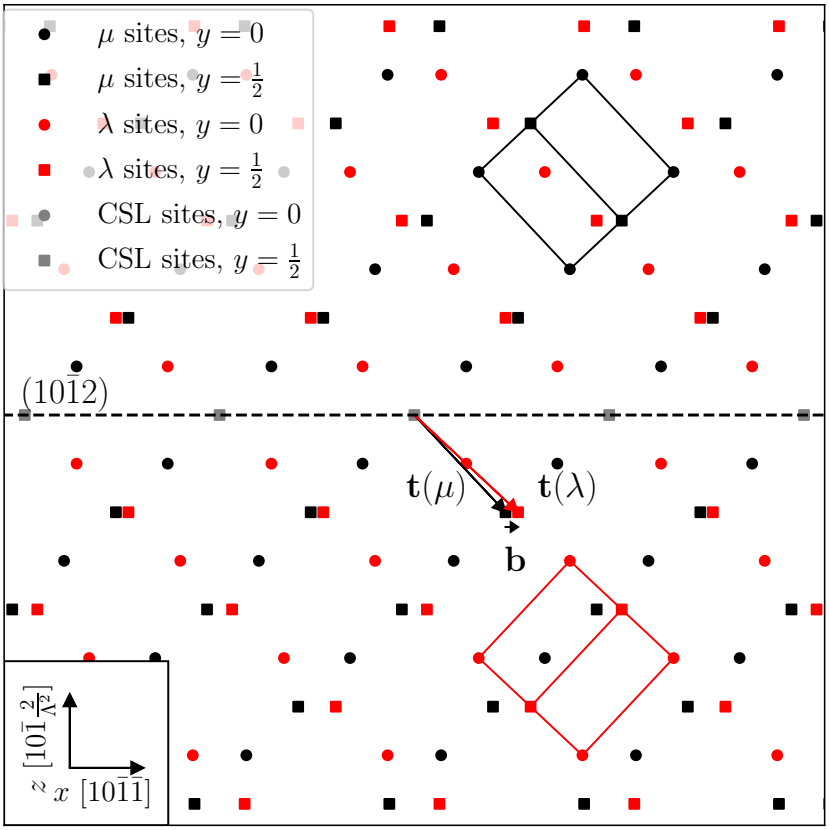

Fig. 2.15 Burgers vector of the twinning disconnection obtained by connecting black and red sites in the dichromatic pattern for the $(10\bar{1}2)$ twin. $\mathbf{t}(\mu)$ and $\mathbf{t}(\lambda)$ denote the translation vectors of the black and red lattices that generate the Burgers vector of the disconnection. $\gamma = 1.624$.

Lastly for the $(10\bar{1}2)$ twin, we briefly discuss the atomic displacements associated with this twinning mode in relation to the twinning disconnection thought to be responsible for

accomplishing the required shear on $(10\bar{1}2)$. We recall from chapter 1 that in earlier theories of classical twinning, atom pairs, called a "motif unit", were assumed to move rigidly and undergo the same homogeneous displacement as the related lattice site [70, 75]. In the topological theory, lattice sites undergo inhomogeneous displacement instead, as all sites within the step are displaced by the same amount, corresponding to the Burgers vector of the twinning disconnections [124]. Thus, the total displacements of basis atoms comprised by the step include both that amounting to the Burgers vector of the disconnection and the atomic shuffles, which only apply to individual atoms. These are not assumed to move rigidly in pairs any longer; instead, the shortest possible shuffle vectors are selected among those connecting μ and λ sites in the dichromatic complex [125]. Consequently, the atomic shuffle vectors envisaged in the topological theory differ from those proposed by Bilby and Crocker [75]; these were explicitly calculated by Pond et al. [124] for the $(10\bar{1}2)$ twin in Zr, and the shuffle mechanism was verified using atomistic simulations by Khater et al. [126].

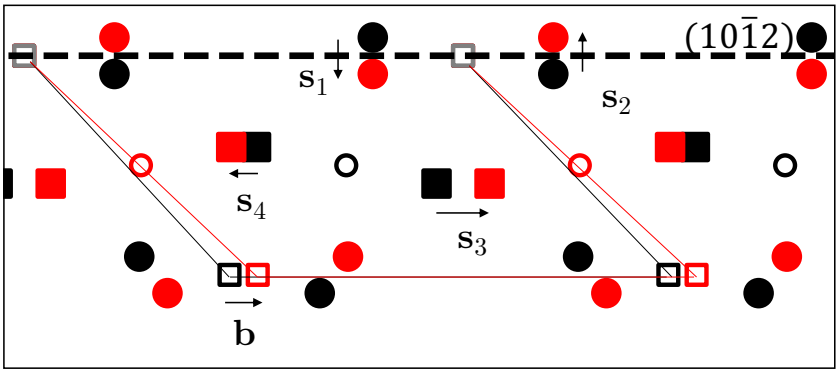

Fig. 2.16 Atomic vector shuffles associated with the twinning disconnection of the $(10\bar{1}2)$ twin. The exchange cells are delineated by solid black and red lines for the μ and λ crystals respectively. Open black and red circles and squares indicate μ and λ lattice points on subsequent $(1\bar{2}10)$ planes; filled black and red circles and squares represent atomic sites belonging to each crystal. Projection along $[1\bar{2}10]$, $\gamma = 1.624$.

The shuffle vectors are easily visualised by constructing an exchange cell or e-cell in the dichromatic complex [124, 125]. This is a cell delineated by the two shortest possible translation vectors in the interface plane and a third vector inclined to it, and it is drawn for both μ and λ. Thus one of the translation vectors is parallel to the shear direction, one is parallel to the normal to the plane of shear and the third is either $\mathbf{t}(\mu)$ or $\mathbf{t}(\lambda)$ for the μ and λ e-cells respectively, i.e. the vectors that define the Burgers vector of the twinning disconnection in the dichromatic

pattern, figure 2.15. This construction is depicted for the dichromatic complex of the $(10\bar{1}2)$ twin in figure 2.16, where lattice sites have also been included and are denoted by open shapes, whilst atomic sites are given by filled symbols; the atomic basis is chosen such that the lattice sites are centres of symmetry. The e-cell is then the unit cell of disconnection motion, as exchange of μ and λ atomic sites during disconnection glide transforms the matrix into the twin. The shortest possible shuffles undergone by atomic sites can be drawn; these are the vectors $\mathbf{s}_i$, $i = 1,2,3,4$ in figure 2.16. Hence, in the topological theory the atomic shuffles are associated with the step character of the disconnection, while the macroscopic shear, which is applied to all atoms during the transformation, is brought about by the dislocation character of the disconnection, i.e. by the displacement associated with the Burgers vector of the disconnection.

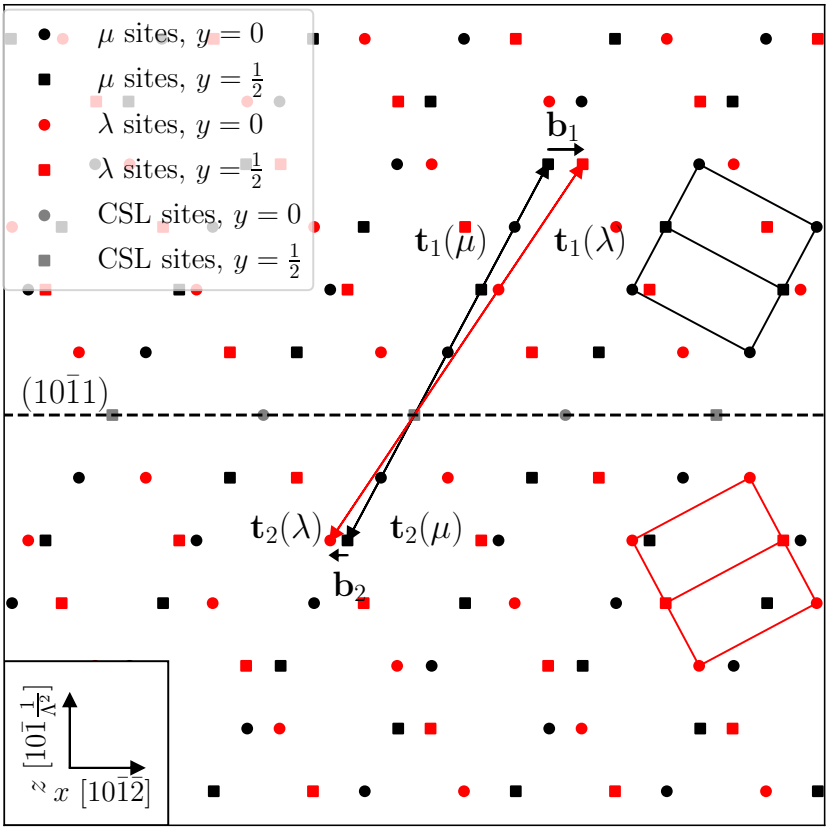

Fig. 2.17 Burgers vectors of the twinning disconnections obtained by connecting black and red sites in the dichromatic pattern for the $(10\bar{1}1)$ twin. The 4-layer disconnection restoring the shear direction is denoted by translation vectors $\mathbf{t}_1(\mu)$, $\mathbf{t}_1(\lambda)$ and Burgers vector $\mathbf{b}_1$; the 2-layer disconnection proposed by Wang et al. [127] is produced by translation vectors $\mathbf{t}_2(\mu)$, $\mathbf{t}_2(\lambda)$ and its Burgers vector is labelled $\mathbf{b}_2$. $\gamma = 1.624$.

In the case of the $(10\bar{1}1)$ twin, the twinning disconnection that accomplishes the required amount of shear has Burgers vector $\mathbf{b} = \frac{2\Lambda^2-3}{2\Lambda^2+1}[10\bar{1}\bar{2}] \approx \frac{1}{9}[10\bar{1}\bar{2}]$ for $\gamma = 1.624$. The corresponding translation vectors of the red and black lattices are respectively $\mathbf{t}(\lambda) = [\bar{1}01\bar{2}]$ and $\mathbf{t}(\mu) = [20\bar{2}0]$, as shown in figure 2.17. The height of the step associated with the disconnection is $h = 4d_{(10\bar{1}1)} = \frac{4\Lambda}{\sqrt{(2\Lambda^2+1)}}$ in units of $a\sqrt{3/2}$, and the corresponding shear is $s = \frac{\sqrt{2}(2\Lambda^2-3)}{4\Lambda}$ [115, 104].

This 4-layer disconnection has been found, in pair-potential simulations of hcp metals, to have low mobility on the K_1 plane due to its large step height and narrow core; conversely, a 2-layer disconnection, also depicted in figure 2.17, has a slightly wider core and would glide more easily on the $(10\bar{1}1)$ plane [115]. The parameters for the 2-layer disconnection are $\mathbf{b} = \frac{1}{3(2\Lambda^2+1)}\boldsymbol{\eta}_1$, $\boldsymbol{\eta}_1 = [(5-2\Lambda^2), -(2\Lambda^2+1), 4(\Lambda^2-1), 3(2\Lambda^2-3)]$ and $h = 2d_{(10\bar{1}1)}$. Thus this disconnection does not shear the crystal along the shear direction observed experimentally for $(10\bar{1}1)$ twinning, due to its additional screw component, as may be seen in figure 2.17: the Burgers vector $\mathbf{b}_2$ obtained from translation vectors $\mathbf{t}_2(\mu)$ and $\mathbf{t}_2(\lambda)$ connects a black square and red circle, such that the two sites do not belong to the same $(1\bar{2}10)$ plane, and $\mathbf{b}_2$ is not parallel to $\boldsymbol{\eta}_1$. Computer simulations suggested that it is energetically favourable to form pairs of 2-layer disconnections with the same screw component and opposite edge components upon interaction of matrix dislocations with a $(10\bar{1}1)$ twin boundary; concerted movement of these disconnections in the same direction does not however lead to twin growth [128, 119]. Wang et al. [127] proposed that the 4-layer disconnections may be recovered as a superposition of two more mobile 2-layer disconnections with screw components of alternating sign, such as to restore the correct shear direction. However, if one of the two 2-layer disconnections were favoured by the shear stress, its prevalence would lead once again to an irrational shear direction incompatible with the twinning elements associated to compression twinning. Moreover, the 4-layer disconnection was actually observed in high-resolution transmission electron microscopy experiments in titanium [129]. Therefore, in all following discussions of this twinning mode involving disconnections we take the 4-layer disconnection as that accomplishing the required shear on the $(10\bar{1}1)$ plane.

Similarly to the case of the $(10\bar{1}2)$ twin, an exchange cell may be drawn within a portion of the dichromatic complex for the $(10\bar{1}1)$ twin; this is shown in figure 2.18. The atomic shuffle vectors can then be found by connecting μ and λ atoms; in the figure, we propose the shortest possible shuffle vectors for the twinning disconnection under consideration. It may be noted that

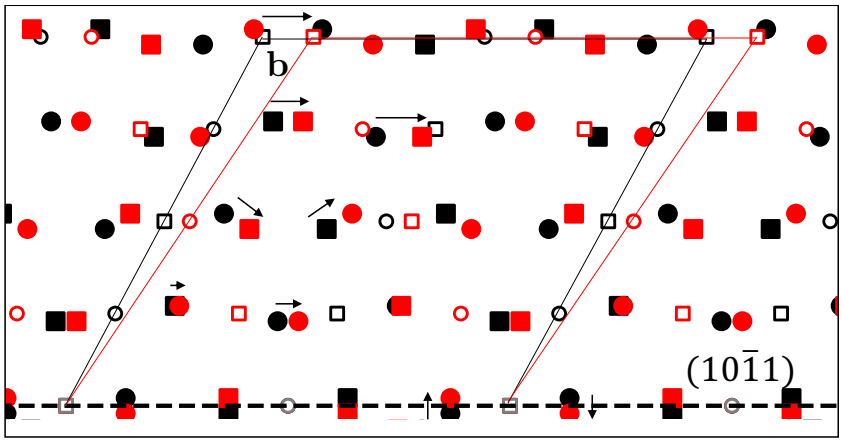

Fig. 2.18 Atomic vector shuffles associated with the twinning disconnection of the $(10\bar{1}1)$ twin. The exchange cells are delineated by solid black and red lines for the μ and λ crystals respectively. Open black and red circles and squares indicate μ and λ lattice points on subsequent $(1\bar{2}10)$ planes; filled black and red circles and squares represent atomic sites belonging to each crystal. Projection along $[1\bar{2}10]$, $\gamma = 1.624$.

in this case, most of the shuffle vectors connect circles and squares, i.e. atoms on different $(1\bar{2}10)$ planes; these atoms thus undergo relatively large displacements. The same is true for atomic shuffles associated with the twinning disconnection of the $(10\bar{1}\bar{3})$ twin, figure 2.20, whereas atomic shuffles associated with the $(10\bar{1}2)$ twinning disconnection occur on the same $(1\bar{2}10)$ plane. The large displacements may thus contribute to the low mobility of the $(10\bar{1}1)$ and $(10\bar{1}\bar{3})$ twinning disconnections.

Finally, we report the twinning disconnection associated with the characteristic shear of the $(10\bar{1}\bar{3})$ twin, which is also the same as the shear of the $(10\bar{1}1)$ twin, since the two modes are reciprocal to each other. The corresponding disconnection has $\mathbf{b} = \frac{2\Lambda^2-3}{2\Lambda^2+9}[30\bar{3}2] \approx \frac{1}{25}[30\bar{3}2]$ for $\gamma = 1.624$, and it can be obtained from translation vectors $\mathbf{t}(\lambda) = [10\bar{1}2]$ and $\mathbf{t}(\mu) = [20\bar{2}0]$, drawn in figure 2.19. The disconnection produces a step of height $h = 4d_{(10\bar{1}\bar{3})} = \frac{4\Lambda}{\sqrt{2\Lambda^2+9}}$, in units of $a\sqrt{3/2}$. We note that in this case as for $(10\bar{1}1)$ twinning, Wang et al. [127] proposed that a 2-layer disconnection with higher mobility may be responsible for shear on the $(10\bar{1}\bar{3})$ plane provided that a second disconnection with opposite screw component act to restore the required shear direction. For the reasons mentioned above, in the following chapters we discuss $(10\bar{1}\bar{3})$ twinning in relation to the 4-layer disconnection instead. Atomic shuffle vectors associated with this twinning disconnections are illustrated along with the relevant e-cell in the dichromatic complex in figure 2.20.

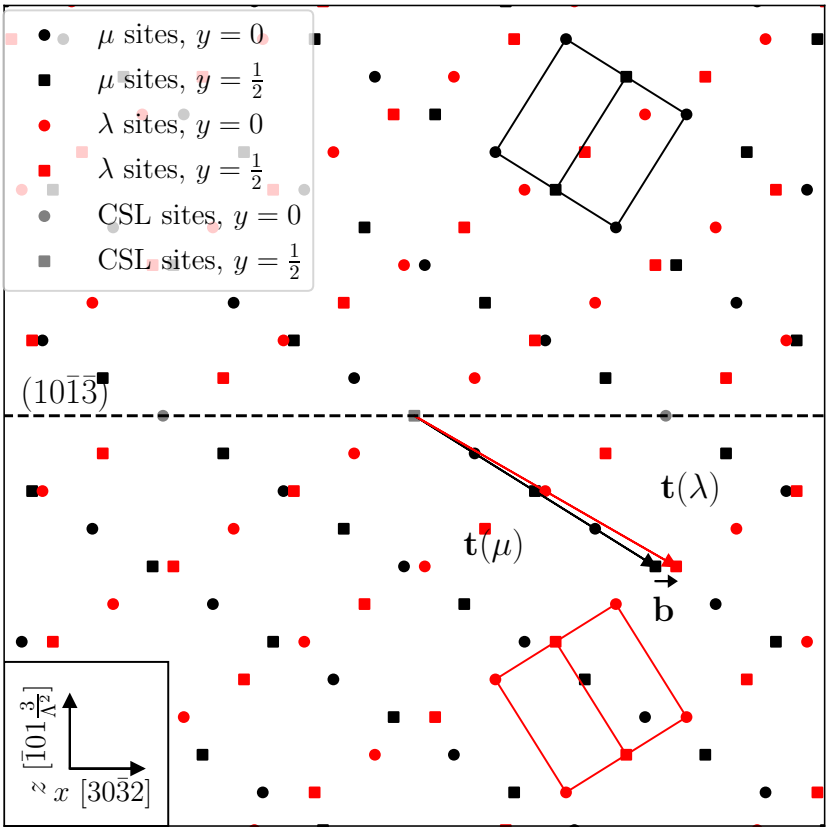

Fig. 2.19 Burgers vector of the twinning disconnection obtained by connecting black and red sites in the dichromatic pattern for the $(10\bar{1}\bar{3})$ twin. $\mathbf{t}(\mu)$ and $\mathbf{t}(\lambda)$ denote the translation vectors of the black and red lattices that generate the Burgers vector of the disconnection. $\gamma = 1.624$.

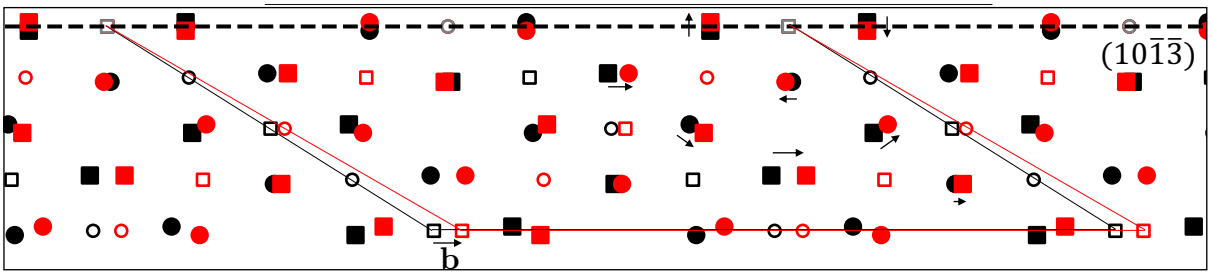

Fig. 2.20 Atomic vector shuffles associated with the twinning disconnection of the $(10\bar{1}\bar{3})$ twin. The exchange cells are delineated by solid black and red lines for the μ and λ crystals respectively. Open black and red circles and squares indicate μ and λ lattice points on subsequent $(1\bar{2}10)$ planes; filled black and red circles and squares represent atomic sites belonging to each crystal. Projection along $[1\bar{2}10]$, $\gamma = 1.624$..

The parameters of the twinning disconnections associated with each twinning mode are summarised in table 2.1, along with the translation vectors of the μ and λ lattices that produce the disconnections.

$\mathbf{t}(\lambda)$	$\mathbf{t}(\mu)$	$\mathbf{b}$	$\lvert\mathbf{b}\rvert$	$h/d_{(hkil)}$	s
$(10\bar{1}2)$ twin; $\hat{\mathbf{n}} = \frac{\Lambda}{\sqrt{2}\sqrt{(2+\Lambda^2)}}[\bar{1}01\bar{2}/\Lambda^2]$; $\boldsymbol{\eta}_1 = [10\bar{1}\,\bar{1}]$					
$[10\bar{1}0]$	$[000\bar{1}]$	$\frac{2-\Lambda^2}{2+\Lambda^2}[10\bar{1}\,\bar{1}]$	$\frac{2-\Lambda^2}{\sqrt{2+\Lambda^2}}$	-2	$\frac{\Lambda^2-2}{\sqrt{2}\Lambda}$
$(10\bar{1}1)$ twin; $\hat{\mathbf{n}} = \frac{\Lambda}{\sqrt{2\Lambda^2+1}}[\bar{1}01\bar{1}/\Lambda^2]$; $\boldsymbol{\eta}_1 = [10\bar{1}\bar{2}]$					
$[\bar{1}01\bar{2}]$	$[20\bar{2}0]$	$\frac{2\Lambda^2-3}{2\Lambda^2+1}[10\bar{1}\bar{2}]$	$\frac{\sqrt{2}(2\Lambda^2-3)}{\sqrt{2\Lambda^2+1}}$	$+4$	$\frac{\sqrt{2}(2\Lambda^2-3)}{4\Lambda}$
$(10\bar{1}\bar{3})$ twin; $\hat{\mathbf{n}} = \frac{\Lambda}{\sqrt{2\Lambda^2+9}}[\bar{1}013/\Lambda^2]$; $\boldsymbol{\eta}_1 = [30\bar{3}2]$					
$[10\bar{1}2]$	$[20\bar{2}0]$	$\frac{2\Lambda^2-3}{2\Lambda^2+9}[30\bar{3}2]$	$\frac{\sqrt{2}(2\Lambda^2-3)}{\sqrt{2\Lambda^2+9}}$	$+4$	$\frac{\sqrt{2}(3-2\Lambda^2)}{4\Lambda}$

Table 2.1 Parameters of the twinning disconnections associated with the $(10\bar{1}2)$, $(10\bar{1}1)$ and $(10\bar{1}\bar{3})$ twinning modes. $\Lambda = \gamma\sqrt{2/3}$. $|\mathbf{b}|$ is given in units of $a\sqrt{3/2}$, where a is the lattice constant.

Chapter 3

Double twinning

"*Double, double toil and trouble*"

Macbeth, WILLIAM SHAKESPEARE

Double twins are observed as compositions of a primary and a secondary twin. In magnesium, while the secondary twin is typically a $(10\bar{1}2)$ tension twin, the primary is either a $(10\bar{1}1)$ compression twin or a $(10\bar{1}\bar{3})$ twin, i.e. the reciprocal twinning mode of $(10\bar{1}1)$; we shall label this twinning sequence compression-tension (C-T) double twinning. However, the opposite twinning sequence, i.e. tension-compression twinning, has also been observed, albeit less frequently. As the theoretical analysis derived in this chapter for compression-tension double twinning is straight-forwardly extended to tension-compression (T-C) double twinning, we hereby consider both cases.

In the following sections, two contrasting models of double twin to matrix interfaces are presented, namely the theory first proposed by A. G. Crocker and then extended by Crocker and coworkers, the ensemble of which we call the phenomenological theories, and the topological treatments, which are based on the topological theory of interfacial defects developed by Bob Pond and introduced in the previous chapter. The former theories propose models for the growth of double (and more generally, non-classical) twins on invariant habit planes, whilst the latter treatments focus on the modification of the primary twin interface caused by internal retwinning, utilising the notion of twinning disconnections and their interplay. Thus, the fundamental difference between the two models is growth of the double twin in one- or two-step processes.

Despite this, we will see that these theories present points of contact, and in some cases lead to the same predictions.

First however, we set aside some space to present the classification of double twins and the relative notation, clarifying conflicting definitions given in the experimental and theoretical literature.

3.1 Double twin misorientation relations

Each of the component twinning mechanisms of a double twinning sequence can be defined by specifying the twinning elements, K_1, K_2, η_1 and η_2, as mentioned in the previous chapter. However, the characterisation of a twin using a set of twinning elements is not unique: for each K_1 plane, there are five more planes equivalent by hexagonal symmetry, and the same consideration holds for the twinning directions, K_2 and the plane of shear P. Hence, each twin can be described equivalently by six sets of twinning elements. When two twins are combined to describe a non-classical double twin, any of the equivalent sets of twinning elements can be used to define the primary and secondary twins, such that there are 36 combinations, named double twin variants. Upon inspection, it is found that only four out of the 36 variants are geometrically distinct, i.e. they produce reorientations of the basal pole by different angles. Formally, these are represented by the misorientation relations between the initial crystal and the twinned volume, where the term misorientation refers to the difference in orientation between the coordinate systems of two crystallites. If the operations representing the orientations of crystallites A and B are denoted respectively by $\mathbf{O}_A$ and $\mathbf{O}_B$, the misorientation $\mathbf{M}_{AB}$ is conventionally defined as the operation that brings the coordinate system of A into coincidence with that of B, such that

$$\mathbf{M}_{AB} = \mathbf{O}_\mathrm{f}\mathbf{O}_\mathrm{i}^{-1}, \tag{3.1}$$

where $\mathbf{O}_\mathrm{i}$ and $\mathbf{O}_\mathrm{f}$ are the operations representing the initial and final orientations respectively, i.e. the matrix and the twin or double twin [45, 46]. For a double twin, we take the orientation of the matrix to be represented by the identity matrix, $\mathbf{O}_\mathrm{i} = \mathbf{I}$, and the final orientation to be the result of successive rotations ascribed to each twinning event; these are e.g. rotations of 180° about the respective shear directions, expressed in their own coordinate systems, and are termed $\mathbf{R}_A$

and $\mathbf{R}_B$. Therefore, the total transformation, expressed in the coordinate system of the matrix, is given by

$$\mathbf{M}_{AB} = \mathbf{R}_A\mathbf{R}_B\mathbf{R}_A^{-1}\mathbf{R}_A = \mathbf{R}_A\mathbf{R}_B. \tag{3.2}$$

It may be noted that in the case where $\mathbf{R}_A$ and $\mathbf{R}_B$ are rotations of 180° about an axis, there is no need for the inverse in equation 3.2. This is easily seen by noticing that two successive rotations of 180° about the same axis necessarily take us back to the starting point, i.e. $\mathbf{R}_A\mathbf{R}_A = \mathbf{I}$; but since we also have that $\mathbf{R}_A\mathbf{R}_A^{-1} = \mathbf{I}$, then necessarily $\mathbf{R}_A = \mathbf{R}_A^{-1}$, i.e. $\mathbf{R}_A$ is said to be *involutory*.

Equation 3.2 can be used to obtain the operation characterising a double twin, e.g. in the form of a rotation matrix. Out of all the possible manners of representing a rotation, the most widely used to denote double twin variants, especially in experimental treatments of the problem, is that of axis/angle pairs. This representation is strictly linked with that of a rotation as a matrix presented in chapter 1. The rotation axis $\hat{\mathbf{n}}$ and rotation angle θ can be extracted from the system of equations 1.32 and are obtained as follows:

$$\cos\theta = \frac{1}{2}(\mathrm{Tr}(\mathbf{R}) - 1), \tag{3.3}$$

$$\hat{n}_1 = \frac{R_{32} - R_{23}}{2\sin\theta}, \tag{3.4}$$

$$\hat{n}_2 = \frac{R_{13} - R_{31}}{2\sin\theta}, \tag{3.5}$$

$$\hat{n}_3 = \frac{R_{21} - R_{12}}{2\sin\theta}. \tag{3.6}$$

Therefore, the axis/angle pairs characterising the misorientation relation of each double twin variant can be found by substituting $\mathbf{R} = \mathbf{M}_{AB}$ in the equations above. Upon doing so for all 36 combinations of primary and secondary twins, one finds only four distinct axis/angle pairs, corresponding to the four geometrically different double twin variants.

In the literature, misorientation relations are often presented in the form of *minimum* axis/angle pairs. This expression refers to the fact that, due to symmetry, the representation of a rotation as a matrix or axis/angle pair is not unique in a hexagonal coordinate system. In particular, given a rotation $\mathbf{R}$ relating two orientations of a crystal with a set of proper symmetry operations $\mathbf{D}_i$, equivalent descriptions of $\mathbf{R}$ are given by the operations $\mathbf{RD}_i$ [62]. Hence, the number of equivalent descriptions of $\mathbf{R}$ is equal to the number of proper point group symmetry operations

of the crystal. The minimum axis/angle pair is obtained by choosing out of all the possible descriptions the one that yields the smallest angle.

In the case of Mg double twinning, the misorientation $\mathbf{M}_{AB}$ relates two hexagonal crystals, hence its equivalent descriptions are obtained by using the proper point group operations of the space symmetry group of hcp crystals, i.e. $P6_3/mmc$. This group comprises 24 point group operations, 12 of which are rotations or reflections, while the remaining 12 are screw rotations or glide reflections; the proper symmetry operations are those that do not include an inversion. The most advantageous way of dealing with hexagonal symmetry operations as well as twin orientations is to express them in the 4D orthogonal coordinate system introduced by Frank [59] and described in chapter 1. In this coordinate system, rotations can be represented as 4×4 matrices, easily obtained via a coordinate transformation, as explained by Pond [62] and briefly reported here.

We label the Frank unit vectors $\mathbf{e}_i,\ i = 1,2,3,4$, with $\mathbf{e}_1 = [1000]_4$ and so on. We then start off by writing the matrix $\mathbf{Q}^{(4)}$ [3] associated with a rotation by an angle θ about the $\mathbf{e}_3$ axis:

$$\mathbf{Q}^{(4)} = \begin{pmatrix} \cos\theta & -\sin\theta & 0 & 0 \\ \sin\theta & \cos\theta & 0 & 0 \\ 0 & 0 & 1 & 0 \\ 0 & 0 & 0 & 1 \end{pmatrix}. \tag{3.7}$$

Our goal is now to find a coordinate transformation $\mathbf{R}^{(4)} = \mathbf{T}^{(4)}\mathbf{Q}^{(4)}{\mathbf{T}^{(4)}}^{-1}$ that will align $\mathbf{e}_3$ with the desired rotation axis, e.g. $\hat{\mathbf{n}} = [u_3\ v_3\ t_3\ \Lambda w_3]_4$ ($\Lambda = \sqrt{2/3}\gamma$, with γ the axial ratio). $\mathbf{T}^{(4)}$ is given by

$$\mathbf{T}^{(4)} = \begin{pmatrix} u_1 & u_2 & u_3 & \frac{1}{\sqrt{3}} \\ v_1 & v_2 & v_3 & \frac{1}{\sqrt{3}} \\ t_1 & t_2 & t_3 & \frac{1}{\sqrt{3}} \\ \Lambda w_1 & \Lambda w_2 & \Lambda w_3 & 0 \end{pmatrix}, \tag{3.8}$$

[3] Matrices referred to 4D Frank space are hereby denoted by the suffix $^{(4)}$ to distinguish them from 3×3 matrices referred to 3D Cartesian space.

where the column vectors are given by the initial axes expressed in the rotated coordinate frame: the first two columns are two unit vectors in the plane perpendicular to $\hat{\mathbf{n}}$, and they must also be perpendicular to each other; the fourth column is the unit vector parallel to $[1110]_4$, which is the direction used to project the Frank space onto the Miller-Bravais subspace.

As we mentioned above, all the twins involved in this study are compound twins, such that we are free to choose whichever of the relations $1-4$ between parent and twin lattice we prefer. We choose to make use of relation 2, i.e that for a type II twin, whose transformation is given by a rotation of 180° about η_1, so $\theta = 180^\circ$, $\hat{\mathbf{n}} = [\hat{\eta}_1]_4$ (i.e. the Frank 4-vector corresponding to $\hat{\eta}_1$) and

$$\mathbf{Q}^{(4)} = \begin{pmatrix} -1 & 0 & 0 & 0 \\ 0 & -1 & 0 & 0 \\ 0 & 0 & 1 & 0 \\ 0 & 0 & 0 & 1 \end{pmatrix}. \tag{3.9}$$

The column vectors of $\mathbf{T}^{(4)}$ are easily obtained: by definition, the 4-vector unit normals to the plane of shear P and to the K_1 plane are both perpendicular to $[\eta_1]_4$ and to each other, and can be taken to be $[u_1\ v_1\ t_1\ \Lambda w_1]_4$ and $[u_2\ v_2\ t_2\ \Lambda w_2]_4$ respectively. In this way, the rotation $\mathbf{R}^{(4)}$ can be used to represent the operation associated with twinning in Frank space. Using this method, the point group operations of the space symmetry group $P6/mmm$ are obtained by Pond [62] as 4×4 matrices in Frank space, and from these the point group operations of $P6_3/mmc$ are easily found as follows: the rotations and reflections are the same as for group $P6/mmm$, while the screw rotations and glide reflections are found by adding an extra glide displacement to the orthogonal part of the transformation, which is common to the operations of both groups. Out of these symmetry operations we select the proper ones, and we label them $\mathbf{D}_i^{(4)}$, as mentioned above.

Reversing the procedure described by Pond also allows us to obtain the axis $\hat{\mathbf{n}} = [u_3\ v_3\ t_3\ \Lambda w_3]_4$ and angle θ of rotation, similarly to how it is done using Cartesian coordinates, starting from the rotation matrix $\mathbf{R}^{(4)}$. The angle θ is obtained via the trace of the rotation matrix, since the trace of $\mathbf{Q}^{(4)}$ is left invariant by the coordinate transformation $\mathbf{R}^{(4)} = \mathbf{T}^{(4)}\mathbf{Q}^{(4)}{\mathbf{T}^{(4)}}^{-1}$: hence $\cos\theta = \frac{1}{2}\mathrm{Tr}(\mathbf{R}^{(4)}) - 1$. To obtain the rotation axis, we first notice that the columns of $\mathbf{R}^{(4)}$ are

unit vectors parallel to the rotated axes. If we subtract from the first two columns the vectors $[1000]_4$ and $[0100]_4$ respectively, then we see that the resulting vectors are perpendicular to the rotation axis, which can be obtained as their cross product, i.e. by calculating the following determinant, with $R_{ij}^{(4)}$ the elements of the matrix $\mathbf{R}^{(4)}$:

$$[u_3\ v_3\ t_3\ \Lambda w_3]_4 = \begin{vmatrix} \mathbf{e}_1 & \mathbf{e}_2 & \mathbf{e}_3 & \mathbf{e}_4 \\ 1 & 1 & 1 & 0 \\ R_{11}^{(4)} - 1 & R_{12}^{(4)} & R_{13}^{(4)} & R_{14}^{(4)} \\ R_{21}^{(4)} & R_{22}^{(4)} - 1 & R_{23}^{(4)} & R_{24}^{(4)} \end{vmatrix}, \tag{3.10}$$

We now possess all the tools we need to calculate the minimum axis/angle pairs describing the misorientation relations for each double twin "type". Usage of this term to distinguish different double twin variants clashes with the two classical twin types I and II defined in chapter 1; however, it is widely used in the literature, and we adopt it in this thesis, accompanied to label of the full twinning sequence to avoid confusion.

We first express the orientations of the primary and secondary twin in 4D Frank coordinates, and label them $\mathbf{R}_A^{(4)}$ and $\mathbf{R}_B^{(4)}$. We then obtain the misorientation matrix $\mathbf{M}_{AB}^{(4)}$ from equation 3.2. Taking $\mathbf{R}^{(4)} = \mathbf{M}_{AB}^{(4)}$, we compute all the symmetrically equivalent descriptions of the misorientation matrix, $\mathbf{M}_{AB}^{(4)}\mathbf{D}_i^{(4)}$, with $\mathbf{D}_i^{(4)}$ the proper point group operations of hcp crystals reported by Pond [62]. Using the method described above, we extract the set of equivalent axis/angle pairs from the misorientation matrix, and out of all the possible descriptions we pick that with the lowest angle. We repeat this procedure for all the combinations of primary and secondary twin in the compression-tension sequence, for both $(10\bar{1}1) - (10\bar{1}2)$ and $(10\bar{1}\bar{3}) - (10\bar{1}2)$ double twins. In table 3.1 we report the results for one particular primary twin combined with all six secondary twins, using the experimental axial ratio for magnesium, i.e. $\gamma = 1.624$. These misorientation relations are consistent with the literature [45, 46, 44].

It is interesting to notice how some of the DT variants are extremely close to each other. In particular, the type 2 $(10\bar{1}1) - (10\bar{1}2)$ DT and type 2 $(10\bar{1}\bar{3}) - (10\bar{1}2)$ DT are characterised by rotations around the same axis by angles that differ only by 0.4°. The type 3 variants of either double twin are also close, as the rotations are about roughly the same axes with only a 2.9° angle difference. These differences are so small that it might conceivably be difficult to measure

1st \ 2nd	$(10\bar{1}2)$	$(\bar{1}012)$	$(0\bar{1}12)$	$(\bar{1}102)$	$(1\bar{1}02)$	$(01\bar{1}2)$
	type 1	type 2	type 3		type 4	
$(10\bar{1}1)$	$-37.5°[1\bar{2}10]$	$-30.1°[1\bar{2}10]$	$-66.5°$["$3\bar{7}42$"] or ["$\bar{3}\bar{4}72$"]	$-66.5°$["$\bar{4}\bar{7}32$"] or ["$\bar{7}432$"]	$-69.8°$["$\bar{4}221$"] or ["$\bar{2}\bar{4}21$"]	$-69.8°$["$\bar{2}\bar{2}41$"] or ["$2\bar{4}21$"]
	type 2	type 1	type 3		type 4	
$(10\bar{1}\bar{3})$	$-29.7°[1\bar{2}10]$	$-22.3°[1\bar{2}10]$	$-63.6°$["$3\bar{8}52$"] or ["$\bar{3}\bar{5}82$"]	$-63.6°$["$\bar{5}\bar{8}32$"] or ["$\bar{8}532$"]	$-66.3°$["$\bar{8}531$"] or ["$\bar{5}\bar{8}31$"]	$-66.3°$["$\bar{3}\bar{5}81$"] or ["$3\bar{8}51$"]

Table 3.1 This table shows the minimum axis/angle pairs describing the misorientation relations of double twin variants for $(10\bar{1}1)-(10\bar{1}2)$ and $(10\bar{1}\bar{3})-(10\bar{1}2)$ double twins, with $\gamma = 1.624$. In the case of type 3 and type 4 DT variants, the rotation axes are irrational directions; hence the indices have been rounded to the nearest integer number and are indicated by inverted commas.

them precisely enough using electron microscopy to be able to distinguish one variant from the other.

Having illustrated how DT variants are categorised, and having reproduced this categorisation for magnesium with real axial ratio, we now briefly compare these results to the ones obtained for magnesium with rational axial ratio squared, i.e. $\gamma = \sqrt{\frac{21}{8}} = 1.620$. This axial ratio was obtained as the parameter minimising the GPT total energy, together with lattice constant $a = 0.324$ nm. It might seem that there is very little difference between this axial ratio and the one calculated experimentally; however, using a rational axial ratio squared ensures that the dichromatic patterns and complexes for all three single twins, i.e. $(10\bar{1}1)$, $(10\bar{1}2)$ and $(10\bar{1}\bar{3})$, are periodic structures with three dimensional coincident site lattices of overlapping black and red atoms, as was shown in the previous chapter. And this also applies to double twins with rational misorientation relations, i.e. variant types 1 and 2. Hence we repeat the procedure described above and calculate the misorientation relations for all double twin variants with $\gamma = \sqrt{\frac{21}{8}}$; the results are listed in table 3.2. The most striking feature of these results is that the type 2 $(10\bar{1}1)-(10\bar{1}2)$ and type 2 $(10\bar{1}\bar{3})-(10\bar{1}2)$ variants are now *identical*. Moreover, the type 3 variants of either DT are even closer.

We now wish to apply the same classification to tension-compression twinning, i.e. the case where primary twinning occurs on $(10\bar{1}2)$, followed by secondary twinning on $(10\bar{1}1)$, or its reciprocal mode. Misorientation relations for this case can be derived from those listed earlier for compression-tension double twins. Working in 3D Cartesian coordinates for simplicity,

we recall the misorientation matrix for the compression-tension double twin $\mathbf{M}_{AB} = \mathbf{R}_A\mathbf{R}_B$, equation 3.2. Maintaining this notation, if we swap the primary and secondary twin, we find that the misorientation matrix for the tension-compression double twin is simply $\mathbf{M}_{BA} = \mathbf{R}_B\mathbf{R}_A$. Generally rotation matrices do not commute; however, the trace of a product of matrices is invariant under cyclic permutations, such that

$$\mathrm{Tr}(\mathbf{M}_{\mathrm{BA}}) = \mathrm{Tr}(\mathbf{M}_{\mathrm{AB}}). \tag{3.11}$$

Therefore, it is clear from equation 3.3 that the angle of rotation corresponding to the misorientation $\mathbf{M}_{\mathrm{BA}}$ will be the same as that calculated from $\mathbf{M}_{AB}$. Moreover one can show using equations 3.4 to 3.6 that the rotation axis obtained from $\mathbf{M}_{BA}$ is the negative of the one given by $\mathbf{M}_{AB}$. Therefore, the misorientation relation of each tension-compression double twin may be seen as a rotation of the same magnitude as that of the corresponding compression-tension mechanism, but in the opposite direction.

1st \ 2nd	$(10\bar{1}2)$	$(\bar{1}012)$	$(0\bar{1}12)$	$(\bar{1}102)$	$(1\bar{1}02)$	$(01\bar{1}2)$
	type 1	type 2	type 3		type 4	
$(10\bar{1}1)$	$-37.6°[1\bar{2}10]$	$-29.9°[1\bar{2}10]$	$-66.4°$[“$3\bar{7}42$”] or [“$\bar{3}\bar{4}72$”]	$-66.4°$[“$\bar{4}7\bar{3}2$”] or [“$\bar{7}432$”]	$-69.9°$[“$\bar{4}221$”] or [“$\bar{2}4\bar{2}1$”]	$-69.9°$[“$\bar{2}\bar{2}41$”] or [“$2\bar{4}21$”]
	type 2	type 1	type 3		type 4	
$(10\bar{1}\bar{3})$	$-29.9°[1\bar{2}10]$	$-22.3°[1\bar{2}10]$	$-63.6°$[“$41\bar{1}73$”] or [“$\bar{4}\bar{7}11\ 3$”]	$-63.6°$[“$\bar{7}11\bar{4}3$”] or [“$\bar{1}1743$”]	$-66.4°$[“$\bar{8}531$”] or [“$\bar{5}\bar{8}\bar{3}1$”]	$-66.4°$[“$\bar{3}\bar{5}81$”] or [“$3\bar{8}51$”]

Table 3.2 This table shows the minimum axis/angle pairs describing the misorientation relations of double twin variants for $(10\bar{1}1)-(10\bar{1}2)$ and $(10\bar{1}\bar{3})-(10\bar{1}2)$ double twins, with $\gamma = \sqrt{\frac{21}{8}} = 1.620$. In the case of type 3 and type 4 DT variants, the rotation axes are irrational directions; hence the indices have been rounded to the nearest integer number and are indicated by inverted commas.

We have thus classified the double twinning mechanisms most commonly observed in magnesium alloys according to their misorientation relations with the surrounding grain. This description is widely used in the experimental literature in light of the fact that the vast majority of experimental observations of double twins in magnesium are carried out using EBSD methods, which yield the relative orientations of neighbouring grains. However, in EBSD the direction of

the mutual rotation between the two grains is not given, such that it is not possible to distinguish between negative and positive rotations about the same axis. Therefore, compression-tension and tension-compression double twins are characterised in the same way, and the twinning sequence cannot be ascertained using this method alone, unless a portion of the primary twin is still present. This topic will be explored further in chapter 4, and it will be argued that transmission electron microscopy is the necessary tool for the study of double twinning.

Having described the relative orientation of double twins with respect to the matrix, we now turn to modelling of the double twin to matrix interface. In this chapter we present two classes of models: phenomenological models, which are based on the interpretation of the double twin transformation as a simple twinning shear, and topological models, which focus on the interplay of twinning disconnections at the interface. In chapter 4 we will then present topological models of faceting in single and double twin interfaces. In all that follows, we limit our discussion of double twinning to mechanisms whose component twinning events have a common plane of shear, i.e. type 1 and 2 mechanisms of table 3.1. Then, all dichromatic patterns and two-dimensional diagrams presented will be projections along the normal to the common plane of shear, $(1\bar{2}10)$.

3.2 Crocker's theory of double twinning

The first theory of double twinning in a hcp metal was proposed by Crocker in 1962 [41], and it was later included in generalised treatments of non-classical twinning by Bevis and Crocker [76, 77] and transformation strains by Acton, Bevis, Crocker and Ross [130]. In the following sections, we will present and review these treatments, focusing on their application to double twinning in magnesium and extending them where necessary.

The main postulate of Crocker's theory is that double twinning, as the combination of two simple shears, should also be represented by a simple shear. The simple shear was described in section 1.3 of chapter 1, and it is a type of invariant-plane strain where the strain is applied in a direction that lies in the invariant plane, such that no volume change is involved. Based on experimental observations made by Reed-Hill and Robertson [40], Crocker assumes that the double twinning transformation is a homogeneous deformation with a plane interface, such that

the deformation is an invariant plane strain. In addition, the double twin has the same structure as the parent, varying in orientation only, such that there is no volume change, and the IPS is reduced to a simple shear. The invariant plane of this transformation will then be the habit plane of the double twin: thus Crocker's theory postulates that a small, newly formed primary twin nucleus quickly retwins internally, transforming into a double twin embryo, which then expands into the parent crystal by growing on an invariant habit plane via a simple shear mechanism.

Therefore, Crocker's treatment of double twinning involves the identification of a plane left invariant by the two simple shears that characterise the primary and secondary twinning modes, thus predicting the existence of a simple equivalent twinning mode describing the double twin transformation. Two simple shears may be combined to produce a simple shear in two ways: either by allowing the two shears to occur on the same K_1 plane and along different shear directions, or along the same shear direction and on different K_1 planes [131]. Neither of these possibilities corresponds to $\{10\bar{1}1\} - \{10\bar{1}2\}$ double twinning, where the component twinning modes have different K_1 planes and $\boldsymbol{\eta}_1$ directions. Hence, in order to obtain a simple shear from the combination of two simple shears of the non-degenerate kind, where neither the K_1 planes or the $\boldsymbol{\eta}_1$ directions of the two shears coincide, an additional rotation is to be allowed. In this way, any plane that has not been distorted by the action of the two simple shears may be rotated back to its original position, thus constituting an invariant plane. There are however further restrictions on the choice of simple shear modes, arising from the requirements that make an homogeneous shape deformation into an invariant plane strain.

Any homogeneous shape deformation, given in matrix form, referred to an orthonormal basis I, as $\mathbf{S}$, may always be decomposed into a pure strain, $\mathbf{P}$, followed by a rotation $\mathbf{R}$, i.e. $\mathbf{S} = \mathbf{RP}$, such that a vector $\mathbf{x}$ is transformed by the deformation into $\mathbf{y}$ as follows:

$$\mathbf{y} = \mathbf{Sx} = \mathbf{RPx} \,. \tag{3.12}$$

Under such a transformation, a sphere is deformed into a triaxial ellipsoid, called the strain ellipsoid, whose principal axes, which were perpendicular before the deformation, remain so after the transformation, though they may have rotated from their initial positions and changed in length. In the special case where three perpendicular vectors are unrotated, the deformation is the pure strain $\mathbf{P}$ [69]. The ratios of the lengths of the principal axes after and before the deformation

is given by the eigenvalues $\lambda_i,\ i = 1,2,3$ of $\mathbf{S}$, which may then be diagonalised by a suitable similarity transformation, $\mathbf{L}$. This transformation amounts to a coordinate transformation where the axes are aligned with the principal axes of strain. In this basis, referred to as $\bar{I}$, the shape deformation is given by

$$\bar{\mathbf{S}} = \mathbf{LSL}^{-1} \ . \tag{3.13}$$

Then, equation 3.12 can also be referred to the principal axes of strain:

$$\bar{\mathbf{y}} = \bar{\mathbf{S}}\bar{\mathbf{x}} = \mathbf{LRL}^{-1}\bar{\mathbf{P}}\bar{\mathbf{x}} \ , \tag{3.14}$$

where $\bar{\mathbf{P}} = \lambda_i \delta_{ij}$. The condition for the vector $\bar{\mathbf{x}}$ to remain the same length after the transformation is given by

$$\bar{\mathbf{y}} \cdot \bar{\mathbf{y}} = \bar{\mathbf{x}}^{\mathrm{T}}\bar{\mathbf{P}}^{\mathrm{T}}\bar{\mathbf{P}}\bar{\mathbf{x}} = \bar{\mathbf{x}} \cdot \bar{\mathbf{x}} \ , \tag{3.15}$$

or, using tensor notation and summing over repeated indices,

$$(\lambda_i^2 - 1)\bar{x}_i^2 = 0 \ . \tag{3.16}$$

Equation 3.16 defines the surfaces containing lines whose length is left unchanged by the deformation; if two such lines lie in the same plane, this plane is undistorted. To verify the existence of such a plane, we intersect equation 3.16 with the plane $\bar{x}_k = 0$, obtaining the following conditions:

$$\frac{\lambda_i^2 - 1}{\lambda_j^2 - 1} = -\frac{\bar{x}_j^2}{\bar{x}_i^2} \ , \tag{3.17}$$

or

$$\frac{(\lambda_i - 1)(\lambda_i + 1)}{(\lambda_j - 1)(\lambda_j + 1)} = -\frac{\bar{x}_j^2}{\bar{x}_i^2} \ , \tag{3.18}$$

For these conditions to hold, the ratio on the left hand side must be negative, such that each $\lambda_i - 1$ (i.e., the principal strains) has opposite sign from the other two; this is only possible if one of the $\lambda_i - 1$ is zero, and the other two differ in sign. Therefore, for the homogeneous deformation $\mathbf{S}$ to be an invariant plane strain, one principal strain must be zero, and the other two must have opposite signs [69]. This can also be shown by drawing a sphere and deforming it into an ellipsoid: if the three principal strains all have the same sign, i.e. if all the principal axes

are either shrunk or elongated, there are no undistorted lines, and thus no invariant planes; if one of the principal strains differs in sign from the other two, a double cone of undistorted lines will be obtained, figure 3.1a, which is reduced to two undistorted planes if one if the principal axes retains its length, i.e. if one of the two principal strains with the same sign is set to zero, figure 3.1b.

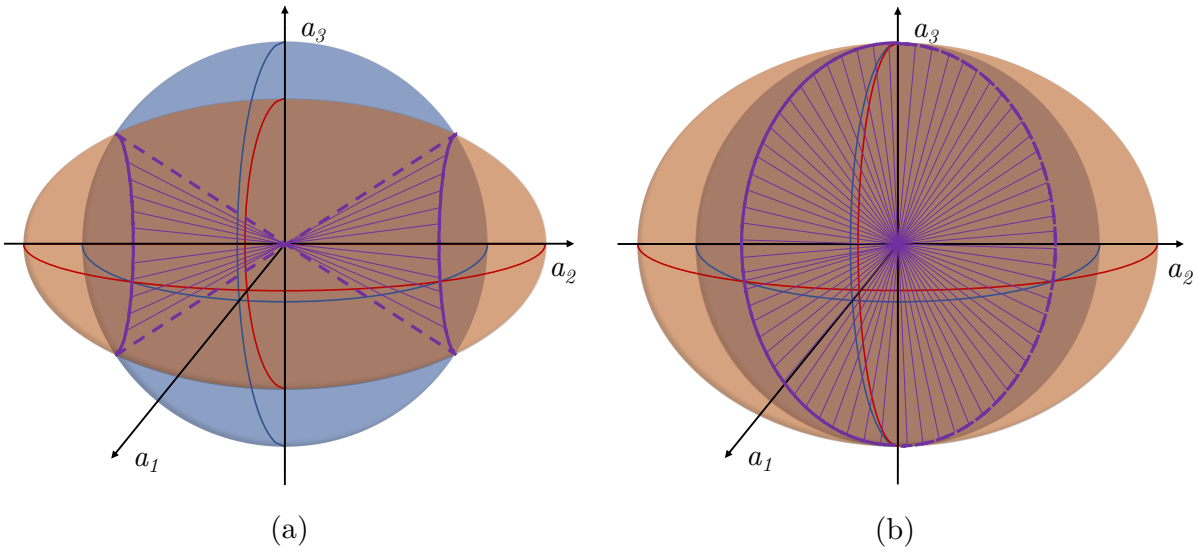

Fig. 3.1 Shape changes following the deformation of a sphere (blue) into an ellipsoid (orange). In (a) two principal strains are negative and one is positive, such that the undistorted lines form a double cone (purple). In (b) one principal strain is zero and the other two have opposite signs, such that the undistorted lines lie in two undistorted planes (purple).

Applying these conditions to the case of double twinning, it is seen that the only case in which they are satisfied is when the component shears are coplanar, i.e. when the two twinning modes have the same plane of shear, such that the normal to this plane is one of the principal axes of the deformation, that corresponding to zero principal strain, as it is neither elongated nor shrunk. The two undistorted planes obtained upon completion of the two shears will then both contain the normal to the plane of shear, and the addition of a rotation about this normal will ensure that one of the undistorted planes is left truly invariant. It should be noted that requiring that the plane of shear is common to the two component twinning modes implies that these modes be compound. This is readily shown in the following way: assuming that both twinning

modes be e.g. type I modes, i.e. that K_{1A}, K_{1B}, $\boldsymbol{\eta}_{2A}$, $\boldsymbol{\eta}_{2B}$ are rational, then the common plane of shear, P, contains two rational directions, and is itself rational; the intersections of K_{1A} and K_{1B} with P are respectively $\boldsymbol{\eta}_{1A}$ and $\boldsymbol{\eta}_{1B}$, which are then also rational, and so are K_{2A} and K_{2B}, such that both component modes are compound. Knowing the plane of shear P, one of the indices of each invariant plane is readily determined, as both must be perpendicular to the plane of shear common to the two twinning modes, and the remaining two indices can be determined by solving the problem in two dimensions.

Therefore, we start with the matrix equation for a simple twinning shear $\mathbf{S}$ of magnitude s, occurring on a plane with unit normal $\mathbf{m}$ in the direction represented by the unit vector $\mathbf{l}$:

$$\mathbf{S} = \mathbf{I} + s\mathbf{l}\mathbf{m}^{\mathrm{T}} \, . \tag{3.19}$$

We then choose the coordinate system where the z-axis is the normal to the plane of shear, while the x- and y-axes are respectively the shear direction $\boldsymbol{\eta}_{1A}$ and the normal to the K_1 plane of the primary twin. Since the plane of shear is common to the two twinning modes, we can omit the third index of each vector, and we write down the shears as two-dimensional matrices:

$$\mathbf{S}_A = \begin{pmatrix} 1 & s_A \\ 0 & 1 \end{pmatrix} \, , \tag{3.20}$$

$$\mathbf{S}_B = \begin{pmatrix} 1 - s_B \sin\alpha\cos\alpha & s_B \cos^2\alpha \\ -s_B \sin^2\alpha & 1 + s_B \sin\alpha\cos\alpha \end{pmatrix} \, . \tag{3.21}$$

Here, s_A and s_B are twinning shears of the primary and secondary twin, respectively, and α is the angle between the primary and secondary K_1 planes. Finding the undistorted planes of the equivalent twinning mode amounts to finding vectors left undistorted by $\mathbf{S}_A\mathbf{S}_B$: such a vector, labelled $\mathbf{p}$, would have its length unchanged by the transformation, such that the resulting vector $\mathbf{q} = \mathbf{S}_B\mathbf{S}_A\mathbf{p}$ would satisfy

$$\mathbf{q}^{\mathrm{T}}\mathbf{q} = \mathbf{p}^{\mathrm{T}}\, \mathbf{S}_A^{\mathrm{T}}\, \mathbf{S}_B^{\mathrm{T}}\, \mathbf{S}_B\mathbf{S}_A\mathbf{p} = \mathbf{p}^{\mathrm{T}}\mathbf{p} \, . \tag{3.22}$$

Although the length of $\mathbf{p}$ is unaltered by the shears, its direction will change; therefore, a rotation $\mathbf{R}_C$ is added to the transformation in order to restore $\mathbf{q}$ to the initial position, such that the total deformation is given by $\mathbf{S}_C = \mathbf{R}_C\mathbf{S}_B\mathbf{S}_A$.

Taking $\mathbf{p} = [\cos\phi, \sin\phi]$ to make an angle ϕ with the x-axis, i.e. with the primary K_1 plane, equation 3.22 can be solved for ϕ, such that two solutions are obtained:

$$\cot\phi = \frac{[s_B(\cos\alpha - s_A\sin\alpha) - D] \pm \sqrt{s_A s_B + s_A s_B D\sin\alpha + D^2}}{s_B \sin\alpha}\,, \tag{3.23}$$

$$D = \frac{s_A - s_B}{s_B\sin\alpha - 2\cos\alpha}\,. \tag{3.24}$$

Since the planes defined by ϕ are left invariant by $\mathbf{S}_C$, which is itself a simple shear, they constitute the K_1 and K_2 planes of the equivalent simple twinning mode corresponding to double twinning. Therefore, the double twinning shear is given as a function of the angle ω between K_1 and K_2 as

$$G = 2\cot\omega = \sqrt{s_A s_B(s_A\sin\alpha - 2\cos\alpha)(s_B\sin\alpha - 2\cos\alpha) + (s_A - s_B)^2}\,. \tag{3.25}$$

Equations 3.24 and 3.25 can then be used to define a double twinning mode, and can be applied to the double twinning mechanisms described in table 3.1. Moreover, an expression for the rotation $\mathbf{R}_C$ needed to make $\mathbf{p}$ truly invariant can be found. This is a rotation about the normal to the common plane of shear, and its magnitude ψ given by the angle through which $\mathbf{p}$ is rotated by $\mathbf{S}_B\mathbf{S}_A$, such that

$$\cos\psi = \mathbf{p}^{\mathrm{T}}\mathbf{q} = \mathbf{p}^{\mathrm{T}}\mathbf{S}_B\mathbf{S}_A\mathbf{p} = 1 - s_A s_B\sin\phi\sin\alpha\cos(\phi-\alpha) + \frac{1}{2}[s_A\sin 2\phi + s_B\sin 2(\phi-\alpha)]. \tag{3.26}$$

The relationship between the parent and doubly twinned crystal is thus fully defined.

The equations derived above can now be used to derive invariant planes for the double twinning mechanisms presented in table 3.1. However, first it should be noted that these present some degeneracies, which are summarised by Crocker in what he calls the Reciprocal Theorem, stated as follows [41]:

> "*If two double twinning mechanisms have first twinning shears which are either the same or reciprocal to each other and second twinning shears which are either the same or reciprocal to each other, then the resulting simple equivalent twinning modes are identical.*"

This is proved by Crocker using equations 3.24 and 3.25; a more rigorous proof will be given in the account of the theories that followed Crocker's. Here the convention is used that a positive twinning shear moves the positive side of the K_1 plane to the right; then a reflection of a shear in any plane changes its direction, and hence the sign of the shear. Therefore, if the $(10\bar{1}1)-(10\bar{1}2)$ simple equivalent twinning mode has component shears s_A and s_B, the $(10\bar{1}1)-(\bar{1}012)$ mode, where the second twinning mode is the reciprocal of the $(10\bar{1}2)$ mode, has component shears s_A and $-s_B$. Moreover, if the angle between $(10\bar{1}1)$ of the parent crystal and $(10\bar{1}2)$ of the primary twin is α, then the angle between $(10\bar{1}1)$ of the parent and $(\bar{1}012)$ of the primary twin is $\alpha-\cot^{-1}(s_A/2)$. Inserting these values in equations 3.24 and 3.25, it can be seen that the $(10\bar{1}1)-(10\bar{1}2)$ and $(10\bar{1}1)-(\bar{1}012)$ simple twinning modes have identical ϕ and G, and therefore occur on the same invariant plane with identical double twinning shears. In the previous section, these twinning mechanisms were labelled types 1 and 2: it is now evident that according to Crocker's theory, these two variants are indistinguishable, if they are to correspond to a simple shear occurring on an invariant plane; the same is valid for the $(10\bar{1}\bar{3})-(10\bar{1}2)$ and $(10\bar{1}\bar{3})-(\bar{1}012)$ double twinning mechanisms.

Secondly, the $(10\bar{1}1)-(10\bar{1}2)$ equivalent simple twinning mode may be compared with that of the $(10\bar{1}\bar{3})-(10\bar{1}2)$ mechanism. For the latter, the component twinning shears are $-s_A$ and s_B, and the angle between $(10\bar{1}\bar{3})$ of the parent and $(10\bar{1}2)$ of the primary twin is $\alpha-\cot^{-1}(s_A/2)$. Substituting these values into equations 3.24 and 3.25, it is seen that a double twinning shear G that is identical to that of the $(10\bar{1}1)-(10\bar{1}2)$ mode is produced, but a different ϕ angle; however, this is now measured with respect to a different primary K_1 plane, which is $\pi-\cot^{-1}(s_A/2)$ from $(10\bar{1}1)$. When this is taken into account, it is found that the $(10\bar{1}1)-(10\bar{1}2)$ and $(10\bar{1}\bar{3})-(10\bar{1}2)$ simple twinning modes have the same invariant plane. Thus, the four mechanisms in the first two columns of 3.1 are all described by the same equivalent simple twinning mode; this will be demonstrated further in the following sections.

3.2.1 $(10\bar{1}1)-(10\bar{1}2)$ double twinning and equivalent modes

As a consequence of the reciprocal theorem, it has been established that the $(10\bar{1}1)-(10\bar{1}2)$, $(10\bar{1}1)-(\bar{1}012)$, $(10\bar{1}\bar{3})-(10\bar{1}2)$ and $(10\bar{1}\bar{3})-(\bar{1}012)$ double twinning mechanisms all belong to the same equivalent simple twinning mode. This twinning mode is described by two invariant

planes, each of which can be seen as the habit plane while the other will be the conjugate plane, i.e. K_1 and K_2. Therefore, the equivalent simple twinning mode is really two modes reciprocal of each other.

This may be verified by studying the $(10\bar{1}1)-(10\bar{1}2)$ and $(10\bar{1}\bar{3})-(10\bar{1}2)$ mechanisms separately at first. Starting with $(10\bar{1}1)-(10\bar{1}2)$, it is seen that the relevant parameters to be used in equations 3.24 and 3.25 can be found in table 2.1; however, the sign of the second twinning shear is reversed, obeying the convention used by Crocker that reflection in any plane changes the sign of a shear, such that, for $\gamma = 1.624$, $s_A = \frac{\sqrt{2}(2\Lambda^2-3)}{4\Lambda} = 0.138$, $s_B = \frac{2-\Lambda^2}{\sqrt{2}\Lambda} = 0.129$ and $\alpha = \tan^{-1}\frac{-3\Lambda}{\sqrt{2}(3+3\Lambda^2)}$. Then, equation 3.24 yields two solutions, $\phi_1 = -8.9^\circ$ and $\phi_2 = 88.5^\circ$, while from equation 3.25 we find that the double twinning shear is $G = 0.258$. If the secondary twinning plane is substituted with its reciprocal, i.e. if we consider $(10\bar{1}1)-(\bar{1}012)$, then $s_A = -\frac{\sqrt{2}(2\Lambda^2-3)}{4\Lambda}$, $s_B = -\frac{2-\Lambda^2}{\sqrt{2}\Lambda}$ and $\alpha = \tan^{-1}\frac{-3\Lambda}{\sqrt{2}(3+3\Lambda^2)} - \cot^{-1}\frac{s_B}{2}$ yield the same ϕ_1, ϕ_2 and G, thus verifying the first part of the reciprocal theorem.

Turning to $(10\bar{1}\bar{3})-(10\bar{1}2)$, the parameters are $s_A = -\frac{\sqrt{2}(2\Lambda^2-3)}{4\Lambda}$, $s_B = \frac{2-\Lambda^2}{\sqrt{2}\Lambda}$ and $\alpha = \tan^{-1}\frac{-3\Lambda}{\sqrt{2}(3+3\Lambda^2)} - \cot^{-1}\frac{s_A}{2}$, producing $\phi_3 = -5.5^\circ$, $\phi_4 = 77.2^\circ$ and $G = 0.258$. ϕ_3 and ϕ_4 are now the angles between the habit planes and $(10\bar{1}\bar{3})$, whereas ϕ_1 and ϕ_2 are measured relative to $(10\bar{1}1)$. Making allowance for this, it is seen that ϕ_1 and ϕ_3 define the same plane C_1, while ϕ_2 and ϕ_4 both define C_2. This corresponds to full verification of the reciprocal theorem. We thus assign the habit plane defined by ϕ_1 to the $(10\bar{1}1)-(10\bar{1}2)$ mechanism, and ϕ_3 to $(10\bar{1}\bar{3})-(10\bar{1}2)$.

The features of the mode describing compression-tension double twinning are summarised in table 3.3. Here, Miller-Bravais indices for the habit planes C_1 and C_2 are calculated, as well as the corresponding shear directions. It is noted that for each choice of habit, the other C plane corresponds to the K_2 plane of the transformation, with the corresponding shear direction becoming $\boldsymbol{\eta}_2$.

In table 3.3, the angle ψ indicating the magnitude of the rotation that is imposed on the doubly twinned crystal to ensure that the habit planes are truly invariant is calculated for each twinning mechanism using equation 3.26. In the bottom line of the table, these angles are then added to those defining the misorientation relation between the basal plane of the parent crystal and that of the double twins, previously calculated and displayed in table 3.1. It is noted that mechanisms with the same habit plane, i.e. those defined as types 1 and 2, present the same misorientation

DT	$(10\bar{1}1)-(10\bar{1}2)$	$(10\bar{1}1)-(\bar{1}012)$	$(10\bar{1}\bar{3})-(10\bar{1}2)$	$(10\bar{1}\bar{3})-(\bar{1}012)$
	type 1	type 2	type 2	type 1
ϕ	$-8.9°$	$-8.9°$	$-5.5°$	$-5.5°$
Label	C_1	C_1	C_2	C_2
Habit plane	$(1.07,0,-1.07,0.70)$ $\approx(30\bar{3}2)$	$(1.07,0,-1.07,0.70)$ $\approx(30\bar{3}2)$	$(0.84,0,-0.84,-3.17)$ $\approx(\bar{1}014)$	$(0.84,0,-0.84,-3.17)$ $\approx(\bar{1}014)$
$\boldsymbol{\eta}_1$	$[0.37,0,-0.37,-1.14]$ $\approx[\bar{1}013]$	$[0.37,0,-0.37,-1.14]$ $\approx[\bar{1}013]$	$[-1.69,0,1.69,-0.90]$ $\approx[\bar{2}02\bar{1}]$	$[-1.69,0,1.69,-0.90]$ $\approx[\bar{2}02\bar{1}]$
ψ	$0.4°$	$-7.0°$	$7.3°$	$-0.1°$
Mis. relation	$-37.1°[1\bar{2}10]$	$-37.1°[1\bar{2}10]$	$-22.4°[1\bar{2}10]$	$-22.4°[1\bar{2}10]$

Table 3.3 Features of the equivalent simple twinning mode describing compression-tension double twinning in magnesium, $\gamma = 1.624$. The angles ϕ and ψ are calculated using equations 3.24 and 3.26, respectively, and they represent rotations about the normal to the $(1\bar{2}10)$ plane of shear.

relations after the rotation $\mathbf{R}_C$ is applied. Therefore, these mechanisms are indistinguishable from each other in Crocker's theory, and only one type of double twin with rational plane of shear exists for each primary K_1 plane chosen. In other words, both for the case of the type 1 and type 2 double twin, a small nucleus of the primary twin retwins internally, and though this happens on different planes, the double twin embryo then expands into the parent on the habit plane C_1 or C_2; in addition, a rotation, which may be accommodated either in the parent or in the double twin, or shared between the two crystals, causes the relative orientation of the matrix and the double twin to be the same for both types. While the misorientation relations for the type 1 mechanisms are effectively unchanged by the added rotation, the type 2 double twins are reoriented by a more sizeable amount: this result implies that only the misorientations of the type 1 mechanisms should be observed experimentally in double twins of a noticeable size. Moreover, table 3.3 shows that ψ is larger for the type 2 mechanisms by an order of magnitude with respect to the type 1 mechanisms; this would then suggest that type 2 double twinning mechanisms for this equivalent twinning mode are less likely to occur, as they require more accommodation.

3.2.2 $(10\bar{1}2)-(10\bar{1}1)$ double twinning and equivalent mechanisms

The case of tension-compression double twinning, i.e. double twinning where $\{10\bar{1}2\}$ is the primary twin and $\{10\bar{1}1\}$ or $\{10\bar{1}\bar{3}\}$ is the secondary twin, such that the order of the twinning events is reversed, may also be studied using Crocker's theory. As was shown in section 3.1, these twinning mechanisms present misorientation relations closely related to those in the compression-tension mode. However the equivalent simple twinning mode for these mechanisms does not generally present the same habit planes as in the previous case. This can be shown using equation 3.24, where we substitute the relevant parameters for $(10\bar{1}2)-(10\bar{1}1)$ double twinning, i.e. $s_A = -\frac{2-\Lambda^2}{\sqrt{2}\Lambda}$, $s_B = -\frac{\sqrt{2}(2\Lambda^2-3)}{4\Lambda}$ and $\alpha = \tan^{-1}\frac{3\Lambda}{\sqrt{2}(3+3\Lambda^2)}$, and obtain as the lower angle $\phi = 9.5°$, defining a habit plane for the $(10\bar{1}2)-(10\bar{1}\bar{3})$ mechanism, as per the reciprocal theorem ; from equation 3.25, we also see that $G = 0.258$ as in the case of compression-tension double twinning. ϕ is here measured with respect to $(10\bar{1}2)$, and though it defines a different habit plane C_3 to that found for $(10\bar{1}1)-(10\bar{1}2)$ double twinning, C_1, it nonetheless bears a connection to it. Indeed, if C_1 is referred to the coordinate system of the $(10\bar{1}1)-(10\bar{1}2)$ double twin instead of that of the parent crystal, C_3 is obtained. This is because the habit C_1 is not a mirror plane of the bicrystal formed by the matrix and double twin, and thus can be referred to using two sets of indices depending on which basis is chosen.

Similarly, for $(\bar{1}012)-(10\bar{1}1)$ and $(\bar{1}012)-(10\bar{1}\bar{3})$ double twinning, we find $\phi = 5.8°$, defining a habit C_4. It can be verified that C_4 is none other than C_2 referred to the coordinate system of the $(10\bar{1}\bar{3})-(10\bar{1}2)$ double twin. Crocker then concludes that compression-tension and tension-compression double twinning mechanisms all belong to the same equivalent simple twinning mode; it should however be noted that the four C planes obtained as a result all have different indices when referred to the matrix, such that each is able to act as the habit plane of a double twinning mechanism.

The angles ϕ, as well as the indices of the habit planes and the corresponding shear directions are summarised in table 3.4, along with the angles ψ rotated by the additional rotation $\mathbf{R}_C$ necessary to restore the invariant plane to its initial position and the corresponding modified misorientation relations between parent and doubly twinned crystals. As was the case for compression-tension double twinning, the so-called type 2 mechanisms require significantly larger accommodation angles, while the misorientation relations of the type 1 mechanisms

DT	$(10\bar{1}2)-(10\bar{1}1)$	$(\bar{1}012)-(10\bar{1}1)$	$(10\bar{1}2)-(10\bar{1}\bar{3})$	$(\bar{1}012)-(10\bar{1}\bar{3})$
	type 1	type 2	type 2	type 1
ϕ	9.5°	5.8°	9.5°	5.8°
Label	C_3	C_4	C_3	C_4
Habit plane	$(0.81,0,-0.81,2.28)$ $\approx(50\bar{5}14)$	$(1.10,0,-1.10,-1.80)$ $\approx(30\bar{3}\bar{4})$	$(0.81,0,-0.81,2.28)$ $\approx(50\bar{5}14)$	$(1.10,0,-1.10,-1.80)$ $\approx(30\bar{3}\bar{4})$
$\boldsymbol{\eta}_1$	$[1.22,0,-1.22,-0.86]$ $\approx[30\bar{3}\bar{2}]$	$[-0.96,0,0.96,-1.18]$ $\approx[\bar{5}05\bar{6}]$	$[1.22,0,-1.22,-0.86]$ $\approx[30\bar{3}\bar{2}]$	$[-0.96,0,0.96,-1.18]$ $\approx[\bar{5}05\bar{6}]$
ψ	$-0.4°$	$-7.7°$	7.4°	0.1°
Mis. relation	$37.1°[1\bar{2}10]$	$22.4°[1\bar{2}10]$	$37.1°[1\bar{2}10]$	$22.4°[1\bar{2}10]$

Table 3.4 Features of the equivalent simple twinning mode describing tension-compression double twinning in magnesium, $\gamma = 1.624$. The angles ϕ and ψ are calculated using equations 3.24 and 3.26, respectively, and they represent rotations about the normal to the $(1\bar{2}10)$ plane of shear.

remain virtually unchanged. It can be seen that these misorientation relations mirror the ones in table 3.3, with one notable difference: the $(\bar{1}012)-(10\bar{1}1)$ mechanism shares its habit plane and misorientation relation with $(\bar{1}012)-(10\bar{1}\bar{3})$, as they have the same primary twin; on the other hand, $(10\bar{1}1)-(\bar{1}012)$ has the same habit and misorientation as $(10\bar{1}1)-(10\bar{1}2)$. It follows that $(\bar{1}012)-(10\bar{1}1)$ and $(10\bar{1}1)-(\bar{1}012)$ no longer have the same misorientation relation, and the same is true for $(10\bar{1}2)-(10\bar{1}\bar{3})$ and $(10\bar{1}\bar{3})-(10\bar{1}2)$. This is a consequence of the reciprocal theorem, because the mechanisms that share a habit plane are the ones with the same primary twinning mode and secondary twinning modes reciprocal of each other. Nonetheless, it is confirmed that while tension-compression double twins present habit planes distinct from those of compression-tension double twins, their misorientation relations differ only in the direction of rotation. Therefore, Crocker's theory of double twinning predicts that only two misorientation relations may be measured in double twins with a common, rational plane of shear: 37.1° and $22.4°\langle 1\bar{2}10\rangle$.

3.3 Bevis & Crocker's theory of non-classical twinning

Crocker's theory of double twinning focused on identifying an invariant habit plane on which the double twinning shear would occur, so that a double twin nucleus would grow on this plane. Bevis and Crocker [76, 77] generalised this concept to include all non-classical twinning modes, i.e. modes characterised by a simple shear that restores the lattice in a different orientation, without requiring that one of the standard misorientation relations of classical twinning be produced. Rather than focusing on the invariant plane of the transformation, Bevis and Crocker instead show that it is possible to characterise a non-classical twinning mode solely by knowing its correspondence matrix. In what follows, we recast the derivation, given by the original authors in tensor notation, in matrix form. This is also done by Christian and Mahajan [64], but care should be taken with a few mistakes that have persisted in the latest edition of Christian's book [132], and which are here rectified.

We start with a lattice defined by a direct basis $\mathbf{a}_i$, $i = 1,2,3$; then, as detailed in section 1.2, the reciprocal basis $\mathbf{a}_i^*$ is related to the direct basis by the metric $G_{ij} = \mathbf{a}_i \cdot \mathbf{a}_j$, $G_{ij}^{-1} = \mathbf{a}_i^* \cdot \mathbf{a}_j^*$. A simple shear of magnitude s on the plane of unit normal $\mathbf{m} = m_i^* \mathbf{a}_i^*$ in the direction of the unit vector $\mathbf{l} = l_i \mathbf{a}_i$ is given by equation 3.19; then $\mathbf{m}^{\mathrm{T}} \mathbf{G}^{-1} \mathbf{m} = 1$ and $\mathbf{l}^{\mathrm{T}} \mathbf{G} \mathbf{l} = 1$. In section 1.3 we saw that by applying this shear to a lattice vector $\mathbf{x}$, we obtain the vector $\mathbf{y}$:

$$\mathbf{y} = \mathbf{S}\mathbf{x} \, . \tag{3.27}$$

But according to the definition of simple shear, $\mathbf{S}$ must restore the original lattice in a new orientation, such that

$$\mathbf{y} = \mathbf{L}\mathbf{z} \, , \tag{3.28}$$

where $\mathbf{L}$ is a rotation and the lattice vector $\mathbf{z}$ is related to the original lattice vector $\mathbf{x}$ by

$$\mathbf{z} = \mathbf{C}\mathbf{x} \, . \tag{3.29}$$

The matrix **C** is the correspondence matrix that was derived in the same way in chapter 1, and it follows from equations 3.27, 3.28 and 3.29 that

$$\mathbf{S} = \mathbf{LC} \, . \tag{3.30}$$

It can be shown that the matrix **C** is unimodular, i.e. that $|\mathbf{C}| = \pm 1$. The determinant of **S** is given by $|\mathbf{S}| = \lambda_1\lambda_2\lambda_3$, i.e. by the product of the ratios of the lengths of the principal axes after and before the deformation, see section 3.2. This is then the ratio of the volume after and before the transformation, and imposing the condition that parent and twin have the same volume per atom, the determinant of **S** is unity [69, 64]. **L** is orthogonal and thus unimodular, hence the determinant of **C** is also unity.

Multiplying both sides of equation 3.30 from the left by $\mathbf{S}^{\mathrm{T}}\mathbf{G}$ and using the identity $\mathbf{L}^{\mathrm{T}}\mathbf{GL} = \mathbf{G}$ [133], we find

$$\begin{aligned} \mathbf{S}^{\mathrm{T}}\mathbf{GS} &= \mathbf{S}^{\mathrm{T}}\mathbf{GLC} \\ \mathbf{S}^{\mathrm{T}}\mathbf{GS} &= \mathbf{C}^{\mathrm{T}}\mathbf{L}^{\mathrm{T}}\mathbf{GLC} \\ \mathbf{S}^{\mathrm{T}}\mathbf{GS} &= \mathbf{C}^{\mathrm{T}}\mathbf{GC} \, . \end{aligned} \tag{3.31}$$

We now seek to restrict the shears **S** to those that satisfy equation 3.31. Substituting 3.19 into 3.31, we find

$$s^2\mathbf{m}\mathbf{m}^{\mathrm{T}} + s(\mathbf{G}\mathbf{l}\mathbf{m}^{\mathrm{T}} + \mathbf{m}\mathbf{l}^{\mathrm{T}}\mathbf{G} + \mathbf{I}) + \mathbf{G} - \mathbf{C}^{\mathrm{T}}\mathbf{GC} = \mathbf{X} = 0 \, , \tag{3.32}$$

Where the matrix **X** has been defined for later use. Multiplying by $\mathbf{G}^{-1}$ from the right and taking the trace, and remembering that the trace of a matrix product is invariant under cyclic permutations, we find a condition for the magnitude of the shear s:

$$s^2 = \mathrm{Tr}\left(\mathbf{C}^{\mathrm{T}}\mathbf{GC}\mathbf{G}^{-1}\right) - 3 \, , \tag{3.33}$$

Since $\mathrm{Tr}\left(\mathbf{m}\mathbf{l}^{\mathrm{T}}\right) = \mathrm{Tr}\left(\mathbf{l}^{\mathrm{T}}\mathbf{m}\right) = 0$, because **m** and **l** are perpendicular, and consequently $\mathrm{Tr}\left(\mathbf{l}\mathbf{m}^{\mathrm{T}}\right) = 0$, too. Using equation 3.32, the normal to the twinning plane **m** and the shear direction **l** can

also be specified. We form the expression

$$2m^*_\alpha m^*_\beta X_{\alpha\beta} - m^{*2}_\beta X_{\alpha\alpha} - m^{*2}_\alpha X_{\beta\beta} \ , \tag{3.34}$$

where the summation convention is suspended for Greek indices, and equate it to zero; upon defining $\mathbf{Y} = \mathbf{G} - \mathbf{C}^{\mathrm{T}}\mathbf{G}\mathbf{C}$, we obtain three quadratic equations for the indices of $\mathbf{m}$:

$$Y_{\alpha\alpha} m^{*2}_\beta - 2Y_{\alpha\beta} m^*_\alpha m^*_\beta + Y_{\beta\beta} m^{*2}_\alpha = 0 \ . \tag{3.35}$$

Then equations 3.35 can be solved for the ratios m^*_α / m^*_β. In general, two solutions will be found for the shear plane: these represent the K_1 and K_2 planes of the transformation.

Once $\mathbf{m}$ and s have been determined using equations 3.35 and 3.33, the indices of $\mathbf{l}$ may be found by solving $X_{\alpha\alpha} = 0$. On the other hand equations similar to 3.35 can be found for $\mathbf{l}$. We start by inverting equation 3.31:

$$\mathbf{S}^{-1}\mathbf{G}^{-1}\mathbf{S}^{-\mathrm{T}} = \mathbf{C}^{-1}\mathbf{G}^{-1}\mathbf{C}^{-\mathrm{T}} \ , \tag{3.36}$$

where we have introduced the notation $\mathbf{C}^{-\mathrm{T}} \equiv (\mathbf{C}^{-1})^{\mathrm{T}}$ and $\mathbf{S}^{-\mathrm{T}} \equiv (\mathbf{S}^{-1})^{\mathrm{T}}$. Using $\mathbf{S}^{-1} = \mathbf{I} - s\mathbf{l}\mathbf{m}^{\mathrm{T}}$, we find

$$s^2\mathbf{l}\mathbf{l}^{\mathrm{T}} - s(\mathbf{G}^{-1}\mathbf{m}\mathbf{l}^{\mathrm{T}} + \mathbf{l}\mathbf{m}^{\mathrm{T}}\mathbf{G}^{-1}) + \mathbf{G}^{-1} - \mathbf{C}^{-1}\mathbf{G}^{-1}\mathbf{C}^{-\mathrm{T}} = \mathbf{W} = 0 \ , \tag{3.37}$$

where $\mathbf{W}$ has been defined. Multiplying from the right by $\mathbf{G}^{-1}$ and taking the trace, another expression is obtained for s^2:

$$s^2 = \mathrm{Tr}\big(\mathbf{C}^{-1}\mathbf{G}^{-1}\mathbf{C}^{-\mathrm{T}}\mathbf{G}\big) - 3 \ . \tag{3.38}$$

Comparing equations 3.33 and 3.38, we find that the correspondence matrix has to obey the condition

$$\mathrm{Tr}\big(\mathbf{C}^{\mathrm{T}}\mathbf{G}\mathbf{C}\mathbf{G}^{-1}\big) = \mathrm{Tr}\big(\mathbf{C}^{-1}\mathbf{G}^{-1}\mathbf{C}^{-\mathrm{T}}\mathbf{G}\big) \ . \tag{3.39}$$

This condition is reported incorrectly in Christian and Mahajan [64] and Christian's *Theory of transformations in metals and alloys*, third edition [132]: in both cases, the right hand side of equation 3.39 reads $\mathrm{Tr}\big(\mathbf{C}^{-\mathrm{T}}\mathbf{G}^{-1}\mathbf{C}^{-1}\mathbf{G}\big)$, which is incorrect as the trace of a matrix product is

only invariant under cyclic permutations. By forming an expression for $\mathbf{W}$ and $\mathbf{l}$ similar to 3.34 and defining $\mathbf{Z} = \mathbf{G}^{-1} - \mathbf{C}^{-1}\mathbf{G}^{-1}\mathbf{C}^{-\mathrm{T}}$, we find three simultaneous equations for the indices of $\mathbf{l}$:

$$Z_{\alpha\alpha}l_\beta^2 - 2Z_{\alpha\beta}l_\alpha l_\beta + Z_{\beta\beta}l_\alpha^2 = 0\ , \tag{3.40}$$

similarly to equations 3.35. It should be noted that as a consequence of the above mentioned error appearing in Christian's book, the matrix $\mathbf{Z}$ is also defined incorrectly in that instance.

It has thus been proven that knowledge of the correspondence matrix is sufficient to fully specify a twinning mode. One may then ask if anything may be extracted from the correspondence's inverse, transpose and transposed inverse, i.e. $\mathbf{C}^{-1}$, $\mathbf{C}^{\mathrm{T}}$ and $\mathbf{C}^{-\mathrm{T}}$: after all, they are also unimodular matrices, and so far we have not imposed any further restrictions on the form of the correspondence matrix. Indeed, they all represent independent twinning modes; however, they are closely related.

To see this, initially for $\mathbf{C}$ and $\mathbf{C}^{-\mathrm{T}}$, we compare equations 3.32 and 3.37: these have the same form, but while $\mathbf{X}(\mathbf{m},\mathbf{l},s,\mathbf{C})$ is a function of a the direct lattice parameters, $\mathbf{W}(\mathbf{l},\mathbf{m},-s,\mathbf{C}^{-\mathrm{T}})$ is a function of the reciprocal lattice parameters. Therefore, $\mathbf{C}^{-\mathrm{T}}$ defines a twinning shear in the reciprocal lattice, and its K_1 plane and $\boldsymbol{\eta}_1$ direction are the respectively the $\boldsymbol{\eta}_1$ direction and K_1 plane of the twinning mode defined by $\mathbf{C}$. However, the mode described by $\mathbf{C}^{-\mathrm{T}}$ may exist independently, as it is valid for all reciprocal lattice parameters.

Another relation exists between the twinning modes defined by $\mathbf{C}$ and $\mathbf{C}^{-1}$. Inverting equation 3.30 and multiplying it from the left by $\mathbf{L}^{-1}$ and from the right by $\mathbf{L}$, we find

$$\mathbf{L}^{-1}\mathbf{C}^{-1} = \mathbf{L}^{-1}\mathbf{S}^{-1}\mathbf{L}\ . \tag{3.41}$$

On the right hand side is a similarity transformation of $\mathbf{S}^{-1}$, such that we define $\bar{\mathbf{S}} = \mathbf{L}^{-1}\mathbf{S}^{-1}\mathbf{L}$; thus $\mathbf{S}^{-1}$ is expressed in the coordinate system defined by $\mathbf{L}$, i.e. that of the lattice that has undergone the shear $\mathbf{S}$. Then, $\bar{\mathbf{S}}$ simply restores the lattice sheared by $\mathbf{S}$ to its original orientation, and equation 3.41 is now rewritten as

$$\bar{\mathbf{S}} = \mathbf{L}^{-1}\mathbf{C}^{-1}\ , \tag{3.42}$$

such that the correspondence matrix $\mathbf{C}^{-1}$ defines $\bar{\mathbf{S}}$. Finally, as $\mathbf{C}^{-1}$ defines an independent shear mode, its transposed inverse, i.e. $\mathbf{C}^{\mathrm{T}}$, describes a twinning mode in reciprocal space, similarly to the relation between $\mathbf{C}$ and $\mathbf{C}^{-\mathrm{T}}$.

A non-classical twinning mode was defined by Bevis and Crocker as any simple shear that will restore the lattice in a different orientation. However, this definition includes classical twinning modes, for which the orientation relations must obey at least one of the conditions set out in chapter 1; therefore it is possible to derive expressions for the correspondence matrices of type I and II twinning. We label unit vectors in the directions normal to K_1 and K_2 respectively as $\mathbf{m} = m_i^* \mathbf{a}_i^*$ and $\mathbf{w} = w_i^* \mathbf{a}_i^*$, and unit vectors in the directions of $\boldsymbol{\eta}_1$ and $\boldsymbol{\eta}_2$ respectively as $\mathbf{l} = l_i \mathbf{a}_i$ and $\mathbf{g} = g_i \mathbf{a}_i$. As we are dealing with lattices, relations 1 and 4 produce the same orientation, and so do relations 2 and 3, that is a reflection in K_1 is identical to a rotation of 180° about its normal, and a rotation of 180° about $\boldsymbol{\eta}_1$ is identical to a reflection in the plane normal to it. Thus we can use as descriptions of $\mathbf{L}$ in equation 3.30 rotations about the normal to K_1 and about $\boldsymbol{\eta}_1$ for type I and II twinning, respectively, such that we obtain

$$\mathbf{L} = -\mathbf{I} + 2\mathbf{G}^{-1}\mathbf{m}\mathbf{m}^{\mathrm{T}} \quad \text{(type I)}, \tag{3.43}$$

$$\mathbf{L} = -\mathbf{I} + 2\mathbf{l}\mathbf{l}^{\mathrm{T}}\mathbf{G} \qquad \text{(type II)}. \tag{3.44}$$

Moreover, we are reminded that the rational crystallographic elements are K_1 and $\boldsymbol{\eta}_2$ for type I twinning, and K_2 and $\boldsymbol{\eta}_1$ for type II twinning; hence, we rewrite equation 3.19 in terms of the rational elements for each case (though it should be noted that these equations are valid for all twinning types):

$$\mathbf{S} = \mathbf{I} + 2\mathbf{G}^{-1}\mathbf{m}\mathbf{m}^{\mathrm{T}} - 2\frac{\mathbf{g}\mathbf{m}^{\mathrm{T}}}{\mathbf{m}^{\mathrm{T}}\mathbf{g}}\,, \tag{3.45}$$

$$\mathbf{S} = \mathbf{I} - 2\mathbf{l}\mathbf{l}^{\mathrm{T}}\mathbf{G} + 2\frac{\mathbf{l}\mathbf{w}^{\mathrm{T}}}{\mathbf{w}^{\mathrm{T}}\mathbf{l}}\,. \tag{3.46}$$

Then, using equation 3.30, we obtain expressions for the correspondence matrices of classical twins:

$$\mathbf{C} = -\mathbf{I} + 2\frac{\mathbf{g}\mathbf{m}^{\mathrm{T}}}{\mathbf{m}^{\mathrm{T}}\mathbf{g}} \quad \text{(type I)}, \tag{3.47}$$

$$\mathbf{C} = -\mathbf{I} + 2\frac{\mathbf{l}\mathbf{w}^{\mathrm{T}}}{\mathbf{w}^{\mathrm{T}}\mathbf{l}} \quad \text{(type II)}. \tag{3.48}$$

For compound twins, both of the equations above are valid, as are all orientation relations 1 to 4. The correspondence matrices defined by equations 3.47 and 3.48 are involutory, i.e. $\mathbf{C} = \mathbf{C}^{-1}$; as such, they satisfy condition 3.39 independently of $\mathbf{G}$, and thus define classical twinning modes in all lattices. Moreover, since $\mathbf{L} = \mathbf{L}^{-1}$ for classical modes, the fact that $\mathbf{C}$ is also involutory implies that in equation 3.42 $\bar{\mathbf{S}} = \mathbf{L}\mathbf{C} = \mathbf{S}$, such that when referred to the sheared lattice, $\mathbf{S}^{-1}$ has the same components as $\mathbf{S}$: this is a consequence of the parent and sheared lattices being mirror images of each other. Finally, $\mathrm{Tr}\,\mathbf{C} = -1$ for both type I and II twinning: this property provides a discriminant for the identification of correspondence matrices giving rise to classical twinning modes.

Having established how knowledge of the correspondence matrix is sufficient to fully define a non-classical twinning mode, we turn to the case of double twinning. In doing so, we follow Acton et al. [130], who generalised Bevis and Crocker's theory to transformation strains, i.e. lattice, lattice-invariant and shape strains, of which twinning is a special case. While we will not delve into the general theory, it is worth mentioning that this covers not only double twinning shears, but also double invariant-plane strains and double shear martensitic transformations.

In section 3.2 it was shown that for two twinning shears to produce an equivalent twinning shear, a rotation must be added to the total transformation, except in particularly degenerate cases. Hence, a double twinning shear can be written as

$$\mathbf{S}_C = \mathbf{R}_C\mathbf{S}_B\mathbf{S}_A \ , \tag{3.49}$$

Where $\mathbf{S}_A$ and $\mathbf{S}_B$ are the component shears. For $\mathbf{S}_A$ we can then write, following equation 3.30,

$$\mathbf{S}_A = \mathbf{L}_A\mathbf{C}_A. \tag{3.50}$$

On the other hand, $\mathbf{S}_B$ is referred to the coordinate system of the parent crystal, rather than that of the primary twin where it actually occurs, such that its form is more complicated. Then, if we label the basis of the primary twin P, we see that $\mathbf{S}_B$ and ${}^P\mathbf{S}_B$, i.e. the form it takes when referred to the basis B, are related by the similarity transformation

$$\mathbf{S}_B = \mathbf{L}_A \, {}^P\mathbf{S}_B \mathbf{L}_A^{-1} \, , \tag{3.51}$$

and now we can write equation 3.30 for ${}^P\mathbf{S}_B$:

$${}^P\mathbf{S}_B = \, {}^P\mathbf{L}_B \, {}^P\mathbf{C}_B \, . \tag{3.52}$$

Then, equation 3.49 becomes

$$\mathbf{S}_C = \, \mathbf{L}_C \mathbf{C}_C \, , \tag{3.53}$$

$$\mathbf{L}_C = \mathbf{R}_C \mathbf{L}_A \mathbf{L}_B \, , \tag{3.54}$$

$$\mathbf{C}_C = \, {}^P\mathbf{C}_B \mathbf{C}_A \, . \tag{3.55}$$

Equation 3.53 is now in the same form as 3.30, and thus $\mathbf{C}_C$ characterises the equivalent simple twinning shear arising from the combination of two twinning modes: all properties of the double twinning mode can then be derived using this correspondence matrix, which in turn is specified by the correspondence matrices of the component twinning modes. $\mathbf{C}_C$ will also retain all the properties of the correspondence matrices defined by Bevis and Crocker; thus it will have the form of the correspondence matrices that we shall now derive.

This formulation also provides the explicit proof of the reciprocal theorem promised in the previous section, as twinning shears reciprocal to one another have the same correspondence matrix: this can be seen from equations 3.35 and 3.40, which give two solutions each for $\mathbf{m}$ and $\mathbf{l}$, i.e. the undistorted planes K_1 and K_2 and their intersections with the plane of shear $\boldsymbol{\eta}_1$ and $\boldsymbol{\eta}_2$, respectively. Then the correspondence matrix that characterises the double twinning shear is left unchanged if either of the component modes used is exchanged for its reciprocal.

Finally, it is worth noting that misorientation relations derived using this method will naturally include the additional rotation $\mathbf{R}_C$ necessary to restore the habit plane to its initial position and thus make it truly invariant.

We now turn to the form of the correspondence matrix itself, and how it might be obtained. If the correspondence can be used to determine the twinning elements, then by analysing all the correspondence matrices that are able to describe a valid relationship between lattice vectors of the parent and shear crystals we may predict all possible twinning modes that are ascribable to a simple shear. There is, of course, an infinite number of matrices that may satisfy equation 3.29, such that a discriminating criterion is needed: in what follows, this will be the magnitude of the shear.

The pillar of the following analysis is the unimodularity of the correspondence matrix. For any given unimodular matrix, further unimodular matrices may be obtained by changing the positions and signs of the rows and columns of the matrix, such that 576 matrices are obtained when degenerate cases and matrices with negative determinant are eliminated. Depending on the symmetry of the lattice, the total number of matrices may be lowered further. For example, when the hexagonal primitive cell is used, it can be seen that since the columns of $\mathbf{C}$ can be regarded as the vectors defining the cell in the twinned lattice in which the initial cell is deformed by the shear, changing the positions of the first two rows and the first two columns or changing the sign of the third row or third column does not lead to new cells, such that each correspondence matrix has 36 crystallographically distinct variants. For the cubic system, it is seen that by symmetry changing the position or sign of any row or column does not produce any new cells, such that there are no further variants of the correspondence matrix.

If the cubic lattice is used, the metric $\mathbf{G}$ is the identity matrix, and equations 3.33 and 3.38 reduce to

$$s^2 = \mathrm{Tr}\left(\mathbf{C}^{\mathrm{T}}\mathbf{C}\right) - 3 \,, \tag{3.56}$$

$$s^2 = \mathrm{Tr}\left(\mathbf{C}^{-1}\mathbf{C}^{-\mathrm{T}}\right) - 3 \,, \tag{3.57}$$

while condition 3.39 becomes

$$\mathrm{Tr}\left(\mathbf{C}^{\mathrm{T}}\mathbf{C}\right) = \mathrm{Tr}\left(\mathbf{C}^{-1}\mathbf{C}^{-\mathrm{T}}\right) \,. \tag{3.58}$$

Though the lattice we are truly interested in is the hexagonal one, we follow Bevis and Crocker in deriving a master table of correspondence matrices for the cubic lattice, and then apply to these the more stringent condition 3.39 for the hexagonal cell. In particular, Bevis and Crocker restrict the correspondence matrices for the cubic system to those that produce shears below a maximum value, as the magnitude of the shear is considered one of the main criteria for the feasibility of a twinning mode. Calling this maximum shear magnitude $s_{\max}$, we rewrite equation 3.56 as an inequality:

$$\mathrm{Tr}\left(\mathbf{C}^{\mathrm{T}}\mathbf{C}\right) \leq s_{\max}^2 + 3 \; . \tag{3.59}$$

We then search for sets of nine integers that satisfy equation 3.59; when possible, these integers are then rearranged to form unimodular matrices, as detailed in Bevis and Crocker's article. The further restriction given by 3.58 is then applied. If instead we allow some of the elements of the correspondence matrix to be fractions, we rewrite equation 3.59 as

$$\mathrm{Tr}\left(\mathbf{W}^{\mathrm{T}}\mathbf{W}\right) \leq m^2(s_{\max}^2 + 3) \; , \tag{3.60}$$

where m is the largest denominator of the elements of $\mathbf{C}$, such that

$$\mathbf{W} = m\mathbf{C} \; . \tag{3.61}$$

The unimodular matrices are then found as in the case of the elements of the correspondence being all integers.

The other criterion which determines the feasibility of twinning modes in Bevis and Crocker's and other classical theories is the complexity of the lattice shuffles involved. As outlined in the previous chapter, not all lattice sites are sheared directly to the twin positions, and must shuffle in addition to being displaced by the shear. The integer m provides a measure of the complexity of the shuffles involved in each twinning mode: for primitive cells, the number of lattice sites that are moved directly to twin positions by the shear is given by $1/m$, with the rest needing additional shuffles. Therefore, the higher m is, the more complex are the lattice shuffles involved, implying that the twinning mode is less likely to occur. It can be noted that m is related to the number q defined in the previous chapter: for even m, $m = q/2$, and for odd m, $m = q$. On the other hand, the number of lattice sites sheared into position may generally

be different for centred lattices, and it will have to be determined by considering the smallest possible superlattice that is common between the parent and twinned lattices. Moreover, m only provides a measure of the lattice points to be sheared into place; when an atomic basis is added to the lattice, additional atomic shuffles may be necessary to restore crystal in the twin orientation, as previously discussed.

The shear magnitudes corresponding to each **C** for the cubic lattice are found using equation 3.56. The correspondence matrices are listed by Bevis and Crocker for $m = 1, 2, 4$ and $s^2_{\max} = 9, 3.5, 2.25$ respectively, and are labelled using integers $m.n$, where n indicates the position of the matrix in the table. For each of the matrices in Bevis and Crocker's table 2 [76], 36 variants arise for the hexagonal lattice, though only those satisfying 3.39 will be considered.

3.3.1 Application to the hexagonal lattice and double twinning

In the following section we apply the theory derived above after Bevis and Crocker to the hexagonal lattice, and in particular to the case of double twinning. The metric for the hexagonal system was given by equation 1.18 in chapter 1, and we report it here, dropping the prefix $^{\text{hex}}$:

$$\mathbf{G} = \begin{pmatrix} 1 & -\frac{1}{2} & 0 \\ -\frac{1}{2} & 1 & 0 \\ 0 & 0 & \gamma^2 \end{pmatrix} a^2. \tag{3.62}$$

Directions and planes derived using this metric are referred to the hexagonal basis, depicted in figure 1.2 on the left. Care should then be taken when working with covariant and contravariant vectors, i.e. vectors expressed in real and reciprocal space, as was explained in chapter 1. While the matrix notation chosen for this section is more compact, it is not as unambiguous as the tensor notation used in the original work by Bevis and Crocker, where upper and lower indices help distinguish between real and reciprocal space components. Therefore, the reader is reminded that the components m^*_i of the vector normal **m** are referred to reciprocal space and are thus the indices of the plane perpendicular to **m**, whilst the real space components m_i are obtained as $m_i = (G^{-1})_{ij} m^*_j$. Similarly, the components l_i of **l** are referred to real space, with the reciprocal space components being given as $l^*_i = G_{ij} l_j$.

The viable twinning modes for the hexagonal lattice are then derived as follows.

1. The 36 variants of the correspondence matrices that are distinct for the hexagonal system are found for each matrix **C** listed by Bevis and Crocker [76] in their table 2, as well as for $\mathbf{C}^{-1}$, $\mathbf{C}^{\mathrm{T}}$ and $\mathbf{C}^{-\mathrm{T}}$.

2. The matrices thus obtained are substituted into equation 3.39 along with **G** for the hexagonal system; matrices that do not satisfy this equation are discarded.

3. Solutions for **m** and **l** are found using equations 3.35 and 3.28 respectively, with the method devised by Paxton [134]. Pairs of solutions that satisfy $\mathbf{m}^{\mathrm{T}}\mathbf{l} = 0$ are retained, as **l**, which is parallel to $\boldsymbol{\eta}_1$, must lie in the plane with normal **m**, i.e. K_1.

4. The corresponding K_2 plane and $\boldsymbol{\eta}_2$ direction are found for each K_1-$\boldsymbol{\eta}_1$ pair. This is done by first obtaining the contravariant normal to the plane of shear p_i as the cross product of **m** and **l**, both referred to the reciprocal lattice; in component form, this is written as

$$p_i = \varepsilon^*_{ijk} l^*_j m^*_k = \varepsilon^*_{ijk} l_r G_{rj} m^*_k, \tag{3.63}$$

where ε^*_{ijk} is the Levi-Civita tensor referred to the reciprocal basis. In a non-orthonormal 3D coordinate system, this is given by

$$\varepsilon_{ijk} = \begin{cases} 0, & \text{if } i = j \text{ or } j = k \text{ or } i = k, \\ \sqrt{|G_{ij}|}, & \text{if } (ijk) \text{ is a cyclic permutation of (123)}, \\ -\sqrt{|G_{ij}|}, & \text{if } (ijk) \text{ is an anticyclic permutation of (123)}, \end{cases} \tag{3.64}$$

where $|G_{ij}|$ is the determinant of **G**; the same is valid for ε^*_{ijk}, provided that $|G_{ij}|$ is substituted with $|(G^{-1})_{ij}|$ [75]. The Miller indices of the plane of shear are then given by $p^*_i = G_{ij} p_j$. A rotation of the vector normal to K_1, referred to real space, by $\pi/2 - \cot s/2$ about **p** produces a vector $\mathbf{g} = g_i \mathbf{c_i}$ parallel to the conjugate shear direction $\boldsymbol{\eta}_2$. The normal **w** to the conjugate twinning plane K_2 is finally given by the cross product of **p** and **g**, both referred to the direct lattice; similarly to equation 3.63,

$$w^*_i = \varepsilon_{ijk} g_j p_k. \tag{3.65}$$

5. The solutions obtained for w_i^* and g_i are substituted into equations 3.35 and 3.28 respectively, to check that a reciprocal mode of shear on the K_2 plane in the $\boldsymbol{\eta}_2$ direction exists with the same magnitude of shear s; if this is not the case, the relative correspondence matrix $\mathbf{C}$ is discarded as one not producing a conventional twinning mode, i.e. we require that the non-classical twinning modes obey the theory of reciprocal twinning, which, albeit being proven only for classical twinning orientation relations, is generally assumed to hold for any twinning mode [135, 136].

Application of the above procedure to the hexagonal lattice should first of all produce the classical twinning modes, which for magnesium, $\gamma = 1.624$, are the component modes of double twinning, i.e. $\{10\bar{1}1\}$ and $\{10\bar{1}2\}$ twinning. These modes are described respectively by variants of the matrices 4.20 and 2.19 in table 2 of Bevis and Crocker, i.e.

$$\mathbf{C}_{4.20} = \frac{1}{4}\begin{pmatrix} 2 & 6 & 3 \\ 2 & \bar{2} & 1 \\ 0 & 0 & \bar{4} \end{pmatrix}, \tag{3.66}$$

$$\mathbf{C}_{2.19} = \frac{1}{2}\begin{pmatrix} 0 & 1 & 0 \\ 4 & 0 & 0 \\ 2 & 1 & \bar{2} \end{pmatrix}. \tag{3.67}$$

Both matrices are involutory, as expected from the analysis above. These correspondences predict correctly all the twinnning elements $K_1K_2\boldsymbol{\eta}_1\boldsymbol{\eta}_2;s$; these are obtained as planes and directions expressed in the three-dimensional hexagonal basis, and when converted to the four-dimensional Miller-Bravais system presented in chapter 1 they are given by:

$$\mathbf{C}_{4.20}^{\mathrm{T}}: \quad \{10\bar{1}1\} \quad \{10\bar{1}\bar{3}\} \quad \langle 10\bar{1}\bar{2}\rangle \quad \langle 30\bar{3}2\rangle\ ; \quad \frac{\sqrt{2}(2\Lambda^2-3)}{4\Lambda}, \tag{3.68}$$

$$\mathbf{C}_{2.19}: \quad \{10\bar{1}2\} \quad \{10\bar{1}\bar{2}\} \quad \langle 10\bar{1}\bar{1}\rangle \quad \langle 10\bar{1}1\rangle\ ; \quad \frac{\Lambda^2-2}{\sqrt{2}\Lambda}. \tag{3.69}$$

It can be noted that for tension twinning, $m = 2$, while for compression twinning $m = 4$; hence, $1/2$ and $1/4$ of the lattice sites are sheared to the final twin positions, with the rest having to shuffle; this is consistent with the early theories of classical twinning presented in chapter 1.

Now, according to the method by Acton et al. [130] detailed above, the correspondence matrices describing double twinning may be found using equation 3.55, as the products of the correspondence matrices of the component twinning modes. Both compression-tension and tension-compression double twinning can be described in this way, and we obtain

$$(10\bar{1}1) - (10\bar{1}2)\ \text{DT}: \qquad \mathbf{C}_{\text{C}-\text{T}} = \mathbf{C}_{2.19}\mathbf{C}_{4.20}^{\text{T}} \tag{3.70}$$

$$(10\bar{1}2) - (10\bar{1}1)\ \text{DT}: \qquad \mathbf{C}_{\text{T}-\text{C}} = \mathbf{C}_{4.20}^{\text{T}}\mathbf{C}_{2.19} \tag{3.71}$$

The connection between $\mathbf{C}_{\text{C}-\text{T}}$ and $\mathbf{C}_{\text{T}-\text{C}}$ can be readily established by remembering that the correspondence matrices in the matrix product are involutory: hence, equation 3.71 can be written as

$$\mathbf{C}_{\text{T}-\text{C}} = \mathbf{C}_{4.20}^{\text{T}}\mathbf{C}_{2.19} = \mathbf{C}_{4.20}^{-\text{T}}\mathbf{C}_{2.19}^{-1} = (\mathbf{C}_{2.19}\mathbf{C}_{4.20}^{\text{T}})^{-1} = \mathbf{C}_{\text{C}-\text{T}}^{-1}\,. \tag{3.72}$$

We recall that the inverse $\mathbf{C}^{-1}$ of a correspondence matrix $\mathbf{C}$ defines an inverse shear $\mathbf{S}^{-1}$ expressed in the coordinate system of the sheared lattice, equation 3.42; then we see that equation 3.72 implies that in the coordinate system of the lattice sheared by the compression-tension transformation, the correspondence matrix of tension-compression twinning defines the inverse shear that restore the lattice sites to their original positions. This is to be expected and is exactly as found by Crocker [41] in his treatment of double twinning, see section 3.2.2.

As was found in Crocker's case however, $\mathbf{C}_{\text{C}-\text{T}}$ and $\mathbf{C}_{\text{C}-\text{T}}^{-1}$ define independent twinning modes when referred to the parent lattice, producing twinning elements with different indices. Albeit products of involutory matrices, the correspondence matrices $\mathbf{C}_{\text{C}-\text{T}}$ and $\mathbf{C}_{\text{T}-\text{C}}$ are not equal to their inverses (which would also make them equal to each other) and thus describe non-classical twinning modes. In the Miller-Bravais coordinate system, the twinning elements $\text{K}_1\text{K}_2\boldsymbol{\eta}_1\boldsymbol{\eta}_2;s$ of the two modes are given by

$$\mathbf{C}_{\text{C}-\text{T}}: \quad (\text{“}30\bar{3}2\text{”})\ \ (\text{“}\bar{1}014\text{”})\ \ [\text{“}\bar{1}013\text{”}]\ \ [\text{“}\bar{2}02\bar{1}\text{”}];\ \ 0.258\,, \tag{3.73}$$

$$\mathbf{C}_{\text{T}-\text{C}}: \quad (\text{“}50\bar{5}14\text{”})\ \ (\text{“}30\bar{3}\bar{4}\text{”})\ \ [\text{“}30\bar{3}\bar{2}\text{”}]\ \ [\text{“}\bar{5}05\bar{6}\text{”}]\,;\ \ 0.258\,, \tag{3.74}$$

where the indices and the shear magnitude are given for $\gamma = 1.624$, and indices in inverted commas indicate irrational indices approximated to the nearest integer. The K_1 and K_2 planes

given above are the same as the habit planes predicted by Crocker and given in this thesis in tables 3.3 and 3.4, and are interpreted as the habits of modes with primary twinning mechanisms reciprocal of each other, as per the statement of the reciprocal theorem.

As the correspondence matrices $\mathbf{C}_{\mathrm{C-T}}$ and its inverse define simple twinning modes, they should be listed among the correspondence matrices of table 2 in Bevis and Crocker's work, but this is not the case. This is because Bevis and Crocker chose to list matrices with $m = 1, 2, 4$; for $m = 4$, they only include matrices that define shear transformations in centred lattices for which at least half of the lattice sites are sheared to the twin positions; this condition is satisfied when $\mathrm{Tr}\left(\mathbf{W}^{\mathrm{T}}\mathbf{W}\right)$ is even for $s^2_{\max} = 2.25$, where $\mathbf{W}$ is defined by equation 3.61. For the double twin correspondence $\mathbf{C}_{\mathrm{C-T}}$ as well as for its inverse, $m = 8$ and $\mathrm{Tr}\left(\mathbf{W}^{\mathrm{T}}\mathbf{W}\right)$ is odd, such that these matrices are not present in table 2 of Bevis and Crocker. The equivalent simple twinning modes for all the double twinning mechanisms considered so far thus entail complex lattice shuffle mechanisms, as only one eighth of the lattice sites are directly sheared to twin positions. This considerably lowers the likelihood of a double twin occurring as a simple twinning mode, despite the relatively low magnitude of the double twinning shear.

Finally, the misorientation relations for the double twinning modes defined by these correspondence matrices may be obtained using equation 3.53 and solving for $\mathbf{L}_C$, i.e.

$$\mathbf{L}_C = \mathbf{S}_C \mathbf{C}_C^{-1} \, . \tag{3.75}$$

Here $\mathbf{C}_C$ is either $\mathbf{C}_{\mathrm{C-T}}$ or $\mathbf{C}_{\mathrm{T-C}}$, and the corresponding matrix $\mathbf{S}_C$ is obtained using equation 3.19 with $\mathbf{m}$ and $\mathbf{l}$ found as solutions to equations 3.35 and 3.28 via the procedure detailed above. Thus the rotation matrix $\mathbf{L}_C$ is obtained; this is however expressed in the three-dimensional hexagonal basis, such that in order to find the corresponding axis/angle pair equations 3.3 to 3.6 cannot be used, as they are only valid for cubic lattices. Three options are presented: *i)* convert $\mathbf{L}_C$ to the Miller-Bravais coordinate system and use the method derived by Pond [62] and outlined in section 3.1; *ii)* convert $\mathbf{L}_C$ to the 3D Cartesian system and use equations 3.3 to 3.6, though this is a little more cumbersome as symmetry operations for the hexagonal systems are usually expressed in hexagonal coordinates, e.g. in the International Tables for Crystallography [137]; *iii)* derive equations 3.3 to 3.6 for the hexagonal lattice with metric given by equation 3.62. We shall illustrate option *iii)*, with the aid of index notation.

A rotation matrix $\mathbf{L}$ in a general coordinate system with metric $\mathbf{G}$ is given by

$$L_{lk} = \delta_{lk}\cos\theta + (1-\cos\theta)\hat{n}_l\hat{n}_k^* + \sin\theta\hat{n}_r^*\varepsilon_{krs}^*(G^{-1})_{ls}, \tag{3.76}$$

where θ is the rotation angle and $\hat{\mathbf{n}}$ is a unit vector in the direction of the rotation axis, and the Levi-Civita symbol is as before [138]. Firstly, we show that equation 3.3 remains valid for any coordinate system by taking the trace of $\mathbf{L}$:

$$\begin{aligned} L_{ll} &= \delta_{ll}\cos\theta + (1-\cos\theta)\hat{n}_l\hat{n}_l^* + \sin\theta n_r^*\varepsilon_{lrs}^*(G^{-1})_{ls}, \\ &= 3\cos\theta + 1 - \cos\theta, \\ \cos\theta &= \frac{L_{ll}-1}{2}, \end{aligned} \tag{3.77}$$

where in the first line ε_{lrs}^* is antisymmetric while $(G^{-1})_{ls}$ is symmetric, such that their product is zero, and $\hat{n}_l\hat{n}_l^* = 1$. Then, in order to derive an expression for the rotation axis, we multiply both sides of equation 3.76 by $\varepsilon_{mxl}^*(G^{-1})_{kx}$:

$$\varepsilon_{mxl}^*(G^{-1})_{kx}L_{lk} = \varepsilon_{mxl}^*(G^{-1})_{kx}\delta_{lk}\cos\theta + (1-\cos\theta)\hat{n}_l\hat{n}_k^*\varepsilon_{mxl}^*(G^{-1})_{kx} + \sin\theta\hat{n}_r^*\varepsilon_{krs}^*(G^{-1})_{ls}\varepsilon_{mxl}^*(G^{-1})_{kx}.$$

Using the properties of the Kronecker delta, we find

$$\begin{aligned} \varepsilon_{mxl}^*(G^{-1})_{kx}L_{lk} &= \varepsilon_{mxl}^*(G^{-1})_{lx}\cos\theta + (1-\cos\theta)\hat{n}_l\hat{n}_k\varepsilon_{mxl}^* + \sin\theta\hat{n}_r^*\varepsilon_{krs}^*\varepsilon_{mxl}^*\delta_{kl}\delta_{xs} \\ &= \sin\theta\hat{n}_r^*\varepsilon_{lrs}^*\varepsilon_{msl}^* \\ &= 2\sin\theta\hat{n}_r^*\delta_{rm}|(G^{-1})_{ij}| = 2\sin\theta\hat{n}_m^*|(G^{-1})_{ij}|, \end{aligned}$$

where the first two terms on the right in the first line are zero as they are products of symmetric and antisymmetric tensors, and to obtain the third line we use $\varepsilon_{lrs}^*\varepsilon_{msl}^* = 2\delta_{rm}|(G^{-1})_{ij}|$. Since we are only interested in the direction of the rotation axis, we drop the constant factors, and we obtain the covariant components of the vector $\mathbf{n}$:

$$n_m^* = \varepsilon_{mxl}^*(G^{-1})_{kx}L_{lk}. \tag{3.78}$$

Then the contravariant components of $\mathbf{n}$ are given by $n_i = (G^{-1})_{im} n^*_m$.

The descriptions of $\mathbf{L}$ equivalent by symmetry are obtained via the point symmetry operations of the hexagonal lattice, as detailed in section 3.1. When axis/angle pairs have been determined for all descriptions using equations 3.77 and 3.78, the minimum axis/angle pair can be chosen. Doing this for $\mathbf{L} = \mathbf{L}_C$, we recover the misorientation relations found by Crocker and given in tables 3.3 and 3.4 for compression-tension and tension-compression double twinning respectively.

It is thus verified that Acton et al.'s treatment of double twinning [130] is entirely equivalent to Crocker's earlier attempt [41], if more general. Acton et al. show how double twinning is a special case of Bevis and Crocker's theory of non-classical twinning [76, 77]. The foundation of this theory is the definition of a twinning transformation as a simple shear that restores the lattice in a different orientation, the form of which need not be limited to the classical orientation relations described by Bilby and Crocker [75]. This was also the assumption of Crocker's treatment of double twinning, i.e. that the two component twinning shears should combine to return a simple shear. The consequence of this requirement is that a rotation is imposed on the twinned lattice relative to the parent, so that two truly invariant planes may exist in the transformation. While the magnitude of this rotation is small for so-called type 1 double twins, it is not insignificant for type 2 double twins, raising questions on its feasibility. In any case, fully formed type 1 and type 2 double twins would appear indistinguishable in these formulations of double twinning, as they present the same habit planes and misorientation relations, which is yet another consequence of requiring that the total transformation be a simple shear. Additionally, while in his earlier theory Crocker forwent any discussion of the lattice shuffles involved in the equivalent simple twinning modes describing double twinning, the analysis carried out by Bevis and Crocker shows that complex lattice shuffle mechanisms arise for the double twinning modes, as only one eighth of lattice sites is sheared directly to twin positions; additional atomic shuffles will also be necessary when the lattice is decorated with the hcp basis. Indeed, consideration of these shuffles lowers the likelihood of double twinning occurring as an equivalent simple twinning mode.

3.4 Topological treatments of double twinning

Having related the so-called phenomenological theories of double twinning, we now turn to treatments employing the topological model described in chapter 2. These treatments focus on the interplay of twinning disconnections, rather than on the individuation of invariant habit planes; the component twinning shears are not assumed to combine to yield an equivalent simple twinning mode describing the double twinning mechanism. Despite these differences, we will see that some parallels can be drawn between the two models.

3.4.1 Disconnections impinging on a flat interface

We initially consider the compression-tension "type 1" double twinning mechanism, with twinning sequence $(10\bar{1}1)^{\mu} - (10\bar{1}2)^{\lambda}$, where we have denoted the parent crystal by μ and the primary twin by λ. We start from an ideal situation, i.e. that of a fully formed primary twin with a flat coherent interface along the $(10\bar{1}1)$ plane. We then take a secondary twinning disconnection gliding on the $(10\bar{1}2)$ plane of the primary twin to impinge on the primary twin interface. Assuming that the movement of atoms in the interface is not constrained by the material surrounding the twin, all the atoms encompassed by the length of the step are sheared by an amount corresponding to the Burgers vector of the secondary twinning disconnection. The next secondary twinning disconnection travelling on a $(10\bar{1}2)$ plane would then shear atoms by twice the Burgers vector, and so on. The result is that the primary twin interface is overall rotated about the normal to the plane of shear common to the two twinning modes. This scenario is depicted in figure 3.2a for a single secondary twinning disconnection with Burgers vector $\mathbf{b}_B$ and step height h_B. The parameters for this disconnection are obtained through the topological model, and were given in table 2.1 in the previous chapter; these are $\mathbf{b}_B = \frac{2-\Lambda^2}{2+\Lambda^2}[10\bar{1}\bar{1}]^{\lambda}$ and $h_B = 2d_{(10\bar{1}2)}$, where $d_{(10\bar{1}2)}$ is the distance between $(10\bar{1}2)$ lattice planes of the primary twin. For $\gamma = 1.624$, $\mathbf{b}_B \approx 0.06a[10\bar{1}\bar{1}]^{\lambda}$, $|\mathbf{b}_B| \approx 0.15a$ and $h_B \approx 1.18a$, where a is the lattice constant of magnesium. It is noted that the length of the Burgers vector relative to the step height in figure 3.2a is exaggerated for clarity, as in reality h_B is approximately eight times the length of $\mathbf{b}_B$.

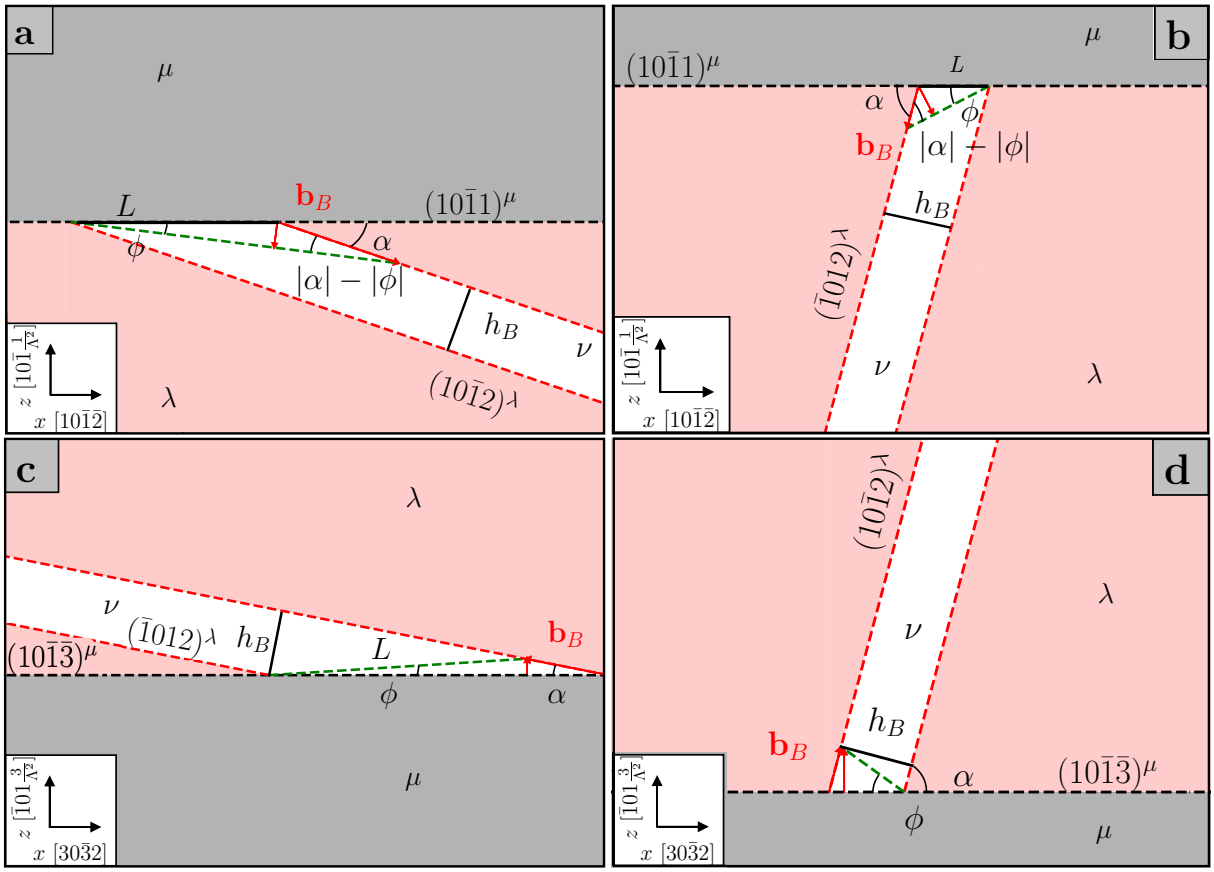

Fig. 3.2 Schematic of a secondary twinning disconnection with Burgers vector $\mathbf{b}_B$ and step height h_B impinging on a flat primary twin boundary. α is the angle between the primary and secondary twinning planes, ϕ the maximum angle the primary twinning plane is rotated through by the secondary twinning disconnections, and the trace of the rotated habit plane is indicated by the green dashed line. The parent, primary and secondary twin are denoted respectively by μ, λ and ν. (a): $(10\bar{1}1) - (10\bar{1}2)$ double twin, i.e. type 1; L is the distance between the origin and the point where the top of the step meets the primary twin interface. (b):$(10\bar{1}1) - (\bar{1}012)$ double twin, i.e. type 2; L is as in (a). (c): $(10\bar{1}\bar{3}) - (\bar{1}012)$ double twin, i.e. type 1; L (in green) is the distance between the origin and the tip of the Burgers vector. (d) $(10\bar{1}\bar{3}) - (10\bar{1}2)$ double twin, i.e. type 2. L (not labelled) is as in (c), in green. In (a) to (c) the length of the Burgers vector is not to scale.

Seeking now to calculate the angle ϕ rotated through by the primary twinning plane as a result of the action of the secondary twinning disconnections, we label the angle between $(10\bar{1}1)^\mu$ and $(10\bar{1}2)^\lambda$ α, and L is the distance between the origin and the top of the step. We then see that the component of $\mathbf{b}_B$ (in red in the figure) perpendicular to the new habit plane, whose trace is given in green in the figure, makes up the short side of two triangles, one with

hypotenuse L and the other with hypotenuse b_B. We can then write the equality

$$L\sin\phi = b_B\sin(|\alpha|-|\phi|)\ , \tag{3.79}$$

where we have used the absolute values of the angles α and ϕ to make sure that the internal angles of all the triangles we use for trigonometric computation sum up to π. Using $L = |h_B|/\sin|\alpha|$, $|s_B| = b_B/|h_B|$ and solving for $|\phi|$, we find

$$|\phi| = \cot^{-1}\left(\frac{|s_B|\sin|\alpha|\cos|\alpha|-1}{|s_B|\sin^2|\alpha|}\right)\ . \tag{3.80}$$

As we have obtained the absolute value of ϕ, to ascertain its sign it is necessary to consider the sign of α and the direction of the Burgers vector $\mathbf{b}_B$; this can be done by observing figure 3.2a: in this case, following the impingement of a secondary twinning disconnection the primary twinning plane undergoes a clockwise rotation, such that ϕ is to be negative. Using equation 3.80 we obtain $|\phi| = 0.7^\circ$, and following the examination of the figure we find that the habit plane of the primary twin undergoes a rotation of magnitude $\phi = -0.7^\circ$ as the double twin is formed.

The scenario examined above was also briefly considered by Crocker in his work on double twinning [41]. In his formulation, the angle ϕ is that by which the primary K_1 plane is rotated by the secondary twinning shear, $\mathbf{S}_B$, which was defined by equation 3.21. The unit vector $\mathbf{l}$ lying in the primary K_1 plane is rotated by the secondary twinning shear to position $\mathbf{S}_B\mathbf{l}$, and recalling that in Crocker's two-dimensional coordinate system the x-axis is aligned with the $\boldsymbol{\eta}_1$ direction of the primary twin, $\mathbf{l} = [1,0]$. Then the angle ϕ is given by

$$\phi = \cot^{-1}\left(\frac{s_B\sin\alpha\cos\alpha - 1}{s_B\sin^2\alpha}\right)\ . \tag{3.81}$$

This is different from equation 3.80, because in this formulation we are able to take into account the sign of α as well as that of the twinning shear s_B, such that the correct sign is computed for ϕ. Indeed, equation 3.81 yields $\phi = -0.7^\circ$. The same procedure can be applied to the $(10\bar{1}1)-(\bar{1}012)$ mechanism, so-called "type 2", figure 3.2b. In this case, the predicted rotation for the habit plane is $\phi = 6.6^\circ$.

A slightly different geometry is to be used for the $(10\bar{1}\bar{3})-(\bar{1}012)$ (type 1) and $(10\bar{1}\bar{3})-(10\bar{1}2)$ (type 2) double twinning mechanisms, due to the direction of the Burgers vector. These instances are schematically depicted in figures 3.2c-d, where once again the length of the Burgers vectors relative to the step height has been exaggerated for clarity. In this case, our focus is the component of the Burgers vector $\mathbf{b}_B$ perpendicular to the primary K_1 plane, rather than the rotated habit. Then L is the distance between the origin and the tip of $\mathbf{b}_B$ (i.e. the green dashed line in figure 3.2c), and we can write

$$L\sin|\phi| = b_B \sin|\alpha| \,, \tag{3.82}$$

where now $L = |h_B|/\sin(|\alpha|+|\phi|)$; this can be seen by considering the triangle containing both ϕ and α in figure 3.2c, where the third internal angle is given by $\pi-|\alpha|-|\phi|$, such that the angle opposite h_B is $|\alpha|+|\phi|$. Solving equation 3.82 for $|\phi|$, we obtain

$$|\phi| = \cot^{-1}\left(\frac{1-|s_B|\sin|\alpha|\cos|\alpha|}{|s_B|\sin^2|\alpha|}\right) . \tag{3.83}$$

Thus we find that for the $(10\bar{1}\bar{3})-(\bar{1}012)$ double twin $\phi = 0.3^\circ$, while for $(10\bar{1}\bar{3})-(10\bar{1}2)$, $\phi = -7.1^\circ$, upon examination of figures 3.2c-d. In both cases, the angle ϕ is measured relative to the $(10\bar{1}\bar{3})$ plane of the matrix.

Similarly, the rotation of the primary K_1 plane caused by the impingement of a secondary twinning disconnection can be found for the four tension-compression mechanisms, figure 3.3. In this case the secondary twinning disconnections are those of $(10\bar{1}1)$ and $(10\bar{1}\bar{3})$ twinning given in table 2.1: for $(10\bar{1}1)$ secondary twinning, $\mathbf{b}_B = \frac{2\Lambda^2-3}{2\Lambda^2+1}[10\bar{1}\bar{2}]^\lambda$ and $h_B = -4d_{(10\bar{1}1)}$; for $(10\bar{1}\bar{3})$ secondary twinning, $\mathbf{b}_B = \frac{2\Lambda^2-3}{2\Lambda^2+9}[30\bar{3}2]^\lambda$ and $h_B = 4d_{(10\bar{1}\bar{3})}$. For the $(10\bar{1}2)-(10\bar{1}1)$ and $(10\bar{1}2)-(10\bar{1}\bar{3})$ mechanisms, equation 3.80 may be derived, while for the $(\bar{1}012)-(10\bar{1}1)$ and $(\bar{1}012)-(10\bar{1}\bar{3})$ mechanisms equation 3.83 holds. The resulting rotation angles about the normal to the plane of shear are given in table 3.5, along with those for the compression-tension mechanisms. These angles represent the maximum rotation of the double twin habit plane that can be brought about by the secondary twinning twinning disconnections encountering a flat primary twin to matrix interface, since in the development above we have assumed that the atoms in the interface were not constrained by the matrix surrounding the twin. In practice however they

might be constrained, and the final rotation may be smaller; if indeed all additional deformation caused by the secondary twinning shear were to be accommodated in the double twin, no rotation would be observed. Finally, the rotation might be partitioned more or less equally between the two crystals. Hence, the values reported in table 3.5 are to be interpreted as limiting values.

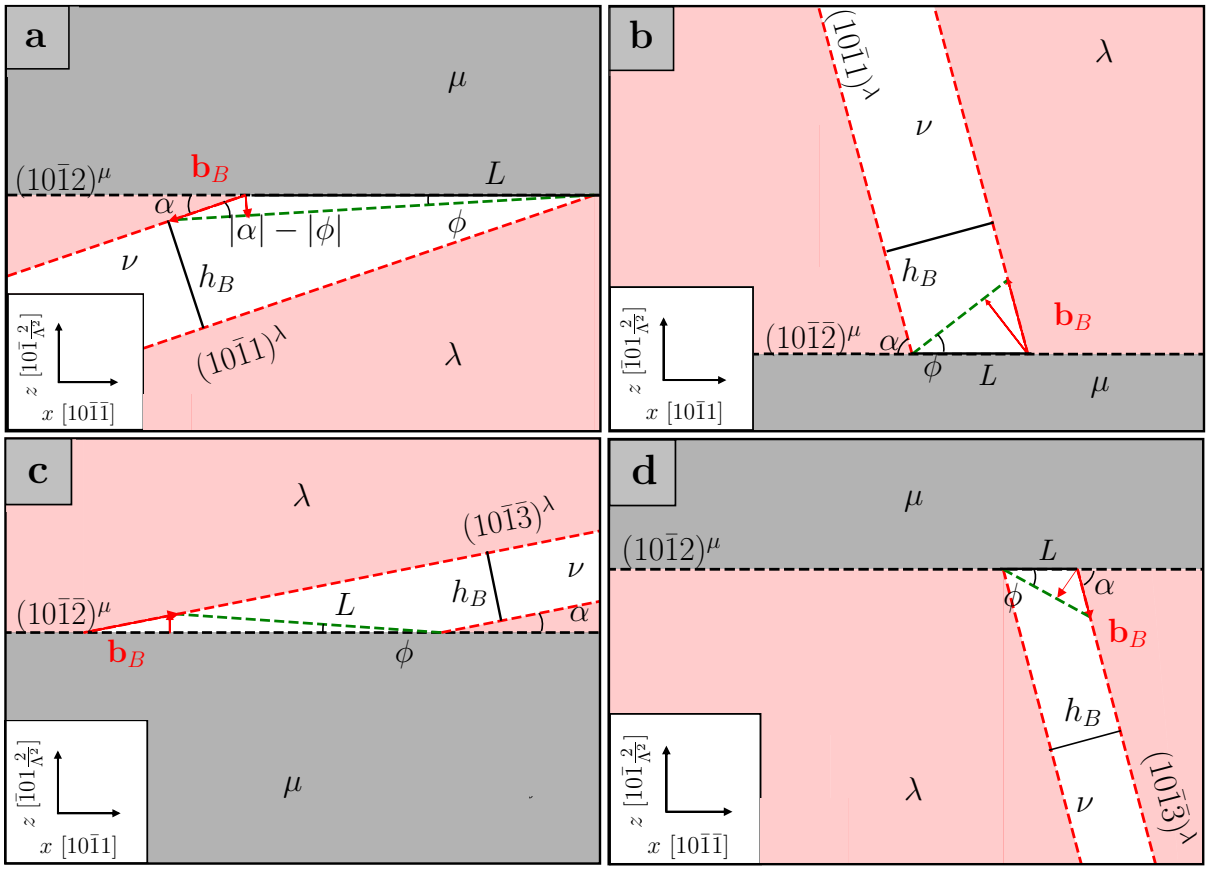

Fig. 3.3 Schematic of a secondary twinning disconnection with Burgers vector $\mathbf{b}_B$ and step height h_B impinging on a flat primary twin boundary. α is the angle between the primary and secondary twinning planes, ϕ the maximum angle the primary twinning plane plane is rotated through by the secondary twinning disconnections, and the trace of the rotated habit plane is indicated by the green dashed line. The parent, primary and secondary twin are denoted respectively by μ, λ and ν. (a): $(10\bar{1}2)-(10\bar{1}1)$ double twin, i.e. type 1; L is the distance between the origin and the point where the top of the step meets the primary twin interface. (b):$(\bar{1}012)-(10\bar{1}1)$ double twin, i.e. type 2; L is as in (a). (c): $(\bar{1}012)-(10\bar{1}\bar{3})$ double twin, i.e. type 1; L (in green) is the distance between the origin and the tip of the Burgers vector. (d) $(10\bar{1}2)-(10\bar{1}\bar{3})$ double twin, i.e. type 2. L is as in (a). In (a) to (c) the length of the Burgers vector is not to scale.

It emerges from the results in table 3.5 that for both the compression-tension and tension-compression double twinning sequences, the type 1 mechanisms lead very small rotation angles, all a fraction of a degree. In contrast, type 2 mechanisms entail larger rotations of the habit plane

C-T DT	$(10\bar{1}1)-(10\bar{1}2)$	$(10\bar{1}1)-(\bar{1}012)$	$(10\bar{1}\bar{3})-(10\bar{1}2)$	$(10\bar{1}\bar{3})-(\bar{1}012)$
	type 1	type 2	type 2	type 1
ϕ	-0.7°	6.6°	-7.1°	0.3°
α	-18.8°	74.9°	75.2°	-11.1°
T-C DT	$(10\bar{1}2)-(10\bar{1}1)$	$(\bar{1}012)-(10\bar{1}1)$	$(10\bar{1}2)-(10\bar{1}\bar{3})$	$(\bar{1}012)-(10\bar{1}\bar{3})$
	type 1	type 2	type 2	type 1
ϕ	0.8°	7.6°	-7.1°	-0.3°
α	18.8°	-74.9°	-75.2°	11.1°

Table 3.5 Angles rotated through by the primary twin interface due to the impingement of a secondary twinning disconnection, for compression-tension and tension-compression double twin mechanisms. The rotation axis is the normal to the plane of shear $(1\bar{2}10)$. The results are given for $\gamma = 1.624$.

by an order of magnitude; this is a consequence of the magnitude of the angle α between the primary and secondary twinning planes, which is larger for the type 2 mechanisms. Therefore, the type 2 mechanisms would require more accommodation to ensure the rotation of the habit plane, which leads us to conclude that they would be less likely to occur; this is indeed the same conclusion that emerged from our analysis of Crocker's invariant plane theory, according to which type 2 mechanisms would involve larger rotations of the double twin relative to the parent.

3.4.2 Mechanistic model of interfaces containing disconnections

In the previous section, we considered a fully formed primary twin with a flat coherent interface, i.e. with no dislocation content. We now remove this constraint, and allow the primary twin interface to contain disconnections, following the approach of Pond and coworkers [139]. We then wish to know how this interface is modified by the arrival of secondary twinning disconnections, as done previously. In order to tackle this problem however, we first take a moment to give a brief introduction on how the dislocation content of an interface may be calculated, following treatments by Christian [56] and Sutton and Balluffi [97].

The question was first posed by Frank [140] and Bilby [141], who, considering an interface separating two lattices related by an affine transformation, sought to calculate the dislocation content needed to make the lattices compatible in such a way that they would fit together at the interface. We take the lattices on either side of the interface to be obtained from a reference lattice via the operations $\mathbf{W}(\lambda)$ and $\mathbf{W}(\mu)$, which transform vectors of the reference lattice into

vectors of the λ and μ lattices respectively. We let the three lattices share a common origin, and we consider a large vector **v**, called the "probe vector", connecting the origin and point V in the interface plane with normal $\hat{\mathbf{n}}$. Taking two points P_1 and P_2 to reside in the μ and λ lattices respectively, we draw the right-handed Burgers circuit connecting the origin, P_1, V and P_2, i.e. VP_1OP_2V. We then map this circuit to the reference lattice: the VP_1O part of the circuit is transformed into T_1Q_1O by the operation $\mathbf{W}(\lambda)^{-1}$, while OP_2V becomes OQ_2T_2 after applying $\mathbf{W}(\mu)^{-1}$. The closure failure of this circuit yields the Burgers vector content crossing the vector **v**, and it is given by $T_2T_1 = OT_1 - OT_2 = \mathbf{W}(\mu)^{-1} - \mathbf{W}(\lambda)^{-1}$, such that

$$\mathbf{b} = (\mathbf{W}(\mu)^{-1} - \mathbf{W}(\lambda)^{-1})\mathbf{v} \,, \tag{3.84}$$

where **b** is expressed in the coordinate system of the reference lattice. This equation is known as the Frank-Bilby equation, and if the reference lattice is taken to be μ, such that the operation $\mathbf{W}(\mu)$ is given by the identity, it can be rewritten as

$$\mathbf{b} = (\mathbf{I} - \mathbf{W}(\lambda)^{-1})\mathbf{v} \,. \tag{3.85}$$

Thus, when no net Burgers vector density crosses the interface, the two lattices are compatible and are fit together by elastic strain, such that the interface is coherent; this implies that the interface is characterised by a long-ranged stress field, which is modelled as a uniform distribution of dislocations located at the interface and named "stress generators" [97], whose Burgers vector density is the negative of that given by the Frank-Bilby equation. Then, the dislocation content predicted by equation 3.84 cancels out that of the stress generators, and these dislocations are therefore called stress annihilators.

Several reasons exist to suggest that this theory should be utilised with care. Principally, more than one description of the operations $\mathbf{W}(\lambda)$ and $\mathbf{W}(\mu)$ exists: as detailed in the previous chapter, equivalent operations are found by multiplying $\mathbf{W}(\lambda)$ and $\mathbf{W}(\mu)$ by the point symmetry group operations of λ and μ respectively. However, each description will yield a different Burgers vector density when used in the Frank-Bilby equation, while the dichromatic pattern is left unchanged, meaning in turn that the physical object described remains the same. Hence, all dislocation descriptions of an interface lead to the same boundary structure after full atomic

relaxation. The question arises then of what is the best description for the dislocation structure of an interface, and the answer is that justification of such a choice is not always possible. A most suitable description may however be chosen in cases where the motion of interfacial dislocations mediates a change in the shape of the crystals: this is the case of twinning, where the glide of disconnections on the interface plane accomplishes the growth of the twin; then the operations $\mathbf{W}(\lambda)$ and $\mathbf{W}(\mu)$ may be chosen to reflect how the twinning transformation is achieved.

With the above remarks in mind, we choose as a description of the twinning transformation that of a simple shear, such that the dislocation description arising from the Frank-Bilby equation is that of interfacial disconnections whose task is to accomplish said shear. To see this, we take as starting configuration a coherent primary twin interface aligned with the K_1 plane of the twin, figure 3.4a . Choosing the twin lattice λ as the reference lattice and the transformation relating the two to be the primary twinning shear referred to the coordinate system of λ, i.e. ${}^{P}\mathbf{S}_A^{-1} = \mathbf{S}_A$, we may rewrite the Frank-Bilby equation as

$$ {}^{P}\mathbf{b} = (\mathbf{S}_A^{-1} - \mathbf{I})\mathbf{v} \, , \tag{3.86} $$

Where the superscript ^{P} indicates that the object is referred to the coordinate system of the primary twin λ, as before. Since the probe vector $\mathbf{v}$ lies in the interface, it is left invariant by the transformation $\mathbf{S}_A^{-1}$; hence, the net dislocation content of the coherent twin interface is zero.

Next, we consider a different configuration, where the interface plane is at an angle ϕ with the K_1 plane of the primary twin, figure 3.4b. We make this bicrystal by creating the dichromatic complex of the primary twin and discarding λ and μ atoms on either side of the plane that makes an angle ϕ with K_1 respectively. This interface is, in general, incoherent, and the probe vector $\mathbf{v}$ which now lies in it is no longer invariant under the shear $\mathbf{S}_A^{-1}$. Substituting $\mathbf{S}_A^{-1} = \mathbf{I} - s_A \mathbf{l}_A \mathbf{m}_A^{\mathrm{T}}$, where $\mathbf{l}_A$ and $\mathbf{m}_A$ are unit vectors along $\boldsymbol{\eta}_1$ and normal to the twinning plane respectively, in equation 3.86, we find

$$ \begin{aligned} {}^{P}\mathbf{b} &= -s_A \mathbf{l}_A \mathbf{m}_A^{\mathrm{T}} \mathbf{v} \\ &= -s_A \cos\Big(\frac{\pi}{2} + \phi\Big) |\mathbf{v}| \mathbf{l}_A \\ &= s_A \sin\phi \, |\mathbf{v}| \mathbf{l}_A \, . \end{aligned} $$

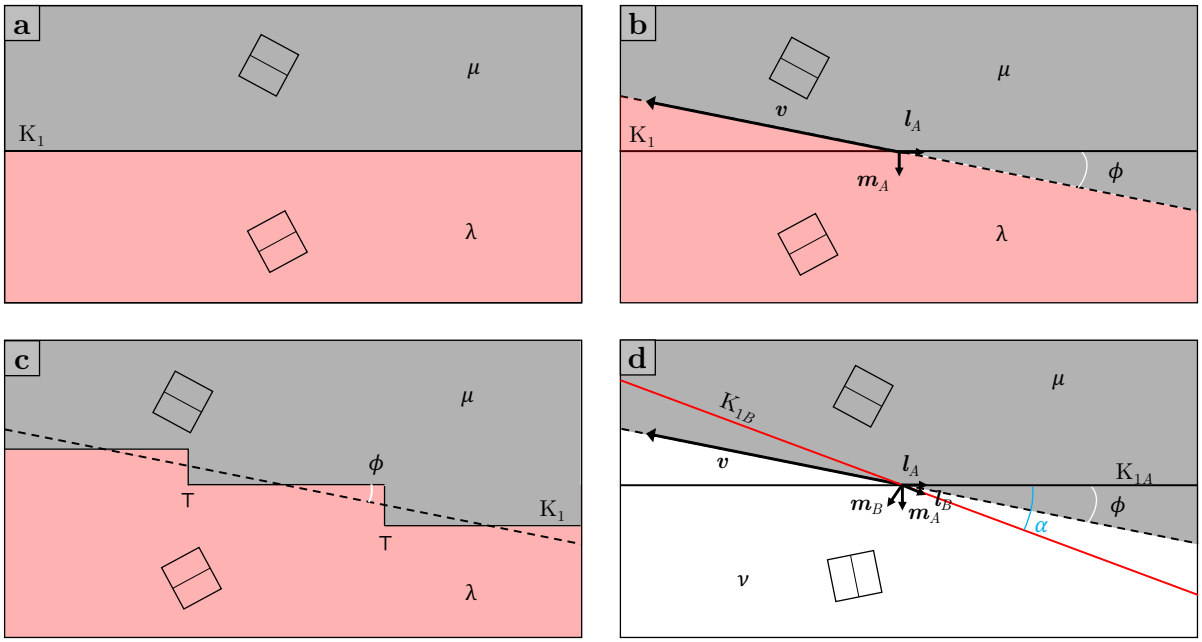

Fig. 3.4 Application of the Frank-Bilby equation to twin interfaces. μ, λ and ν denote the matrix, primary and secondary twin respectively. (a) Coherent twin interface with no dislocation content crossing the interface. (b) Incoherent interface making an angle ϕ with the K_1 plane, such that the Burgers vector content of the interface may be calculated using the Frank-Bilby equation. $\mathbf{v}$ is the interfacial probe vector, $\mathbf{m}_A$ is the unit normal to the twinning plane and $\mathbf{l}_A$ is a unit vector parallel to the shear direction. (c) Dislocation content predicted by the Frank-Bilby equation for the interface in (c) resolved into twinning disconnections separating coherent terraces of twin boundary. (d) Incoherent interface between the matrix and the double twin, whose dislocation content can be calculated using the Frank-Bilby equation. $\mathbf{m}_B$ and $\mathbf{l}_B$ are respectively the unit normal to the secondary K_1 plane and a unit vector parallel to $\boldsymbol{\eta}_1$ of the secondary twin.

Thus the Burgers vector content of this interface is parallel to the $\boldsymbol{\eta}_1$ direction, and we can envisage an array of twinning disconnections to make up the dislocation content. Using that for a twinning disconnection $s_A = |\mathbf{b}_A|/h_A$, we see that $|\mathbf{b}_A|\mathbf{l}_A = \mathbf{b}_A$, i.e. the Burgers vector of the disconnection. Defining the disconnection spacing as $L_A = h_A/\sin\phi$ and dividing through by $|\mathbf{v}|$, we find the Burgers vector density

$$\frac{{}^{P}\mathbf{b}}{|\mathbf{v}|} = \frac{\mathbf{b}_A}{L_A}\,. \tag{3.87}$$

Although this Burgers vector content is referred to the coordinate system of the primary twin, it has the same indices in the coordinate system of the parent lattice, since the Burgers vector $\mathbf{b}_A$ is invariant under the primary twinning shear.

Hence, this interface is formed by coherent terraces parallel to the primary twin plane separated by twinning disconnections, as shown in figure 3.4c. This is consistent with the model

of a lenticular twin, where loops of twinning disconnections enlarge the twin by gliding on the composition plane, and while doing so ensure that the habit plane is macroscopically rotated.

In the case of double twinning however, this is a transient configuration; in fact it is modified by the arrival of secondary twinning disconnections as the secondary twin grows inside the primary twin. These disconnections now raise the possibility that the misfit introduced by the primary twinning disconnections across the interface may be removed [139]. The zero misfit condition is achieved by interfacial dislocations when the total Burgers vector content parallel to the interface plane is zero [142, 143], such that if the incoming secondary twinning disconnections compensate the Burgers vector content of the primary twinning disconnections parallel to the interface, the boundary plane will be free of misfit.

In order to achieve the zero-misfit condition, we first establish the Burgers vector content of an interface that makes an angle ϕ with the primary K_1 plane, but now separates the parent and double twin, i.e. crystals μ and ν, figure 3.4d. The reference lattice is still λ: thus, the Frank-Bilby equation can be written as

$$\begin{aligned} {}^{P}\mathbf{b} &= (\mathbf{S}_A^{-1} - {}^{P}\mathbf{S}_B^{-1})\mathbf{v} \\ &= (-s_A \mathbf{l}_A \mathbf{m}_A^{\mathrm{T}} + s_B \, {}^{P}\mathbf{l}_B \, {}^{P}\mathbf{m}_B^{\mathrm{T}})\mathbf{v} \, . \end{aligned} \tag{3.88}$$

With the aid of figure 3.4d, we notice that ${}^{P}\mathbf{m}_B^{\mathrm{T}}\mathbf{v} = \cos\left(\frac{\pi}{2} - \alpha + \phi\right)|\mathbf{v}| = \sin(\alpha - \phi)|\mathbf{v}|$, where α is the angle between the primary and secondary K_1 planes. Then $s_B = |\mathbf{b}_B|/h_B$, such that $|\mathbf{b}_B| \, {}^{P}\mathbf{l}_B^{\mathrm{T}} = {}^{P}\mathbf{b}_B$. The spacing of the secondary twinning disconnections is thus given by $L_B = h_B/\sin(\alpha - \phi)$, such that the Burgers vector density of the interface is finally

$$\frac{{}^{P}\mathbf{b}}{|\mathbf{v}|} = \frac{\mathbf{b}_A}{L_A} + \frac{{}^{P}\mathbf{b}_B}{L_B} \, . \tag{3.89}$$

For simplicity, we now refer this Burgers vector content to the coordinate system of the matrix, such that

$$\frac{\mathbf{b}}{|\mathbf{v}|} = \frac{\mathbf{R}_A^{-1} \, {}^{P}\mathbf{b}}{|\mathbf{v}|} = \frac{\mathbf{b}_A}{L_A} + \frac{\mathbf{b}_B}{L_B} \, , \tag{3.90}$$

Where $\mathbf{R}_A$ is one of the descriptions of the transformation that relates the matrix and primary twin, e.g. a rotation by π about the primary $\boldsymbol{\eta}_1$ direction.

Now it is possible to apply the condition for zero misfit across the interface, i.e. that the total Burgers vector content parallel to the interface be equal to zero. This condition can only be achieved if the component of the Burgers vector of the secondary twinning disconnection that is parallel to the vector **v** has opposite sign to the same component of the Burgers vector of the primary twinning disconnection, i.e. if

$$\frac{|\mathbf{b}_A^{\parallel}|}{L_A} - \frac{|\mathbf{b}_B^{\parallel}|}{L_B} = 0 \,, \tag{3.91}$$

where the superscript $\parallel$ indicates the component parallel to the habit plane that makes an angle ϕ with the primary K_1 plane. These components are given by $|\mathbf{b}_A^{\parallel}| = |\mathbf{b}_A|\cos\phi$ and $|\mathbf{b}_B^{\parallel}| = |\mathbf{b}_B|\cos(\alpha-\phi)$. Then, reintroducing s_A and s_B to simplify the expressions, equation 3.91 becomes

$$s_A \sin\phi\cos\phi - s_B \sin(\alpha-\phi)\cos(\alpha-\phi) = 0 \,. \tag{3.92}$$

Solving for ϕ, we find

$$\phi = \frac{1}{2}\tan^{-1}\left(\frac{s_B \sin 2\alpha}{s_A + s_B \cos 2\alpha}\right) . \tag{3.93}$$

Thus, ϕ defines a habit plane where the spacing of the primary and secondary twinning disconnections that make up its dislocation content is such that misfit across the interface is removed.

Once the primary and secondary twinning disconnections are arranged such that misfit is compensated, we are however left to deal with the components of the Burgers vectors of the disconnections that are perpendicular to the interface. The Burgers vector content perpendicular to the plane that makes an angle ϕ with the primary twinning plane is given by

$$\frac{\mathbf{b}^{\perp}}{|\mathbf{v}|} = \frac{\mathbf{b}_A^{\perp}}{L_A} + \frac{\mathbf{b}_B^{\perp}}{L_B} \,. \tag{3.94}$$

The effect of this dislocation content is to cause a rotation of the lattices relative to each other, i.e. a tilt, such that the additional rotation contributes to the macroscopic rotation of the interface [142]. According to the topological model, this rotational distortion field is to be partitioned equally between the two crystals in the homogeneous isotropic case [143, 144]; in the case of double twinning, the crystals on either side of the interface are in the same phase and have the

same elastic constants, but they are not isotropic, such that the equal partitioning of the distortion field is an approximation. Hence, if the additional tilt is given by the angle ψ, each crystal will be rotated by $\psi/2$, and the final orientation of the interface is given by $\phi \pm \psi/2$ where the sign of $\psi/2$ differs for the two crystals. If the perpendicular components of the Burgers vectors of the twinning disconnections have the same sign, the angle ψ can be found from

$$\tan\psi = \frac{|\mathbf{b}^{\perp}|}{|\mathbf{v}|} = \frac{|\mathbf{b}_A^{\perp}|}{L_A} + \frac{|\mathbf{b}_B^{\perp}|}{L_B} \,. \tag{3.95}$$

For small ψ, $\tan\psi \approx \psi$, and we find

$$\psi = \frac{|\mathbf{b}^{\perp}|}{|\mathbf{v}|} = s_A \sin^2\phi + s_B \sin^2(\alpha - \phi) \,. \tag{3.96}$$

Thus a misfit-free double twin interface is envisaged, where the total transformation is accompanied by a rotational distortion of the two crystals. It is however emphasised that as mentioned above, the condition for the misfit to be removed is that the components of the Burgers vectors of the primary and secondary twinning disconnections parallel to the interface have opposite sign. This is indeed the case for which this treatment was envisaged, i.e. that of intersection of classical twins in Ni_2MnGa [139]. However, should the parallel components have the same sign, the secondary twinning disconnections will only add to the misfit introduced by the primary twinning disconnections.

Hence, we now analyse the specific case of double twinning in magnesium, where the component mechanisms are those given in the previous sections, i.e. $(10\bar{1}1)$ and $(10\bar{1}2)$ twinning, to understand whether misfit compensation brought about by twinning disconnections is possible. We envisage a lenticular primary twin based on the disconnection model of twinning presented above, where the macroscopic interface plane is rotated from the primary twin plane by the angle ϕ. We then take a secondary twin embryo to form inside the primary twin on a plane that makes an angle α with the primary twin plane. For interfaces where misfit accommodation is possible, the angle ϕ that the interface makes with the primary twinning plane can be calculated using equation 3.93, and the tilt ψ is given by equation 3.96, and the results are reported in table 3.6 for all the compression-tension and tension-compression double twinning mechanisms.

We now consider each of these mechanisms in detail with the aid of figures 3.5 and 3.6. Starting from the $(10\bar{1}1)-(10\bar{1}2)$ mechanism, figure 3.5a, we see that the components of the Burgers vectors of the primary and secondary twinning disconnections, $\mathbf{b}_A$ and $\mathbf{b}_B$, that are parallel to the interface making an angle ϕ with the primary K_1 plane point in the same direction: thus, the secondary twinning disconnections add to the misfit at the interface, and misfit cancellation is not possible for this mechanism. The same holds for the $(10\bar{1}\bar{3})-(10\bar{1}2)$ and $(10\bar{1}\bar{3})-(\bar{1}012)$ twinning sequences, figures 3.5c-d. Conversely, in the case of $(10\bar{1}1)-(\bar{1}012)$ double twinning, figure 3.5b, the components of $\mathbf{b}_A$ and $\mathbf{b}_B$ parallel to the interface have opposite sign, such that misfit cancellation may be achieved. However, it should be noted that in this case the tilt components of the Burgers vectors of the primary and secondary twinning disconnections, i.e. the components perpendicular to the interface plane, have opposite sign, such that this should be reflected by equation 3.96, and the total tilt is given by the difference of the magnitudes of these components. Applying the same analysis to the tension-compression double twinning sequences, we find that misfit compensation across the interface is possible for the $(10\bar{1}\bar{2})-(10\bar{1}1)$ (figure 3.6b) mechanism, while it may not be achieved for $(10\bar{1}2)-(10\bar{1}1)$ (figure 3.6a), $(10\bar{1}2)-(10\bar{1}\bar{3})$ (figure 3.6d) and $(10\bar{1}\bar{2})-(10\bar{1}\bar{3})$ (figure 3.6c) double twinning.

The misfit-free interfaces thus obtained for the double twinning mechanisms where misfit compensation is possible are immobile, because a finite diffusive flux of atoms would be needed for the interlocked primary and secondary twinning disconnections to move, i.e. the intersection of twinning disconnections is not glissile [145]. Thus the double twin cannot grow on the habit plane defined by $\phi+\frac{\psi}{2}$, and is restricted to the original size of the primary twin.

Comparing the habit planes defined in table 3.6 with those predicted by Crocker's model (tables 3.3 and 3.4), we notice that similar results are obtained, and we shall discuss this in detail in the next section. However, though this model predicts macroscopic habit planes with similar orientations to those calculated using Crocker's method, only for some of the double twinning mechanisms may the misfit-free condition be achieved, as shown above. In the other cases, the Burgers vectors of the primary and secondary twinning disconnections actually do not have opposite components parallel to the interface: instead, these components have the same sign, such that the secondary twinning disconnections add to the misfit introduced by the primary twinning disconnections. Therefore, the zero-misfit condition in these double twin interfaces may

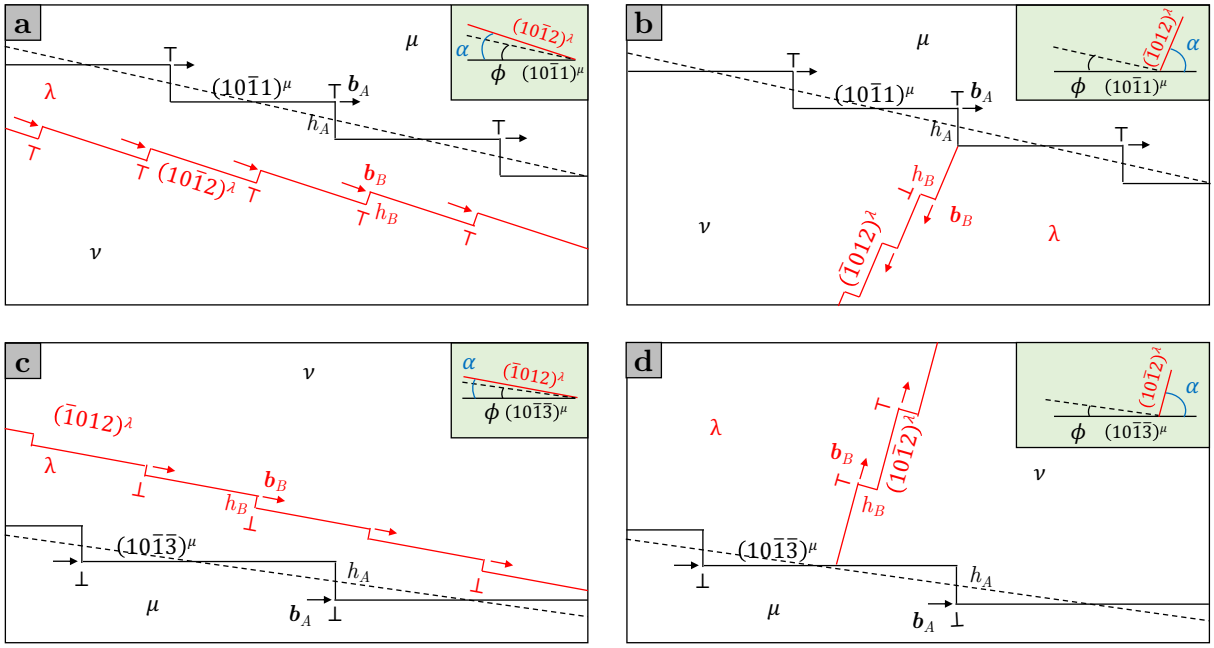

Fig. 3.5 Diagrams illustrating the possibility of misfit compensation across the double twin to matrix interface by combination of primary and secondary twinning disconnections for the compression-tension mechanisms. In (a) to (d) μ, λ and ν indicate the matrix, primary and secondary twin respectively.

not be achieved by the interplay of disconnections, meaning that there is no viable disconnection mechanism that describes the formation of double twin interfaces consistent with Crocker's predictions.

3.5 Comparison between the topological and phenomenological models

An instructive comparison may now be drawn between Crocker's model of double twinning on an invariant plane, as well as successive models of non-classical twinning, and the topological model of misfit-free interfaces described above. In particular, one may wish to understand why these two models yield similar predictions for the habit plane of a double twin, albeit starting from different postulates. In the phenomenological theories, it is assumed that a double twin nucleus may be able to grow on a plane left invariant by the combined shear transformations of the two twinning mechanisms. On the other hand, the topological model is based on the notion that twinning disconnections of the primary and secondary twins will arrange themselves as to

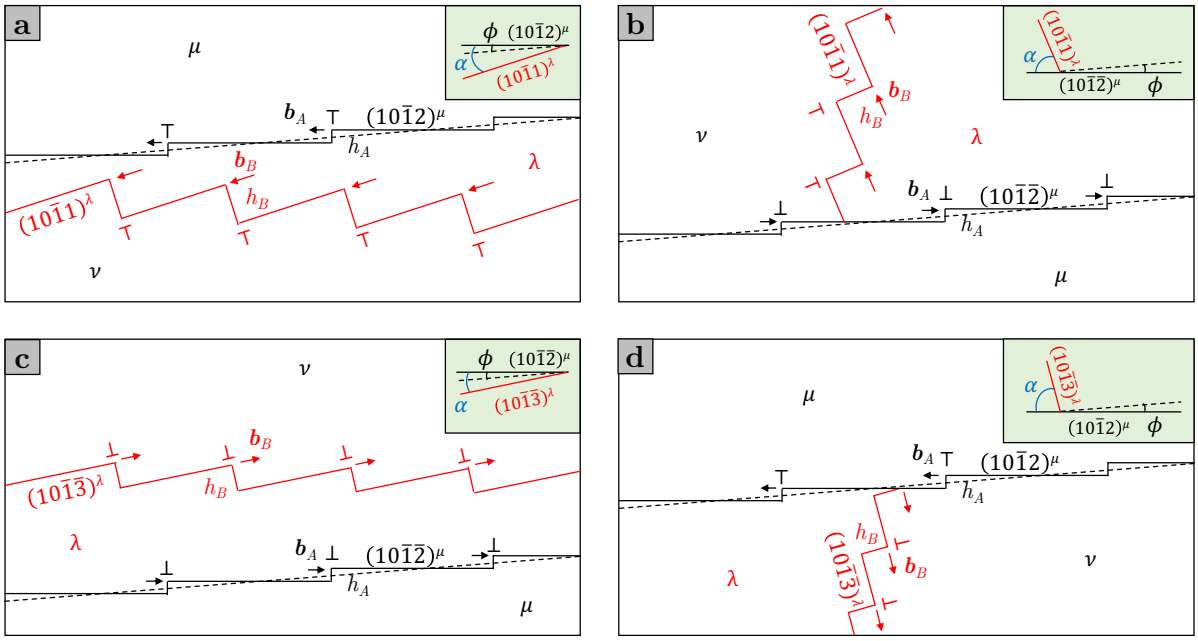

Fig. 3.6 Diagrams illustrating the possibility of misfit compensation across the double twin to matrix interface by combination of primary and secondary twinning disconnections for the tension-compression mechanisms. In (a) to (d) μ, λ and ν indicate the matrix, primary and secondary twin respectively.

eliminate misfit in the macroscopic double twin interface. However, the misfit-free condition is built into the definition of an invariant plane strain, as if an undistorted plane is picked as the interface, there is no misfit across it. Thus the topological theory models explicitly the minimisation of misfit, which is instead modelled implicitly in the phenomenological theories [139]. We have however seen how the premises for the achievement of a misfit-free interface by twinning disconnections exist only for some of the double twinning mechanisms under consideration, such that the construction of interfaces aligned with the predicted habit planes is not always possible.

Secondly, Crocker's theory predicts the existence of a mutual rotation between the parent and doubly twinned lattices, necessary in order to render any undistorted plane also unrotated and thus truly invariant. This rotation concerns the entirety of the doubly twinned volume, and is accommodated wholly by the parent lattice. In contrast, the topological theory imputes a local lattice distortion to the additional component of the interfacial Burgers vector content that is perpendicular to the interface, which causes the interface to tilt. This rotation is partitioned between the parent and the double twin, and for an infinite interface, the range of the distortion

C-T DT	$(10\bar{1}1)-(10\bar{1}2)$	$(10\bar{1}1)-(\bar{1}012)$	$(10\bar{1}\bar{3})-(10\bar{1}2)$	$(10\bar{1}\bar{3})-(\bar{1}012)$
	type 1	type 2	type 2	type 1
ϕ	-9.1°	-7.3°	-7.2°	-5.4°
ψ	0.4°	-7.4°	7.1°	-0.1°
$\phi+\frac{\psi}{2}$	-8.9°	-11.0°	-3.6°	-5.5°
misfit-free	no	yes	no	no
T-C DT	$(10\bar{1}2)-(10\bar{1}1)$	$(\bar{1}012)-(10\bar{1}1)$	$(10\bar{1}2)-(10\bar{1}\bar{3})$	$(\bar{1}012)-(10\bar{1}\bar{3})$
	type 1	type 2	type 2	type 1
ϕ	9.7°	7.8°	7.7°	5.8°
ψ	-0.4°	-7.6°	7.6°	0.1°
$\phi+\frac{\psi}{2}$	9.5°	4.0°	11.5°	5.8°
misfit-free	no	yes	no	no

Table 3.6 Angles defining misfit-free interfaces with added rotational distortion as described by the topological model, for compression-tension and tension-compression double twin mechanisms. ϕ is calculated using equation 3.93 and ψ is calculated using equation 3.96 (where a minus sign is introduced for the $(10\bar{1}1)-(\bar{1}012)$ mechanism where the tilt components of the primary and secondary twinning disconnections have opposite signs). The rotation axis is the normal to the plane of shear $(1\bar{2}10)$. The results are given for $\gamma = 1.624$. Whether the misfit-free condition may be achieved for each mechanism is marked by a yes or no in the "misfit-free" row.

field is of the order of the spacing of the disconnections, and thus relatively localised [139]. Hence, although the phenomenological and topological models predict essentially the same lattice rotation, as may be seen by comparing values of ψ in table 3.6 with those in tables 3.3 and 3.4, this is a long-ranged distortion in the former case, and a short-ranged one in the latter.

Finally, the main distinction between the two models is in their treatments of the mechanisms of formation of the double twin to matrix interface. The phenomenological theory postulates that soon after the formation of a small primary twin nucleus, this retwins internally, thus becoming a double twin embryo. The double twin then expands by growing via a simple shear mechanism on a new habit plane that is an invariant plane of the double twin transformation. Conversely, according to the topological model, twin growth is the result of the motion of twinning disconnections. An array of residual primary twinning disconnections in the primary twin boundary then interacts with incoming secondary twinning disconnections, and the spacing in each array is adjusted such that misfit across the interface may be minimised. The final interface is thus rendered immobile, and further growth of the double twin is impeded. Hence, the topological model requires that a sizeable primary twin be formed first, subsequently undergoing

internal retwinning that prevents any expansion of the doubly twinned volume. Indeed, it may be shown that there are no admissible twinning disconnections that may be glissile on the misfit-free habit planes predicted by the topological model, or the invariant habit planes of Crocker's theory. It is then clear that the two models propose what may be referred to as one- and two-step processes for double twin formation: the phenomenological theory predicting that a double twin may grow on an invariant plane in one step, and the topological model envisaging the full formation of a primary twin followed by internal growth of the secondary twin in two distinct steps. The narrow size of double twins observed experimentally points in the direction of impeded growth, and thus of the two-step process of the topological model. This possibility will be investigated further in the next chapter, with a study on the interplay of twinning disconnections that does not include the requirement of a final interface that is misfit-free, as well as with experimental observations.

Chapter 4

Faceting at twin interfaces

"There is nothing like looking, if you want to find something (or so Thorin said to the young dwarves). You certainly usually find something, if you look, but it is not always quite the something you were after."

The Hobbit, JOHN R. R. TOLKIEN

In this chapter we examine a case that was not considered in the previous chapter on double twinning: that of faceted interfaces. We proposed topological models for secondary twinning disconnections impinging on *i)* a flat coherent primary twin interface (section 3.4.1) and *ii)* a terraced primary twin interface containing equally spaced disconnections (section 3.4.2). However, high-resolution experimental observations of twin boundaries in hcp metals often show that the interfaces are not flat, but contain facets of varying length. In the following sections, we review the theoretical and experimental literature on faceting at single twin interfaces, and then proceed to study how such interfaces may be modified as a consequence of secondary twinning. In the second part of the chapter, we then validate theoretical predictions against transmission electron microscopy (TEM) observations of twinning in a magnesium alloy.

4.1 Topological models of facets

Facets are often reported in twin interfaces in hcp metals. These are segments of interface that are inclined at an angle to the K_1 plane, and that are aligned with rational planes on either side

of the interface. They are conventionally designated by the initials of the planes brought into coincidence at the facet interface. In this section, we adopt the following notation: the plane of the matrix is listed first, followed by the plane of the twin, such that e.g. BP stands for $\mathrm{B}^{\mathrm{matrix}}\mathrm{P}^{\mathrm{twin}}$.

4.1.1 Facets in $(10\bar{1}2)$, $(10\bar{1}1)$ and $(10\bar{1}\bar{3})$ twin interfaces

The facets observed at $(10\bar{1}2)$ tension twin interfaces present the basal (B) plane of the matrix in alignment with the prismatic (P) plane of the twin (BP facet) or vice versa (PB facet). The occurrence of such facets in the tension twin interface may be explained in the topological model of chapter 2 through the notion of twinning disconnections. In figure 4.1a, we propose once again the dichromatic pattern for the $(10\bar{1}2)$ twin, drawing, as before, translation vectors of the matrix μ and twin λ that produce the Burgers vector of the twinning disconnection responsible for the growth of the twin, whose step has height $h = -2d_{(10\bar{1}2)}$. The translation vectors are given by $\mathbf{t}(\mu) = [000\bar{1}]$ and $\mathbf{t}(\lambda) = [10\bar{1}0]$, such that it may be noticed that $\mathbf{t}(\mu)$ lies in the prismatic plane of the matrix and $\mathbf{t}(\lambda)$ lies in the basal plane of the twin, and for this reason we label them $\mathbf{P}(\mu)$ and $\mathbf{B}(\lambda)$ in figure. Therefore, this disconnection creates an interface where the prismatic plane of the matrix (μ) and the basal plane of the twin (λ) are brought into coalescence, and it may be seen as small PB facet, or microfacet [146]. Ostapovets et al. [147] have shown that the disconnection is able to accommodate the mismatch between the basal plane of the twin and the prismatic plane of the matrix, which indeed are not parallel. Similarly, a BP facet may be created by taking λ as the matrix and μ as the twin.

Successive twinning disconnections grow the twin by an amount corresponding to the height of their step as they glide on the composition plane, as was explained in chapter 2. If however an obstacle is placed along the twin interface, the motion of a disconnection may be stopped, at least until enough stress is applied that the disconnection is able to overcome it; such obstacles may be represented by solute atoms or precipitates. The disconnections arriving behind the pinned disconnection then pile up behind the latter, forming a macrostep, and resulting in a longer facet; this is possible because at short range, there is an attractive force between the disconnections [125]. Such a situation, shown schematically in figure 4.1b-c, was observed in computer simulations of magnesium modelled with EAM potentials [147–149], suggesting

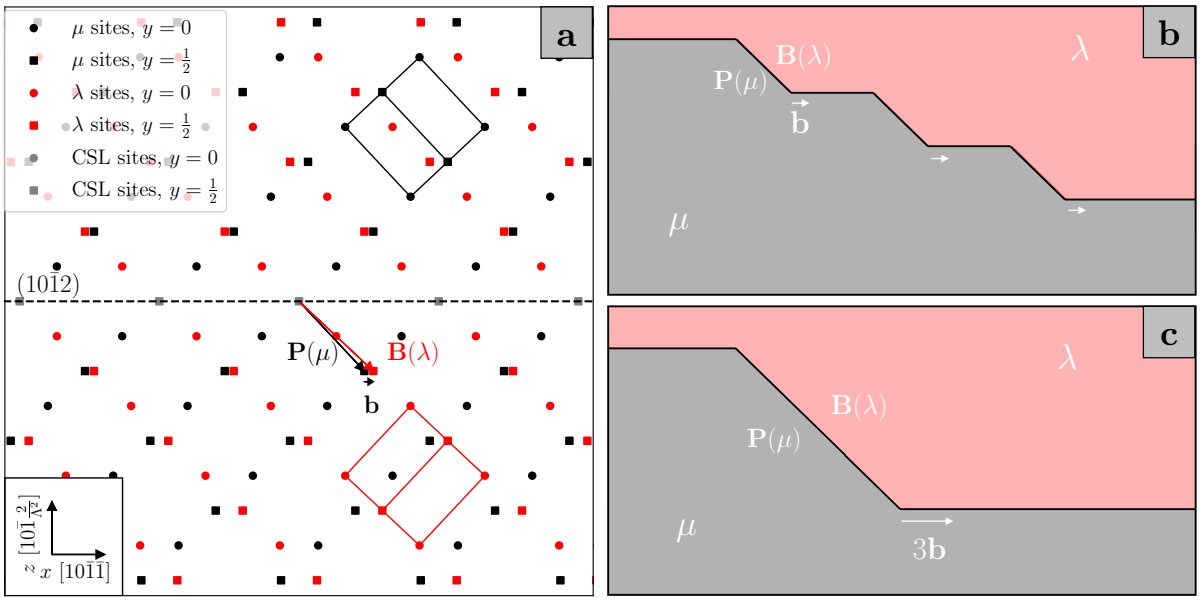

Fig. 4.1 (a) Twinning disconnection bringing into coincidence the prismatic plane of the matrix μ and the basal plane of the twin λ in a $(10\bar{1}2)$ twin interface, for $\gamma = 1.624$. μ sites, in black, belong to the matrix; λ sites, in red, belong to the twin. The hexagonal unit cells are similarly drawn for each lattice. The translation vectors that define the disconnections are denoted by the names of the planes they lie in, in order to highlight the kinds of facets they can form. The projection direction is $[1\bar{2}10]$. (b)-(c) schematic of a pileup of twinning disconnections leading to the formation of a PB facet in a $(10\bar{1}2)$ twin boundary.

that an accumulation of twinning disconnections may be responsible for the BP and PB facets observed experimentally. Moreover, the formation energy of facets of this kind was found to be comparable to that of the tension twin boundary, thus pointing towards the stability of the facets [147].

This model provides a mechanism for facet migration as well as formation. Upon overcoming the obstacle or following its removal, the component disconnections are emitted from the facet and glide once more on the composition plane, as opposed to movement of the facet as a whole, such that it would be misleading to identify the facet as a "superdisconnection" [147].

Facets may also be modelled as disclinations, i.e. defects that arise when point symmetry operations from either crystal do not coincide in the bicrystal, such that they are characterised by a rotation (see chapter 2). In particular, an interfacial facet may be described as a disclination dipole by decomposing the Burgers vector of the twinning disconnections that form it into a disclination dipole vector plus the Burgers vector of a residual dislocation [150–152, 125, 153].

This is possible because a disclination dipole has dislocation character, that is it may be modelled as a dislocation tilt wall [154].

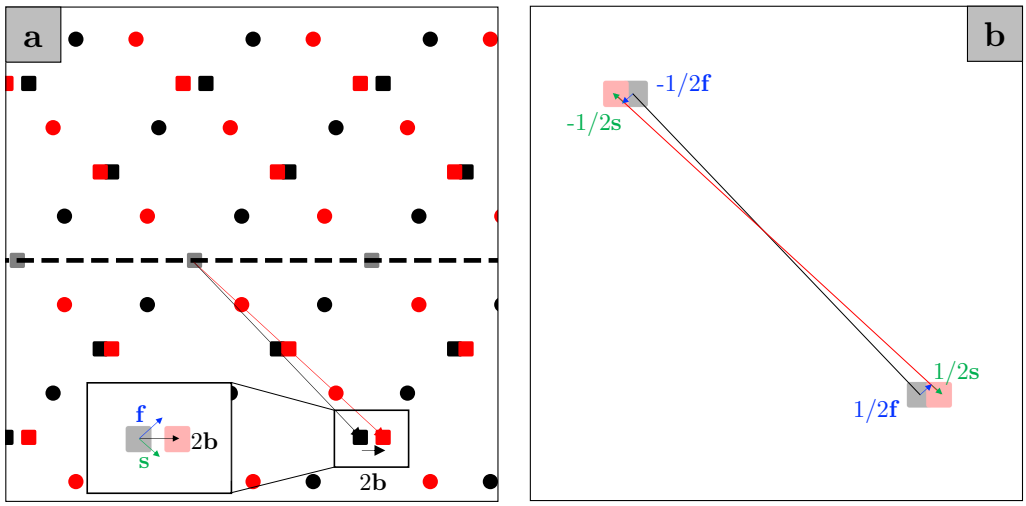

Fig. 4.2 (a) Decomposition of a twinning disconnection bringing into coincidence the prismatic plane of the matrix μ and the basal plane of the twin λ in a $(10\bar{1}2)$ twin interface, for $\gamma = 1.624$, into a disclination with Frank vector $\mathbf{f}$ and a dislocation with Burgers vector $\mathbf{s}$. μ sites, in black, belong to the matrix; λ sites, in red, belong to the twin. (b) Partitioning of the Frank vector into a disclination dipole.

The decomposition may be understood with the help of the dichromatic pattern once again, figure 4.2a. First of all, we notice that in order to align the prismatic plane of the matrix with the basal plane of the twin, we may rotate the two crystals relative to each other about the normal to the plane of shear by an angle θ, which for magnesium, $\gamma = 1.624$, is 3.14°. The dislocation content of a disclination obtained by applying such a rotation $\mathbf{R}$ is given by the Frank vector $\mathbf{f}$ [155], drawn in blue in figure 4.2a:

$$\mathbf{f} = \mathbf{R}\mathbf{o} - \mathbf{o}, \tag{4.1}$$

where $\mathbf{o}$ is the vector connecting the poles of the disclination. It is now evident that $\mathbf{f}$ may be subtracted from the Burgers vector of the twinning disconnection forming the facet, obtaining a dislocation with Burgers vector parallel to the facet plane [150]. So far it has been assumed that only one of the two crystals is rotated by the disclination, but in practice this rotation, which corresponds to a lattice distortion, has to be partitioned between the two crystals. For this reason, the disclination is effectively two disclinations with the same θ meeting at a midpoint, and the Frank vector is partitioned into components $\pm\frac{\mathbf{f}}{2}$ at the two extremities [125], as shown in figure

4.2b. The disclination dipole derived in this way has the long range stress field of a dislocation [156, 157].

In addition to disconnection accumulation behind an obstacle, a second mode of formation of facets in a $(10\bar{1}2)$ boundary has been reported, and it was mentioned in chapter 2 amid discussion of the creation of loops of twinning disconnections. This is the interaction of matrix dislocations with the twin interface, which, while producing twinning disconnections, also leaves behind residual defects in the boundary that may be seen as facets [116, 119, 117, 123, 118, 158]. In order to discuss these mechanisms in more detail we introduce a simple notation used in the literature on the subject: the Burgers vector of dislocations and disconnections is denoted by $\mathbf{b}_{p/q}$, where p and q are the number of $(10\bar{1}2)$ lattice planes of λ and μ along $\mathbf{t}(\lambda)$ and $\mathbf{t}(\mu)$ respectively, such that $p = h(\lambda)/d_{(10\bar{1}2)}$ and $q = h(\mu)/d_{(10\bar{1}2)}$. For twinning disconnections, p and q are equal, since $h(\lambda) = h(\mu)$ as derived in chapter 2, equation 2.46. Thus the 2-layer twinning disconnection in the dichromatic pattern in figure 4.3a is denoted by $\mathbf{b}_{-2/-2}$, and a matrix dislocation is denoted by $\mathbf{b}_{p/0}$.

The first interaction studied is that of a basal dislocation with $\mathbf{b}_{1/0} = \frac{1}{3}[11\bar{2}0]$ inclined 60° to the $(10\bar{1}2)$ twin boundary. Serra and Bacon [116] and Serra et al. [159] showed that this dislocation may decompose into twinning disconnections and other products following the reaction

$$\mathbf{b}_{1/0} = n\mathbf{b}_{2/2} + \mathbf{b}_{-(2n-1)/-2n}. \tag{4.2}$$

In their many-body potential simulation of Ti, Serra and Bacon [116] found that the most frequently occurring reaction was that with $n = 3$, that is

$$\mathbf{b}_{1/0} = 3\mathbf{b}_{2/2} + \mathbf{b}_{-5/-6}. \tag{4.3}$$

This reaction is shown in figure 4.3c.

It may be seen from the dichromatic pattern in figure 4.3a that the defect $\mathbf{b}_{-5/-6}$ brings together the prismatic plane of the matrix μ and the basal plane of the twin λ, thus creating a PB facet, whose length may be increased following the addition of $\mathbf{b}_{2/2}$ twinning disconnections. This defect is immobile, but under shear stress it may emit twinning disconnection pairs with

opposite Burgers vector that cause the twin interface to migrate by $2d_{(10\bar{1}2)}$ and the defect $\mathbf{b}_{-5/-6}$ to be displaced laterally [117]; this mechanism is shown in figure 4.3d.

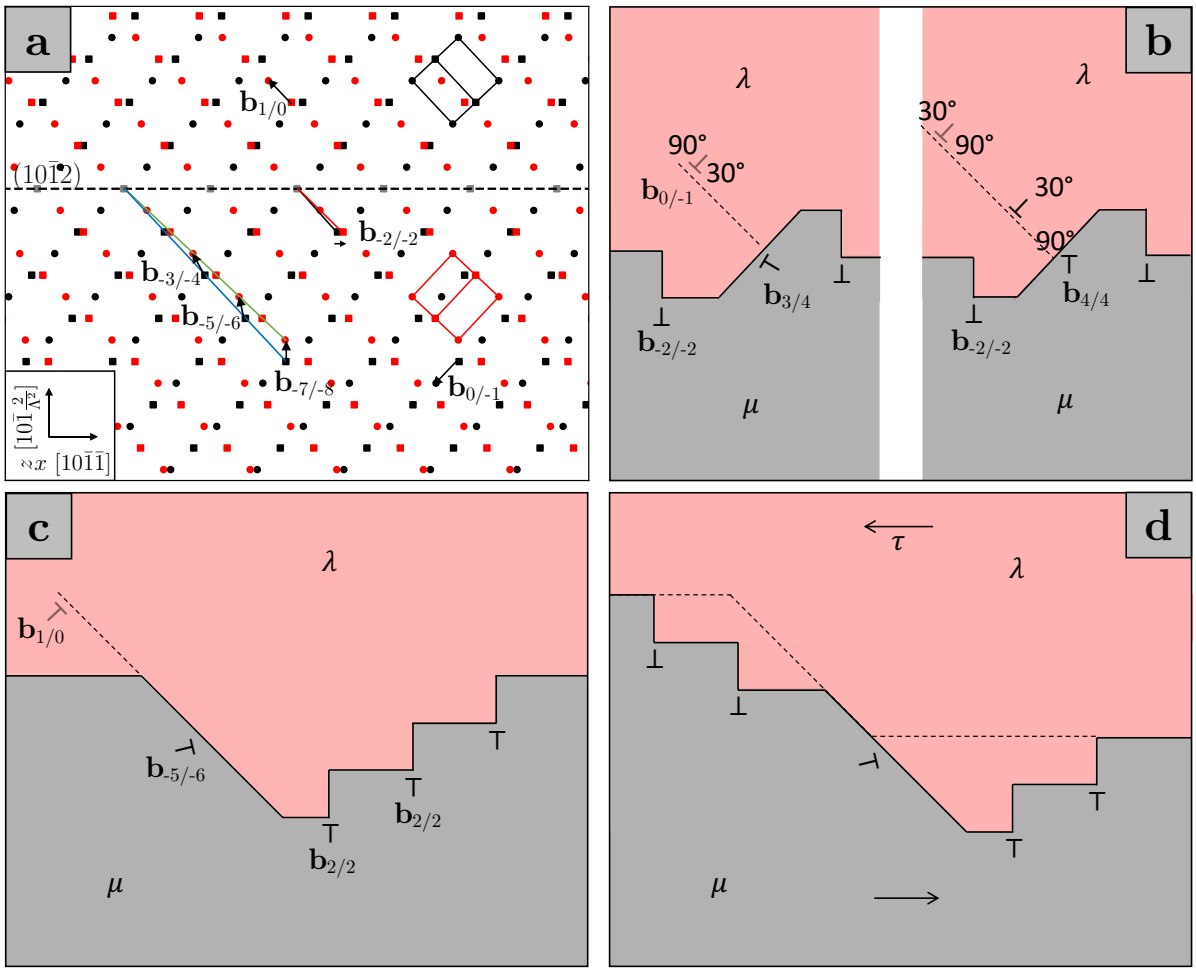

Fig. 4.3 Figure adapted for magnesium $\gamma = 1.624$ from [118]. (a) Dichromatic pattern of the $(10\bar{1}2)$ twin depicting the Burgers vectors (in black) of matrix dislocations and interfacial defects. The legend is as in figure 4.1a, with μ sites in black and λ sites in red. (b) Mechanisms of formation of an interfacial BP facet as a consequence of the interaction between the $(10\bar{1}2)$ twin boundary and a $\mathbf{b}_{0/-1}$ dislocation. (c) Mechanism of formation of an interfacial PB facet via the interaction between the $(10\bar{1}2)$ twin boundary and a $\mathbf{b}_{1/0}$ dislocation. (d) Displacement of the PB facet created in (c) via the emission of twinning disconnections. In (b) and (c), the dislocations depicted at the top of the dotted lines are to be interpreted as the initial lattice dislocations, with the products of dislocation reactions indicated at the lower end of the lines.

More recently, using a larger cell and periodic boundary conditions in simulations of Zr, Serra and Bacon [123] found that the reaction

$$\mathbf{b}_{1/0} = 4\mathbf{b}_{2/2} + \mathbf{b}_{-7/-8} \tag{4.4}$$

occurred more often than the one producing a $\mathbf{b}_{-5/-6}$ defect, which however was also observed by Serra et al. [118] in molecular dynamics simulations of Zr. In practice, the $\mathbf{b}_{-7/-8}$ defect behaves as the $\mathbf{b}_{-5/-6}$ one, emitting disconnection pairs when a high enough shear stress is applied [160].

The second interaction of a matrix dislocation with a $(10\bar{1}2)$ twin boundary that has attracted focus is that entailing a basal dislocation with opposite sign, $\mathbf{b}_{-1/0} = \frac{1}{3}[\bar{1}\bar{1}20]$. This dislocation dissociates into two partial dislocations, labelled $\mathbf{b}^{90}$ and $\mathbf{b}^{30}$ as their Burgers vectors make angles of 90° and 30° respectively with $\mathbf{b}_{-1/0}$; the dislocation reaction occurring at the twin interface depends on which of these is the leading partial, arriving at the boundary first; both reactions are shown in figure 4.3b. If the $\mathbf{b}^{90}$ partial is leading, this is absorbed by the boundary while the $\mathbf{b}^{30}$ partial is left isolated from the boundary by a stacking fault, and the dislocation reaction is the following [159, 123, 118]:

$$\mathbf{b}_{-1/0} = 2\mathbf{b}_{-2/-2} + \mathbf{b}^{30} + (\mathbf{b}^{90} + \mathbf{b}_{4/4}). \tag{4.5}$$

The $\mathbf{b}_{4/4}$ disconnection brings into coincidence the basal plane of the matrix and the prismatic plane of the twin, thus forming a BP facet.

If the leading partial is $\mathbf{b}^{30}$, both partials are absorbed by the boundary, as the attraction between the $\mathbf{b}^{90}$ partial and the twin interface pushes the entire basal dislocation towards it; the dislocation reaction is then [123, 118]

$$\mathbf{b}_{-1/0} = 2\mathbf{b}_{-2/-2} + \mathbf{b}_{3/4}, \tag{4.6}$$

where the $\mathbf{b}_{3/4}$ defects forms a BP facet. Upon applying a shear stress to either the $\mathbf{b}_{4/4} + \mathbf{b}^{90}$ or $\mathbf{b}_{3/4}$ configurations, the facet is displaced with migration of the twin boundary via the emission of twinning disconnection pairs [123, 118]. These dislocation reactions, along with the ones resulting from the interaction of a $\mathbf{b}_{1/0}$ dislocation with a $(10\bar{1}2)$ twin boundary, were recently studied and validated based on high-resolution TEM observations of a magnesium alloy [161].

Faceting of $(10\bar{1}1)$ twin interfaces has not been studied as extensively. However, this case may be treated similarly to that of facets in the $(10\bar{1}2)$ twin interface. From the dichromatic pattern of the $(10\bar{1}1)$ twin (figure 4.4a), we may surmise that two kinds of facet can form

in this interface as a consequence of disconnection morphology. Taking $\mathbf{t}_1(\mu) = [10\bar{1}2]$ and $\mathbf{t}_1(\lambda) = [\bar{2}020]$, we see that $\mathbf{t}_1(\mu)$ lies in the first pyramidal plane (Py, $(\bar{1}011)$) of the matrix μ and $\mathbf{t}(\lambda)$ lies in the basal plane of the twin λ, such that the resulting 4-layer disconnection with Burgers vector $\mathbf{b}_1$ brings the two planes into coincidence. It may thus be regarded as a small PyB facet [146], and equivalently, a BPy facet may be obtained by exchanging μ and λ. The second kind of microfacet is produced by taking $\mathbf{t}_2(\mu) = [30\bar{3}\bar{2}]$ and $\mathbf{t}_2(\lambda) = [000\bar{4}]$, which lie respectively in the third pyramidal plane (3Py, $(10\bar{1}3)$) of μ and in the prismatic plane of λ. Although the resulting Burgers vector $\mathbf{b}_2$ is the same as that originating from the first pair of translation vectors, the planes brought into coincidence by the disconnection are different, and in this way a small 3PyP facet is formed, or a P3Py facet if μ and λ are interchanged [152]. As for tension twin interfaces, facets can form in a $(10\bar{1}1)$ twin boundary as a consequence of the accumulation of twinning disconnections behind an obstacle [146]. This accumulation may also be modelled as a disclination dipole, following the procedure illustrated for the $(10\bar{1}2)$ twin: the Burgers vector of the twinning disconnection is understood to decompose into the Frank vectors of the disclination dipoles and the Burgers vector of a dislocation parallel to the facet plane. This analysis was carried out by Barrett et al. [152].

Contrary to the case of the $(10\bar{1}2)$ twin, interaction of matrix dislocations with the $(10\bar{1}1)$ interface has not been found to lead to the creation of facets. In particular, a $\mathbf{b}_{1/0} = \frac{1}{3}[11\bar{2}0]$ basal dislocation was observed, in many-body potential simulations of Ti, to be stopped by the $(10\bar{1}1)$ interface without being absorbed or transmitted [119]. A $\mathbf{b}^{\text{screw}} = \frac{1}{3}[1\bar{2}10]$ screw dislocation interacting with the $(10\bar{1}1)$ twin boundary was also simulated, and in the ensuing reaction two disconnections of height $2d_{(10\bar{1}1)}$ and Burgers vector of opposite sign, of the kind described in chapter 2, were created, with no residual defects in the boundary [128]. Not only was no facet created, but the two steps formed, upon moving concertedly, do not displace the twin boundary, and thus do not jointly represent a twinning disconnection.

Finally, facets may also occur in a $(10\bar{1}\bar{3})$ twin boundary, as we notice from the dichromatic pattern in figure 4.4b. Similarly to the $(10\bar{1}1)$ twin, we may take $\mathbf{t}_1(\mu) = [\bar{1}01\bar{2}]$ and $\mathbf{t}_1(\lambda) = [\bar{2}020]$, such that they lie respectively in the first pyramidal plane of μ and the basal plane of λ. Then the resulting Burgers vector $\mathbf{b}_1$ gives rise to a disconnection that may be seen as a small PyB facet, and a BPy facet may be obtained by exchanging matrix and twin. Alternatively, the

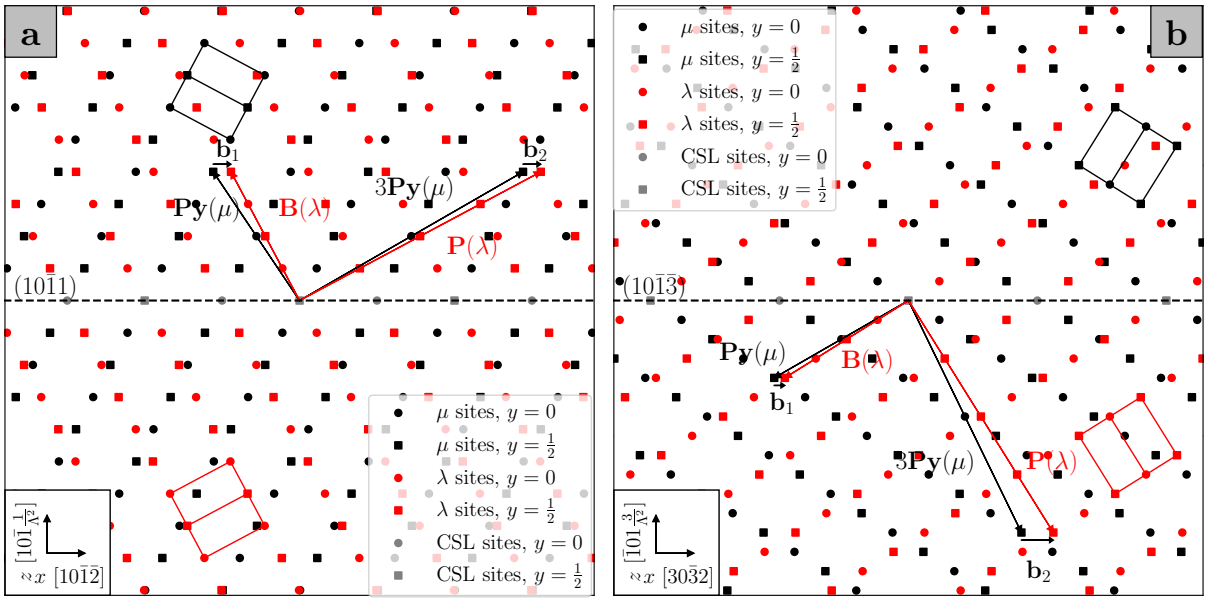

Fig. 4.4 Twinning disconnections bringing into coincidence the first pyramidal plane of the matrix μ and the basal plane of the twin λ (Burgers vector $\mathbf{b}_1$) or the third pyramidal plane of the matrix μ and the prismatic plane of the twin λ (Burgers vector $\mathbf{b}_2$) in (a) a $(10\bar{1}1)$ twin interface and (b) a $(10\bar{1}\bar{3})$ twin interface. The translation vectors that define the disconnections are denoted by the names of the planes they lie in, in order to highlight the kinds of facets they can form. $\gamma = 1.624$. μ sites, in black, belong to the matrix; λ sites, in red, belong to the twin. The hexagonal unit cells are similarly drawn for each lattice. The projection direction is $[1\bar{2}10]$.

translation vectors producing a twinning disconnection may be taken to be $\mathbf{t}_2(\mu) = [30\bar{3}\bar{2}]$ and $\mathbf{t}_2(\lambda) = [0004]$: then $\mathbf{t}_2(\mu)$ lies in the third pyramidal plane of the matrix, and $\mathbf{t}(\lambda)$ lies in the prismatic plane of the twin, and the twinning disconnection can be regarded as a small 3PyP facet, with a P3Py facet obtained by exchanging μ and λ. This disconnection, however, is characterised by a Burgers vector $\mathbf{b}_2$ that is three times larger than that of the previous disconnection presented and a step height of $12d_{(10\bar{1}\bar{3})}$, making it much less likely to occur; P3Py and 3PyP facets in the $(10\bar{1}\bar{3})$ twin interface are therefore unlikely to form. Conversely, accumulation of disconnections of the first kind behind an obstacle will lead to the formation of macroscopic interfacial PyB or BPy facets. Comparing these with the previous analysis of the compression twin, it may be noticed that these facets are the same as those formed in the $(10\bar{1}1)$ twin interface. They have been similarly treated as disclination dipoles by Barrett and coworkers [152].

As mentioned above, facets have been observed in experimental analyses of tension and compression twin boundaries using high-resolution transmission electron microscopy. In particular, BP and PB facets in $(10\bar{1}2)$ interfaces were widely reported to occur in magnesium, cobalt and

zinc [161–169], including around the deformed tip of a twin [170, 171]. BPy, PyB, P3Py and 3PyP facets were found in $(10\bar{1}1)$ twin boundaries in titanium [172], magnesium [173, 174] and cobalt [175]. BPy and PyB facets were observed in $(10\bar{1}3)$ twin boundaries in cobalt [176]. In many cases, the macroscopic twin boundaries were reported to deviate from the K_1 planes by significant amounts [172, 162, 174]; it is reasonable to infer that these deviations may be attributed to the presence of facets in the twin boundaries, with the length and density of the facets determining the magnitude of the deviation.

4.1.2 Faceting in double twin boundaries

Having discussed the admissible interfacial facets for tension and compression twinning in magnesium, we now focus on how these facets may be affected by secondary twinning. As we have shown that facets can be present in single twin boundaries, it follows that in the case of double twinning, they will arise in both the primary and secondary twin interface. We shall take the view that the facets result from the accumulation of twinning disconnections, as mentioned above. As the secondary twin grows, facets in the internal interface between primary and secondary twin disintegrate into the component secondary twinning disconnections, which move towards the primary twin interfaces. If the primary twin interface is faceted, the secondary twinning disconnections impinge on two kinds of interface: *i)* the flat coherent terraces parallel to the K_1 plane of the primary twin and *ii)* the preexisting facets formed by primary twinning disconnections. The situation in *i)* was examined in section 3.4.1, where it was concluded that the effect of secondary twinning disconnections encountering a flat primary twin boundary would be to rotate the boundary by a maximum of a fraction of a degree for type 1 double twinning mechanisms and a few degrees for type 2 mechanisms. We shall now discuss situation *ii)*, and ascertain how facets in the primary twin interface are transformed by the arrival of secondary twinning disconnections.

We begin by analysing compression-tension mechanisms, in particular the $(10\bar{1}1) - (10\bar{1}2)$ type 1 double twin sequence, figure 4.5a. In order to visualise the double twinning transformation in stages, we construct a trichromatic pattern, i.e. a pattern with three sets of lattice points: the first two represent the matrix μ and the primary twin λ, and are given by black and red circles and squares respectively, as before; the third set of points represents the secondary twin ν, given

by white open circles. As discussed in previous chapters, λ sites are obtained by applying a rotation of 180° about the $\boldsymbol{\eta}_1$ direction of the primary twin, $\mathbf{R}_A$, to μ sites; ν sites are obtained by applying to the μ lattice the total double twin transformation $\mathbf{R}_A\mathbf{R}_B$ (equation 3.2), where $\mathbf{R}_B$ is a rotation of 180° about the $\boldsymbol{\eta}_1$ direction of the secondary twin, expressed in the coordinate system of the primary twin. The trichromatic pattern is projected along the normal to the plane of shear common to the $(10\bar{1}1)$ and $(10\bar{1}2)$ mechanisms, i.e. $(1\bar{2}10)$, and we are now able to visualise the Burgers vectors of both secondary and primary twinning disconnections. In particular, in figure 4.5a we choose as the pair of translation vectors producing the Burgers vector of the primary twinning disconnection $\mathbf{t}_1(\mu) = \mathbf{Py}(\mu)$ and $\mathbf{t}_1(\lambda) = \mathbf{B}(\lambda)$ of figure 4.4a, which give rise to a PyB microfacet; the Burgers vector of this disconnection is labelled $\mathbf{b}_A$, and it shears a μ site into the primary twin position λ. The λ site then undergoes the secondary twinning shear and is brought to a ν site: this is accomplished by two secondary twinning disconnections with Burgers vector $\mathbf{b}_B = \frac{2-\Lambda^2}{2+\Lambda^2}[10\bar{1}\bar{1}]^\lambda$ (see chapter 2). The translation vectors $\mathbf{t}(\lambda)$ and $\mathbf{t}(\nu)$ from which $\mathbf{b}_\mathrm{B}$ is obtained lie respectively in the basal plane of the primary twin and in the prismatic plane of the secondary twin. Thus, a PyB facet in the primary twin boundary combines with a BP facet of the secondary twin to form a PyP facet in the double twin boundary as a result of the combination of two secondary twinning disconnections for every one primary twinning disconnection. The total Burgers vector that generates such a PyP facet is then given in the coordinate frame of the matrix by

$$\mathbf{b}_\mathrm{PyP} = \mathbf{b}_A + 2\mathbf{R}_A\mathbf{b}_B. \tag{4.7}$$

On the other hand, the other set of translation vectors producing a primary twinning disconnection presented in figure 4.4a may be chosen, such that $\mathbf{t}_2(\mu) = 3\mathbf{Py}(\mu)$ and $\mathbf{t}_2(\lambda) = \mathbf{P}(\lambda)$. This disconnection then produces a 3PyP facet. In order to shear site λ into site ν, four secondary twinning disconnections will now be necessary, as one can see from figure 4.5b. In this case $\mathbf{t}(\nu)$ lies in the basal plane of the secondary twin, and the resulting double twin facet is a combination of a 3PyP facet in the primary twin interface and a PB facet in the secondary twin interface, i.e. a 3PyB facet. Its Burgers vector content is given by

$$\mathbf{b}_\mathrm{3PyB} = \mathbf{b}_A + 4\mathbf{R}_A\mathbf{b}_B. \tag{4.8}$$

Consequently, two kinds of commensurate facets can be formed in a type 1 $(10\bar{1}1)-(10\bar{1}2)$ double twin interface: PyP and 3PyB.

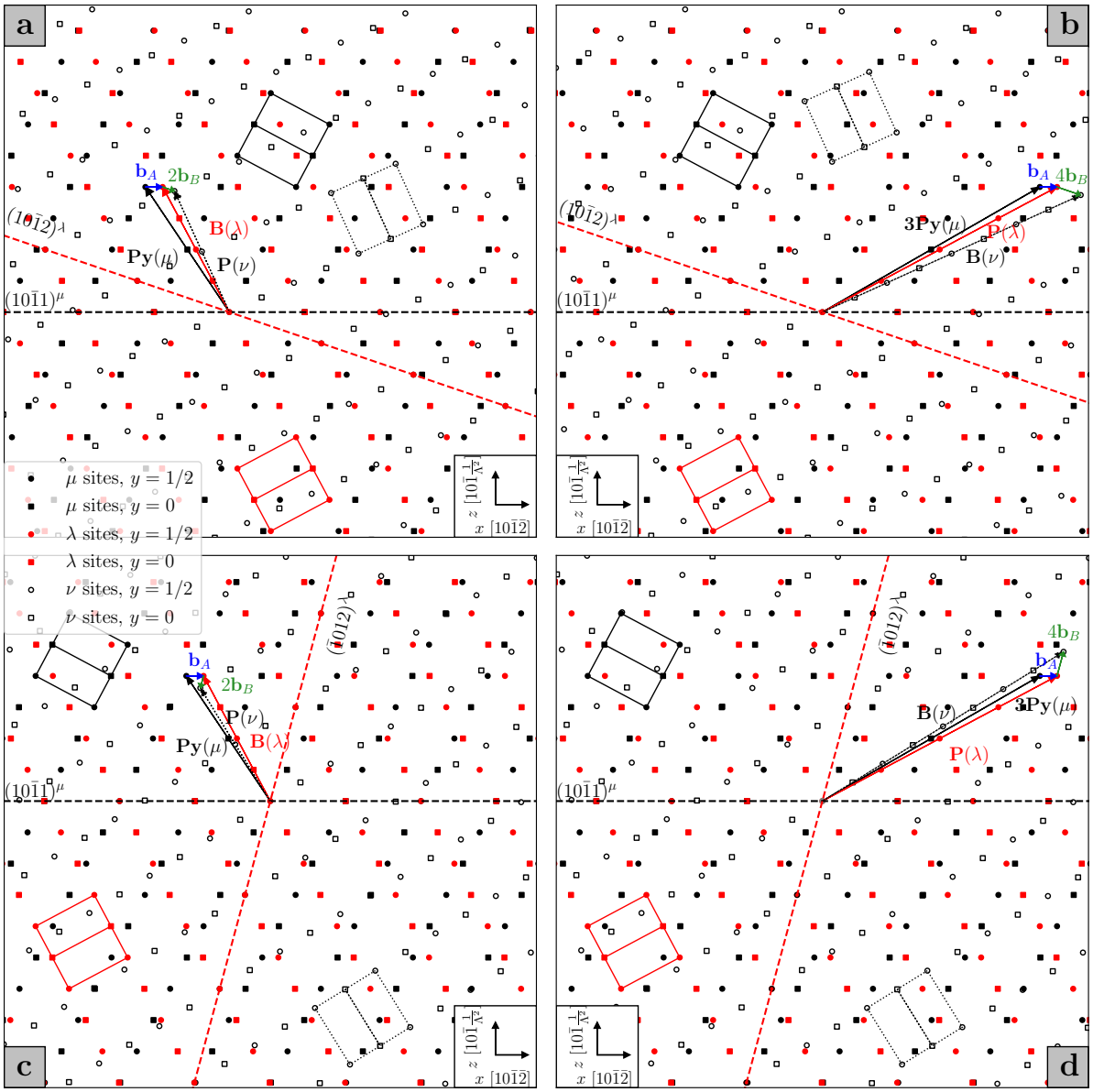

Fig. 4.5 $(10\bar{1}1)-(10\bar{1}2)$ double twin facets for types 1 ((a) and (b)) and 2 ((c) and (d)), $\gamma = 1.624$. μ sites, in black, belong to the matrix; λ sites, in red, belong to the primary twin; ν sites, in white, belong to the secondary twin. The hexagonal unit cells are similarly drawn for each lattice. The translation vectors that define the disconnections are denoted by the names of the planes they lie in, in order to highlight the kinds of facets they can form. The projection direction is $[1\bar{2}10]$.

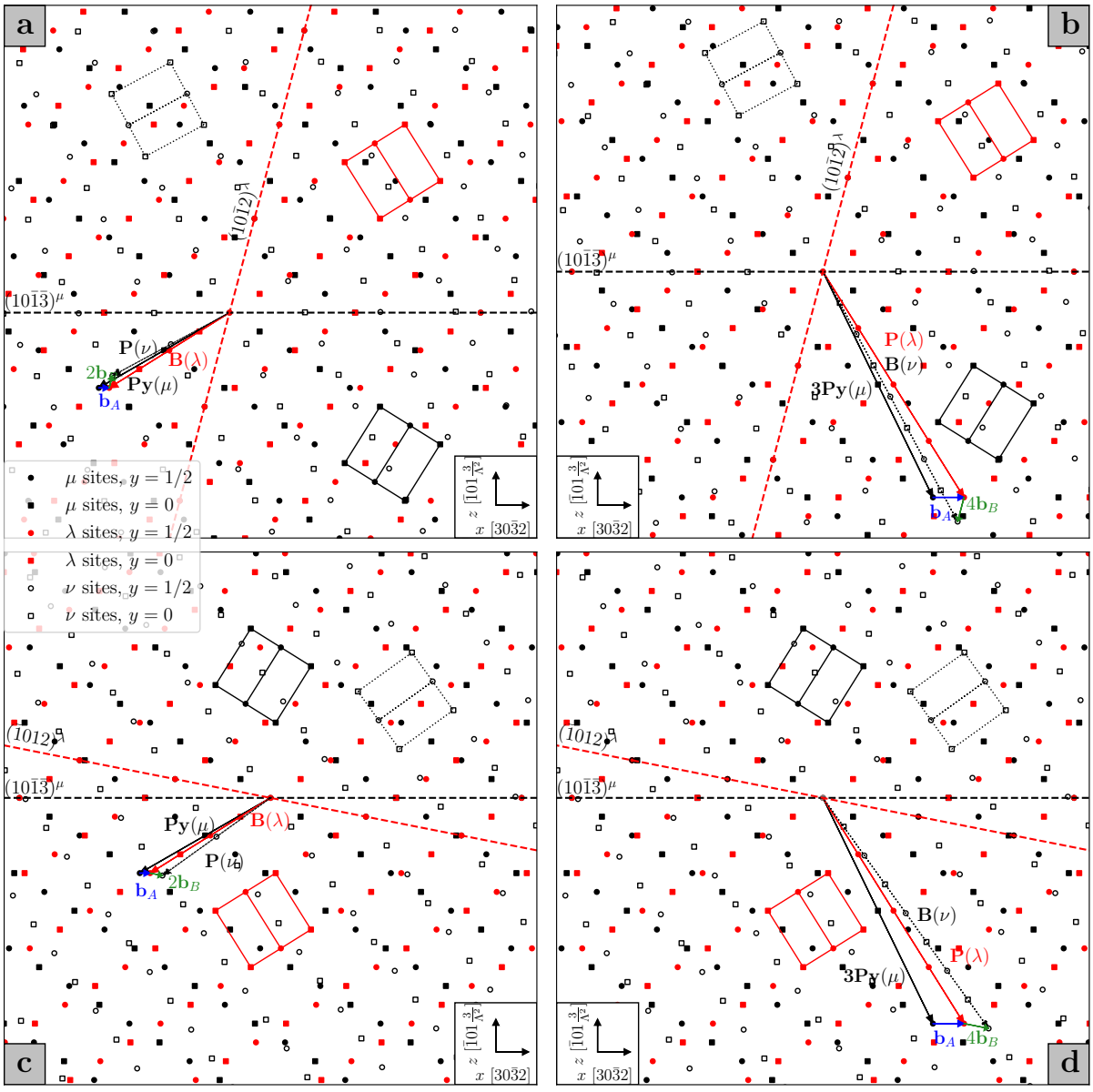

Fig. 4.6 $(10\bar{1}\bar{3}) - (10\bar{1}2)$ double twin facets for types 2 ((a) and (b)) and 1 ((c) and (d)), $\gamma = 1.624$. μ sites, in black, belong to the matrix; λ sites, in red, belong to the primary twin; ν sites, in white, belong to the secondary twin. The hexagonal unit cells are similarly drawn for each lattice. The translation vectors that define the disconnections are denoted by the names of the planes they lie in, in order to highlight the kinds of facets they can form. The projection direction is $[1\bar{2}10]$.

Similarly we may examine the case of $(10\bar{1}1) - (\bar{1}012)$ double twin interfaces, i.e. type 2, and show that the same kinds of facets may be created as in the type 1 mechanism. This situation is illustrated by the trichromatic patterns of figure 4.5c-d: the secondary K_1 plane is now $(\bar{1}012)$, but the twinning disconnections at play are unchanged. If the primary twinning disconnection is taken to generate a PyB facet of the primary twin interface, then two secondary twinning disconnections

forming a BP facet on the internal secondary twin interface transform the initial facet into a PyP facet of the double twin, figure 4.5c. If instead a primary twinning disconnection forming a 3PyP facet in the interface is present, four secondary twinning disconnections describing secondary PB facets will be needed to create a 3PyB facet in the double twin interface, figure 4.5d.

Moreover, the same treatment may be applied to the derivation of facets in $(10\bar{1}\bar{3})-(10\bar{1}2)$ double twin interfaces, as the facets that may be produced in the $(10\bar{1}\bar{3})$ interface are the same as those of the $(10\bar{1}1)$ twin case. This is illustrated by the trichromatic patterns of figure 4.6. From figure 4.6a, depicting the lattices in the $(10\bar{1}\bar{3})-(10\bar{1}2)$ type 2 twinning sequence, one can see that by combining a PyB facet of the primary twin with a BP facet of the secondary twin a PyP facet is obtained. This is produced by one primary twinning disconnection and two secondary twinning disconnections, so that equation 4.7 for the total Burgers vector content applies: the only difference is that $\mathbf{R}_A$ is now the characteristic rotation of $(10\bar{1}\bar{3})$ twinning, i.e. a rotation of 180° about $\boldsymbol{\eta}_1 = [30\bar{3}2]$. A similar PyP facet may arise in the case of the type 1 mechanism, $(10\bar{1}\bar{3})-(\bar{1}012)$, as it can be noted from figure 4.6c. On the other hand, a primary twinning disconnection producing a 3PyP facet in the primary twin interface may be chosen: then, four secondary twinning disconnections, forming a PB facet, are necessary to form a 3PyB facet in the double twin to matrix interface, such that equation 4.8 applies, provided that $\mathbf{R}_A$ is modified according to $(10\bar{1}\bar{3})$ twinning parameters. This facet is illustrated for both type 2 (figure 4.6b) and type 1 (figure 4.6d) double twinning. However, as explained in the previous section, the 3PyP facet is far less likely to occur than a PyB facet in a $(10\bar{1}\bar{3})$ twin interface as a disconnection, due to its large Burgers vector and step height; hence, 3PyB facets are deemed also unlikely to occur in $(10\bar{1}\bar{3})-(10\bar{1}2)$ double twin to matrix interfaces of both type 1 and type 2, and were only reported here for the sake of completeness.

We now extend the analysis above to tension-compression double twinning mechanisms, where primary twinning occurs on $(10\bar{1}2)$ and secondary twinning occurs on $(10\bar{1}1)$ or $(10\bar{1}\bar{3})$ of the primary twin. Discussing first $(10\bar{1}2)-(10\bar{1}1)$ type 1 double twinning, figure 4.7a, we take $\mathbf{t}(\mu)$ to lie in the prismatic plane of μ and $\mathbf{t}(\lambda)$ to lie in the basal plane of λ, producing the 2-layer disconnection with Burgers vector $\mathbf{b}_A$ that accomplishes $(10\bar{1}2)$ twinning. Secondary twinning disconnections accomplishing the shear on $(10\bar{1}1)^{\lambda}$ have Burgers vector $\mathbf{b}_B = \frac{2\Lambda^2-3}{2\Lambda^2+1}[10\bar{1}\bar{2}]$, and that producing a BPy facet in the secondary twin interface may combine with two primary

twinning disconnections to form a PPy facet in the double twin interface. The Burgers vector content of such a facet is

$$\mathbf{b}_{\mathrm{PPy}} = 2\mathbf{b}_A + \mathbf{R}_A\mathbf{b}_B. \tag{4.9}$$

It may be noticed that this is the same kind of facet created in a $(10\bar{1}1)-(10\bar{1}2)$ type 1 double twin interface, only the order is reversed, as the prismatic plane of the matrix and the first pyramidal plane of the double twin are brought into coincidence in the facet. It follows that the second kind of facet that may be created in a $(10\bar{1}2)-(10\bar{1}1)$ type 1 double twin boundary is a B3Py facet, figure 4.7b, generated by the combination of four primary twinning disconnections (BP facet in the primary twin interface) and one secondary twinning disconnection (P3Py facet in the internal secondary twin interface), such that

$$\mathbf{b}_{\mathrm{B3Py}} = 4\mathbf{b}_A + \mathbf{R}_A\mathbf{b}_B. \tag{4.10}$$

In addition, similar facets can be encountered in $(10\bar{1}\bar{2})-(10\bar{1}1)$ type 2 double twin interfaces: a PPy facet (figure 4.7c) and a B3Py facet (figure 4.7d).

Finally, we list possible interfacial facets for $(10\bar{1}2)-(10\bar{1}\bar{3})$ double twins, figure 4.8. Unsurprisingly, these facets may also be found by reversing the order of the facet planes of the opposite twinning sequence, $(10\bar{1}\bar{3})-(10\bar{1}2)$. In particular, a PPy facet is obtained by combining two primary twinning disconnections, forming a PB facet in the primary twin boundary, with one secondary twinning disconnection, forming a BPy facet in the secondary twin boundary, such that the Burgers vector content of the facet is found using equation 4.9; this is possible for both $(10\bar{1}2)-(10\bar{1}\bar{3})$ type 2 (figure 4.8a) and $(10\bar{1}\bar{2})-(10\bar{1}\bar{3})$ type 1 (figure 4.8c) double twinning. Conversely, a B3Py double twin facet results from the combination of four primary twinning disconnections (a BP facet in the primary twin boundary) and one secondary twinning disconnection (a P3Py facet in the secondary twin boundary), for both type 2 (figure 4.8b) and type 1 (figure 4.8d) mechanisms, with the Burgers vector content of the facet given by equation 4.10. Again, we remark on the unlikelihood of this facet in double twin interfaces, as a consequence of the large Burgers vector and step height of the secondary twinning disconnection, and report this facet for the sake of completeness.

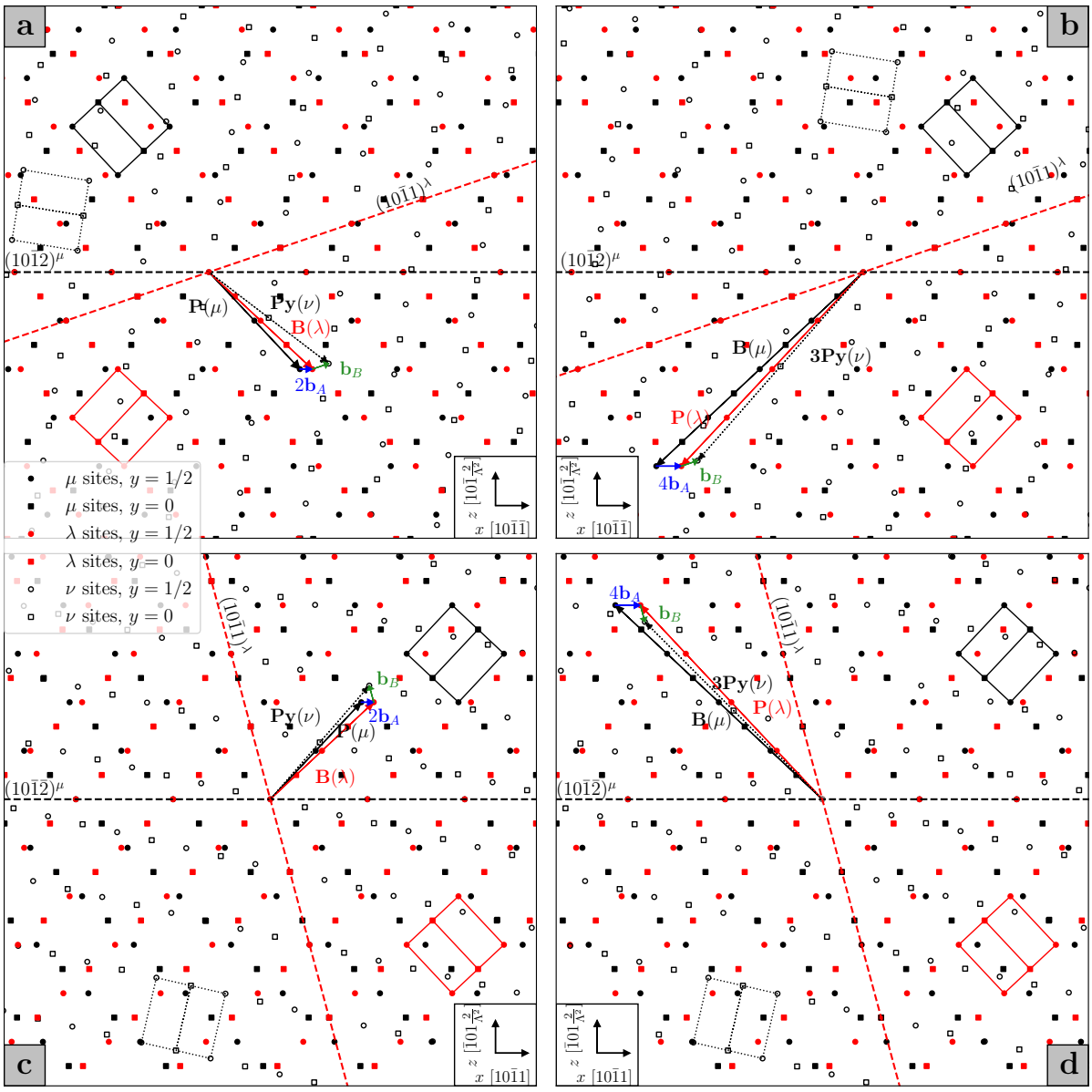

Fig. 4.7 $(10\bar{1}2)-(10\bar{1}\bar{1})$ double twin facets for types 1 ((a) and (b)) and 2 ((c) and (d)), $\gamma = 1.624$. μ sites, in black, belong to the matrix; λ sites, in red, belong to the primary twin; ν sites, in white, belong to the secondary twin. The hexagonal unit cells are similarly drawn for each lattice. The translation vectors that define the disconnections are denoted by the names of the planes they lie in, in order to highlight the kinds of facets they can form. The projection direction is $[1\bar{2}10]$.

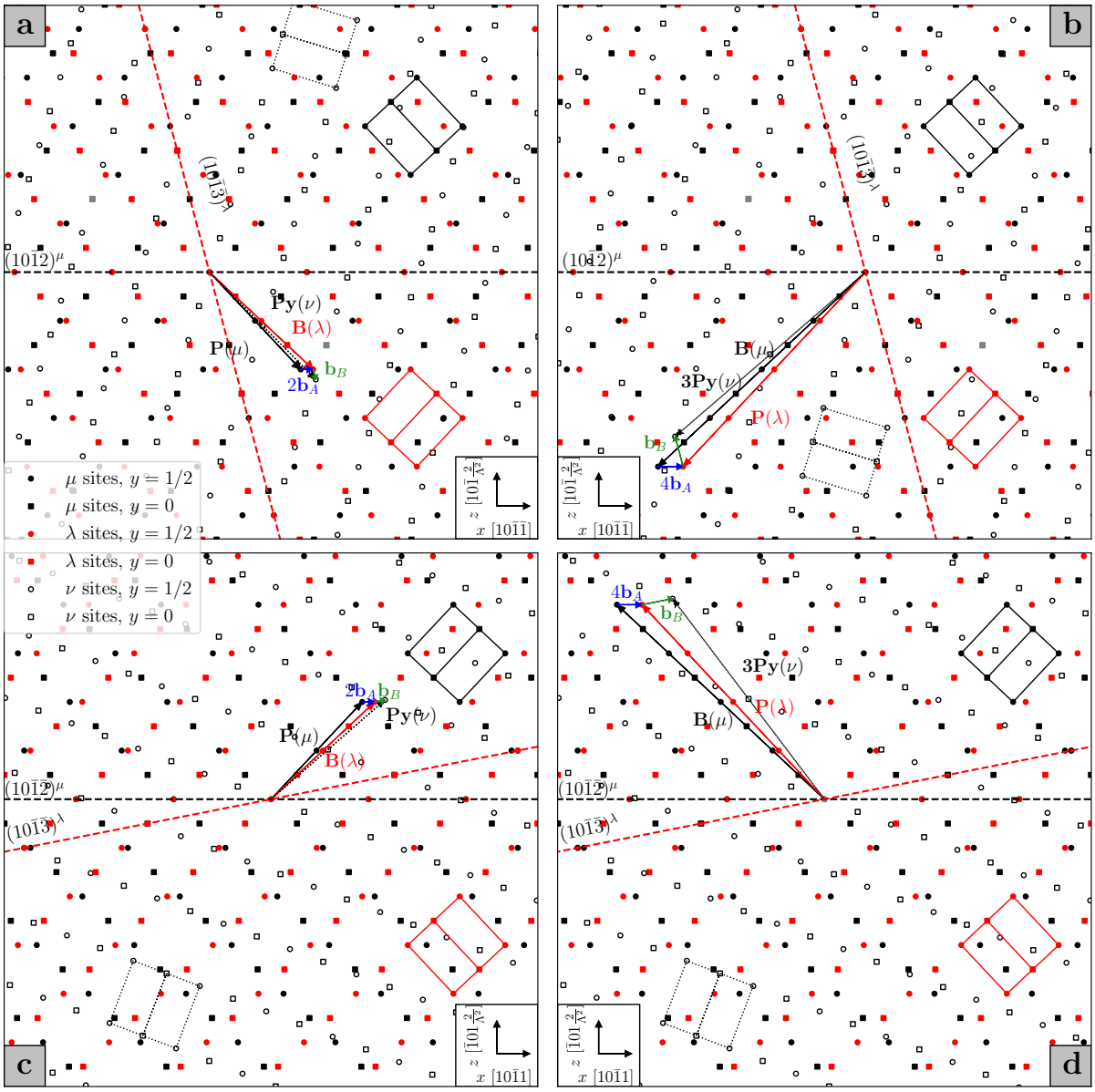

Fig. 4.8 $(10\bar{1}2)-(10\bar{1}\bar{3})$ double twin facets for types 2 ((a) and (b)) and 1 ((c) and (d)), $\gamma = 1.624$. μ sites, in black, belong to the matrix; λ sites, in red, belong to the primary twin; ν sites, in white, belong to the secondary twin. The hexagonal unit cells are similarly drawn for each lattice. The translation vectors that define the disconnections are denoted by the names of the planes they lie in, in order to highlight the kinds of facets they can form. The projection direction is $[1\bar{2}10]$.

We have thus shown that commensurate facets in primary twin interfaces, formed via the accumulation of primary twinning disconnections, may be converted into commensurate facets in the double twin interface through the action of secondary twinning disconnections. On the other hand, facets in the primary twin boundary are separated by segments of commensurate interface parallel to the K_1 plane of the primary twin; upon impingement of the secondary twinning

disconnections, these terraces become incommensurate, as discussed in section 3.4.1. Segments of twin interface originally parallel to the K_1 plane may undergo a rotation whose maximum magnitude corresponds to the values calculated in table 3.5 when internal retwinning occurs. Hence, the double twin to matrix interface is composed of sections of incommensurate boundary, whose orientation is close to that of the primary K_1 plane, and commensurate facets of the kind illustrated above. The main consequence of this analysis is that the macroscopic orientation of the double twin to matrix interface is largely predetermined by that of the primary twin to matrix interface, and in particular by the density and length of the facets that existed in it prior to secondary twinning.

4.1.3 Triple twinning and facets in triple twin interfaces

Though the focus of this thesis is double twinning, in the present section we briefly examine the phenomenon of triple twins, which, as is detailed in the following sections, were unexpectedly observed in experimental work carried out with the main objective of characterising double twin to matrix interfaces.

The occurrence of multiple twinning events in hcp metals is not unheard of, and the phenomenon has sometimes been termed hierarchical twinning [177]. Here we concentrate our discussion on tension-compression-tension (T-C-T) triple twinning, i.e. tension-compression double twins that have retwinned internally for a third time. More specifically, we focus on the $(10\bar{1}2)-(10\bar{1}1)-(10\bar{1}2)$ twinning sequence. As was noted in the previous chapter, $(10\bar{1}2)-(10\bar{1}1)$ double twins exhibit two variants where the component twinning mechanisms share a common plane of shear, and these are termed types 1 and 2. Then, the tertiary K_1 plane may be either $(10\bar{1}2)$ or $(\bar{1}012)$, such that there are two triple twin variants for each double twin type, if only twinning mechanisms with common plane of shear are considered. The four triple twin variants are thus named type 1a, 1b, 2a and 2b, and their misorientation relations with the matrix are listed in table 4.1 for magnesium, $\gamma = 1.624$.

Following the discussion of previous sections and chapters, we take the view that tertiary twinning is accomplished via the motion of tertiary twinning disconnections, as is the case for primary and secondary twinning. Therefore, the tertiary twinning disconnections can, in principle, form facets in the internal tertiary twin boundary, and for the case of tertiary tension

twinning analysed here, the facets are of BP and PB kind. Considering now the situation of tertiary twinning disconnections gliding towards a faceted double twin to matrix interface, we see that the commensurate facets of the double twin cannot be transformed into commensurate facets in the triple twin to matrix interface. Indeed, the facets in the double twin to matrix interface are of two kinds, PPy and B3Py, for both type 1 and type 2 T-C double twins, such that no rational planes of the matrix and triple twin can be brought into coalescence by a combination of primary, secondary and tertiary twinning disconnections; this may be seen more clearly with the reminder that e.g. here PPy stands for $P^{M}Py^{T_2}$, and the PB facet of the tertiary twin may be written as $P^{T_2}B^{T_3}$, with M, T_1, T_2, T_3 denoting the matrix, primary, secondary and tertiary twin, such that these two facets may not be combined to form a commensurate facet in the triple twin to matrix interface. Similarly, this is seen to be the case for all kinds of available facets. It follows that for all variants of the T-C-T twinning sequence under consideration, the resulting triple twin to matrix interface is fully incommensurate.

K_1 planes	Label	Axis/angle
$(10\bar{1}2)-(10\bar{1}1)-(10\bar{1}2)$	T-C-T type 1a	$-48°[1\bar{2}10]$
$(10\bar{1}2)-(10\bar{1}1)-(\bar{1}012)$	T-C-T type 1b	$-56°[1\bar{2}10]$
$(10\bar{1}2)-(\bar{1}011)-(10\bar{1}2)$	T-C-T type 2a	$-56°[1\bar{2}10]$
$(10\bar{1}2)-(\bar{1}011)-(\bar{1}012)$	T-C-T type 2b	$-64°[1\bar{2}10]$

Table 4.1 Labels and axis/angle pairs of some magnesium triple twinning modes, $\gamma = 1.624$.

Testing of this hypothesis is lacking in the experimental literature; observation of T-C-T triple twins is not common in magnesium alloys. Additionally, the interface between a triple twin and the matrix has not been observed before: in previous studies of T-C-T triple twinning, it was found that the primary tension twin had grown to consume either large portions of the grain [178, 179] or its near entirety [179–183]. C-T double twins were then shown to have nucleated inside the large primary twins in thin lamellae, such that only interfaces between double twin and matrix could be effectively observed.

4.2 TEM observations of twin interfaces

Having discussed faceting in single, double and triple twin to matrix interfaces from a theoretical standpoint, in this section we present electron microscopy observations of twins in a magnesium alloy that were obtained to seek clarification and, if possible, corroboration of theoretical results, in a collaboration with the University of Sheffield. In particular, we sought to find answers to the following questions. *i)* Is double twinning a one- or a two-step process, i.e. do double twins grow on a (invariant) habit plane, or are they formed by internal secondary retwinning of a fully formed primary twin? *ii)* What is the orientation of the double twin to matrix interface? *iii)* Is the double twin to matrix interface faceted?

Question *i)* has found some answers in the experimental literature. In particular, electron back-scatter diffraction (EBSD) observations of magnesium alloys have shown twin-like objects containing sections of material with different misorientation relations separated by internal boundaries: measurement of the misorientation indicated that some portions of the twin had undergone compression twinning on the $(10\bar{1}1)$ plane, and other portions had undergone double twinning via internal tension retwinning on the $(10\bar{1}2)$ plane. This has been most commonly observed for $(10\bar{1}1)-(10\bar{1}2)$ type 1 double twinning [45, 46, 184, 26, 185, 186], but also for $(10\bar{1}1)-(10\bar{1}2)$ twins of types 2, 3 and 4 [185, 187]. These results have found further confirmation in transmission electron microscopy (TEM) studies of magnesium alloys, where internal boundaries separating regions of primary and secondary twin were clearly seen [44, 188, 189].

On the other hand, the orientation of double twin to matrix interfaces, question *ii)*, has not been as thoroughly investigated in magnesium. The main reason for this is that such a measurement requires the use of transmission electron microscopy, which is more expensive than scanning electron microscopy and EBSD and allows only for the investigation of small samples, whose preparation is itself lengthy. The most extensive study on this subject to date was performed by Cizek and Barnett [44], who analysed 58 twin-like objects in a commercial Mg alloy, identifying a high proportion of these as $(10\bar{1}1)-(10\bar{1}2)$ double twins, as well as some $(10\bar{1}\bar{3})-(10\bar{1}2)$ double twins, and measuring the orientation of their interfaces with the matrix. This study did not produce unambiguous results for the orientation of the double twin to matrix interface, which for the $(10\bar{1}1)-(10\bar{1}2)$ double twins was found to vary between the

$\{30\bar{3}4\}$, $\{10\bar{1}1\}$ and $\{20\bar{2}3\}$ planes. However, this was not a high-resolution TEM investigation, such that only the macroscopic orientation of twin boundaries could be measured. Therefore, the possible presence of facets in the interfaces could not be ascertained, nor their link to the uncertainty in measurements of double twin boundary orientations.

High-resolution studies of double twin boundaries in magnesium and magnesium alloys are lacking in the literature, and faceting of double twin to matrix interfaces has not been studied before. Hence, in what follows we present high-resolution TEM observations of double twins, in an attempt to answer some long-standing questions on the orientation of their interfaces. We start with an overview of the experimental methods used, and then proceed to the results of the investigation and their discussion.

4.2.1 Experimental methods

The field of microscopy was on the brink of change when Louis de Broglie, in 1925, showed that the energy of an electron is related to its wavelength [190], thus opening up the possibility that high-energy electrons may be used to magnify objects with a resolution beyond the capability of visible-light microscopes. According to the Rayleigh criterion, the smallest distance that can be resolved using any type of radiation is proportional to the radiation wavelength. Green light, which lies in the middle of the visible spectrum, has a wavelength of 550 nm; in contrast, the wavelength of a 100 keV electron is approximately 0.004 nm. It is then immediately clear that accelerated electrons, if used for imaging, have the potential for yielding vastly better resolution than that obtained using visible light to illuminate the specimen, and even atomic resolution. The first electron microscope was built by Max Knoll and Ernst Ruska in Berlin, and the term for the new instrument first appeared in a paper in 1932 [191]. Electron microscopes for commercial use started to be produced only four years later, and became widely available after the end of World War II [192]. A most important advancement in the field was the development, in the middle of the century, of techniques aimed at thinning samples so that they would achieve electron transparency, thus boosting the field of transmission electron microscopy. Today, the typical resolution of a TEM is of the order of 0.3 nm [192], which is three orders of magnitude better than that of visible-light microscopes at around 300 nm. It is thus indubitable that electron microscopy is a powerful tool for science, in particular materials science and biology.

The main components of an electron microscope are an electron gun and a system of electromagnetic lenses, which focus the electron beam. The electrons are scattered when they interact with the specimen, and we distinguish between forward scattering, where an electron is scattered through an angle with the incident beam of less than 90°, and back scattering, where the scattering angle is more than 90°. It is forward scattering that is most important in the TEM, where information is collected from the transmitted beam. While some of the electrons pass though the specimen unchanged, forming the direct beam, others are diffracted by the specimen, and, if the kinematic approximation is taken to be valid, in crystalline materials the diffracted beams behave as if they were reflected off atomic planes, following Bragg's law [193]. The angle between these Bragg diffracted beams and the incident beam is small, and they are focused with the aim of producing a transmission diffraction pattern [194]. Diffraction patterns are obtained by using restricting apertures (called selected-area diffraction or SAD apertures) that only select scattered electrons that deviate from the incident beam by small angles, and they can be seen as a two-dimensional projection of the reciprocal lattice of the crystal. The sample orientation is then related to the projection direction, and by tilting the sample projections of the reciprocal lattice along different axes can be obtained. Thus three-dimensional information may be recovered from the diffraction pattern, which can be used to establish the orientation of specific lattice planes in the crystal.

As the object of the present study is a hcp metal, we now briefly discuss what diffraction patterns for such a crystal look like. We follow the discussions presented in refs [194] and [192]. We start from the amplitude of an electron beam scattered from a unit cell, where the diffracted beam makes an angle θ with the incident beam: at distances r large compared with the lattice constant, this is given by

$$A_{\text{cell}} = \frac{e^{2\pi ikr}}{r} \sum_j f_j(\theta) e^{-2\pi i \mathbf{K}\cdot\mathbf{r}_j}, \tag{4.11}$$

where k is the length of the wave vector of the incident beam, such that $k = 1/\lambda$, with λ the electron wavelength; $\mathbf{K}$ is the difference between the wave vectors of the transmitted and incident beams, $\mathbf{r}_j$ are the positions of atoms in the unit cell, such that $-2\pi i\mathbf{K}\cdot\mathbf{r}_j$ is the phase difference between a wave scattered from an atom j and a wave scattered at the origin. $f_j(\theta)$ are the atomic-scattering factors for atoms j and the summation is over all atoms in the unit cell. The

scattering factor $F(\theta)$ of the unit cell is then called the structure factor:

$$F(\theta) = \sum_j f_j(\theta) e^{-2\pi i \mathbf{K}\cdot\mathbf{r}_j}. \tag{4.12}$$

In order to produce a perfect crystal, we stack together a number of unit cells, and find that its scattered amplitude is given by (leaving out $e^{2\pi ikr}/r$ in equation 4.11)

$$A_{\text{crystal}} = \sum_n F_n e^{-2\pi i \mathbf{K}\cdot\mathbf{r}_n}, \tag{4.13}$$

where F_n is the structure factor of cell n and

$$\mathbf{r}_n = n_i \mathbf{a}_i, \tag{4.14}$$

with $\mathbf{a}_i$, $i = 1,2,3$ the primitive lattice vectors and n_i integers (the Einstein summation convention over repeated indices was applied). Expressing $\mathbf{K}$ as a vector in reciprocal space, we have

$$\mathbf{K} = h\mathbf{a}_1^* + k\mathbf{a}_2^* + l\mathbf{a}_3^*, \tag{4.15}$$

such that equation 4.13 becomes

$$A_{\text{crystal}} = \sum F_n e^{-2\pi i(n_1 h + n_2 k + n_3 l)}. \tag{4.16}$$

Then strong diffraction occurs when $(n_1 h + n_2 k + n_3 l)$ is an integer for all n_i, meaning when h, k and l are also integers. We have thus derived the Laue conditions [195] for Bragg reflection from (hkl) planes, which may be expressed as

$$\mathbf{K}\cdot\mathbf{a}_1 = h, \tag{4.17}$$

$$\mathbf{K}\cdot\mathbf{a}_2 = k, \tag{4.18}$$

$$\mathbf{K}\cdot\mathbf{a}_3 = l. \tag{4.19}$$

Hence, in this case **K** is a reciprocal lattice vector, satisfying

$$|\mathbf{K}| = \frac{1}{d_{hkl}}. \tag{4.20}$$

But recalling that $k = 1/\lambda$ and that θ is the angle between the incident and the refracted beams, we also have that

$$|\mathbf{K}| = 2\frac{\sin\theta}{\lambda}, \tag{4.21}$$

such that Bragg's law for a strong reflection is obtained:

$$\lambda = 2d_{hkl}\sin\theta. \tag{4.22}$$

Not all reciprocal lattice points, however, produce a Bragg reflection. The reason for this is the presence of the structure factor in equation 4.13: the contributions of each cell n to the amplitude of the scattered electron beam are weighted by F_n, and for some reciprocal lattice points, F_n is zero and no Bragg reflections are seen. The structure factors for reciprocal lattice points may be found by rewriting equation 4.12 as

$$F_{hkl} = \sum_j f_j(\theta) e^{-2\pi i(hu_j + kv_j + lw_j)}, \tag{4.23}$$

where u_j, v_j, w_j are the coordinates of atom j.

For the hcp crystal structure, the primitive lattice vectors are $\mathbf{a}_1 = a\left[\frac{1}{2}, -\frac{\sqrt{3}}{2}, 0\right]$, $\mathbf{a}_2 = a\left[\frac{1}{3}, \frac{\sqrt{3}}{2}, 0\right]$ and $\mathbf{c} = [0,0,c]$, with a the lattice constant and c/a the axial ratio, as discussed in previous chapters. Then the coordinates of the atoms in the primitive unit cell, expressed as fractions of the lattice vectors, are $[0,0,0]$ and $\left[\frac{1}{2}, \frac{2}{3}, \frac{1}{2}\right]$. Substituting these in equation 4.23, we find

$$F_{hkl} = f(1 + e^{-2\pi i(\frac{h}{3} + \frac{2k}{3} + \frac{l}{2})}). \tag{4.24}$$

The expression may be simplified by setting $X = \frac{h}{3} + \frac{2k}{3} + \frac{l}{2}$ and by noticing that the intensity of the diffracted beam depends on $|F_{hkl}|^2$:

$$|F_{hkl}|^2 = f^2(2 + e^{2\pi iX} + e^{-2\pi iX}) = f^2(4\cos^2\pi X). \tag{4.25}$$

We then have the following rules for hcp crystals:

$$|F_{hkl}|^2 = \begin{cases} 0, & \text{if } h+2k = 3m \text{ and } l \text{ is odd,} \\ 4f^2, & \text{if } h+2k = 3m \text{ and } l \text{ is even,} \\ 3f^2 & \text{if } h+2k = 3m \pm 1 \text{ and } l \text{ is odd,} \\ f^2 & \text{if } h+2k = 3m \pm 1 \text{ and } l \text{ is even,} \end{cases} \tag{4.26}$$

where m is an integer.

The most important consequence of these conditions is that the 0001 reciprocal lattice point produces no Bragg reflection, and the 0001 spot will be absent in diffraction patterns of the hexagonal crystal structure. This is often called a kinematically forbidden reflection, from the kinematical approximation that is made in calculating the scattered electron beam amplitude, according to which the amplitude of the scattered wave is only a small fraction of that of the incident wave. When the scattered amplitude becomes large, there is a higher probability that the diffracted wave be itself scattered by atoms, and the kinematic approximation breaks down. One of the effects of these dynamical scattering events is the appearance of kinematically forbidden reflections in diffraction patterns due to rediffraction; indeed, it will be observed that the 0001 spot is often present in diffraction patterns produced by hexagonal materials.

Diffraction patterns for the hcp structure for different projections may be found in standard TEM textbooks; for example, some are given in Williams and Carter [192]. However, for hcp the spacing of the spots depends on the axial ratio of the material: in Williams and Carter's textbook, the axial ratio of titanium, $c/a = 1.589$, is used, such that the angles given in their DPs are only valid for this material.

For the purpose of the present chapter, we are particularly interested in the diffraction pattern produced by projection along the $[1\bar{2}10]$ axis: this is the normal to the plane of shear of all twinning mechanisms analysed in this work, as noted in the previous section. We thus draw the reader's attention to a comparison of real and reciprocal space projections of the hexagonal lattice along this axis, which is particularly instructive as an aid to interpret diffraction patterns. Spots in figure 4.9a represent lattice points in reciprocal space, where the distance between the spots and the origin corresponds to $1/d_{(hkil)}$, with $d_{(hkil)}$ the spacing of $(hkil)$ planes; in

figure 4.9b, circles and squares denote different layers of lattice sites as seen when looking down the $[1\bar{2}10]$ projection, rotated clockwise by 90°. It should be noted that $\frac{N}{L} = \frac{N'}{L'}$, such that the two projections are identical except for scaling. Therefore, when considering diffraction patterns obtained by placing the aperture over regions of the material presenting different crystal orientations, such as is the case for twin interfaces, the interpretation of these may be assisted by comparison with the dichromatic patterns of the twins under consideration.

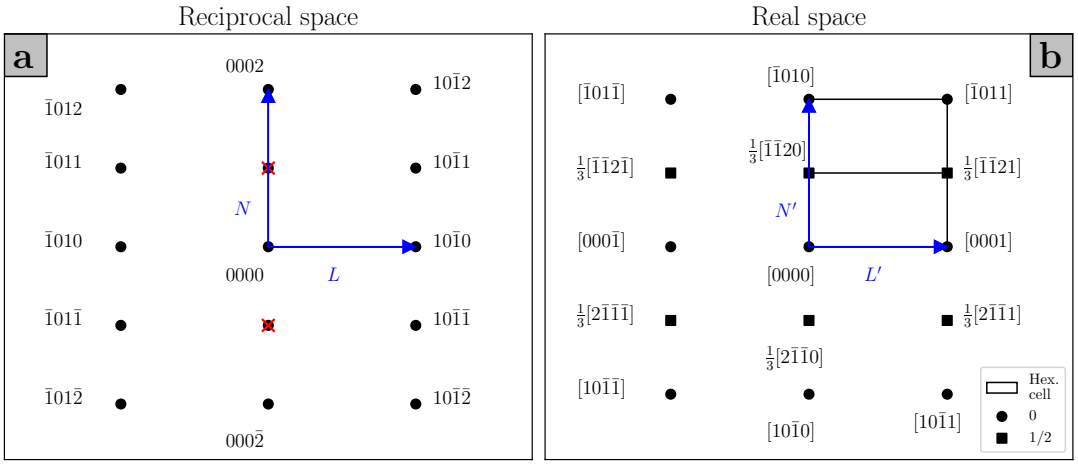

Fig. 4.9 Relationship between reciprocal (a) and real space (b) projections along the $[1\bar{2}10]$ direction of the hexagonal lattice, for $\gamma = 1.624$. The real space projection is rotated clockwise by 90°. Red crosses in the reciprocal space projection indicate kinematically forbidden reflections.

In practice, the electron beam is scattered incoherently when it interacts with the specimen, i.e. the scattered electrons travel in all directions, and are often said to be diffusively scattered. These electrons may then be Bragg diffracted by the crystal planes, and for this reason so-called Kikuchi patterns may form along with the bright spots in a diffraction pattern if the sample is thick enough. Kikuchi lines, which were first observed by Seishi Kikuchi in 1928 [196], are traces of the hyperbolae formed by the intersection of cones of Bragg diffracted electrons with the screen or the detector, and they can be useful in a number of ways, among which is aiding individuation of zone axes and providing more accurate information on crystal orientation.

So far we have focused on diffraction patterns, and we have neglected discussion of the electron micrograph. If, instead of a SAD aperture, an aperture that blocks Bragg reflections is used, the image is formed by the direct beam and any low angle inelastic scattering: such an image is termed a bright field image. In these images the contrast is produced by the different

intensities of beams diffracted in different parts of the specimen, and is thus called diffraction contrast [194].

The combination of bright field images and diffraction patterns furnishes the investigator with a wealth of information on the specimen, making the TEM a most suitable tool for characterising crystals as well as their defects from a three-dimensional standpoint. Hence, we chose this technique to investigate twinning events in magnesium, as our objective was the measurement of the orientation of twin boundaries and thus of specific crystallographic planes in the specimen.

As we noted in the previous section however, TEM analysis requires small samples that are to be thinned to "foils" in order to achieve electron transparency and yield the best possible resolution. It is therefore necessary to investigate a small region of interest in the sample, and preliminary analysis using other microscopy tools is desirable. In particular, a scanning electron microscope (SEM) can be used to image the surface of larger samples without the need for lengthy preparation.

In the most common SEM imaging mode, information is gathered from secondary electrons, which are the byproduct of the ionisation of the sample by primary electrons (i.e. the incident beam), and thus of inelastic scattering. Secondary electrons have low energies compared to primary electrons, of the order of 50 eV, and a mean escape depth of about 1 nm in metals [197, 198], such that they provide very localised information about the surface of the specimen. Back-scattered electrons can also be detected and used for SEM imaging, mainly using electron back-scatter diffraction (EBSD) equipment. In EBSD set-up, the sample is tilted by around 70° from the original SEM position, such that the surface makes an angle of about 20° with the incident beam; tilting the sample ensures that the volume of material with which the electrons interact is elongated, resulting in more scattered electrons being able to leave the sample [199]. The scattered electrons then undergo Bragg diffraction from the atomic planes of the crystal, and the diffracted beams collected by the detector consequently produce Kikuchi diffraction patterns [200]. From the Kikuchi patterns information can be extracted on the crystallographic orientation of the grains in the sample, making EBSD a helpful tool in characterisation of the microstructure.

4.2.2 Materials and preliminary results

For this study we used a magnesium alloy developed by Xun Zeng for his PhD work [201]. The alloy was prepared by direct chill casting of pure Mg, Al, Nd feed stock. The final composition was characterised via X-ray spectroscopy, and it was found to be Mg-1.18wt%Al-1.77wt%Nd. The melt was stirred under an argon and 3 volume% SF_6 gas atmosphere for 30 minutes at 720° C and subsequently cast into a steel mold coated in boron nitride, preheated to 680° C. Quenching of the filled mold was achieved by slowly lowering it into a water bath. Homogenisation was then carried out at 450° C, and finally the material was machined into slabs with dimensions of $100 \times 50 \times 10$ mm.

Slabs were hot rolled at 420° C in multiple passes alternated with ten-minute annealing steps at the rolling temperature, in order to minimise cracking associated with the temperature drop. The reduction at each pass was 10-15%. The final thickness of 2.3 mm was achieved after eleven passes with a total strain of 0.77. After the final rolling pass no further annealing was performed and the slabs were allowed to cool in air; this was sufficiently rapid that further recrystallisation was prevented and any twins introduced during the final deformation step were retained.

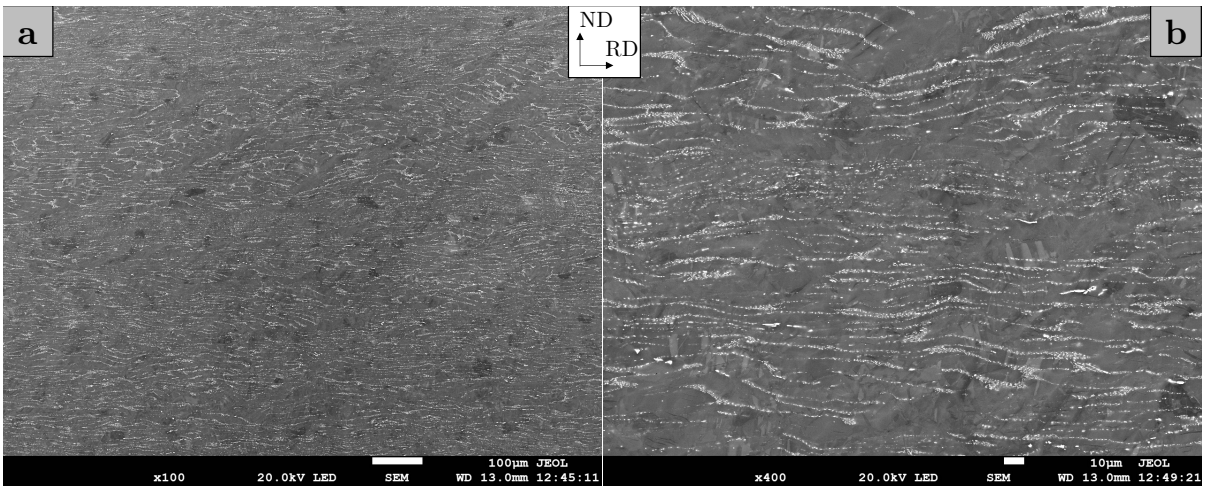

Fig. 4.10 SEM images of the microstructure of the processed Mg-1.18wt%Al-1.77wt%Nd alloy used in this study, at (a) $\times$100 and (b) $\times$400 magnification.

A preliminary study of the microstructure was carried out post processing using SEM and EBSD techniques by Xun Zeng with the collaboration and under the direction of the present author. For this purpose, one of the slabs was selected as a sample and ground with emery papers from 800 to 2500 grit. Mechanical polishing was carried out with oxide polishing suspension;

finally, electrolytic polishing was used to remove the deformation layer produced by mechanical polishing. SEM and EBSD observations were conducted with a field emission gun SEM, JEOL JSM-7900F, operating at 20 kV; a step size of 0.3 μm was used in EBSD measurements, given an average grain size of 13 μm.

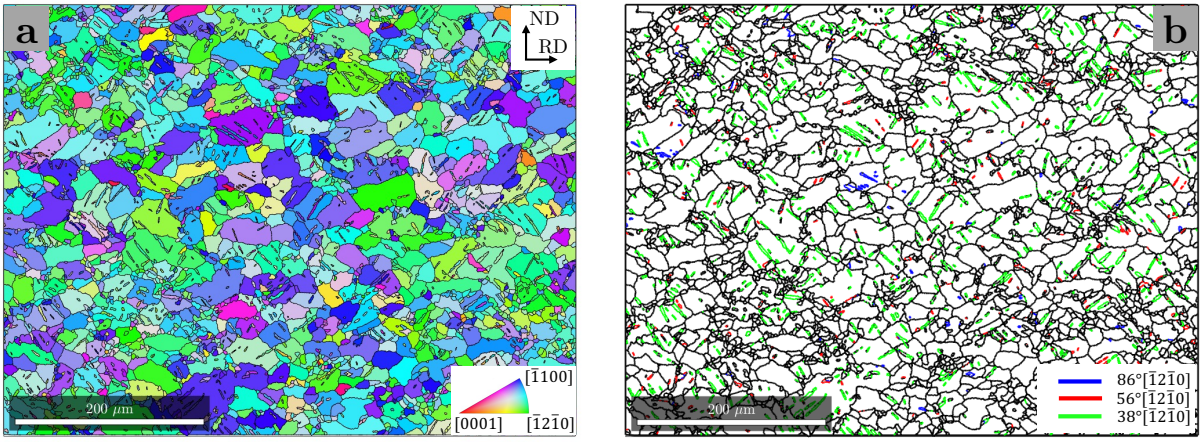

Fig. 4.11 (a) EBSD inverse pole figure map of the microstructure of the processed Mg-1.18wt%Al-1.77wt%Nd alloy used in this study. (b) Boundaries exhibiting the tension twin (blue), compression twin (red) and $(10\bar{1}1)-(10\bar{1}2)$ or $(10\bar{1}2)-(10\bar{1}1)$ double twin (green) misorientation relations.

SEM images of the sample are shown in figure 4.10 at different magnifications. The most striking feature is the presence of large Nd-Al precipitates in the microstructure, denoted by the bright contrast. An EBSD inverse pole figure map of the sample in projection along the transverse direction is shown in figure 4.11a, along with a map of boundaries with misorientations corresponding to those of tension, compression and $(10\bar{1}1)-(10\bar{1}2)$ or $(10\bar{1}2)-(10\bar{1}1)$ type 1 double twins in figure 4.11b. It is evident from the figure that a high proportion of double twins was observed; in turn this prompted us to proceed to TEM investigation of the specimen, in order to characterise the morphology of double twin to matrix interfaces.

Preparation of the TEM foil ensued; this was carried out by John Nutter as directed by this author. As a strong basal texture was detected in projection along the normal direction, the specimens were sectioned parallel to the plane containing the rolling and transverse directions. Electropolishing, rather than ion beam thinning, was chosen to prepare the TEM foils, as the process is more rapid and does not deform the sample at surface level [202]. Thus TEM specimens were prepared by mechanically thinning the sections to approximately 100 μm followed by electropolishing in a Tenupol-5 twin jet electropolisher using a solution of 8.8 g

lithium chloride, 18.6 g manganese perchlorate, 160 ml 2-butoxyethanol and 840 ml methanol at -35° C. The samples were then rinsed with a methanol solution and examined in an optical microscope. Specimens that presented little etching were singled out for TEM investigation. TEM analysis was carried out using a JEOL JEM-F200 TEM operated at 200 kV by John Nutter under the guidance of this author, who interpreted the diffraction patterns and directed the experiment. The samples were tilted down the $[1\bar{2}10]$ zone axis using a JEOL dual tilt beryllium holder, which allows tilting of the specimen by up to $\pm 30^\circ$ in two directions (e.g. the x and y directions). A photo of the holder is shown in figure 4.12.

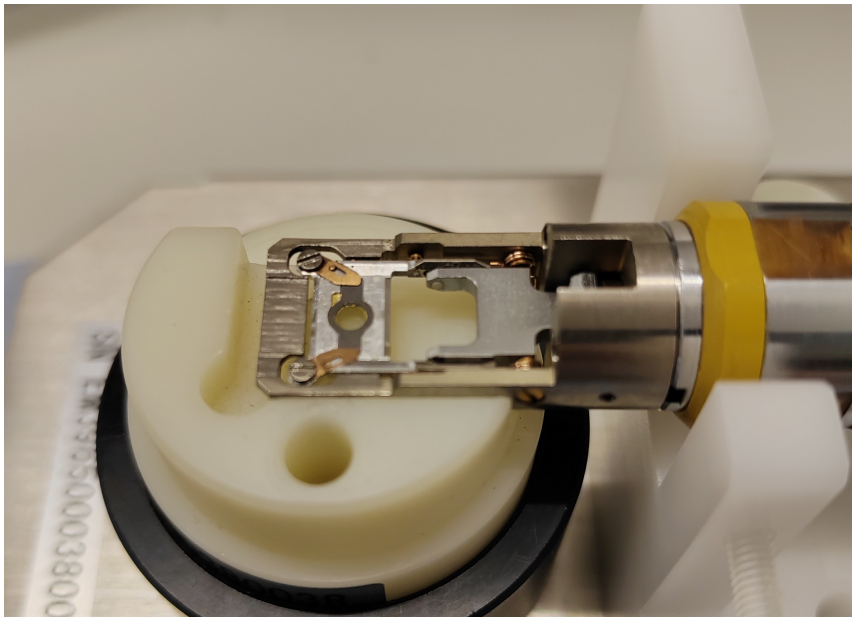

Fig. 4.12 Photo of the JEOL dual tilt beryllium holder used to carry out TEM observations.

In order to aid the interpretation of high-resolution TEM images, the bright field images were compared with images of the same areas processed via Fourier filtering by the present author. This involves fast-Fourier transforming the HRTEM image, thus effectively obtaining the associated diffraction pattern. Spots associated with the 0002 and $10\bar{1}0$ reciprocal lattice points are then picked out and used to create a mask; the mask is applied to the FFT image, which is then processed again with an inverse FFT. The result in the processed HRTEM image is the enhancement of the atomic planes picked out for the mask, which in turn can be of help when seeking to identify facets and interfaces.

4.2.3 Experimental results

Due to the nature of the chosen method of preparation of the foils, we were able to identify several areas of interest in one sample: since electropolishing produces a central hole in the foil, it is possible to find regions suitable for high-resolution investigation all around it, as the material is thinner in the immediate vicinity of the hole. We were thus able to observe multiple twinning events in the same sample; in particular, various twin-like objects were found, both in the form of long narrow bands and clusters of twins. Here, we present three areas of interest on which in-depth investigation was conducted, via the combination of selected-area diffraction (SAD) patterns, low- and high-resolution bright field images.

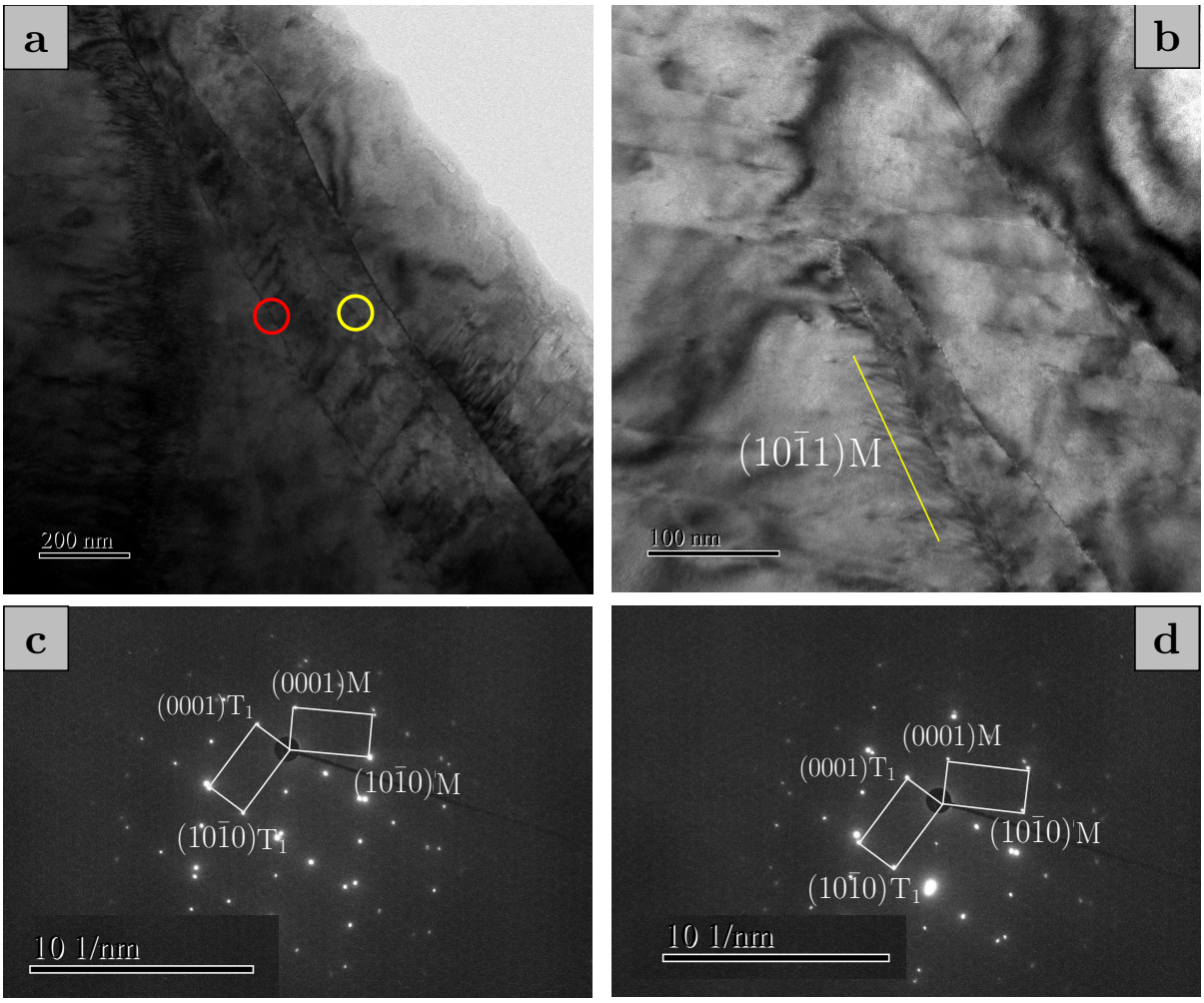

Fig. 4.13 (a) TEM Bright field image the first area of interest, a long narrow twin, at low magnification. (b) Bright field image of the tip of the twin in (a). (c)-(d) Indexed SAD patterns of the regions denoted by the red and yellow circles in (a) respectively.

The first area of interest is a long narrow twin, figure 4.13a, roughly aligned with the edge of the foil. SAD patterns of interfacial regions containing both the matrix and the twin were taken for boundaries on either side of the twin, as denoted by the red and yellow circles in figure 4.13a, and they are shown in figures 4.13c-d. A misorientation of 59° about the $[1\bar{2}10]$ zone axis between the matrix and the twin was measured for both SAD patterns; this is consistent with the $(10\bar{1}1)$ compression twin misorientation relation ($56°[1\bar{2}10]$). Figure 4.13b shows a magnified view of the twin tip, which appears to be surrounded by basal stacking faults; the trace of the $(10\bar{1}1)$ plane of the matrix has been drawn, and it can be seen that while the boundary to the left of the twin tip is roughly aligned with it, the boundary to the right appears slightly bent.

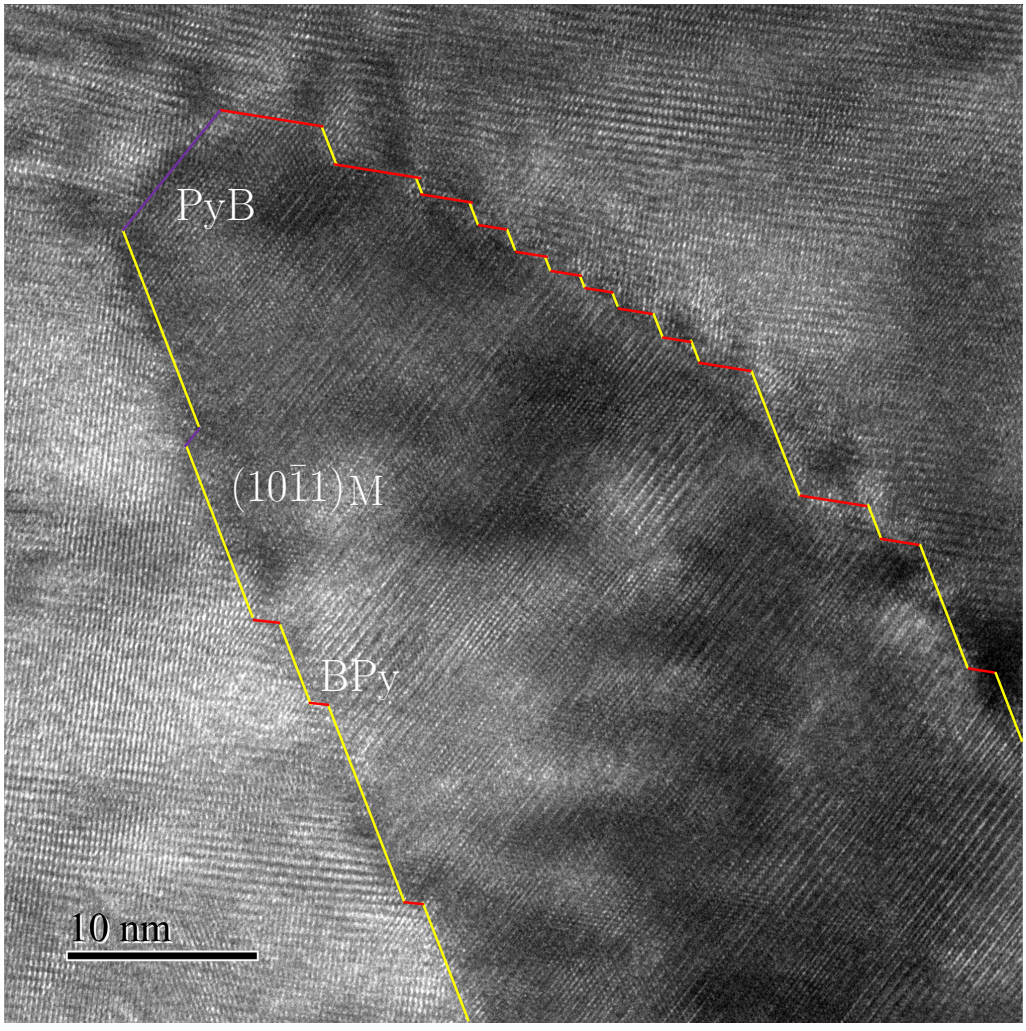

Fig. 4.14 High-resolution TEM bright field image of the twin tip in figure 4.13b. Boundaries have been drawn using the following colour scheme. Yellow: $(10\bar{1}1)$ plane of the matrix and twin; red: BPy facets; purple: PyB facets.

The twin tip in figure 4.13b was selected for further investigation: figure 4.14 shows a high-resolution bright field image of the area, where the interface has been drawn using different colours depending on orientation. This reveals that terraces of $(10\bar{1}1)$ twin boundary are separated by BPy and PyB facets, consistent with predictions of the topological theory presented in the previous section; BPy facets are particularly numerous in the interface on the right hand side, which appears as considerably deviated from a flat $(10\bar{1}1)$ twin boundary. The blunt tip of the twin is seen to be made up of a long PyB facet. It can be noted that the matrix around the twin tip is affected by a distortion, more evidently so near the boundary on the right hand side, which has a higher density of facets; interestingly, this distortion does not appear to affect the twin as considerably as it does the matrix.

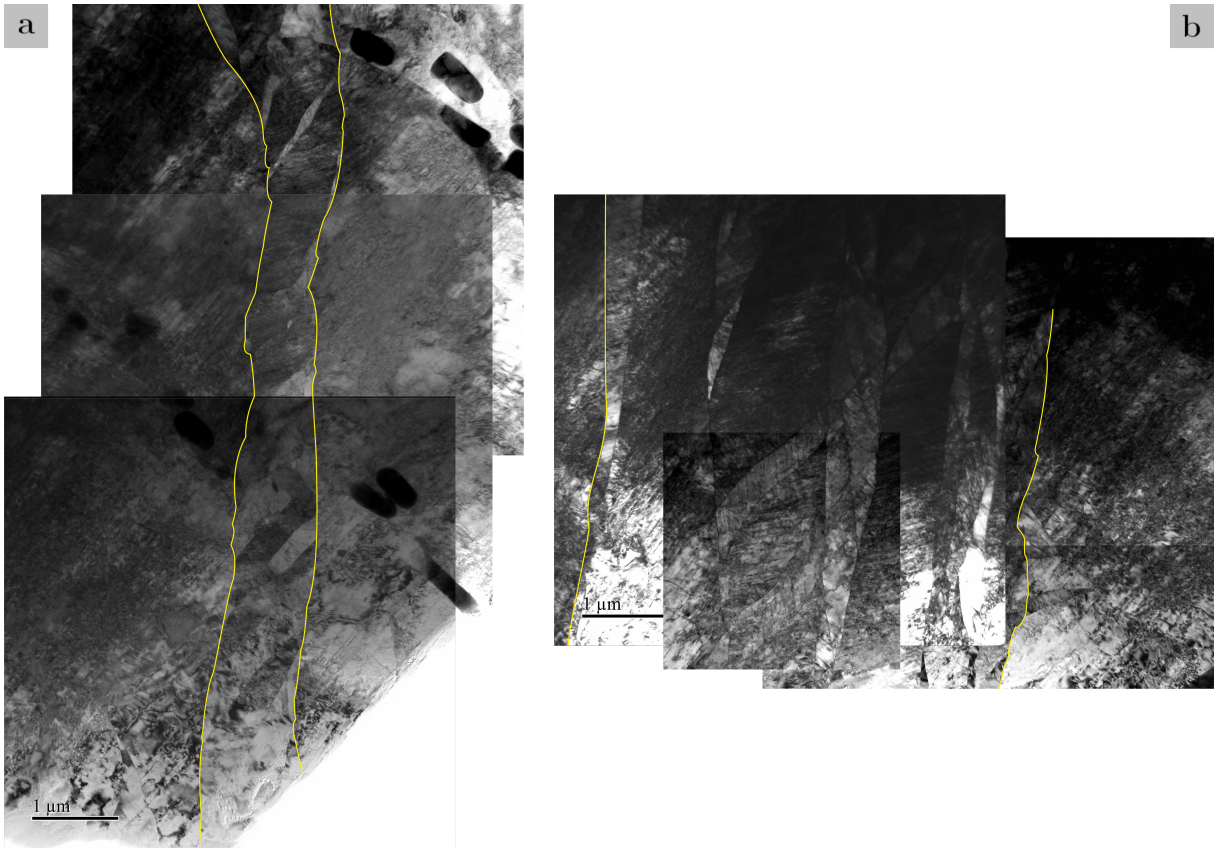

Fig. 4.15 TEM bright field images of the second and third areas of interest identified in the sample: (a) a long, narrow twin-like object, traversed by internal boundaries; (b) a cluster of twins. The contours of the two objects were delineated for clarity.

The second and third areas of interest are shown respectively in figures 4.15a-b. These are a long, narrow twin-like object traversed by internal boundaries (figure 4.15a) and a cluster

of twins, also crossed by internal boundaries (figure 4.15b). Starting from the object in figure 4.15a, we select the region closest to the electropolishing hole for further investigation; this is shown in figure 4.16a, where different regions have been coloured in order to aid interpretation. A SAD pattern was taken at the interface between the matrix (in yellow) and one of the twin regions (in blue), as denoted by the red circle in figure 4.16a: this is shown in figure 4.16c. The diffraction pattern shows that the blue region has a misorientation of $-38^\circ[1\bar{2}10]$ with respect to the matrix, which is consistent with either a tension-compression or compression-tension type 1 double twin, as discussed in section 3.1 and shown in table 3.1; consequently, we label this region T_2. However, HRTEM investigation of the interface between the matrix and T_2 reveals that a sliver of primary twin is left between the matrix and the double twin, figures 4.16b-d: measurement of the orientation of the primary twin boundary, aided by the relative SAD pattern, confirms that this is a tension twin growing on the $(\bar{1}012)$ plane of the matrix (marked in blue in the HRTEM images), while secondary twinning occurs on the $(\bar{1}011)$ plane of the primary twin. Hence, we conclude that the region T_2 is a $(\bar{1}012)-(\bar{1}011)$ type 1 double twin. Moreover, facets may be observed in the high-resolution images: BP and PB facets of the primary twin to matrix interface are seen to combine with P3Py and BPy facets of the internal secondary to primary twin interface to form B3Py and PPy facets in the double twin to matrix interface, as expected from the theoretical discussion in section 4.1.2. On the other hand, segments of the original $(\bar{1}012)$ primary twin boundary appear to be left unchanged by the impingement of secondary twinning disconnections.

In order to extract information on the region coloured in green in figure 4.17a, SAD patterns were taken at the interface of this region with the matrix and with T_2, as denoted by the red and yellow circles respectively. The SAD patterns are shown in figures 4.17c-d, and the measured misorientations between the green area and the matrix, as well as between the green area and T_2 are $48^\circ[1\bar{2}10]$ and $-86^\circ[1\bar{2}10]$ respectively. The latter is consistent with the misorientation relation of a tension twin, whose K_1 plane is $(\bar{1}012)$, as the corresponding $\bar{1}012$ spots are seen to coincide in the SAD pattern, such that it is revealed that the area in green is a tertiary twin; the $48^\circ[1\bar{2}10]$ misorientation with the matrix is then consistent with that of a T-C-T type 1a triple twin, as shown in table 4.1, and the green region is labelled T_3. Hence, the twinning sequence for the object in figure 4.17a is as follows: primary twinning first occurred on the $(\bar{1}012)$ plane

of the matrix; the primary twin then retwinned internally on its $(\bar{1}011)$ plane, and the so formed T-C double twin finally twinned again on the $(\bar{1}012)$ plane of T_2. Finally, the appearance of the internal tertiary twin boundary and of the triple twin to matrix interface were investigated via HRTEM images. Figure 4.17e shows that while commensurate facets of the BP and PB kind may be created in the internal tertiary to secondary twin interface, with a concentration of steps near the junction with the double twin and the matrix indicating a high density of tertiary twinning disconnections, no commensurate facets may be found in the triple twin to matrix interface, figure 4.17b, and facets along the B and P planes of the matrix are not parallel to any rational plane of the triple twin. Therefore, the triple twin to matrix interface for this twinning sequence is fully incommensurate, as expected from theoretical considerations. SAD patterns similar to those in figures 4.16c and 4.17c-d were collected from interfaces all along the length of the twin-like object in figure 4.15a, such that alternating regions of triple and double twin were observed. No sizeable portions of the primary twin appeared to be left, other than in narrow sections in the HRTEM images.

The third area of interest, figure 4.15b, appears to be a rather complicated cluster of narrow twins. Identification of the twinning events entailed the collection and investigation of SAD patterns for all the visible interfaces; from this analysis, it is concluded that the cluster is made of bands containing all three twinning stages in the T-C-T type 1a twinning sequence already observed in the object in figure 4.15a, interspersed with portions of matrix, i.e. material with similar orientation to that measured on either side of the cluster. Hence, the colour coding scheme utilised for the previous area of interest is once again proposed here, with the addition of red for the primary tension twin labelled T_1; yellow is then assigned to the matrix, blue to $(\bar{1}012)-(\bar{1}011)$ type 1 double twin and green to T-C-T type 1a triple twin. A coloured in version of figure 4.15 is proposed in figure 4.19, to illustrate the multiplicity of twinning events in the cluster as well as in the second area of interest previously analysed. Many curved boundaries may be observed inside the cluster of twins, and it is reasonable to assume that this may be attributed to faceting at the atomic level; in order to elucidate this point, HRTEM images were taken of an area on the lower left hand side of the cluster, shown in figure 4.18a, where optimal resolution is obtained due to the vicinity of the electropolishing hole.

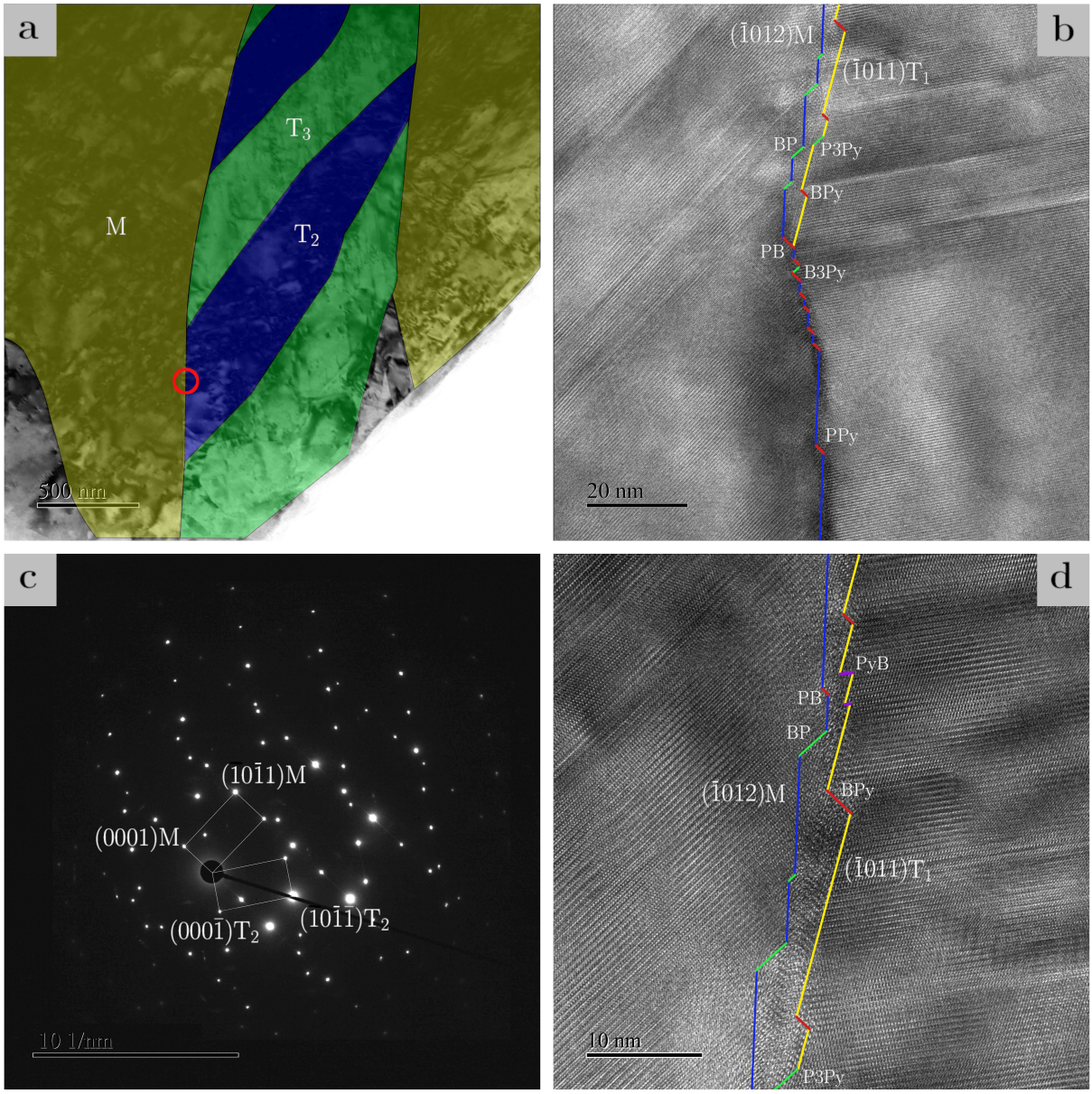

Fig. 4.16 (a) Bright field image of the lower portion of the first area of interest, at low magnification; the matrix (M) is depicted in yellow, the secondary twin (T_2) in blue, the tertiary twin (T_3) in green. (b) HRTEM image of the region denoted by the red circle in (a); boundaries have been drawn using the following colour scheme. Blue: $(\bar{1}012)$ plane of the matrix and primary twin; yellow: $(\bar{1}011)$ plane of the primary and secondary twins; red: PB facets of the primary twin, BPy facets of the secondary twin and PPy facets of the double twin; green: BP facets of the primary twin, P3Py facets of the secondary twin and B3Py facets of the double twin; purple: PyB facets of the secondary twin. (c) Indexed SAD pattern of the region denoted by the red circle in (a). (d) HRTEM image of the upper region of (b), higher magnification, colour coding as in (b).

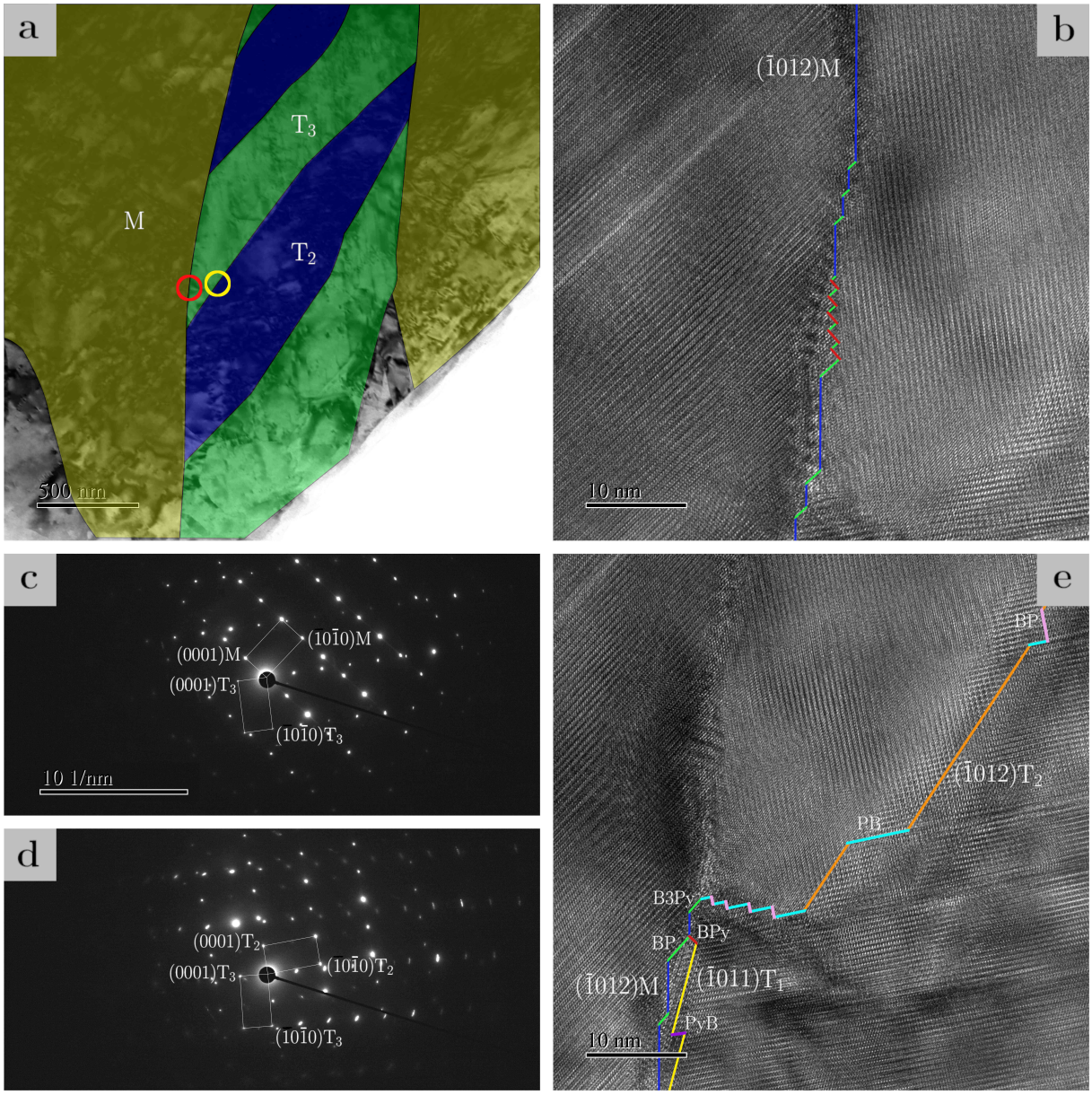

Fig. 4.17 (a) Bright field image of the lower portion of the first area of interest, at low magnification; the matrix (M) is depicted in yellow, the secondary twin (T_2) in blue, the tertiary twin (T_3) in green. (b) HRTEM image of the region denoted by the red circle in (a), periodic contrast in the centre we interpret as moiré patterning; boundaries have been drawn using the following colour scheme. Blue: $(\bar{1}012)$ plane of the matrix and primary twin; green: B plane of the matrix; red: P plane of the matrix. It should be noted that facets in the triple twin boundary are incommensurate, such that B and P planes of the matrix are not coincident with any rational planes of the triple twins. (c) Indexed SAD pattern of the region denoted by the red circle in (a). (d) Indexed SAD pattern of the region denoted by the yellow circle in (a). (e) HRTEM image of the junction between matrix, triple twin and double twin, directly below (b). Colour scheme is as follows. Blue: $(\bar{1}012)$ plane of the matrix and primary twin; yellow: $(\bar{1}011)$ plane of the primary and secondary twins; red: BPy facets of the secondary twin; green: BP facets of the primary twin and B3Py facets of the double twin; purple: PyB facets of the secondary twin; orange: $(\bar{1}012)$ plane of the secondary and tertiary twin; aquamarine: PB facets of the tertiary twin; pink: BP facets of the tertiary twin.

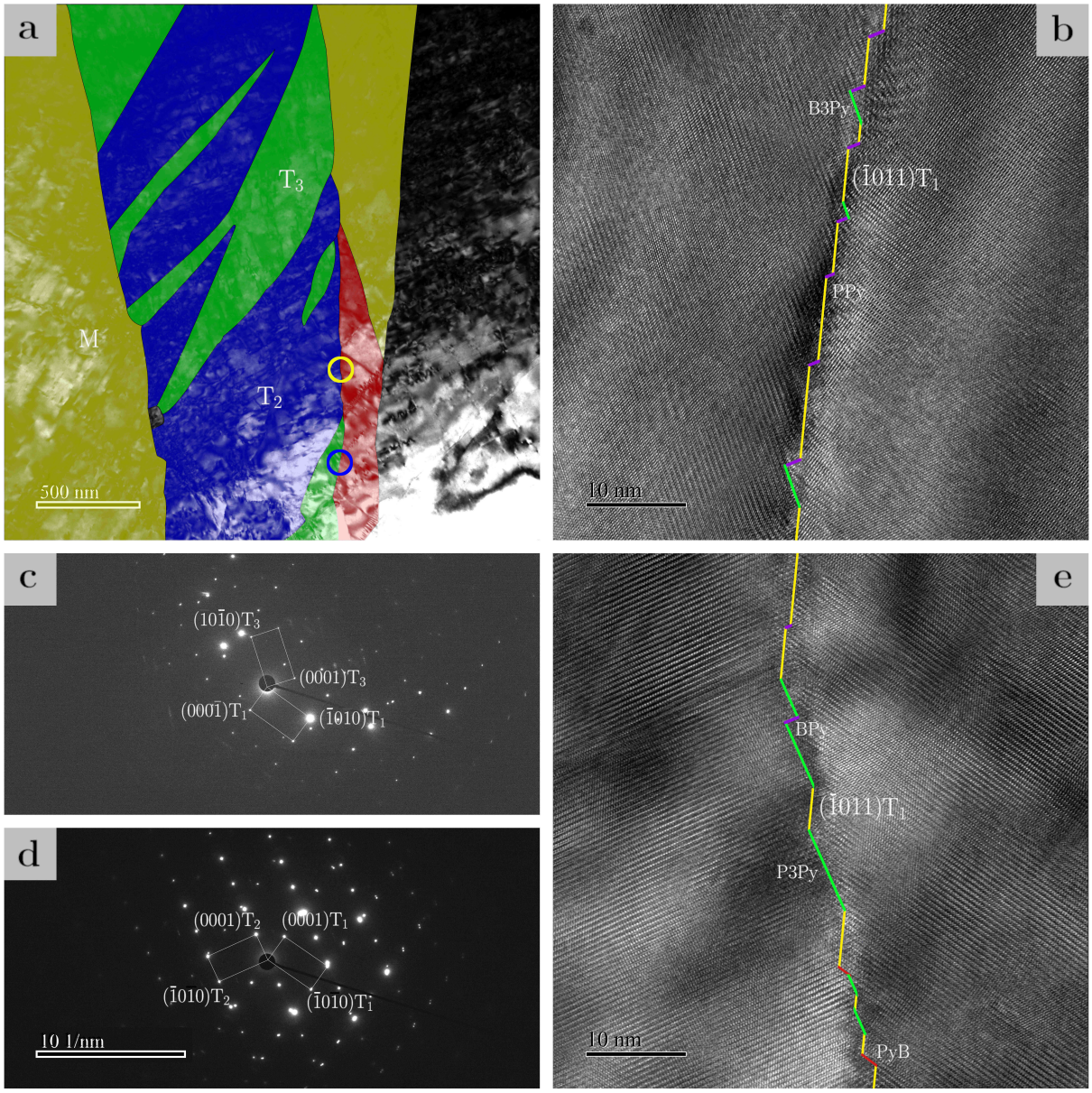

Fig. 4.18 (a) Bright field image of the second area of interest, at low magnification; the matrix (M) is depicted in yellow, the primary twin (T_1) in red, the secondary twin (T_2) in blue, the tertiary twin (T_3) in green. (b) HRTEM image of the region denoted by the blue circle in (a); boundaries have been drawn using the following colour scheme. Yellow: $(\bar{1}011)$ plane of the matrix and primary twin; green: B3Py facets of the double twin; purple: PPy facets of the double twin. (c) Indexed SAD pattern of the region denoted by the blue circle in (a). (d) Indexed SAD pattern of the region denoted by the yellow circle in (a). (e) HRTEM image of the region denoted by the yellow circle in (a); boundaries have been drawn using the following colour scheme. Yellow: $(\bar{1}011)$ plane of the matrix and primary twin; red: PyB facets of the primary twin; green: P3Py facets of the primary twin; purple: BPy facets of the primary twin; red: PyB facets of the primary twin.

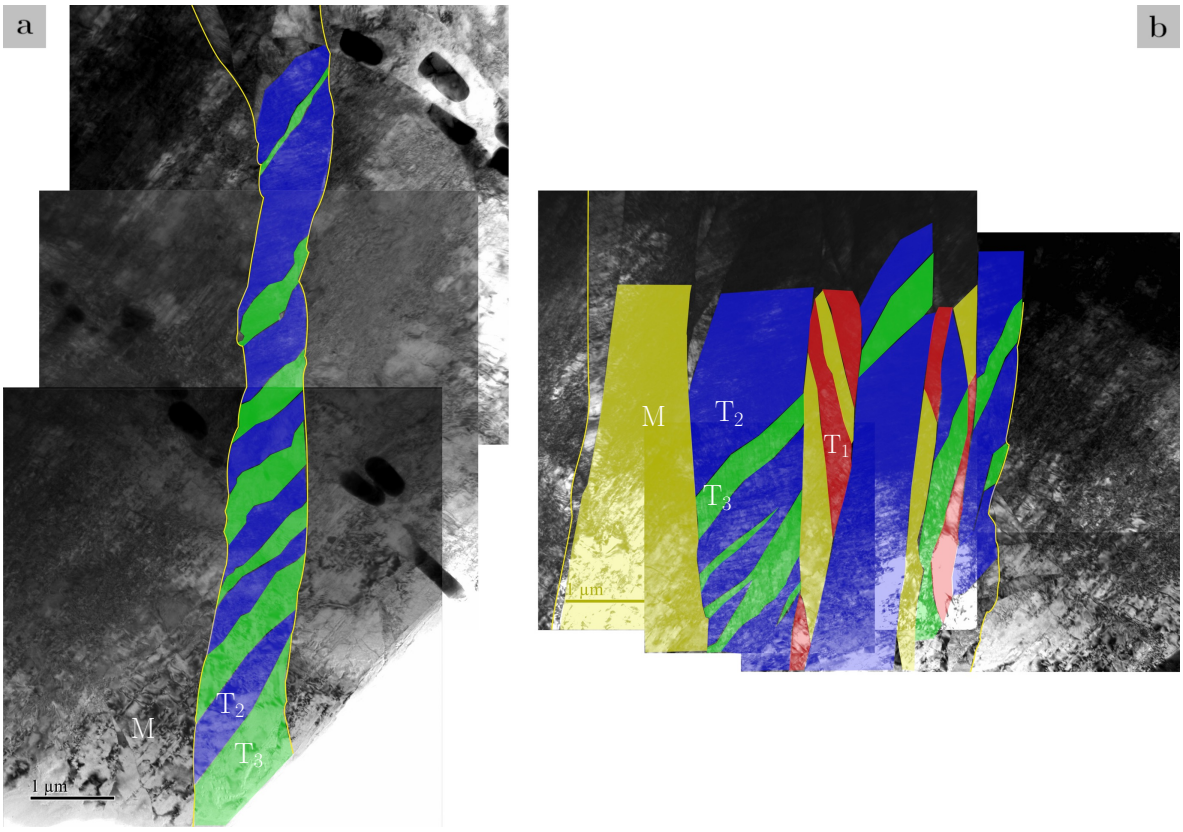

Fig. 4.19 TEM bright field images of the second and third areas of interest identified in the sample, colour coded according to the twinning stage: yellow denotes the matrix, red the primary tension twin T_1, blue the secondary compression twin T_2, green the tertiary tension twin T_3.

In particular, we select the interfaces marked by the yellow and blue circles in figure 4.18a for investigation. The corresponding SAD patterns show misorientation relations of $-35°[1\bar{2}10]$ and $58°[1\bar{2}10]$ for the blue and yellow circles respectively, and the boundaries are identified as interfaces between the primary and secondary twins (red and blue regions) and between the primary and tertiary twins (red and green regions). Thus the presence of left-over primary twin in this cluster allows us to observe what is effectively a C-T type 1 double twin to matrix interface in the form of an interface between T_1 and T_3. A high-resolution image of this interface is shown in figure 4.18b, where segments of the $(\bar{1}011)$ secondary twin interface are seen, interspersed with B3Py and PPy facets, as anticipated in the theoretical discussion (there referred to as 3PyB and PyP, honouring the convention of listing the plane of the matrix first and that of the double twin second). Facets may also be observed in the interface between the primary and secondary twins, effectively a compression twin to matrix interface: this is shown in figure 4.18e. Here,

BPy, PyB and P3Py facets are found, with the latter appearing to have a length comparable to that of the segments of $(\bar{1}011)$ twin interface, and consequently the overall orientation of the interface is seen to deviate from $(\bar{1}011)$ considerably. In the bright field image, however, the interface between T_1 and T_2 and that between T_1 and T_3, though curved, appear to have similar orientations, suggesting that the large deviation from $(\bar{1}011)$ observed in figure 4.18e may be a local phenomenon due to the presence of longer facets.

4.2.4 Discussion of experimental results

As we have noted before, observations of double twins with $(10\bar{1}1)-(10\bar{1}2)$ type 1 twinning sequence are usually based on the measurement of a misorientation relation between the double twin and the surrounding grain in the vicinity of $38^\circ\langle 1\bar{2}10\rangle$, via methods such as EBSD. However, unless a twin has only partially retwinned, this misorientation relation may also be attributed to $(10\bar{1}2)-(10\bar{1}1)$ type 1 double twinning, and distinction of the two modes is only possible by measurement of the relevant crystallographic planes. It is also to be noted that this misorientation relation can be attributed to interfaces between adjacent tension and compression twins, and it is thus necessary to consider the shape and position of the twins to identify them properly.

These uncertainties are overcome in TEM experiments, where SAD patterns may be analysed in concert with bright field observations, thus enabling a thorough investigation of the K_1 planes and determination of the sequence of twinning events, as presented in the previous section. Of course, in the TEM quality comes at the expense of quantity, by reason of the limited size and lengthy preparations of the specimens. It is thus difficult to make multiple observations in TEM experiments, and to date this has been done only by Cizek and Barnett [44], who were able to analyse a large number of double twins, albeit having to forgo high-resolution imaging of their interfaces. Such high-resolution imaging we were able to perform, leading to the identification of facets in single and double twin boundaries with both C-T and T-C twinning sequence.

A $(10\bar{1}1)-(10\bar{1}2)$ type 1 double twin interface was studied via HRTEM by Lentz et al. [181]; in their case however a small residue of primary twin was present between the matrix and the secondary twin, such that the double twin to matrix interface was not observed. This led the authors to conclude that such a residue is always present in double twin interfaces, and that direct interfaces between a double twin and the matrix are never observed. Our findings contradict

this statement: we have shown that in the case of both tension-compression (figure 4.16b) and compression-tension (figure 4.18b) type 1 double twinning direct interfaces between the double twin and the matrix are formed, and that these contain commensurate facets consistent with the combination of primary and secondary twinning disconnections envisaged in the theoretical analysis pursued in section 4.1.2. In a study conducted by Ando at al. [188] on a magnesium alloy, a C-T double twin to matrix twin interface was imaged using HRTEM, but the resolution was still too low to ascertain the presence of facets in the interface. Hence, high-resolution imaging allows us for the first time to shed a light on the morphology of C-T double twin to matrix interfaces.

We are thus able to conclude that the orientation of the double twin interface is largely predetermined by that of the primary twin interface. This is seen to contain facets for both types of primary twin analysed, i.e. $(\bar{1}012)$ and $(\bar{1}011)$. Upon arrival of secondary twinning disconnections, facets in the primary twin interface may remain commensurate and transform into facets of the double twin; segments of interface originally aligned with the primary K_1 plane are however seen to remain largely unchanged, thus becoming incommensurate, which is consistent with the small angles comprising the rotation of a flat primary twin interface following the impingement of secondary twinning disconnections calculated in section 3.4.1. Indeed, these angles (fractions of a degree for both T-C and C-T type 1 double twins) correspond to the maximum possible rotations imposed on a flat interface by secondary twinning disconnections. Thus, the deviation of the double twin to matrix interface from the primary K_1 plane is attributable to the presence of facets in the interface, which in turn results from the occurrence of facets in the primary twin interface. The magnitude of this deviation however depends on the length and density of the facets, such that it is not surprising that previous measurements of the macroscopic orientation of double twin interfaces yielded results that spread around the pole corresponding to the primary K_1 plane.

We now measure the macroscopic orientation of double twin interfaces in the second and third areas of interest, figure 4.15. We start with the boundary of the $(\bar{1}012)-(\bar{1}011)$ T-C type 1 double twin in figure 4.15a; though curved, this double twin to matrix interface is approximately aligned with the trace of the $(\bar{2}025)$ plane of the matrix, which is $\sim 6^\circ$ from the primary K_1 plane, $(\bar{1}012)$. In the second area of interest, figure 4.15b, we identify a number of T-C type 1 double

twin boundaries, which are evidently considerably curved; the average orientations are measured to be approximately along the traces of $(\bar{2}025)$, $(\bar{1}014)$ ($\sim 18^\circ$ from $(\bar{1}012)$) and $(\bar{1}013)$ ($\sim 11^\circ$ from $(\bar{1}012)$). As a consequence of the presence of regions of the primary twin in parts of the cluster, see e.g. the area considered in figure 4.18a, we may also measure the macroscopic orientation of a C-T type 1 double twin to matrix interface, revealing that this is close to the trace of the $(\bar{4}045)$ plane of the primary twin, $\sim 6^\circ$ from $(\bar{1}011)$. However, we have also observed that the primary twin interface deviates from $(\bar{1}011)$, by reason of the facets observed in figure 4.18e; the macroscopic orientation of this twin interface appears close to the trace of the $(\bar{2}023)$ plane. Cizek and Barnett [44] reported that a fraction of the double twin to matrix interfaces they examined were aligned with the trace of the $(\bar{2}023)$ plane: our findings suggest that this may have already been the macroscopic orientation of the primary twin interface.

As we remarked at the beginning of this chapter, C-T double twins with $(10\bar{1}1) - (10\bar{1}2)$ twinning sequence are by far the most widely observed in magnesium alloys. In contrast, T-C double twins are less common, and the study presented here includes the first high-resolution investigation of T-C double twin interfaces in a magnesium alloy. This is because this twinning mode is reported in magnesium only in instances where the primary tension twin has consumed large portions of the grain, such that compression twins formed inside them do not reach the primary twin to matrix interfaces. To our knowledge, the only TEM observation of T-C double twins surrounded by untwinned material in a hcp metal occurred in a cold rolled Zr alloy studied by An et al. [203]. They also investigated the single and double twin to matrix interfaces using HRTEM, and their observations of facets in these boundaries are consistent with the ones reported in this thesis for magnesium.

In this thesis and in the related publication [204] we also report the first observation of interfaces between T-C-T triple twins and the matrix. Triple twins are rarely observed, and a review of the available literature shows that for the T-C-T triple twins under consideration, the primary $(10\bar{1}2)$ twin has grown to a size covering between 50% and the near entirety of the grain. Conversely, nucleation of the secondary $(10\bar{1}1)$ twin is limited to a thin lamella, the size of which does not change when tertiary $(10\bar{1}2)$ twinning is initiated inside it. Therefore, in these studies the secondary and tertiary twins never reach the primary twin to matrix interface (of which very little may be left) and the tertiary twin is entirely contained within the primary twin.

Therefore, only interfaces between the primary and tertiary twin may be observed, which are indistinguishable from interfaces of C-T double twins with the matrix.

In contrast, the triple twins observed in the present work interface directly with the matrix. In all areas investigated in our sample, the primary tension twins were found to have remained small in size, never growing in thickness beyond a few microns before retwinning twice, such that the $\sim 48^{\circ}$ misorientation between the triple twin and the matrix was measured. Indeed, barely any thin residues of primary twin are left in the twin analysed in figure 4.16, and only narrow regions are found in the cluster in figure 4.15b. The secondary compression twin mostly grows to consume the primary twin, while the tertiary twin forms relatively thin bands within the secondary twin, not retwinning it fully. Nor does the last twinning event appear to change the orientation of the double twin to matrix interface considerably; this is in accord with the theory discussed in section 4.1.3, as the commensurate facets of the double twin are turned into incommensurate facets in the triple twin and left unchanged.

One may then ask why our observation of triple twinning differs so markedly from that of previous studies, and several reasons can be proposed. One important factor may be alloy composition. In the reported literature, magnesium alloys that did not contain rare-earth elements were utilised: Mg-3.3Al-1Zn [180, 178, 183], Mg-4Li [181], pure Mg [179] and Mg-2.6Al-0.9Zn-0.37Mn [182]. Conversely, we investigated an alloy containing neodymium, which is characterised by a large atomic radius compared to that of magnesium, and is known to segregate to twin boundaries [15, 205, 206]; Nd atoms may then act as an obstacle to the glide of twinning disconnections, thus inhibiting twin growth and promoting the formation of facets in twin interfaces. In addition, the chosen technique for this study was hot rolling, whilst in previous investigations the materials were either warm rolled [180, 178] or tensile tested at room temperature [179, 181–183]. In order to inquire as to the presence of Nd at twin interfaces, scanning transmission electron microscopy energy dispersive X-ray spectroscopy (STEM-EDS) mapping of the region containing the twin cluster in figure 4.15b was performed. In this technique, a coherent electron beam is raster scanned across the sample; the spectrum of the emitted X-rays is recorded for each position of the beam, such that information on the chemical composition at each point can be extracted [207–210]. In the area of interest, no segregation of Al or Nd to the twin interfaces was observed, with Nd found to be below the

detection threshold. This result indicates that the vast majority of the Nd contained in the alloy under consideration was tied up in the large Nd-Al rich precipitates observed in the SEM images of figure 4.10. However, precipitates have also been reported to inhibit tension twin growth while promoting twin nucleation, thus leading to a larger number of narrow twins; this was observed in experimental investigations of Mg-Al-Zn [211, 212], Mg-Zn [213] and Mg-Al [214] alloys, as well as computer simulations [215–217]. Precipitates have been found to oppose the glide of tension twinning disconnections and discourage further twin growth even after they have been enveloped by the twin [218]. Finally, precipitates were observed to suppress compression twin growth in a Mg-Zn alloy [219]. The density of precipitates in the alloy used in this study is not so high as to single-handedly justify the limited growth of all twins in the sample; however, the presence of precipitates is likely to be a contributing factor, unlike solute segregation at twin boundaries, which was not detected in the microstructure examined here.

Thus, the experimental observations illustrated in this chapter complement the theoretical predictions based on the topological model presented in the previous sections. SEM and EBSD techniques were used to produce preliminary observations of the microstructure and ensure the presence of double twins in the Mg-1.18wt%Al-1.77wt%Nd alloy studied here; subsequently, the combination of SAD patterns and HRTEM allowed us to uniquely identify double and triple twins, and to characterise the morphology of their interfaces. Facets consistent with theoretical predictions were observed in all twin interfaces, and high-resolution imaging of T-C double twin and T-C-T triple twin to matrix interfaces was reported for the first time. Deviations of the twin interfaces from the primary K_1 planes, also observed in the literature, were ascribed to the presence of facets in the interfaces.

Chapter 5

Further work and conclusions

"*Let the unseen days be. Today is more than enough.*"

The Children of Húrin, JOHN R. R. TOLKIEN

The purpose of this thesis was to investigate the structure of double twin to matrix interfaces in magnesium. Double twins have been found to play a role in mediating the development of a randomised texture in both rare-earth and non-rare-earth magnesium alloys, thus highlighting the importance of studying this phenomenon. While classical twins in hcp metals have been amply examined in the literature, as was explained in chapter 1 of this thesis, double twinning has not been analysed as thoroughly, particularly with regards to nucleation and morphology of the double twin interface, such that we focused on the latter.

The tool chosen to investigate the double twinning problem was bicrystallography and its application in the topological theory of interfacial defects, introduced in chapter 2. This was applied to classical twinning in magnesium, which occurs on the $(10\bar{1}2)$, $(10\bar{1}1)$ and $(10\bar{1}\bar{3})$ planes: for each twin, the interfacial structures with lowest energy were found and relaxed using atomistic simulations in the form of the DFT-based aGPT, and the parameters of characteristic twinning disconnections were derived, as summarised in table 2.1.

In chapter 3, the subject of double twinning was introduced, treating both compression-tension and tension-compression double twinning, i.e. twinning sequences $(10\bar{1}1)-(10\bar{1}2)$, $(10\bar{1}\bar{3})-(10\bar{1}2)$, $(10\bar{1}2)-(10\bar{1}1)$ and $(10\bar{1}2)-(10\bar{1}\bar{3})$. As a consequence of hexagonal symmetry, four geometrically distinct variants exist for each double twinning sequence, and they were labelled according to their misorientation relations with the matrix as types 1 to 4. Attention

was then focused on double twin types 1 and 2, for which the component mechanisms share the same plane of shear. These were analysed using Crocker's theory of double twinning [41], which involves treating the double twin transformation as a simple shear resulting from the combination of the two simple shears describing the component twinning modes. Thus invariant planes of the total double twin transformation were found for all the double twins under consideration. In particular, it was shown that $(10\bar{1}1) - (10\bar{1}2)$ and $(10\bar{1}\bar{3}) - (10\bar{1}2)$ double twinning belong to the same simple equivalent twinning mode, whose invariant planes represent the K_1 and K_2 planes of the transformation, in accordance with Crocker's reciprocal theorem. The reverse twinning sequences also produce the same invariant planes, though these are now referred to the coordinate system of the double twin, such that the indices are different. Moreover, it is found that in order to restore the invariant planes in their original orientation, the double shear has to be accompanied by a mutual rotation of the two lattices; this modifies the double twin misorientation relations, ensuring that type 1 and type 2 transformations produce the same invariant planes. These results are reported in tables 3.3 and 3.4.

Crocker's treatment of double twinning was later extended by Bevis and Crocker in a more comprehensive theory of non-classical twinning [76]. This was defined as a twinning shear that restores the lattice in a different orientation, which does not have to obey one of the classical orientation relations derived by Bilby and Crocker [75] and presented in chapter 1; moreover, it was shown that all the twinning parameters may be derived using a unitary matrix, i.e. the correspondence matrix. Double twinning is a special case of non-classical twinning, as was formally shown by Acton et al. [130]. In chapter 3, we applied Bevis and Crocker's theory to the hexagonal lattice with magnesium axial ratio, and recovered the classical twinning modes as well as the double twinning modes predicted by Crocker, thus verifying that the two treatments are equivalent. Notably, Bevis and Crocker's theory does not require that a rotation is added to the total transformation in order to restore the invariant planes in their original orientation, as this is already implicitly included in the derivation of said planes from the correspondence matrix.

In Crocker's theory, the invariant planes of the simple equivalent twinning mode corresponding to a given double twinning mechanism are taken to be the K_1 and K_2 planes of the transformation, such that the double twin may grow on one of these planes, in a one-step process. However, experimental observations suggest that a fully formed primary twin retwins internally,

thus pointing towards a two-step process. This was modelled in chapter 3 using the concept of twinning disconnections derived using the topological theory. Firstly the case of secondary twinning disconnections arriving at a flat primary twin to matrix interface was analysed, and it was found that if atoms in the interface are not constrained by the surrounding matrix, the double twin to matrix interface may be macroscopically rotated from the initial orientation of the primary K_1 plane. The maximum angles of rotation were calculated for each double twin type in table 3.5, and were found to be less than 1° for type 1 mechanisms and less than 10° for type 2 mechanisms. Secondly, secondary twinning disconnections arriving at a stepped primary twin interface were investigated. It was proposed by Pond [139] that the secondary twinning disconnections may compensate the misfit introduced by primary twinning disconnections in the primary interface. For the case of double twinning in magnesium, we found that misfit compensation on the part of secondary twinning disconnections was not always possible, as in most mechanisms the direction of their Burgers vectors implied that they would add to the misfit rather than reduce it. However, were misfit compensation possible, it was found that the macroscopic orientation of the double twin to matrix interface would be rotated from the primary K_1 plane by an amount in good agreement with the orientation of the invariant planes produced by Crocker's theory. The topological model in this instance also predicts that the twinning disconnections would introduce a short ranged lattice distortion, which is to be partitioned between the matrix and the double twin; this corresponds to the lattice rotation in Crocker's theory, which however was long ranged and not explicitly partitioned between the two crystals. Finally, the topological model infers that the misfit-free interface thus created is immobile, as opposed to Crocker's proposition that the double twin should be able to grow on the invariant plane. Indeed, no twinning disconnection may be found to be glissile on the invariant planes resulting from Crocker's treatment. Thus in this thesis we present for the first time a unification of not only the phenomenological theories of double twinning of Crocker and coworkers, which are shown to yield equivalent results, but also of the models based on the topological theory of interfacial defects, such that the points of connection between the two treatments are highlighted. These may be summarised as follows:

- The elimination of misfit parallel to the double twin to matrix interface may be modelled using both the phenomenological and the topological theories: in the latter, this is modelled explicitly by means of the compensation of misfit on the part of arrays of primary and

secondary twinning disconnections in the interface; in Crocker's theory, the misfit-free condition is built into the requirement that the final double twin interface plane be an invariant plane of the transformation. Thus, similar predictions for the orientation of the double twin interface can be obtained using the two models.

- The existence of a lattice distortion resulting in a mutual rotation between the parent and doubly twinned crystals is predicted by both models: in the phenomenological theory, this rotation is long ranged and stems from the need for the undistorted planes of the double twin transformation to also be unrotated; in the topological model a short ranged distortion is introduced by the components of the Burgers vectors of the twinning disconnections that are perpendicular to the interface, and it is partitioned between the parent and the double twin.

Type 3 and 4 double twin variants are not covered by the phenomenological theories, as the requirement for the component twinning shears to produce a double twinning simple shear is that they share a common plane of shear, a condition which is not satisfied by type 3 and 4 mechanisms. On the other hand, the topological models have no such requirement, and thus need not be limited to treatment of type 1 and 2 double twinning mechanisms. While examination of the type 3 and 4 variants is more challenging due to the lack of a common plane of shear onto which the dichromatic pattern may be projected, the topological theory can in principle be applied to these cases, and further research could extend the results obtained here to these variants.

In chapter 4 the requirement of misfit removal across the double twin interface was put aside, and the concept of faceted interfaces was introduced. It was shown that in single twin to matrix interfaces, facets may occur as an accumulation of twinning disconnections behind an obstacle or, in the case of the $(10\bar{1}2)$ twin, as sessile byproducts of the interaction between matrix dislocations and the twin boundary. It was thus acknowledged that single twin to matrix interfaces are often made of terraces of twin boundary parallel to the K_1 plane separated by commensurate facets. We then sought to establish how such a configuration may be affected by the arrival of secondary twinning disconnection. It was found that for all the double twinning sequences analysed and for both type 1 and 2 variants, facets in the primary twin interface can

combine with facets of the secondary twin to form commensurate facets in the double twin to matrix interface.

The theoretical investigation of facets in double twin interfaces is an area that would benefit from further research. In particular, atomistic simulations may be employed to model the interaction between secondary twinning disconnections and existing facets in the primary twin to matrix interface, as the mechanism by which the facet is created in the double twin to matrix interface is not yet clear. In this endeavour, the aGPT will be a powerful tool, providing DFT accuracy at greatly reduced computational cost. The aGPT may also be used to test the topological model of double twin to matrix interfaces free of misfit by simulating secondary twinning disconnections interacting with an array of equally spaced primary twinning disconnections in the primary twin interface.

The second part of chapter 4 dealt with experimental observations of twin interfaces. For this purpose, a rare-earth magnesium alloy subjected to hot rolling was selected for investigation via transmission electron microscopy. The sample was initially imaged using EBSD techniques to ascertain the presence of double twins, followed by preparation of the TEM foils through electropolishing. In the TEM, the sample was tilted down the $[1\bar{2}10]$ zone axis, and three areas of interest were then identified for in-depth analysis. The first object was a twin presenting a rounded tip, which was identified as a $(10\bar{1}1)$ compression twin with the aid of selected-area diffraction patterns. High-resolution TEM imaging was used to capture the twin to matrix interface, and facets of the kind envisaged by the topological model were observed; the density of facets was particularly high around the twin tip, resulting in its macroscopically rounded appearance.

The second area of interest contained a long twin-like object traversed by internal boundaries. Investigation of the SAD patterns and HRTEM images led to the discovery that this was a $(\bar{1}012) - (\bar{1}011)$ tension-compression type 1 double twin with portions that had retwinned internally for a third time, thus producing a $(\bar{1}012) - (\bar{1}011) - (\bar{1}012)$ type 1a triple twin. We were then able to observe a triple twin to matrix interface for the first time in a magnesium alloy; additionally, TEM imaging with good enough resolution to capture facets in interfaces had not previously been carried out on double twins in magnesium. Hence we were able to identify in the double twin to matrix interface the commensurate facets arising from the combination of

primary and secondary twinning disconnections predicted by the topological model. These were separated by terraces of the original interface parallel to the primary K_1 plane, which appeared unchanged in orientation, though they were rendered incommensurate; this is in accordance with the topological model of secondary twinning disconnections impinging on a flat primary twin interface presented in chapter 3. Conversely, the triple twin to matrix interface was found to be fully incommensurate. This was expected from the analysis of the topological model, as no combination of primary, secondary and tertiary twinning disconnections for this twinning sequence could form commensurate facets.

The third area of interest was a cluster of twins with noticeably curved boundaries. Investigation of the SAD patterns revealed that the cluster was formed of single, double and triple twins with the same twinning sequence as the isolated twin-like object in the previous area of interest, i.e. $(\bar{1}012)-(\bar{1}011)-(\bar{1}012)$. However, in this case more sizeable portions of the primary twin remained, and this enabled us to observe interfaces between the primary and tertiary twin. These are effectively $(\bar{1}011)-(\bar{1}012)$ type 1 double twin to matrix interfaces, such that it was possible to image this interface using high-resolution; the commensurate facets expected from the topological model for this twinning sequence were once again confirmed to be present.

Several points were gathered from the TEM observations of chapter 4. The first is that the macroscopic orientation of twin to matrix interfaces does not necessarily correspond to the K_1 plane of the transformation; facets occur in single twins and appear to change the overall orientation of their interfaces. When internal retwinning occurs, the facets preexisting in the primary twin to matrix interface are transformed into facets of the double twin, and thus they affect the macroscopic orientation of double twin to matrix interfaces as well. Consequently, the overall orientation of double twin boundaries is largely predetermined by that of the initial primary twin interface, and this may explain why the orientation of such double twin interfaces has not been measured unambiguously so far in TEM experiments: only high-resolution observations can assess the length and density of facets in a given interface. This in turn highlights the importance of TEM and HRTEM experiments not only in determining the structure of the interfaces, but also in identifying the twinning sequences unequivocally; this cannot be done except in special cases using EBSD, as only the relative orientation of neighbouring grains may be measured,

such that structures that present the same misorientation relation across the interface cannot be distinguished.

Some open questions remained after discussion of these experimental results. In particular, it is still not entirely clear to us why the primary tension twins in our sample did not appear to grow as much as observed in other experimental studies, instead retwinning internally twice. In light of STEM-EDS observations, it was inferred that the twin interfaces were effectively free of solute atoms, such that these may not have hindered twin growth; a high density of Nd-Al precipitates was found in the sample, and these may be partly responsible for inhibited twin growth. It is thought that the interplay of internal local stresses is likely to have played a part in producing the observed twin morphology; however, this would be difficult to quantify.

The next problem up for debate is that of double twin nucleation. Having ascertained that double twin formation is a two-step process, explaining how it might occur is desirable. It was pointed out in chapter 1 that only two theories of double twin nucleation in magnesium have been proposed so far; neither includes tension-compression double twinning, and only one features all four variants of compression-tension double twinning. To our knowledge these theories have not been tested using atomistic simulations, nor have experiments been conducted purporting to observed double twin nucleation. More research is thus needed in this area.

References

[1] G.V. Raynor. The Physical Metallurgy of Magnesium and Its Alloys. International Series of Monographs in the Science of the Solid State. Elsevier Science & Technology, 1959.

[2] T. Al-Samman and X. Li. Sheet texture modification in magnesium-based alloys by selective rare earth alloying. Materials Science and Engineering: A, 528(10):3809–3822, 2011.

[3] Z. R. Zeng, Y. M. Zhu, S. W. Xu, M. Z. Bian, C. H. J. Davies, N. Birbilis, and J. F. Nie. Texture evolution during static recrystallization of cold-rolled magnesium alloys. Acta Materialia, 105:479–494, 2016.

[4] A. Imandoust, C. Barrett, T. Al-Samman, K. Inal, and H. El Kadiri. A review on the effect of rare-earth elements on texture evolution during processing of magnesium alloys. Journal of Materials Science, 52:1–29, 2017.

[5] S. Sandlöbes, S. Zaefferer, I. Schestakow, S. Yi, and R. Gonzalez-Martinez. On the role of non-basal deformation mechanisms for the ductility of Mg and Mg–y alloys. Acta Materialia, 59(2):429–439, 2011.

[6] I. Basu, T. Al-Samman, and G. Gottstein. Shear band-related recrystallization and grain growth in two rolled magnesium-rare earth alloys. Materials Science and Engineering: A, 579:50–56, 2013.

[7] J. Hirsch and T. Al-Samman. Superior light metals by texture engineering: Optimized aluminum and magnesium alloys for automotive applications. Acta Materialia, 61(3):818–843, 2013.

[8] M. A. Steiner, J. J. Bhattacharyya, and S. R. Agnew. The origin and enhancement of $\{0001\}\ \langle 11\bar{2}0\rangle$ texture during heat treatment of rolled AZ31B magnesium alloys. Acta Materialia, 95:443–455, 2015.

[9] J. J. Bhattacharyya, S. R. Agnew, and G. Muralidharan. Texture enhancement during grain growth of magnesium alloy AZ31B. Acta Materialia, 86:80–94, 2015.

[10] S. R. Agnew and J. F. Nie. Preface to the viewpoint set on: The current state of magnesium alloy science and technology. Scripta Materialia, 63:671–673, 2010.

[11] N. Stanford, D. Atwell, A. Beer, C. Davies, and M. R. Barnett. Effect of microalloying with rare-earth elements on the texture of extruded magnesium-based alloys. Scripta Materialia, 59(7):772–775, 2008.

[12] M. Sanjari, A. Farzadfar, A. S. H. Kabir, H. Utsunomiya, I. Jung, R. Petrov, L. Kestens, and S. Yue. Promotion of texture weakening in magnesium by alloying and thermomechanical processing:(I) alloying. Journal of Materials Science, 49:1408–1425, 2014.

[13] N. Stanford and M. R. Barnett. The origin of "rare earth" texture development in extruded Mg-based alloys and its effect on tensile ductility. Materials Science and Engineering: A, 496(1):399–408, 2008.

[14] D. Griffiths. Explaining texture weakening and improved formability in magnesium rare earth alloys. Materials Science and Technology, 31(1):10–24, 2015.

[15] D. Guan, W. M. Rainforth, L. Ma, B. Wynne, and J. Gao. Twin recrystallization mechanisms and exceptional contribution to texture evolution during annealing in a magnesium alloy. Acta Materialia, 126:132–144, 2017.

[16] N. Stanford, G. Sha, J. H. Xia, S. P. Ringer, and M. R. Barnett. Solute segregation and texture modification in an extruded magnesium alloy containing gadolinium. Scripta Materialia, 65(10):919–921, 2011.

[17] J. P. Hadorn, T. T. Sasaki, T. Nakata, T. Ohkubo, S. Kamado, and K. Hono. Solute clustering and grain boundary segregation in extruded dilute Mg–Gd alloys. Scripta Materialia, 93:28–31, 2014.

[18] J. P. Hadorn, K. Hantzsche, S. Yi, J. Bohlen, D. Letzig, J. A. Wollmershauser, and S. R. Agnew. Role of solute in the texture modification during hot deformation of Mg-rare earth alloys. Metallurgical and Materials Transactions A, 43(4):1347–1362, 2011.

[19] J. D. Robson, S. J. Haigh, B. Davis, and D. Griffiths. Grain boundary segregation of rare-earth elements in magnesium alloys. Metallurgical and Materials Transactions A, 47(1):522–530, 2015.

[20] E. A. Ball and P. B. Prangnell. Tensile-compressive yield asymmetries in high strength wrought magnesium alloys. Scripta Metallurgica et Materialia, 31(2):111–116, 1994.

[21] J. D. Robson, X. Zhou, and G. E. Thompson. Magnesium research: Scientific challenges. Materials Technology, 24(3):133–136, 2009.

[22] J. Bohlen, M. R. Nürnberg, J. W. Senn, D. Letzig, and S. R. Agnew. The texture and anisotropy of magnesium–zinc–rare earth alloy sheets. Acta Materialia, 55(6):2101–2112, 2007.

[23] I. Basu and T. Al-Samman. Triggering rare earth texture modification in magnesium alloys by addition of zinc and zirconium. Acta Materialia, 67:116–133, 2014.

[24] F. J. Humphreys and M. Hatherly. Recrystallization and related annealing phenomena. Elsevier, 2012.

[25] M. R. Barnett, M. D. Nave, and C. J. Bettles. Deformation microstructures and textures of some cold rolled Mg alloys. Materials Science and Engineering: A, 386(1):205–211, 2004.

[26] C. Drouven, I. Basu, T. Al-Samman, and S. Korte-Kerzel. Twinning effects in deformed and annealed magnesium–neodymium alloys. Materials Science and Engineering: A, 647:91–104, 2015.

[27] D. Guan, W. M. Rainforth, J. Gao, J. Sharp, B. Wynne, and L. Ma. Individual effect of recrystallisation nucleation sites on texture weakening in a magnesium alloy: Part 1-double twins. Acta Materialia, 135:14–24, 2017.

[28] D. Guan, B. Wynne, J. Gao, Y. Huang, and W. M. Rainforth. Basal slip mediated tension twin variant selection in magnesium WE43 alloy. Acta Materialia, 170:1–14, 2019.

[29] D. Guan, X. Liu, J. Gao, L. Ma, B. P. Wynne, and W. M. Rainforth. Exploring the mechanism of "rare earth" texture evolution in a lean Mg–Zn–Ca alloy. Scientific reports, 9(1):1–11, 2019.

[30] D. Kay. Schaum's Outline of Tensor Calculus. Schaum's Outline Series. McGraw-Hill Companies, Incorporated, 1988.

[31] R. von Mises. Mechanik der plastischen Formänderung von Kristallen. ZAMM-Journal of Applied Mathematics and Mechanics/Zeitschrift für Angewandte Mathematik und Mechanik, 8(3):161–185, 1928.

[32] Y. Huang and J. Jiang. A critical review of von Mises criterion for compatible deformation of polycrystalline materials. Crystals, 13(2), 2023.

[33] P. W. Bakarian and C. H. Mathewson. Slip and twinning in magnesium single crystals at elevated temperatures. Transactions of the AIME, 152:226, 1943.

[34] C. S. Roberts. Magnesium and Its Alloys. Wiley series on the science and technology of materials. Wiley, 1960.

[35] R. E. Reed-Hill. A study of the $(10\bar{1}1)$ and $(10\bar{1}3)$ twinning modes in magnesium. Transactions of the American Institute of Mining and Metallurgical Engineers, 218(3):554–558, 1960.

[36] P. G. Partridge. The crystallography and deformation modes of hexagonal close-packed metals. Metallurgical Reviews, 12(1):169–194, 1967.

[37] H. Yoshinaga and R. Horiuchi. Deformation mechanisms in magnesium single crystals compressed in the direction parallel to hexagonal axis. Transactions of the Japan Institute of Metals, 4(1):1–8, 1963.

[38] H. Yoshinaga, T. Obara, and S. Morozumi. Twinning deformation in magnesium compressed along the C-axis. Materials Science and Engineering, 12(5):255–264, 1973.

[39] S. L. Couling and C. S. Roberts. New twinning systems in magnesium. Acta Crystallographica, 9(11):972–973, 1956.

[40] R. E. Reed-Hill and W. D. Robertson. Additional modes of deformation twinning in magnesium. Acta Metallurgica, 5(12):717–727, 1957.

[41] A. G. Crocker. Double twinning. Philosophical Magazine, 7(83):1901–1924, 1962.

[42] W. H. Hartt and R. E. Reed-Hill. The irrational habit of second-order $\{10\bar{1}1\} - \{10\bar{1}2\}$ twins in magnesium. Transactions of the Metallurgical Society of the AIME, 239(10), 1967.

[43] B. C. Wonsiewicz and W. A. Backofen. Independent slip systems and ductility of hexagonal polycrystals. Transaction of the Metallurgical Society of the AIME, 239:1422–1433, 1967.

[44] P. Cizek and M. R. Barnett. Characteristics of the contraction twins formed close to the fracture surface in Mg–3Al–1Zn alloy deformed in tension. Scripta Materialia, 59(9):959–962, 2008.

[45] M. R. Barnett, Z. Keshavarz, A. G. Beer, and X. Ma. Non-Schmid behaviour during secondary twinning in a polycrystalline magnesium alloy. Acta Materialia, 56(1):5–15, 2008.

[46] É. Martin, L. Capolungo, L. Jiang, and J. J. Jonas. Variant selection during secondary twinning in Mg–3%Al. Acta Materialia, 58(11):3970–3983, 2010.

[47] H. Kwon, H. Nakano, M. Mabuchi, and Y. Chino. Twinning behaviour of AZ31 Mg alloy alternately compressed in two orthogonal directions. Philosophical Magazine, 94(34):3960–3977, 2014.

[48] M. D. Nave and M. R. Barnett. Microstructures and textures of pure magnesium deformed in plane-strain compression. Scripta Materialia, 51(9):881–885, 2004.

[49] J. Jain, J. Zou, C. W. Sinclair, and W. J. Poole. Double tensile twinning in a Mg–8Al–0.5 Zn alloy. Journal of microscopy, 242(1):26–36, 2011.

[50] G. Gottstein. Physical Foundations of Materials Science. Springer Berlin Heidelberg, 2004.

[51] E. Schmid and W. Boas. Plasticity of Crystals with Special Reference to Metals. F.A. Hughes & Co. Ltd., 1950.

[52] S. Godet, L. Jiang, A. A. Luo, and J. J. Jonas. Use of Schmid factors to select extension twin variants in extruded magnesium alloy tubes. Scripta Materialia, 55(11):1055–1058, 2006.

[53] S. Mendelson. Dislocation dissociations in hcp metals. Journal of Applied Physics, 41(5):1893–1910, 1970.

[54] I. J. Beyerlein, J. Wang, M. R. Barnett, and C. N. Tomé. Double twinning mechanisms in magnesium alloys via dissociation of lattice dislocations. Proceedings of the Royal Society A, 468(2141):1496–1520, 2012.

[55] S. H. Simon. The Oxford solid state basics. OUP Oxford, 2013.

[56] J. W. Christian. The Theory of Transformations in Metals and Alloys, Part 1 (Second edition). International series on materials science and technology. Elsevier Science, 1975.

[57] M. De Graef and M. E. McHenry. Structure of Materials: An Introduction to Crystallography, Diffraction and Symmetry (Second Edition). Cambridge University Press, 2012.

[58] P. R. Okamoto and G. Thomas. On the four-axis hexagonal reciprocal lattice and its use in the indexing of transmission electron diffraction patterns. physica status solidi (b), 25(1):81–91, 1968.

[59] F. C. Frank. On Miller–Bravais indices and four-dimensional vectors. Acta Crystallographica, 18(5):862–866, 1965.

[60] R. C. Pond. Seminal ideas on the structure of interfaces. Sir Charles Frank OBE, FRS, An Eightieth Birthday Tribute, 1991.

[61] R. C. Pond, M. Aindow, and W. A. T. Clark. Hexagonal crystallography and interphase boundary dislocations. Scripta Metallurgica, 21(7):971–974, 1987.

[62] R. C. Pond, N. A. McAuley, A. Serra, and W. A. T. Clark. Transformation matrices for hexagonal and trigonal crystals. Scripta Metallurgica, 21(2):197–202, 1987.

[63] H. K. D. H. Bhadeshia. Worked examples in the geometry of crystals (Second edition). The Institute of Materials, 2001.

[64] J. W. Christian and S. Mahajan. Deformation twinning. Progress in Materials Science, 39(1):1–157, 1995.

[65] R. W. Cahn. Soviet work on mechanical twinning. Il Nuovo Cimento Series 9, 10(4 Supplement):350–386, 1953.

[66] R. W. Cahn. Twinned crystals. Advances in Physics, 3(12):363–445, 1954.

[67] E. O. Hall. Twinning and diffusionless transformations. Butterworths, 1954.

[68] N. V. Klassen-Neklyudova. Mechanical twinning of crystals. Plenum Press, 1964.

[69] J. W. Christian. The Theory of Transformations in Metals and Alloys (First edition). International series on materials science and technology. Elsevier Science, 1965.

[70] M. A. Jaswon and D. B. Dove. Twinning properties of lattice planes. Acta Crystallographica, 9(8), 1956.

[71] M. A. Jaswon and D. B. Dove. The prediction of twinning modes in metal crystals. Acta Crystallographica, 10(1):14–18, 1957.

[72] M. A. Jaswon and D. B. Dove. The crystallography of deformation twinning. Acta Crystallographica, 13(3), 1960.

[73] H. Kiho. The cristallographic aspect of the mechanical twinning in metals. Journal of the Physical Society of Japan, 9(5):739–747, 1954.

[74] H. Kiho. The crystallographic aspect of the mechanical twinning in Ti and U. Journal of the Physical Society of Japan, 13(3):269–272, 1958.

[75] B. A. Bilby and A. G. Crocker. The theory of the crystallography of deformation twinning. Proceedings of the Royal Society of London A, 288(1413):240–255, 1965.

[76] M. Bevis and A. G. Crocker. Twinning shears in lattices. Proceedings of the Royal Society of London A, 304(1476):123–134, 1968.

[77] M. Bevis and A. G. Crocker. Twinning modes in lattices. Proceedings of the Royal Society of London A, 313(1515):509–529, 1969.

[78] A. Serra, D. J. Bacon, and R. C. Pond. The crystallography and core structure of twinning dislocations in H.C.P. metals. Acta Metallurgica, 36(12):3183 – 3203, 1988.

[79] M. H. Yoo. Slip, twinning, and fracture in hexagonal close-packed metals. Metallurgical Transactions, A; (United States), 12, 1981.

[80] A. G. Crocker. PhD thesis, University of Sheffield, 1959.

[81] J. A. Moriarty. Zero-order pseudoatoms and the generalized pseudopotential theory. Physical Review B, 10:3075–3091, 1974.

[82] J. A. Moriarty. First-principles interatomic potentials in transition metals. Physical Review Letters, 55:1502–1505, 1985.

[83] John A. Moriarty. Density-functional formulation of the generalized pseudopotential theory. III. Transition-metal interatomic potentials. Physical Review B, 38:3199–3231, 1988.

[84] J. A. Moriarty and J. D. Althoff. First-principles temperature-pressure phase diagram of magnesium. Physical Review B, 51:5609–5616, 1995.

[85] N.W. Ashcroft and N.D. Mermin. Solid State Physics. HRW international editions. Holt, Rinehart and Winston, 1976.

[86] B. J. Austin, V. Heine, and L. J. Sham. General theory of pseudopotentials. Physical Review, 127(1):276, 1962.

[87] S. Ichimaru and K. Utsumi. Analytic expression for the dielectric screening function of strongly coupled electron liquids at metallic and lower densities. Physical Review B, 24(12):7385, 1981.

[88] S. H. Vosko, L. Wilk, and M. Nusair. Accurate spin-dependent electron liquid correlation energies for local spin density calculations: a critical analysis. Canadian Journal of physics, 58(8):1200–1211, 1980.

[89] J. D. Althoff, P. B. Allen, R. M. Wentzcovitch, and J. A. Moriarty. Phase diagram and thermodynamic properties of solid magnesium in the quasiharmonic approximation. Physical Review B, 48(18):13253, 1993.

[90] G. C. G. Skinner, A. T. Paxton, and J. A. Moriarty. Local volume effects in the generalized pseudopotential theory. Physical Review B, 99(21):1–11, 2019.

[91] M. Ruffino, G. C. G. Skinner, E. I. Andritsos, and A. T. Paxton. Ising-like models for stacking faults in a free electron metal. Proceedings of the Royal Society A, 476(2242), 2020.

[92] G. C. G. Skinner. Novel quantum-based interatomic potentials applied to magnesium and its alloys. PhD thesis, King's College London, 2019.

[93] J. A. Moriarty and R. Phillips. First-principles interatomic potentials for transition-metal surfaces. Physical Review Letters, 66:3036–3039, 1991.

[94] R. C. Pond. The crystallographic theory of dislocations in interfaces. MRS Proceedings, 122:49, 1988.

[95] A. Shubnikov, V. A. Koptsik, G. D. Archard, D. Harker, and S. C. Abrahams. Symmetry in Science and Art. Plenum, 1974.

[96] T. Hahn. International Tables for Crystallography, Volume A: Space Group Symmetry. International Tables for Crystallography. Springer Netherlands, 2005.

[97] A. P. Sutton and R. W. Balluffi. Interfaces in Crystalline Materials. Monographs on the Physics and Chemistry of Materials. Clarendon Press, 1996.

[98] R. C. Pond and F. R. N. Nabarro (Editor). Line defects in interfaces. Dislocations in Solids, 8, 1989.

[99] R. C. Pond and D. S. Vlachavas. Bicrystallography. Proceedings of the Royal Society A, 386(1790):95–143, 1983.

[100] N. V. Belov and T. N. Tarkhova. Groups of colour symmetry (in Russian). Soviet Physical Crystallography I, pages 4–13, 1956.

[101] M. A. Fortes. Coincidence site lattices. physica status solidi (b), 54(1):311–319, 1972.

[102] H. Grimmer. Coincidence-site lattices. Acta Crystallographica Section A, 32(5):783–785, 1976.

[103] M. A. Fortes. Coincidence site lattices in non-cubic lattices. physica status solidi (b), 82(1):377–382, 1977.

[104] R. C. Pond, D. J. Bacon, A. Serra, and A. P. Sutton. The crystallography and atomic structure of line defects in twin boundaries in hexagonal-close-packed metals. Metallurgical Transactions A, 22:1185–1196, 1991.

[105] R. C. Pond and J. P. Hirth. Defects at surfaces and interfaces. Solid State Physics, 47:287–365, 1994.

[106] V. Volterra. Sur l'équilibre des corps élastiques multiplement connexes. Annales scientifiques de l'École Normale Supérieure, 24:401–517, 1907.

[107] J. P. Hirth. Dislocations, steps and disconnections at interfaces. Journal of Physics and Chemistry of Solids, 55(10):985–989, 1994.

[108] J. P. Hirth and R. C. Pond. Steps, dislocations and disconnections as interface defects relating to structure and phase transformations. Acta Materialia, 44(12):4749–4763, 1996.

[109] W. Bollmann. Crystal Defects and Crystalline Interfaces. Springer Berlin Heidelberg, 1970.

[110] E. Bitzek, P. Koskinen, F. Gähler, M. Moseler, and P. Gumbsch. Structural relaxation made simple. Physical Review Letters, 97:170201, 2006.

[111] A. Serra and D. J. Bacon. Computer simulation of twinning dislocation in magnesium using a many-body potential. Philosophical Magazine A, 63(5):1001–1012, 1991.

[112] K. V. Vladimirskij. Journal of Experimental and Theoretical Physics, 1947.

[113] J. H. Van Der Merwe F. C. Frank. One-dimensional dislocations. II. misfitting monolayers and oriented overgrowth. Proceedings of the Royal Society A, 198(1053):216–225, 1949.

[114] P. M. Anderson, J. P. Hirth, and J. Lothe. Theory of Dislocations. Cambridge University Press, 2017.

[115] A. Serra, R. C. Pond, and D. J. Bacon. Computer simulation of the structure and mobility of twinning disclocations in H.C.P. metals. Acta Metallurgica et Materialia, 39(7):1469–1480, 1991.

[116] A. Serra and D. J. Bacon. A new model for $\{10\bar{1}2\}$ twin growth in HCP metals. Philosophical Magazine A, 73(2):333–343, 1996.

[117] R. C. Pond, A. Serra, and D. J. Bacon. Dislocations in interfaces in the h.c.p. metals—II. Mechanisms of defect mobility under stress. Acta Materialia, 47(5):1441–1453, 1999.

[118] A. Serra, N. Kvashin, and N. Anento. On the common topological conditions for shear-coupled twin boundary migration in bcc and hcp metals. Letters on Materials, 10(4s):537–542, 2020.

[119] A. Serra and D. J. Bacon. On the generation of twinning dislocations in HCP twin boundaries. In Intergranular and Interphase Boundaries in Materials II, volume 207 of Materials Science Forum, pages 553–556. Trans Tech Publications Ltd, 1996.

[120] D. J. Bacon, R. C. Pond, and A. Serra. The structure of defects formed by absorption of crystal dislocations in interfaces in the HCP metals. MRS Online Proceedings Library (OPL), 578:371, 1999.

[121] A. Serra and D. J. Bacon. A model for simulating the motion of line defects in twin boundaries in HCP metals. Zeitschrift für Metallkunde, 95:242–243, 2004.

[122] A. Serra and D. J. Bacon. Modelling the motion of $\{11\bar{2}2\}$ twinning dislocations in the hcp metals. Materials Science and Engineering: A, 400-401:496–498, 2005. Dislocations 2004.

[123] A. Serra and D. J. Bacon. Interaction of a moving $\{10\bar{1}2\}$ twin boundary with perfect dislocations and loops in an hcp metal. Philosophical Magazine, 90:845–861, 2010.

[124] R. C. Pond, J. P. Hirth, A. Serra, and D. J. Bacon. Atomic displacements accompanying deformation twinning: shears and shuffles. Materials Research Letters, 4(4):185–190, 2016.

[125] J. P. Hirth, J. Wang, and C. N. Tomé. Disconnections and other defects associated with twin interfaces. Progress in Materials Science, 83:417–471, 2016.

[126] H. A. Khater, A. Serra, and R. C. Pond. Atomic shearing and shuffling accompanying the motion of twinning disconnections in zirconium. Philosophical Magazine, 93(10-12):1279–1298, 2013.

[127] J. Wang, I. J. Beyerlein, J. P. Hirth, and C. N. Tomé. Twinning dislocations on $\{\bar{1}011\}$ and $\{\bar{1}013\}$ planes in hexagonal close-packed crystals. Acta Materialia, 59(10):3990–4001, 2011.

[128] A. Serra and D. J. Bacon. Computer simulation of screw dislocation interactions with twin boundaries in H.C.P. metals. Acta Metallurgica et Materialia, 43(12):4465–4481, 1995.

[129] R. C. Pond, D. J. Bacon, and A. Serra. Interfacial structure of $\{10\bar{1}1\}$ twins and twinning dislocations in titanium. Philosophical Magazine Letters, 71(5):275–284, 1995.

[130] A. B. Acton, M. Bevis, A. G. Crocker, and N. D. H. Ross. Transformation strains in lattices. Proceedings of the Royal Society of London A, 320(1540):101–113, 1970.

[131] J. K. Mackenzie and J. S. Bowles. The crystallography of martensite transformations—IV body-centred cubic to orthorhombic transformations. Acta Metallurgica, 2(2):138, 1954.

[132] J. W. Christian. The Theory of Transformations in Metals and Alloys. International series on materials science and technology. Elsevier Science, 2002.

[133] A. J. McConnell. Applications of Tensor Analysis. Dover Books on Mathematics. Dover Publications, 1957.

[134] A. T. Paxton. Deformation twinning in the intermetallic compound Cu_2Sb, Third year Project, 1984. Department of Metallurgy, University of Sheffield.

[135] A. G. Crocker, F. Heckscher, M. Bevis, and D. M. M. Guyoncourt. A single surface analysis of deformation twins in crystalline mercury. Philosophical Magazine, 13(126):1191–1205, 1966.

[136] A. T. Paxton and A. R. Entwisle. Deformation twinning in the intermetallic compound Cu_2Sb. Philosophical Magazine A, 52(4):573–579, 1985.

[137] T. Hahn. International Tables for Crystallography. Brief Teaching Edition of Volume A, Space-group Symmetry. International Union of Crystallography, 1985.

[138] W. Bollmann. Crystal Lattices, Interfaces, Matrices. 1982.

[139] R. C. Pond, B. Karki, and P. Mullner. Non-classical twinning: Phenomenological and mechanistic modelling. In preparation.

[140] F. C. Frank. Symposium on the the plastic deformation of crystalline solids, 1950.

[141] B. A. Bilby. Report on the conference on defects in crystalline solids, 1955.

[142] J. P. Hirth, R. C. Pond, R. G. Hoagland, X.-Y. Liu, and J. Wang. Interface defects, reference spaces and the Frank–Bilby equation. Progress in Materials Science, 58(5):749–823, 2013.

[143] J. P. Hirth and R. C. Pond. Strains and rotations in thin deposited films. Philosophical Magazine, 90(23):3129–3147, 2010.

[144] J. Wang, J. P. Hirth, R. C. Pond, and J. M. Howe. Rotational partitioning at two-phase interfaces. Acta Materialia, 59(1):241–251, 2011.

[145] R. C. Pond and S. Celotto. Special interfaces: military transformations. International Materials Reviews, 48(4):225–245, 2003.

[146] A. Ostapovets and A. S. Gornakova. On faceting of $\{10\bar{1}1\}$ and $\{10\bar{1}2\}$ twin boundaries in hcp metals. Materials Letters, 247:99–101, 2019.

[147] A. Ostapovets and R. Gröger. Twinning disconnections and basal–prismatic twin boundary in magnesium. Modelling and Simulation in Materials Science and Engineering, 22(2):025015, 2014.

[148] A. Ostapovets and A. Serra. Characterization of the matrix–twin interface of a $(10\bar{1}2)$ twin during growth. Philosophical Magazine, 94(25):2827–2839, 2014.

[149] A. Ostapovets, J. Buršík, and R. Gröger. Deformation due to migration of faceted $\{10\bar{1}2\}$ twin boundaries in magnesium and cobalt. Philosophical Magazine, 95(36):4106–4117, 2015.

[150] C. D. Barrett and H. El Kadiri. The roles of grain boundary dislocations and disclinations in the nucleation of $\{10\bar{1}2\}$ twinning. Acta Materialia, 63:1–15, 2014.

[151] C. D. Barrett and H. El Kadiri. Fundamentals of mobile tilt grain boundary faceting. Scripta Materialia, 84-85:15–18, 2014.

[152] C. D. Barrett and H. El Kadiri. Impact of deformation faceting on $\{10\bar{1}2\}$,$\{10\bar{1}1\}$ and $\{10\bar{1}3\}$ embryonic twin nucleation in hexagonal close-packed metals. Acta Materialia, 70:137–161, 2014.

[153] M. Gong, J. P. Hirth, Y. Liu, Y. Shen, and J. Wang. Interface structures and twinning mechanisms of twins in hexagonal metals. Materials Research Letters, 5(7):449–464, 2017.

[154] J. P. Hirth, R. C. Pond, and J. Lothe. Disconnections in tilt walls. Acta Materialia, 54(16):4237–4245, 2006.

[155] A. E. Romanov. Disclinations in crystalline solids. Dislocations in solids, 9, 1992.

[156] T. Laub and J. D. Eshelby. The velocity of a wave along a dislocation. Philosophical Magazine, 14(132):1285–1293, 1966.

[157] J. C. M. Li. Disclination model of high angle grain boundaries. Surface Science, 31:12–26, 1972.

[158] Y. Yue and J. F. Nie. Interaction between migrating $(10\bar{1}2)$ twin boundary and extended $\langle a \rangle$ dislocations inside twin in pure Mg. Scripta Materialia, 218:114842, 2022.

[159] A. Serra, D. J. Bacon, and R. C. Pond. Dislocations in interfaces in the h.c.p. metals—I. Defects formed by absorption of crystal dislocations. Acta Materialia, 47(5):1425–1439, 1999.

[160] H. Khater. PhD thesis, The University of Liverpool, 2008.

[161] H. Su, X. Zhou, S. Zheng, H. Ye, and Z. Yang. Atomic-resolution studies on reactions between basal dislocations and $\{10\bar{1}2\}$ coherent twin boundaries in a Mg alloy. Journal of Materials Science & Technology, 66:28–35, 2021.

[162] X. Y. Zhang, B. Li, X. L. Wu, Y. T. Zhu, Q. Ma, Q. Liu, P. T. Wang, and M. F. Horstemeyer. Twin boundaries showing very large deviations from the twinning plane. Scripta Materialia, 67(10):862–865, 2012.

[163] J. Tu, X. Zhang, J. Wang, Q. Sun, Q. Liu, and C. N. Tomé. Structural characterization of $\{10\bar{1}2\}$ twin boundaries in cobalt. Applied Physics Letters, 103(5):051903, 2013.

[164] J. Zhang, G. Xi, X. Wan, and C. Fang. The dislocation-twin interaction and evolution of twin boundary in AZ31 Mg alloy. Acta Materialia, 133:208–216, 2017.

[165] H. Su, X. Zhou, S. Zheng, H. Ye, and Z. Yang. Dislocation facilitated formation and evolution of basal-prismatic/prismatic-basal interfaces in a Mg alloy. Scripta Materialia, 206:114237, 2022.

[166] D.F. Shi, C.Y. Wang, C.M. Cepeda-Jiménez, and M.T. Pérez-Prado. Atomic scale interactions of basal dislocations and twin boundaries with ultrathin precipitates in magnesium alloys. Acta Materialia, 221:117442, 2021.

[167] F. Wang, C. D. Barrett, R. J. McCabe, H. El Kadiri, L. Capolungo, and S. R. Agnew. Dislocation induced twin growth and formation of basal stacking faults in $\{10\bar{1}2\}$ twins in pure Mg. Acta Materialia, 165:471–485, 2019.

[168] N. M. della Ventura, A. Sharma, S. Kalácska, M. Jain, T. E. J. Edwards, C. Cayron, R. Logé, J. Michler, and X. Maeder. Evolution of deformation twinning mechanisms in magnesium from low to high strain rates. Materials & Design, 217:110646, 2022.

[169] S. Lay and G. Nouet. Morphology of $(01\bar{1}2)$ twins in zinc and related interfacial defects. Philosophical Magazine A, 72(3):603–617, 1995.

[170] T. Braisaz, P. Ruterana, and G. Nouet. Twin tip defects related to the nucleation and growth mechanisms of the twin $(10\bar{1}2)$ in zinc characterized by high-resolution electron microscopy. Philosophical Magazine A, 76(1):63–84, 1997.

[171] Q. Sun, X. Y. Zhang, Y. Ren, J. Tu, and Q. Liu. Interfacial structure of $\{10\bar{1}2\}$ twin tip in deformed magnesium alloy. Scripta Materialia, 90-91:41–44, 2014.

[172] Y. J. Li, Y. J. Chen, J. C. Walmsley, R. H. Mathinsen, S. Dumoulin, and H. J. Roven. Faceted interfacial structure of $\{10\bar{1}1\}$ twins in Ti formed during equal channel angular pressing. Scripta Materialia, 62(7):443–446, 2010.

[173] H. Li, Q. Zeng, P. Yang, Q. Sun, J. Wang, J. Tu, and M. Zhu. Towards understanding twinning behavior near fracture surface in magnesium. Journal of Materials Science & Technology, 43:230–237, 2020.

[174] J. Zhang, G. Xi, and X. Wan. $(10\bar{1}1)$ twin boundary showing very large deviation from the theoretical one in deformed magnesium alloy. Materials Characterization, 132:280–283, 2017.

[175] Q. Sun, X. Y. Zhang, Y. C. Wang, Y. Ren, L. Tan, and Q. Liu. Structural characterization of $\{10\bar{1}1\}$ twin boundaries in deformed cobalt. Materials Characterization, 116:44–47, 2016.

[176] Q. Sun, X. Y. Zhang, R. S. Yin, Y. Ren, and L. Tan. Structural characterization of $\{10\bar{1}3\}$ twin boundaries in deformed cobalt. Scripta Materialia, 108:109–112, 2015.

[177] I. Basu and T. Al-Samman. Hierarchical twinning induced texture weakening in lean magnesium alloys. Frontiers in Materials, 6, 2019.

[178] R. Xin, M. Wang, X. Huang, C. Guo, and Q. Liu. Observation and Schmid factor analysis of multiple twins in a warm-rolled Mg–3Al–1Zn alloy. Materials Science and Engineering: A, 596:41–44, 2014.

[179] Q. Yu, Y. Jiang, and J. Wang. Tension-compression-tension tertiary twins in coarse-grained polycrystalline pure magnesium at room temperature. Philosophical Magazine Letters, 95(4):194–201, 2015.

[180] S. Mu, J. J. Jonas, and G. Gottstein. Variant selection of primary, secondary and tertiary twins in a deformed Mg alloy. Acta Materialia, 60(5):2043–2053, 2012.

[181] M. Lentz, R. S. Coelho, B. Camin, C. Fahrenson, N. Schaefer, S. Selve, T. Link, I. J. Beyerlein, and W. Reimers. In-situ, ex-situ EBSD and (HR-)TEM analyses of primary, secondary and tertiary twin development in an Mg–4wt%Li alloy. Materials Science and Engineering: A, 610:54–64, 2014.

[182] P. Chen, F. Wang, J. Ombogo, and B. Li. Formation of $60^\circ\langle 01\bar{1}0\rangle$ boundaries between $\{10\bar{1}2\}$ twin variants in deformation of a magnesium alloy. Materials Science and Engineering: A, 739:173–185, 2019.

[183] L. Carneiro, D. Culbertson, Q. Yu, and Y. Jiang. Twinning in rolled AZ31B magnesium alloy under free-end torsion. Materials Science and Engineering: A, 801:140405, 2021.

[184] Q. Li, H. Yan, and R. Chen. Effect of rolling reduction on deformation mechanism and twinning behavior of WE43 magnesium alloy. Transactions of Nonferrous Metals Society of China, 32(12):3901–3913, 2022.

[185] S. Niknejad, S. Esmaeili, and N. Y. Zhou. The role of double twinning on transgranular fracture in magnesium AZ61 in a localized stress field. Acta Materialia, 102:1–16, 2016.

[186] L. Tang, Y. Zhao, N. Liang, R. K. Islamgaliev, R. Z. Valiev, and Y. T. Zhu. Localized deformation via multiple twinning in a Mg–Gd–Y–Zr alloy processed by high-pressure torsion. Materials Science and Engineering: A, 677:68–75, 2016.

[187] J. Luo, H. Yan, L. W. Lu, R. S. Chen, A. R. Wu, and F. C. Yin. Cold rollability improvement by twinning and twin–slip synergy in an Mg–Zn–Gd alloy with rare earth texture. Journal of Alloys and Compounds, 883:160813, 2021.

[188] D. Ando, J. Koike, and Y. Sutou. Relationship between deformation twinning and surface step formation in AZ31 magnesium alloys. Acta Materialia, 58(13):4316–4324, 2010.

[189] X. Wang, L. Jiang, A. Luo, J. Song, Z. Liu, F. Yin, Q. Han, S. Yue, and J. J. Jonas. Deformation of twins in a magnesium alloy under tension at room temperature. Journal of Alloys and Compounds, 594:44–47, 2014.

[190] L. De Broglie. Recherches sur la théorie des Quanta. Annales de Physique, 10(3):22–128, 1925.

[191] M. Knoll and E. Ruska. Das Elektronenmikroskop. Zeitschrift fur Physik, 78(5-6):318–339, 1932.

[192] D. B. Williams and C. B. Carter. Transmission Electron Microscopy: A Textbook for Materials Science. Cambridge library collection. Springer, 2009.

[193] W. H. Bragg and W. L. Bragg. The reflection of X-rays by crystals. Proceedings of the Royal Society A, 88(605):428–438, 1913.

[194] P. B. Hirsch and A. Howie. Electron Microscopy of Thin Crystals. R. E. Krieger Publishing Company, 1977.

[195] M. von Laue. Kritische Bemerkungen zu den Deutungen der Photogramme von Friedrich und Knipping. Physikalische Zeitschrift, 14(10):421–423, 1913.

[196] S. Nishikawa and S. Kikuchi. Diffraction of cathode rays by mica. Nature, 121(3061):1019–1020, 1928.

[197] H. Seiler. Secondary electron emission in the scanning electron microscope. Journal of Applied Physics, 54(11):R1–R18, 1983.

[198] A. Zangwill. Physics at Surfaces. Cambridge University Press, 1988.

[199] V. Randle. Electron backscatter diffraction: Strategies for reliable data acquisition and processing. Materials Characterization, 60(9):913–922, 2009.

[200] R. A. Schwarzer, D. P. Field, B. L. Adams, M. Kumar, and A. J. Schwartz. Present State of Electron Backscatter Diffraction and Prospective Developments. 2008.

[201] X. Zeng. Deformation and recrystallization mechanisms of Mg-Al-Nd and Mg-Zn-Nd alloys. PhD thesis, Technischen Universität Berlin, 2021.

[202] J. F. Aebersold, P. A. Stadelmann, and M. Matlosz. A rotating disk electropolishing technique for TEM sample preparation. Ultramicroscopy, 62(3):157–169, 1996.

[203] X. An, S. Ni, and M. Song. A new double twinning mode in a cold-rolled Zr alloy. Philosophical Magazine Letters, 99(1):21–28, 2019.

[204] M. Ruffino, J. Nutter, X. Zeng, D. Guan, W. M. Rainforth, and A. T. Paxton. Triple and double twin interfaces in magnesium—the role of disconnections and facets. Scientific Reports, 13(1), 2023.

[205] X. Zhao, H. Chen, N. Wilson, Q. Liu, and J. F. Nie. Direct observation and impact of co-segregated atoms in magnesium having multiple alloying elements. Nature Communications, 10(1), 2019.

[206] J. Zhang, Y. Dou, and Y. Zheng. Twin-boundary segregation energies and solute-diffusion activation enthalpies in Mg-based binary systems: A first-principles study. Scripta Materialia, 80:17–20, 2014.

[207] A. J. D'Alfonso, B. Freitag, D. Klenov, and L. J. Allen. Atomic-resolution chemical mapping using energy-dispersive X-ray spectroscopy. Physical Review B, 81:100101, 2010.

[208] M.-W. Chu, S. C. Liou, C.-P. Chang, F.-S. Choa, and C. H. Chen. Emergent chemical mapping at atomic-column resolution by energy-dispersive X-ray spectroscopy in an aberration-corrected electron microscope. Physical Review Letters, 104:196101, 2010.

[209] D. O. Klenov and J. M. O. Zide. Structure of the InAlAs/InP interface by atomically resolved energy dispersive spectroscopy. Applied Physics Letters, 99(14):141904, 2011.

[210] G. Kothleitner, M. J. Neish, N. R. Lugg, S. D. Findlay, W. Grogger, F. Hofer, and L. J. Allen. Quantitative elemental mapping at atomic resolution using X-ray spectroscopy. Physical Review Letters, 112:085501, 2014.

[211] S. R. Kada, P. A. Lynch, J. A. Kimpton, and M. R. Barnett. In-situ X-ray diffraction studies of slip and twinning in the presence of precipitates in AZ91 alloy. Acta Materialia, 119:145–156, 2016.

[212] N. Stanford, A. S. Taylor, P. Cizek, F. Siska, M. Ramajayam, and M. R. Barnett. $\{10\bar{1}2\}$ Twinning in magnesium-based lamellar microstructures. Scripta Materialia, 67(7):704–707, 2012.

[213] J. D. Robson and M. R. Barnett. The effect of precipitates on twinning in magnesium alloys. Advanced Engineering Materials, 21(4):1800460, 2019.

[214] X. Ma, Q. Jiao, L. J. Kecskes, J. A. El-Awady, and T. P. Weihs. Effect of basal precipitates on extension twinning and pyramidal slip: A micro-mechanical and electron microscopy study of a Mg–Al binary alloy. Acta Materialia, 189:35–46, 2020.

[215] H. Fan, Y. Zhu, J. A. El-Awady, and D. Raabe. Precipitation hardening effects on extension twinning in magnesium alloys. International Journal of Plasticity, 106:186–202, 2018.

[216] M. R. Barnett, H. Wang, and T. Guo. An Orowan precipitate strengthening equation for mechanical twinning in Mg. International Journal of Plasticity, 112:108–122, 2019.

[217] C. Liu, P. Shanthraj, J. D. Robson, M. Diehl, S. Dong, J. Dong, W. Ding, and D. Raabe. On the interaction of precipitates and tensile twins in magnesium alloys. Acta Materialia, 178:146–162, 2019.

[218] J. D. Robson. The effect of internal stresses due to precipitates on twin growth in magnesium. Acta Materialia, 121:277–287, 2016.

[219] J. Wang, M. Reza Ghandehari Ferdowsi, P. A. Lynch, S. R. Kada, and M. R. Barnett. Influence of precipitation on tension and compression twinning in Mg-6.5Zn alloy. Scripta Materialia, 207:114253, 2022.